PASSIVE IMAGING AND CHARACTERIZATION OF THE SUBSURFACE WITH DISTRIBUTED ACOUSTIC SENSING

A DISSERTATION
SUBMITTED TO THE INSTITUTE FOR COMPUTATIONAL AND MATHEMATICAL ENGINEERING
AND THE COMMITTEE ON GRADUATE STUDIES
OF STANFORD UNIVERSITY
IN PARTIAL FULFILLMENT OF THE REQUIREMENTS
FOR THE DEGREE OF
DOCTOR OF PHILOSOPHY

Eileen R. Martin
June 2018

Abstract

Active seismic surveys for subsurface imaging are expensive and logistically difficult in populated areas where they have potential to impact day-to-day life, so continuous monitoring experiments are rarely done. I combine two methods to make continuous subsurface monitoring cheaper: estimating wave equation Green's functions from passive vibration recordings, and measuring meter-scale strain rate profiles along fiber optic cables which may already exist in urban areas or can easily be installed along infrastructure.

These methods may make continuous high-resolution subsurface imaging possible where it was not previously, but there are challenges. The shift from particle velocity data of seismometers to axial strain rates recorded by fibers leads to different responses to the same source. Additionally, signals extracted from ambient seismic noise interferometry are masked by a fundamentally different receiver response. I use data from multiple fiber optic surface arrays: two with fiber directly coupled to the ground intended for permafrost thaw monitoring, and one with fiber sitting loosely in existing telecommunications conduits. Although these data look different, the arrival times of earthquakes at known times verify that the arrays record vibrations over a wide range of frequencies.

Care must be taken to understand and mitigate the effects of non-ideal anthropogenic noise when doing ambient seismic noise in urban areas and around infrastructure. I use interferometry to extract repeatable signals for near-surface geotechnical characterization near infrastructure, even between fiber channels that are not collinear. I investigate temporal stability and changes in signals extracted throughout large arrays in the presence of a changing subsurface and noise field. As ambient noise practitioners begin using denser arrays, the typical cross-correlation process can become expensive, so I propose a new algorithm for dispersion image calculation that is an order of magnitude faster and parallelizable.

Preface

The electronic version of this report[1] makes the included programs and applications available to the reader. The markings **ER**, **CR**, and **NR** are promises by the author about the reproducibility of each figure result. Reproducibility is a way of organizing computational research that allows both the author and the reader of a publication to verify the reported results. Reproducibility facilitates the transfer of knowledge within SEP and outside of SEP.

ER denotes Easily Reproducible and are the results of processing described in the paper. The author claims that you can reproduce such a figure from the programs, parameters, and makefiles included in the electronic document. The data must either be included in the electronic distribution, be easily available to all researchers (e.g., SEG-EAGE data sets), or be available in the SEP data library[2]. We assume you have a UNIX workstation with Fortran, Fortran90, C, Python (with typical free packages available through Anaconda), C++, X-Windows system and the software downloadable from our website (including SEPlib), or other free software such as SU or FFTW. Before the publication of the electronic document, someone other than the author tests the author's claim by destroying and rebuilding all ER figures. Some ER figures may not be reproducible by outsiders because they depend on data sets that are too large to distribute, or data that we do not have permission to redistribute but are in the SEP data library, or that the rules depend on commercial packages such as Matlab or Mathematica.

CR denotes Conditional Reproducibility. The author certifies that the commands are in place to reproduce the figure if certain resources are available. The primary reasons

[1] http://sepwww.stanford.edu/public/docs/sep173
[2] http://sepwww.stanford.edu/public/docs/sepdatalib/toc_html/

for the CR designation is that the data are not in the SEP library or the processing requires 20 minutes or more.

NR denotes Non-Reproducible figures. SEP discourages authors from flagging their figures as NR except for figures that are used solely for motivation, comparison, or illustration of the theory, such as: artist drawings, scannings, or figures taken from SEP reports not by the authors or from non-SEP publications.

Our testing is currently limited to LINUX 2.6 (using the Intel Fortran90 compiler) and the SEPlib-6.4.6 distribution, but the code should be portable to other architectures. Reader's suggestions are welcome. For more information on reproducing SEP's electronic documents, please visit *http://sepwww.stanford.edu/research/redoc/*.

Acknowledgments

I never expected funding sources to have much of an impact on my work beyond writing a check, but my funding sources throughout graduate school (and more importantly, the interactions tied to that funding) has shaped me as a researcher. My first four years of graduate school were funded by the US Department of Energy Computational Science Graduate Fellowship Program under grant DE-FG02-97ER25308. In my practicum at Lawrence Livermore National Laboratory, where I was mentored by Dr. Steve Langer, I got to explore a totally different problem, laser-plasma simulations. Every year at the program review I learned new things and got to develop some wonderful friendships. I greatly appreciate the efforts of the late Dr. James Corones and the Krell Institute staff to keep this program strong even in the face of budget cuts and calls for graduate fellowship consolidation, and I know it will continue to mold students long into the future. In my fifth year, I was funded partially through a Schlumberger Innovation Fellowship, a partnership between ICME and Schlumberger's Software Technology Innovation Center, where I also spent one summer doing an exciting project as a high performance computing intern.

I joined the Stanford Exploration Project research group in summer 2013, and have received funding through the SEP affiliates program throughout my time in the group, with it being my primary funding source my fifth and sixth years of graduate school. I have learned so much from discussions with our many sponsors in the energy industry at our annual affiliates meeting. In particular, I would like to thank Dr. Martin Karrenbach and Dr. Steve Cole, both SEP alums and geophysicists at OptaSense. Martin's efforts to facilitate the long-term interrogator unit loan for the experiment at Stanford have allowed me the opportunity to work on a unique and exciting experiment from acquisition design to data acquisition to computational analysis and theoretical understanding. Martin and

Steve's guidance on working with the data, particularly Steve's insights into earthquake observations, have been invaluable. In addition to OptaSense, there were a number of groups at Stanford who make the DAS array possible: Stanford IT who installed and continue to support the fibers, School of Earth Sciences IT who support our data flow and gave us a safe location for the interrogator unit, and Stanford Center for Computational Earth and Environmental Sciences who provide computing and data storage resources.

To my advisor, Dr. Biondo Biondi, thank you for facilitating an environment where students are expected to define their own research, ask their own questions, work together, make connections and collaborations outside our university, and mentor junior students as they move forward. This approach ensured that I came out of school ready to work independently and prepared for multiple career paths. SEP is an ecosystem with many creatures. Dr. Bob Clapp is certainly the plankton of the group, giving the rest of us the resources and ability to pursue our goals. Whether discussing imaging, algorithm parallelization, cloud computing, data compression, or generally how to do research, I always get something useful from time with Bob. If I were an otter, Jason Chang would be a kelp forest. I often show up at his office, get wrapped up in a conversation about an ambient noise problem, then he keeps me from floating off into the ocean of minor secondary effects, and instead gets me to spend my time trying to open the mollusk that is the actual problem I showed up there to understand. Additionally, my collaborations with Fantine Huot have been fun and exciting. Each person in SEP has contributed to my experience: Jon Claerbout, Stewart A. Levin, Shuki Ronen, Sjoerd de Ridder, Adam Halpert, Elita Li, Mandy Wong, Xukai Shen, Yang Zhang, Chris Leader, Ali Almomin, Musa Maharramov, Yi Shen, Ohad Barak, Gustavo Alves, Huy Le, Taylor Dahlke, Yinbin Ma, Guillaume Barnier, Ettore Biondi, Alejandro Cabrales, Kaixi Ruan, Rahul Sarkar, Joe Jennings, Stuart Farris, Miguel Ferrer, Rustam Akhmadiev, and Siyuan Yuan.

The efforts of many people and groups have made the data collection at the Stanford Fiber Optic Seismic Observatory possible: Stanford IT fiber infrastructure team (particularly Gary Gutfeld and Gregory Kersey), ongoing support from the Stanford School of Earth Sciences IT, continued support from OptaSense, and computing resources through the Stanford Center for Computational Earth and Environmental Sciences.

During my LLNL practicum, I rented a room Livermore from Brian Bonner and Eva

Westerlin, who are generous, fun people, and fabulous stir fry chefs! I had been trying and mostly failing to come up with a thesis topic. Since Brian is a rock physicist, we had some great conversations about geophysics problems. Realizing that my interests aligned with an upcoming permafrost thaw monitoring experiment at Lawrence Berkeley Lab (LBL), Brian put me in touch with Dr. Jonathan Ajo-Franklin.

To Jonathan, thank you for getting me involved in the area of continuous seismic monitoring and fiber optics, for serving on my committee, for your enthusiasm, and for being an inspiring role model who easily flexes from science to engineering, and from experiment to theory to computation. I would like to thank all the researchers at LBL and the US Army Corps of Engineers Cold Regions Research and Engineering Laboratory working on the project "Developing Smart Infrastructure for a Changing Arctic Environment Using Distributed Fiber-Optic Sensing Methods" led by PI Dr. Jonathan Ajo-Franklin and co-PI Dr. Anna Wagner and funded through SERDP grand RC-2437. This includes: Kevin Bjella, Dr. Shan Dou, Tom Daley, Ian Ekblaw, Dr. Barry Freifeld, Nate Lindsey, Michelle Robertson, and Craig Ulrich. Having this critical mass of people working on many experiments with some of the same methods has led to a really exciting environment in which to do research. This team has been incredibly generous in sharing data sets, letting me get some field experience at Richmond Field Station, discussing and comparing results and patterns in data, and tips for working with fiber optics. I have particularly enjoyed my collaborations with Shan and Nate as we have all worked on using ambient noise collected by DAS arrays, and with Nate on earthquake observations.

ICME has been a wonderful environment in which to learn and work. Dr. Margot Gerritsen and the staff have put a great deal of effort into developing the institute. It has become a noticeably better and more diverse program over the past six years. ICME is defined by its students, and I have had some wonderful classmates during my time at Stanford. I would like to thank my ICME professor, Dr. George Papanicolaou, for serving on my committee and teaching wonderful classes on stochastics and imaging. George is enthusiastic about not just mathematics, but also the impact it has on experimentation, and his perspective has been quite valuable to me. I must thank George and Margot for encouraging me last year to think again about a career in applied math, as it was a time I really needed a push. I would also like to thank my ICME professor, Dr. Lexing Ying, for

the opportunity to work on the butterfly factorization, and my collaborators, Haizhao Yang, Yingzhou Li and Dr. Ken Ho. I would also like to thank Lexing for being so generous with his time as my math professor while I was an undergrad at UT-Austin. He taught my first numerical methods course, and I learned many methods that I still use today from a reading course with him. When it came time to apply to graduate schools, he encouraged me to apply to the most competitive programs, and his guidance in selecting a school helped me make the choice to come to Stanford.

I've been lucky to have two homes at Stanford because the geophysics faculty, staff and students have always made me feel welcome. I can't thank Chris Castillo enough for his many hours of work on both calibrating the array and organizing and carrying out the active source node and DAS survey on campus. I would like to thank Dr. Bill Ellsworth, who is serving on my oral exam committee, Dr. Greg Beroza, who served on my geophysics M.S. presentation committee and now my Ph.D. oral exam committee, and Dr. Simon Klemperer, who advised us on the active survey. My conversations on ambient noise with Dr. Nori Nakata during and following his time as a postdoc at Stanford have been helpful. I enjoyed working on projects with undergrads Ethan Williams and Paphop Stock Sawasdee.

Many people have contributed directly to my research efforts, but there were also many other ways that my friends, family, and in-laws have helped me make it though grad school. They have helped me to stay focused, to put things in perspective, to evaluate my priorities, to have fun and relax, and have been a critical source of support. To Mom, Dad, and Ben, thank you for helping me grow and letting me be myself. My grandparents Margie and Lou Fullen were true lifelong learners, and even after my grandfather's passing last spring, their hard work and passion for education has continued to inspire me. No one has supported me more than my husband, Sam Meininger, who has been with me since we were high schoolers, and words cannot express my gratitude.

To Mrs. Rothenberg,
Thank you for asking so many questions.

Contents

List of Tables

List of Figures

Chapter 1

Introduction and Background

Permanent, dense seismic monitoring with controlled seismic sources around infrastructure and in urban areas with geophones or seismometers could potentially help improve earthquake hazard analysis maps, detect degradation in the structural stability of permafrast zones, or possibly even detect changes in saturated areas that could lead to sinkholes formation or landslides.

Unfortunately this type of repeated, controlled-source imaging is prohibitively costly and logistically difficult for many applications due to the continuing cost of a source crew, and the permitting difficulties of running a strong source of vibrations in populated areas (the areas where society might benefit most directly from such imaging). Thus, in this thesis I explore the use of passive monitoring, particularly ambient noise interferometry to image the near surface with noises already normally occurring around infrastructure and in populated areas. In addition to ambient noise interferometry, by continuously recording data, these data also record any earthquakes that may occur.

In addition to cutting costs and permitting challenges on the source side, I also explore the potential of cutting costs on the receiver side by using fiber optic cables repurposed for Distributed Acoustic Sensing (DAS). When nodes or seismometers are used for continuous seismic monitoring, permits must be acquired for their placement, there is a risk of sensors being stolen or damaged if near the surface, and individual sensor batteries must be replaces approximately every month, so cost structures often lead scientists to the trade-off of a temporary dense array or a sparse permanent array. DAS uses a single laser interrogator

unit with a power source to probe a fiber optic cable so as to infer an axial strain rate profile over time along that fiber, effectively repurposing it as a seismic array with a sensor density on the scale of 1 meter to 10 meters. A fiber optic cable can be securely buried in a trench or even deployed in an existing telecommunications conduit to avoid permitting difficulties. In fact, fiber optic cables are already ubiquitously deployed in many cities.

In this thesis, I explore passive DAS data from several deployments, both from cables directly coupled to the ground and relying solely on friction with existing buried telecommunications conduits. First, I develop the theory of strain rate sensitivity, both for recording active sources and ambient noise interferometry. I show that even when sacrificing direct cable-to-ground-coupling by using fibers in existing telecommunications conduits, a DAS array can record a variety of nearby to teleseismic earthquakes. DAS technology enables researchers to record dense data in new environments including near infrastructure and in urban areas where it was previously not feasible, but these are difficult noise environments that regularly violate the assumptions of ambient noise theory, so I show examples of ways these noises effect ambient noise correlation functions and strategies for managing those changes. Existing ambient noise processing workflows typically require $O(n^2)$ cross-correlations per time window when there are n sensors, an issue which only gets worse as DAS enables us to record data from thousands of sensors simultaneously on a single interrogator unit. To reduce the cost of dispersion-domain surface wave inversion I introduce a novel $O(n)$ serial algorithm to speed up dispersion image calculation. Finally, I test time-lapse ambient noise interferometry at two DAS arrays: testing whether 18 months of data collected by fibers in existing telecommunications conduits show seasonal saturation trends in Rayleigh wave interferometry, and testing whether noise correlation functions between trenched orthogonal fiber lines show seismic velocity drops during two months of an active permafrost thaw experiment.

1.1 Review of Ambient Noise Interferometry

Given a wavefield generated by random white (independent identically distributed) seismic sources evenly distributed around two vibration sensors, one can cross-correlate or deconvolve data from the two sensors, average the resulting signal over enough time, and recover

the response of one of those sensors to a virtual source located at the same position as the other sensor, often referred to as Green's function estimation [1], [65], [66]. Typically most of the energy extracted is surface waves and their wavelengths are proportional to their depth of peak sensitivity [1], [33], but sometimes body waves may emerge [49]. The extraction of coherent signals from ambient seismic noise has become increasingly common in near-surface imaging at the scale of naturally occurring frequencies [7], [15], [72], and at smaller higher frequency scales [50], [17], [18], [3], [11], [42], [71], [70]. Resulting seismic velocity images may be interpreted to predict ground motion in the event of an earthquake, evaluate landslide risk, detect permafrost, find sinkholes and tunnels, or track near-surface changes during drilling activities. In cases of complex near-surface conditions, characterizing this complexity is needed for a high-quality image of the deeper subsurface.

A fundamental tool used in interferometry is cross-correlation, which yields a time series revealing how similar two time-lagged time series are two each other at many lags. More specifically, given real time series data $d(\mathbf{x}_A, t)$ recorded at location $\mathbf{x}_A$ and $d(\mathbf{x}_B, t)$ recorded at $\mathbf{x}_B$ for $t \in [0, T]$, the cross-correlation is

$$C(\mathbf{x}_A, \mathbf{x}_B, \tau) = \int_0^T d(\mathbf{x}_A, t + \tau) d(\mathbf{x}_B, t) dt. \tag{1.1}$$

From this definition, if the source of a vibration is closer to $\mathbf{x}_A$ than $\mathbf{x}_B$, then the sound it creates would be recorded in $d(\mathbf{x}_A, t)$ at an earlier time than in $d(\mathbf{x}_B, t)$, so that source would contribute most to the signal of $C(\mathbf{x}_A, \mathbf{x}_B, \tau)$ at a $\tau > 0$. This can be expressed in the Fourier domain as a frequency-wise multiplication (where $\hat{\cdot}$ denotes the Fourier transform of a time series):

$$\hat{C}(\mathbf{x}_A, \mathbf{x}_B, \omega) = \hat{d}(\mathbf{x}_A, \omega) \hat{d}^*(\mathbf{x}_B, \omega). \tag{1.2}$$

Alternatively, in some situations deconvolution math be used, which is a frequency-wise division [62]. In this thesis, I only show results of cross-correlation techniques.

A typical workflow to extract a Green's function estimate, also called a noise correlation function, from passive data d at a pair of receivers at $\mathbf{x}_A$ and $\mathbf{x}_B$ requires hours, days, perhaps even months of noise. That noise is segmented into N windows [58], and some preprocessing may be applied so that the vibrations more closely resemble vibrations due to a diffuse homogeneous random noise field [7]. For each time window from time t_i

to t_{i+1}, $d_i(\mathbf{x}_A, t)$ is cross-correlated or deconvolved with $d_i(\mathbf{x}_B, t)$, yielding a time series $C_i(\mathbf{x}_A, \mathbf{x}_B, \tau)$ where τ is a time-lag between the two data. Finally, those correlation time series are averaged to yield a Green's function estimate, $C(\mathbf{x}_A, \mathbf{x}_B, \tau)$:

$$C(\mathbf{x}_A, \mathbf{x}_B, \tau) = \sum_{i=0}^{N} w_i C_i(\mathbf{x}_A, \mathbf{x}_B, \tau) \tag{1.3}$$

where w_i may simply be 1, some normalization (often 1 divided by $\|C_i(\mathbf{x}_A, \mathbf{x}_B, \tau)\|_2$ or $\|C_i(\mathbf{x}_A, \mathbf{x}_B, \tau)\|_1$), or a weighting factor to enhance coherence of the average signal. Under ideal noise source distribution assumptions, as N grows, $C(\mathbf{x}_A, \mathbf{x}_B, \tau)$ approaches a Green's function between $\mathbf{x}_A$ and $\mathbf{x}_B$.

Often, ideal noise assumptions are not met in practice at frequencies above 1-2 Hz, so $C(\mathbf{x}_A, \mathbf{x}_B, \tau)$ is simply referred to as a 'noise correlation function' in this thesis. A major bottleneck in the practical application of ambient noise theory is careful processing to identify and mitigate deviations from the underlying theoretical assumption of a superposition of uncorrelated seismic waves propagating in all directions.

1.2 Review of Distributed Acoustic Sensing

Ideally, geophysicists can deploy a dense array of high quality multi-component sensors, but the installation and long-term maintenance cost is rarely feasible, particularly in populated areas. Shallow near-surface imaging requires collecting higher frequencies, which requires dense sampling and motivates us to use more sensors that are lower cost. One recently explored option is microelectromechanical systems (MEMS) [23]. Alternatively, we are testing fiber optic distributed acoustic sensing (DAS) arrays which are cheap to deploy in existing telecommunications conduits. DAS is a rapidly developing new acquisition technology [5] being increasingly adopted in the energy industry for microseismic monitoring [68] and time-lapse seismic surveys [14], [44], [48]. DAS probes a fiber optic cable with a laser interrogator unit (IU) then interprets information about the resulting optical backscattering to repurpose that cable as a series of densely sampled (spacing between 1 and 20 meters) sensors reporting the average axial strain along short subsets of the same fiber. DAS

has a lower signal-to-noise ratio and more limited angular sensitivity than geophones, but this may be outweighed by the benefits of a dense series of permanently installed seismic sensors communicating over long distances and running on a single power source.

Distributed Acoustic Sensing (DAS) uses a standard fiber optic cable as both an axial strain rate sensor and a means of transmitting data to a storage array. A laser probes the cable with a short pulse repeatedly, then an optical interferometry system measures backscattered light, correlating changes in the backscattered light from one location to strain in the fiber at that location, similar to the optical time-domain reflectometry (OTDR) technique [59], [54]. The signal is gated into channels, so that the data are made up of a time series proportional to the strain or strain rate within each channel of fiber. The optical interferometric measurement process counts photons within a gauge length, and optical phase shifts are measured over that gauge length which are roughly linearly proportional to the amount by which the corresponding subset of fiber was stretched or compressed. Channels may overlap if the gauge length is larger than the channel spacing. There are trade-offs when designing an interrogator unit or selecting recording parameters: a larger gauge length smears out spatial data resolution but also decreases statistical uncertainty in measurements over the gauge, a finer channel spacing can improve the spatial resolution but also may lead to difficult-to-manage data volumes.

1.2.1 The DAS Measurement Process

Let a wave be described by particle velocity

$$\dot{\mathbf{u}}(x, y, z, t) = (\dot{u}_x(x, y, z, t), \dot{u}_y(x, y, z, t), \dot{u}_z(x, y, z, t))$$

then the axial strain rate in the x-direction at a point is $\frac{\partial \dot{u}_x}{\partial x}|_{(x,y,z,t)}$. Let's say more generally one wants to observe this wave field using a horizontal fiber measuring an axial strain rate in the $(\cos(\theta), \sin(\theta), 0)$ direction. As seen in Appendix A, by applying tensor rotation matrices, the axial strain rate observed in the $(\cos(\theta), \sin(\theta), 0)$ direction at that point is

$$\dot{\sigma}_\theta = C_\theta^2 \frac{\partial \dot{u}_x}{\partial x} + C_\theta \mathcal{S}_\theta \left(\frac{\partial \dot{u}_x}{\partial y} + \frac{\partial \dot{u}_y}{\partial x} \right) + \mathcal{S}_\theta^2 \frac{\partial \dot{u}_y}{\partial y} \tag{1.4}$$

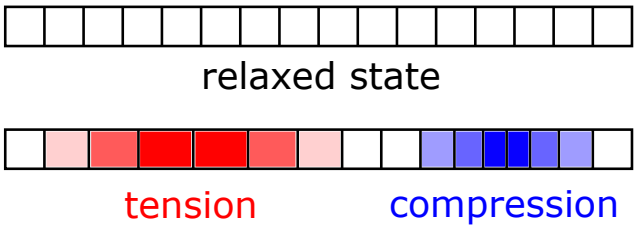

Figure 1.1: If a single gauge length of fiber, pictured in its relaxed state at top, were to experience as much tension as compression due to a wavelength the same size as the gauge length (or an integer factor of the gauge length), no average strain would be recorded along that channel. **NR**

where I use C_θ and S_θ as short notation for $\cos(\theta)$ and $\sin(\theta)$, respectively, and $\dot{\sigma}_\theta$ and all derivatives of $\dot{\mathbf{u}}$ are evaluated at (x, y, z, t). The measurement that would be detected by a fiber optic channel at that same θ orientation centered on (x, y, z) is the average axial strain rate over a gauge length of straight fiber:

$$\dot{\sigma}_{\theta,g}(x, y, z, t) = \int_{-g/2}^{g/2} \dot{\sigma}_\theta(x + \nu C_\theta, y + \nu S_\theta, z, t) d\nu \tag{1.5}$$

The gauge length g over which the interrogator unit averages the axial strain is in general different from the channel spacing. The channel spacing is the distance between the starting point of new segments. So, for instance if the channel spacing were 1 meter with a gauge length of 10 meters, the we would have a channel that observes the average axial strain along the fiber between 1 and 11 meters from the interrogator, the next channel would return the average axial strain between distances 2 and 12 meters, etc... The ability of the user (person acquiring data) to vary gauge length and channel spacing varies depending on manufacturer and age of the model. One difficulty is that if there is as much tension as there is compression within one gauge length, as pictured in Figure 1.1, the DAS system would be totally blind to that wave as it would detect zero average strain rate over the gauge length.

In Chapter 2, I assume simplified geophone measurements, $\dot{\mathbf{u}}$ at a given point with true amplitude response at all frequencies. I also make two simplifying assumptions on DAS systems to keep these results more general across different DAS implementations: (1) It

is possible some DAS implementations may use a different weighted averaging over the gauge length, and it has been shown that the signal may vary depending on pulse shape and gauge length [8]. We simply pretend that the axial strain rate along all points of the gauge are weighted equally. (2) We assume that the average along the gauge length of the axial strain rate of the medium is observed. In reality there is a scaling coefficient provided by each manufacturer, and the Lamé parameters of the fiber and jacket as well as the friction between the fiber, jacket and ground affect these measurements. More details on this effect can be found in [30]. To first order, we expect the math in this paper to explain the most significant changes observed when switching from geophone to DAS measurements, but more accurate modeling of any given data set could account for these implementation-specific details provided by the DAS interrogator unit manufacturer.

1.2.2 Previous Uses of DAS

Prior to the experiments outlined in this thesis, the vast majority of work recording seismic data with distributed acoustic sensing was performed in a downhole environment with particular attention paid to repeatable vertical seismic profile imaging [14], [47], [45], [43], [46], microseismicity monitoring during hydraulic fracturing [68], [5], [29], or fluid flow monitoring through production [14]. The applications of these studies range from oil & gas production to CO_2 sequestration, but the methods developed over the past 5 years show promise for a broader range of applications in subsurface control. A significant finding of this line of work was the importance of installation technique: cables clamped to the side of a well performed better than loose straight fibers, cemented cables performed better than clamped cables [45]. Although the small amount of slack between clamps was an issue compared to cementing, when a cable is given significantly more slack such that it can wind around to touch the sides of the well, it may perform adequately [13].

While the majority of studies published using DAS focused on fibers deployed in wells, there were several studies (some happening at the same time as the experiments in this thesis) that used fibers deployed in the near surface. The applications these studies were designed for included traffic monitoring, near surface characterization at a geothermal site [31], [71], [70], characterizing a frozen lake [9], and landslide monitoring [27]. The

deployment techniques for these purposes varied significantly, and there has been less effort to standardize installation techniques for the wide variety goals of near-surface seismic recording than there has been in the community of scientists and engineers doing downhole seismic recording. In [31], a rectangular fiber array was deployed by digging a trench 0.3 m below the surface, laying the fiber along the bottom, then backfilling. In another surface array experiment, a fiber was frozen into ice above a lake to test distance and azimuth response to active sources [9]. Fiber optic sensing is also making inroads into geotechnical monitoring applications, particularly detecting the potential for landslides before they occur [27]. Two studies, at Brady Hot Springs and Garner Valley, investigate the use of DAS for ambient noise interferometry, but are restricted to using co-linear channels, which can only yield Rayleigh waves. Upon writing (Spring 2016) there are currently at least two test cases where DAS interrogator units were plugged into 10+ km cables that were already existing [4], [28].

Chapter 2

Theoretical Response of DAS

Distributed acoustic sensing (DAS) measures the average axial strain (strain rate) along a subset of a fiber optic cable, as opposed to the particle displacement (velocity) at a particular small point sensor. In shifting from measuring a vector field to a tensor field, DAS changes the directional sensitivity of measurements of every type of seismic wave when compared to single-component geophones, particularly Love and S waves. I show this through theoretical analysis of planar Rayleigh, Love, P- and S-waves over both infinitesimally small and realistic gauge lengths. In fact, after doing this analysis, it was brought to my attention that a very different type of strain measurement device was studied nearly a century ago [6], so Figures 7 and 8 of Benioff (1935) actually show up in my analysis in this chapter. I extend the analysis of individual sensor detection of surface plane waves waves to inter-receiver cross-correlations of these detections. Finally I simulate random sources distributed around particle velocity and axial strain sensors in several configurations. The extraction of Rayleigh wave signals from ambient noise interferometry is more straightforward than Love wave signals, but with appropriate fiber cable geometries and source distributions both Rayleigh and Love wave arrival times may be extracted.

2.1 Plane wave analysis of body and surface waves

I am interested in characterizing sensitivity of fiber channels as a function of wavefield incidence angle to understand which directions are emphasized for each type of wave. This

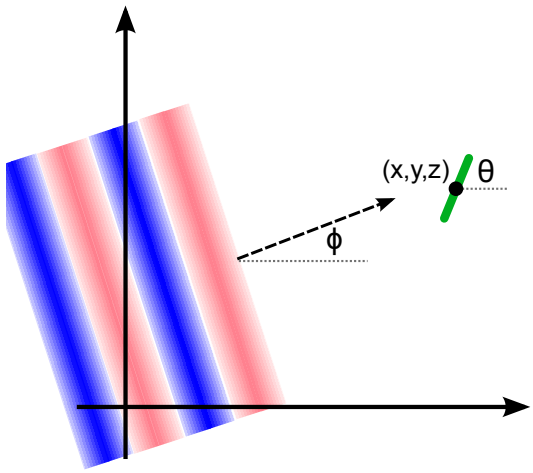

Figure 2.1: We study surface waves (indicated by the red and blue bars) that propagate in the direction $(C_\phi, \mathcal{S}_\phi, 0)$ as they are observed by horizontal sensors (indicated by the green line) at (x, y, z) oriented in the $(C_\theta, \mathcal{S}_\theta, 0)$ direction. **NR**

angular dependence changes how data appear both when sources are directly recorded, and when I perform ambient noise interferometry. Wavefields generated by far away sources can be well approximated with plane waves, so we study this approximation. Depending on whether the wave detected is a P, S, Rayleigh or Love wave, different source angles are emphasized. In Appendix B following the notation of [55] we derive the sensitivity of a horizontal fiber oriented in the direction $(C_\theta, \mathcal{S}_\theta, 0)$ to surface waves (Rayleigh and Love) propagating in the direction $(C_\phi, \mathcal{S}_\phi, 0)$, as drawn in Figure 2.1. Similarly, we derive these results for body waves (P and S) propagating in the direction $(C_{\phi_1}C_{\phi_2}, \mathcal{S}_{\phi_1}C_{\phi_2}, \mathcal{S}_{\phi_2})$. Here, we use standard spherical coordinates and ϕ_1 is the horizontal orientation (same as ϕ for surface waves), and ϕ_2 is the angle from the horizontal plane. We assume these are monochromatic plane waves traveling in a half-space at phase velocity c, wavenumber k and frequency $\omega = kc$. For each type of wave, we use the following parameters to describe their particle displacement and velocity in Table 2.1.

- **Rayleigh waves:** We assume a homogeneous half-space. Let α and β be the velocities

of the irrotational and solenoidal parts of the solution to the elastic wave equation (so $\mathbf{u}_\alpha + \mathbf{u}_\beta = \mathbf{u}$, $\nabla \times \mathbf{u}_\alpha = 0$ and $\nabla \cdot \mathbf{u}_\beta = 0$). Then define $\gamma_\alpha = \sqrt{1 - \frac{c^2}{\alpha^2}}$ and $\gamma_\beta = \sqrt{1 - \frac{c^2}{\beta^2}}$. A and B are amplitude factors, whose ratio defines the ellipticity of the Rayleigh wave.

- **Love waves:** We assume a homogeneous half-space with group velocity β_2 underneath a top layer of thickness H with group velocity β_1. In this paper, we consider only surface seismic, so we just use the displacement in the top H meters of the subsurface. Let A and B be amplitude terms of the depth factor in the top layer (independent of the A and B used to describe Rayleigh waves), and $\eta_1 = \sqrt{\frac{c^2}{\beta_1^2} - 1}$.

- **P waves:** We assume a homogeneous half space. Let A be an amplitude factor (independent of amplitudes of other wave types). All other notation is common to all plane waves.

- **S waves:** We assume a homogeneous half space. We split the S-wave motion into two parts: SH which is just the horizontal particle motion, and SV which occurs in the plane spanned by the z-axis and the direction of propagation. Let A be an amplitude factor (independent of amplitudes of other wave types). All other notation is common to all plane waves.

As summarized in Table 2.2, in Appendix B we calculate the geophone particle velocity response to each type of wave in the $(C_\theta, S_\theta, 0)$ direction, which we denote by $\dot{u}_\theta(x, y, z, t)$. We also calculate the point-wise axial strain rate in the same direction $\dot{\sigma}_\theta(x, y, z, t)$ and the expected DAS signal denoted by $\dot{\sigma}_{\theta,g}(x, y, z, t)$. Note that in the long wavelength ($k \to 0$) limit, a DAS channel with a finite gauge length is predicted to yield the same signal as a point-wise axial strain rate measurement.

Given a predicted measurement, $\dot{u}_\theta, \dot{\sigma}_\theta, \dot{\sigma}_{\theta,g}$, to a particular wave, define its sensitivity as that measurement disregarding any terms only dependent on depth and any oscillatory terms. In general, for $\dot{u}_\theta, \dot{\sigma}_\theta$ and $\dot{\sigma}_{\theta,g}$ when g is short enough relative to the wavelength, the sensitivity is similar for P-waves, SV-waves and Rayleigh waves (a two-lobed sensitivity pattern). Love waves and SH-waves are similar to each other, but, $\dot{u}_\theta$ has a $\pi/2$ rotated two-lobed sensitivity pattern, while $\dot{\sigma}_\theta$, and $\dot{\sigma}_{\theta,g}$ (for small enough g) have four-lobed sensitivity

Table 2.1: Plane wave propagation directions, particle displacements and velocities. The oscillatory factors are $o_{RL} = e^{ik(ct - xC_\phi - yS_\phi)}$, and $o_{PS} = e^{ik(ct - xC_{\phi_1}C_{\phi_2} - yS_{\phi_1}C_{\phi_2} - zS_{\phi_2})}$.

Wave type	quantity	value	quantity	value
Rayleigh	prop. dir.	$(C_\phi, S_\phi, 0)$		
	u_x	$C_\phi \left(Ae^{-\gamma_\alpha kz} + iB\gamma_\beta e^{-\gamma_\beta kz}\right) o_{RL}$	$\dot{u}_x$	$ikcC_\phi \left(Ae^{-\gamma_\alpha kz} + iB\gamma_\beta e^{-\gamma_\beta kz}\right) o_{RL}$
	u_y	$S_\phi \left(Ae^{-\gamma_\alpha kz} + iB\gamma_\beta e^{-\gamma_\beta kz}\right) o_{RL}$	$\dot{u}_y$	$ikcS_\phi \left(Ae^{-\gamma_\alpha kz} + iB\gamma_\beta e^{-\gamma_\beta kz}\right) o_{RL}$
	u_z	$\left(-i\gamma_\alpha Ae^{-\gamma_\alpha kz} + Be^{-\gamma_\beta kz}\right) o_{RL}$	$\dot{u}_z$	$ikc\left(-i\gamma_\alpha Ae^{-\gamma_\alpha kz} + Be^{-\gamma_\beta kz}\right) o_{RL}$
Love	prop. dir.	$(C_\phi, S_\phi, 0)$		
	u_x	$-S_\phi(Ae^{-i\eta_1 kz} + Be^{i\eta_1 kz})o_{RL}$	$\dot{u}_x$	$-ikcS_\phi(Ae^{-i\eta_1 kz} + Be^{i\eta_1 kz})o_{RL}$
	u_y	$C_\phi(Ae^{-i\eta_1 kz} + Be^{i\eta_1 kz})o_{RL}$	$\dot{u}_y$	$ikcC_\phi(Ae^{-i\eta_1 kz} + Be^{i\eta_1 kz})o_{RL}$
	u_z	0	$\dot{u}_z$	0
P	prop. dir.	$(C_{\phi_1}C_{\phi_2}, S_{\phi_1}C_{\phi_2}, S_{\phi_2})$		
	u_x	$AC_{\phi_1}C_{\phi_2}o_{PS}$	$\dot{u}_x$	$ikcAC_{\phi_1}C_{\phi_2}o_{PS}$
	u_y	$AS_{\phi_1}C_{\phi_2}o_{PS}$	$\dot{u}_y$	$ikcAS_{\phi_1}C_{\phi_2}o_{PS}$
	u_z	$AS_{\phi_2}o_{PS}$	$\dot{u}_z$	$ikcAS_{\phi_2}o_{PS}$
SV	prop. dir.	$(C_{\phi_1}C_{\phi_2}, S_{\phi_1}C_{\phi_2}, S_{\phi_2})$		
	u_x	$-AC_{\phi_1}S_{\phi_2}o_{PS}$	$\dot{u}_x$	$-ikcAC_{\phi_1}S_{\phi_2}o_{PS}$
	u_y	$-AS_{\phi_1}S_{\phi_2}o_{PS}$	$\dot{u}_y$	$-ikcAS_{\phi_1}S_{\phi_2}o_{PS}$
	u_z	$AC_{\phi_2}o_{PS}$	$\dot{u}_z$	$ikcAC_{\phi_2}o_{PS}$
SH	prop. dir.	$(C_{\phi_1}C_{\phi_2}, S_{\phi_1}C_{\phi_2}, S_{\phi_2})$		
	u_x	$AS_{\phi_1}o_{PS}$	$\dot{u}_x$	$ikcAS_{\phi_1}o_{PS}$
	u_y	$-AC_{\phi_1}o_{PS}$	$\dot{u}_y$	$-ikcAC_{\phi_1}o_{PS}$
	u_z	0	$\dot{u}_z$	0

Table 2.2: Plane wave particle velocity, $\dot{u}_\theta$, point-wise axial strain rate, $\dot{\sigma}_\theta$, and strain rate averaged over a gauge length, $\bar{\sigma}_\theta$ in the $(C_\theta, \mathcal{S}_\theta, 0)$ direction. The oscillatory factor o_{RL} in the surface waves $o_{RL} = e^{ik(ct - xC_\phi - y\mathcal{S}_\phi)}$, and the oscillatory factor o_{PS} in the body waves is $o_{PS} = e^{ik(ct - xC_{\phi_1}C_{\phi_2} - y\mathcal{S}_{\phi_1}C_{\phi_2} - z\mathcal{S}_{\phi_2})}$.

Wave type	quantity	value
Rayleigh	propagation direction	$(C_\phi, \mathcal{S}_\phi, 0)$
	$\dot{u}_\theta$	$ickC_{(\phi-\theta)}\left(Ae^{-\gamma_\alpha kz} + iB\gamma_\beta e^{-\gamma_\beta kz}\right) o_{RL}$
	$\dot{\sigma}_\theta$	$ck^2C^2_{(\phi-\theta)}\left(Ae^{-\gamma_\alpha kz} + iB\gamma_\beta e^{-\gamma_\beta kz}\right) o_{RL}$
	$\dot{\sigma}_{\theta,g}$	$\frac{2ck}{g}C_{(\phi-\theta)}\sin\left(\frac{kgC_{(\theta-\phi)}}{2}\right)\left(Ae^{-\gamma_\alpha kz} + iB\gamma_\beta e^{-\gamma_\beta kz}\right) o_{RL}$
Love	propagation direction	$(C_\phi, \mathcal{S}_\phi, 0)$
	$\dot{u}_\theta$	$-ick\mathcal{S}_{(\phi-\theta)}(Ae^{-i\eta_1 kz} + Be^{i\eta_1 kz})o_{RL}$
	$\dot{\sigma}_\theta$	$-\frac{ck^2}{2}\mathcal{S}_{2(\phi-\theta)}(Ae^{-i\eta_1 kz} + Be^{i\eta_1 kz})o_{RL}$
	$\dot{\sigma}_{\theta,g}$	$-\frac{2ck}{g}\mathcal{S}_{(\phi-\theta)}\sin\left(\frac{kgC_{(\phi-\theta)}}{2}\right)(Ae^{-i\eta_1 kz} + Be^{i\eta_1 kz})o_{RL}$
P	propagation direction	$(C_{\phi_1}C_{\phi_2}, \mathcal{S}_{\phi_1}C_{\phi_2}, \mathcal{S}_{\phi_2})$
	$\dot{u}_\theta$	$ickC_{(\phi_1-\theta)}C_{\phi_2}Ao_{PS}$
	$\dot{\sigma}_\theta$	$ck^2C^2_{(\phi_1-\theta)}C^2_{\phi_2}Ao_{PS}$
	$\dot{\sigma}_{\theta,g}$	$\frac{2ck}{g}C_{(\phi_1-\theta)}C_{\phi_2}\sin\left(\frac{gkC_{(\phi_1-\theta)}C_{\phi_2}}{2}\right)Ao_{PS}$
SV	propagation direction	$(C_{\phi_1}C_{\phi_2}, \mathcal{S}_{\phi_1}C_{\phi_2}, \mathcal{S}_{\phi_2})$
	$\dot{u}_\theta$	$-ickC_{(\phi_1-\theta)}\mathcal{S}_{\phi_2}Ao_{PS}$
	$\dot{\sigma}_\theta$	$-\frac{ck^2}{2}C^2_{(\phi_1-\theta)}\mathcal{S}_{2\phi_2}Ao_{PS}$
	$\dot{\sigma}_{\theta,g}$	$-\frac{ck}{g}\frac{C_{(\phi_1-\theta)}\mathcal{S}_{2\phi_2}}{C_{\phi_2}}\sin\left(\frac{kgC_{(\phi_1-\theta)}C_{\phi_2}}{2}\right)Ao_{PS}$
SH	propagation direction	$(C_{\phi_1}C_{\phi_2}, \mathcal{S}_{\phi_1}C_{\phi_2}, \mathcal{S}_{\phi_2})$
	$\dot{u}_\theta$	$ick\mathcal{S}_{(\phi_1-\theta)}Ao_{PS}$
	$\dot{\sigma}_\theta$	$\frac{ck^2}{2}\mathcal{S}_{2(\phi_1-\theta)}C_{\phi_2}Ao_{PS}$
	$\dot{\sigma}_{\theta,g}$	$\frac{2ck}{g}\mathcal{S}_{(\phi_1-\theta)}\sin\left(\frac{kgC_{(\phi_1-\theta)}C_{\phi_2}}{2}\right)Ao_{PS}$

patterns.

2.1.1 Surface wave response

First, let's look at the surface waves sensitivities. We plot the sensitivity to Rayleigh and Love waves coming from different angles in Figure 2.2 for a geophone, a point-wise axial strain rate measurement,and a DAS channel with gauge length 10 meters (a typical setting for seismic acquisition). While the geophone is most sensitive to Rayleigh waves with $\phi - \theta = 0, \pi$, it is equally sensitive to Love waves with $\phi - \theta = \pm\pi/2$ in the sense that these sensitivity patterns are just rotated versions of each other. Like the geophone, the point-wise axial strain rate measurement is also most sensitive to Rayleigh waves such that $\phi - \theta = 0, \pi$, but the sensitivity is more concentrated around these peak angles (i.e. is scaled by an extra $kC_{(\phi-\theta)}$ compared to the geophone). Unlike the geophone, the point-wise axial strain rate has a four-lobed sensitivity to Love waves with peak sensitivity to Love waves coming in at $\phi - \theta = \pm\pi/4, \pm 3\pi/4$. Further, at its peak sensitivity angles to Love waves, the point-wise axial strain rate measurment only detects half the amplitude that would be detected by the same theoretical sensor to Rayleigh waves at $\phi - \theta = 0, \pi$. Thus, the switch to strain means Love wave sensitivity is weaker and distributed over more angles. For wavelengths a few times longer than g the sensitivity patterns of $\dot{\sigma}_\theta$ well-approximate the sensitivity of $\dot{\sigma}_{\theta,g}$. As seen in Figure 2.2, for wavelengths just slightly bigger than g the sensitivity patterns become more flattened out near peak-sensitivity angles, then for wavelengths shorter than g, additional sensitivity lobes form, consistent with the description for P-waves in [19]. This trend can be seen in more detail in Figure 2.3, which shows that for larger gauge lengths, these stranger behaviors (deviating from the 2-lobe and 4-lobe trends) can occur at even longer wavelengths.

2.1.2 Body wave response

The response to body waves is slightly more complicated depending on how vertically the wave is propagating, indicated by ϕ_2. We plot the sensitivity for $\phi_2 = 3\pi/8, \pi/4$, and $\pi/8$ in Figures 2.4, 2.5, and 2.6, respectively. In general, the P-wave and SV-wave sensitivity patterns are more like Rayleigh wave sensitivity (two lobed), while the SH-wave

sensitivity is more like Love wave sensitivity (four lobed). When ϕ_2 is closer to $\pi/2$ that means the wave is propagating almost vertically, so most particle displacement is closer to vertical and there is less P-wave sensitivity for all three horizontal measurements compared to P-waves traveling at smaller ϕ_2 values. While SV geophone response is maximized for nearly-vertically propagating waves ($\phi_2 = \pi/2$) and minimized for nearly horizontally propagating waves ($\phi_2 = 0$), the point-wise strain rate and DAS responses are minimized for both horizontal and vertically propagating waves and maximized when there is as much vertical as their is horizontal propagation ($\phi_2 = \pi/4$). On the other hand, the geophone response to SH waves is independent of how much energy is propagating vertically, but the point-wise strain rate and DAS measurements are maximized when an SH-wave is propagating horizontally ($\phi_2 = 0$).

2.2 Sensitivity of DAS Cross-correlations

When attempting to use weak signals, as in ambient noise interferometry or some microseismicity detection methods, we often cross-correlate two time series signals, $s(x_A, y_A, z_A, t)$ and $s(x_B, y_B, z_B, t)$, recorded concurrently at different sensors to bring their joint signal, $C(\tau) = \frac{1}{2T}\int_{-T}^{T} s(x_A, y_A, z_A, t)s^*(x_B, y_B, z_B, t+\tau)dt$, above the noise level. In particular, this is used to more accurately detect and locate microseismic events using an array, and is also used to extract surface wave Green's function approximations from ambient noise recorded by surface arrays. Important questions must be answered before analyzing and interpreting DAS data cross-correlations. While the extensive sensor coverage of DAS is clearly an advantage in microseismicity detection, could the use of certain channel geometries relative to events lead to different biases in the estimated statistical distribution of events? When performing ambient noise interferometry in the presence of an ideal noise field, does the extracted signal actually approximate the same arrival times as the true Green's functions?

The answers to these questions begin by studying the differences between cross-correlations of pairs of geophones, point-wise axial strain rate measurements, and DAS channels responding to plane waves. When using 3C geophones, we can rotate any pair of sensors into radial and transverse horizontal components that clearly yield Rayleigh and

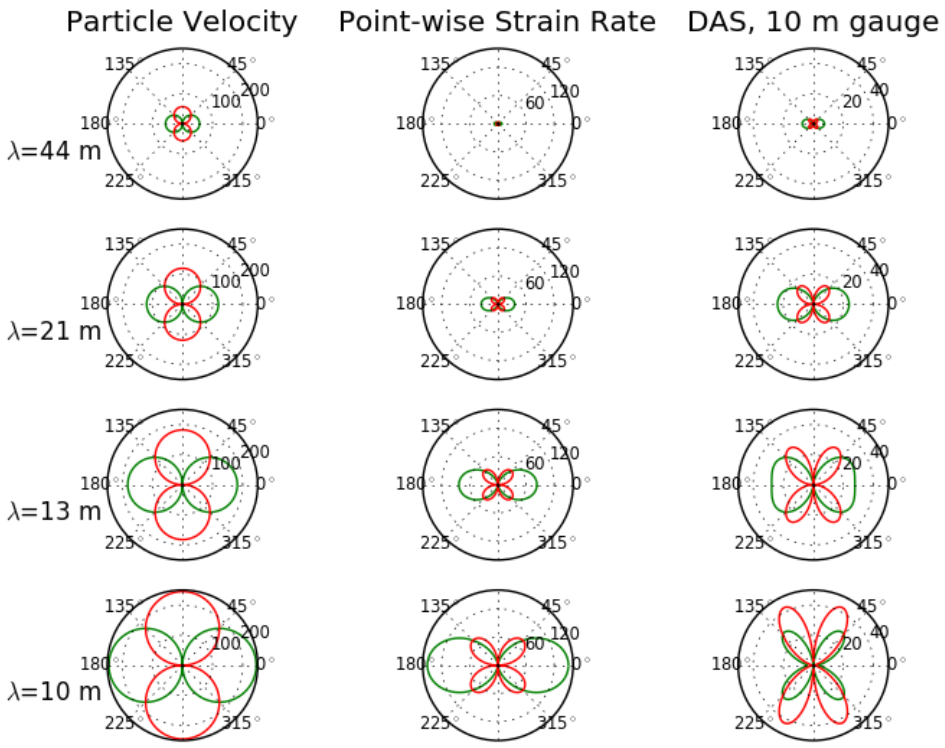

Figure 2.2: Each polar plot shows the amplitude response of a measurement to planar surface waves of varying azimuth and wavelength. The radius of each line represents the sensitivity of geophones (left), point-wise strain measurements (middle) and DAS with a 10 meter gauge length (right) to a range of wavelengths in a 400 m/s velocity material for both Rayleigh (green) and Love (red) plane waves coming from each angle . The plots represent sensitivities for 9 Hz (top), 19 Hz (2nd row), 29 Hz (3rd row), and 39 Hz (bottom). **ER**

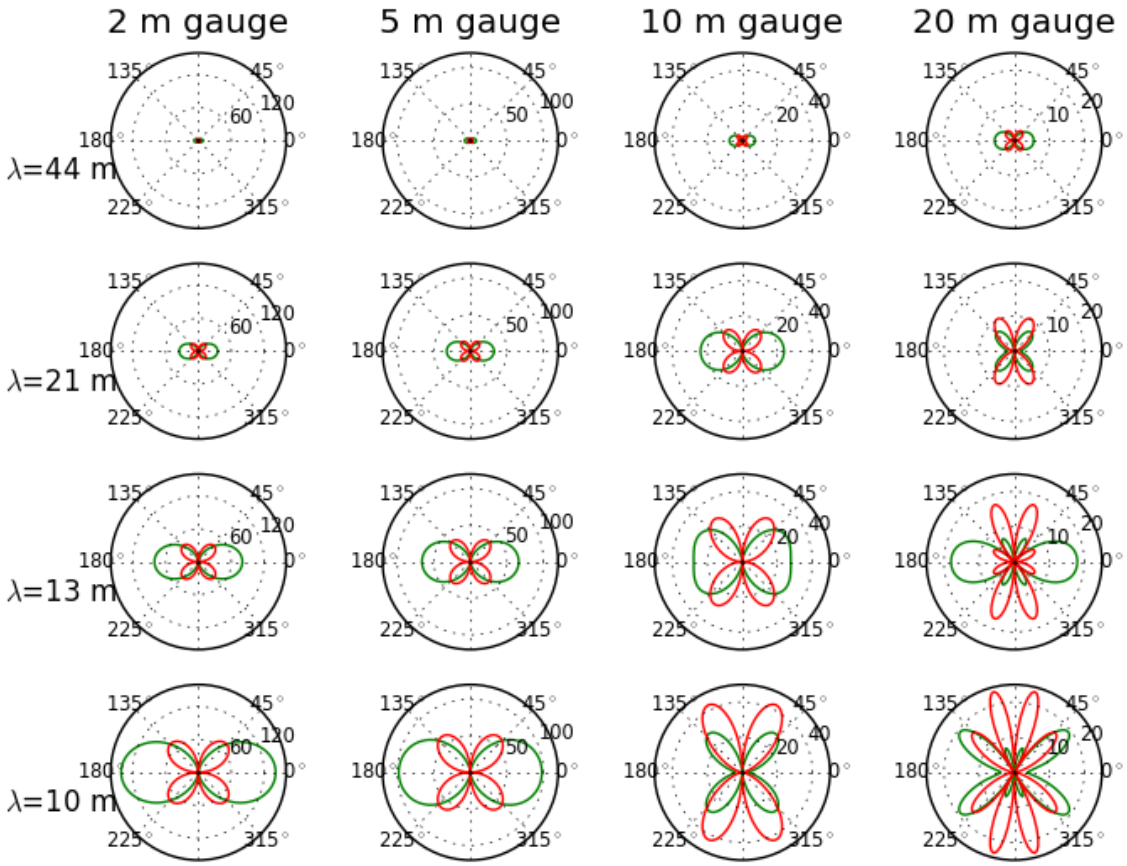

Figure 2.3: Each polar plot shows the amplitude response of a measurement to planar surface waves of varying azimuth and wavelength. The radius of each line represents the sensitivity of DAS with a 2 meter (left), 5 meter (2nd column), 10 meter (3rd column) and 20 meter (right) gauge length to a range of wavelengths in a 400 m/s velocity material for both Rayleigh (green) and Love (red) plane waves coming from each angle . The plots represent sensitivities for 9 Hz (top), 19 Hz (2nd row), 29 Hz (3rd row), and 39 Hz (bottom). **ER**

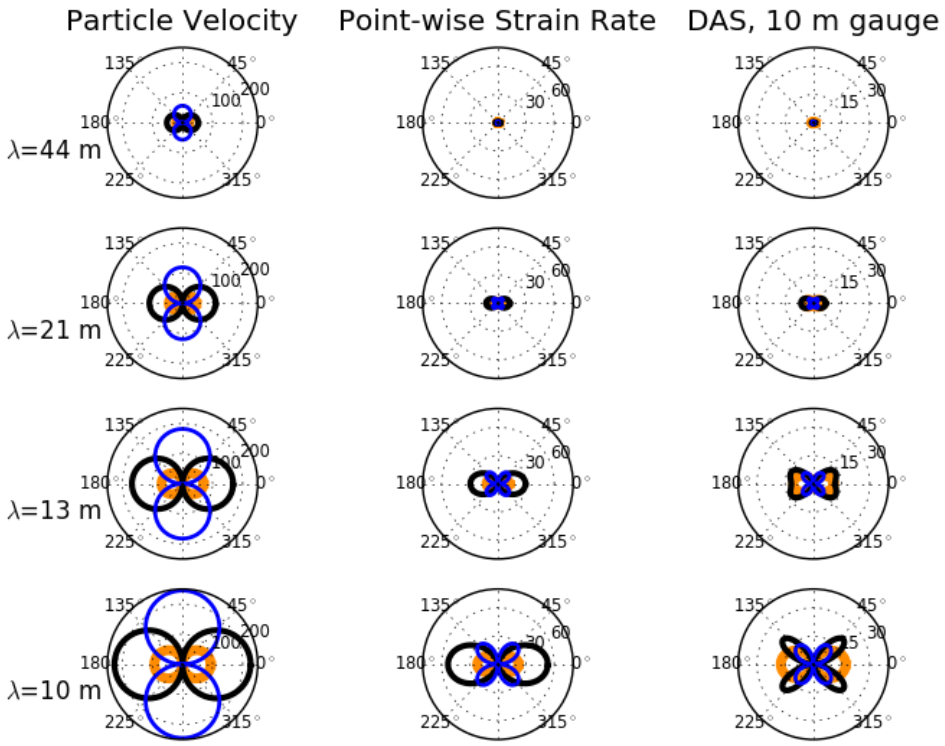

Figure 2.4: The radius of each line represents the sensitivity of geophones (left), point-wise strain measurements (middle) and DAS with a 10 meter gauge length (right) to a different wavelengths in a 400 m/s velocity material for both P (orange), SH (blue) and SV (black) plane waves coming from each horizontal angle $\phi_1 - \theta$ and vertical angle $\phi_2 = 3\pi/8$. The plots represent sensitivities for 9 Hz (top), 19 Hz (2nd row), 29 Hz (3rd row), and 39 Hz (bottom). **ER**

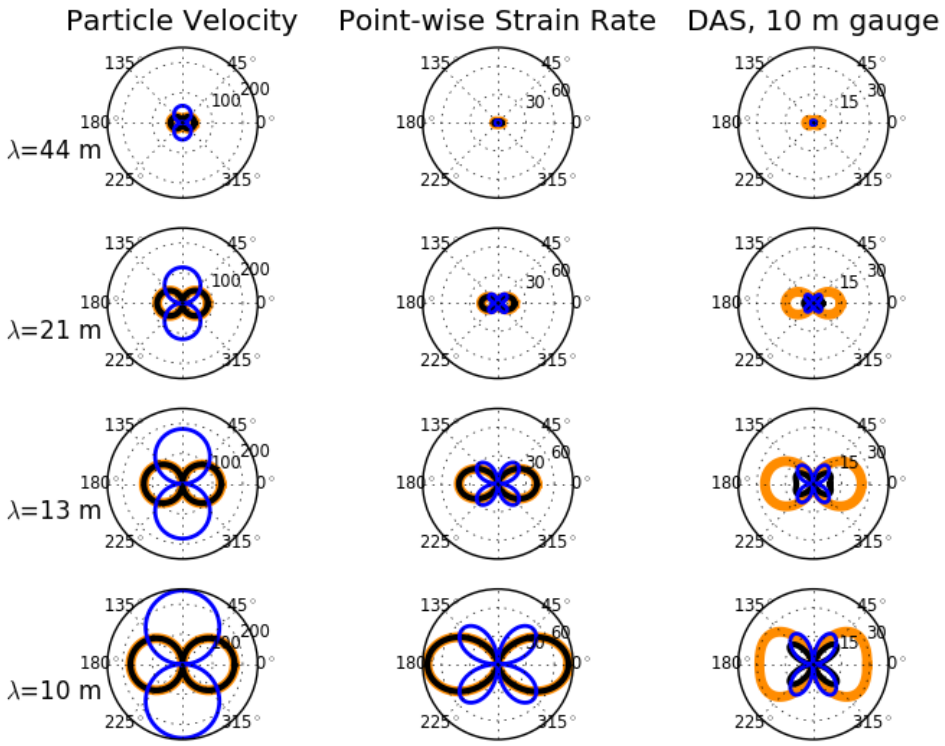

Figure 2.5: The radius of each line represents the sensitivity of geophones (left), point-wise strain measurements (middle) and DAS with a 10 meter gauge length (right) to a different wavelengths in a 400 m/s velocity material for both P (orange), SH (blue) and SV (black) plane waves coming from each horizontal angle $\phi_1 - \theta$ and vertical angle $\phi_2 = \pi/4$. The plots represent sensitivities for 9 Hz (top), 19 Hz (2nd row), 29 Hz (3rd row), and 39 Hz (bottom). **ER**

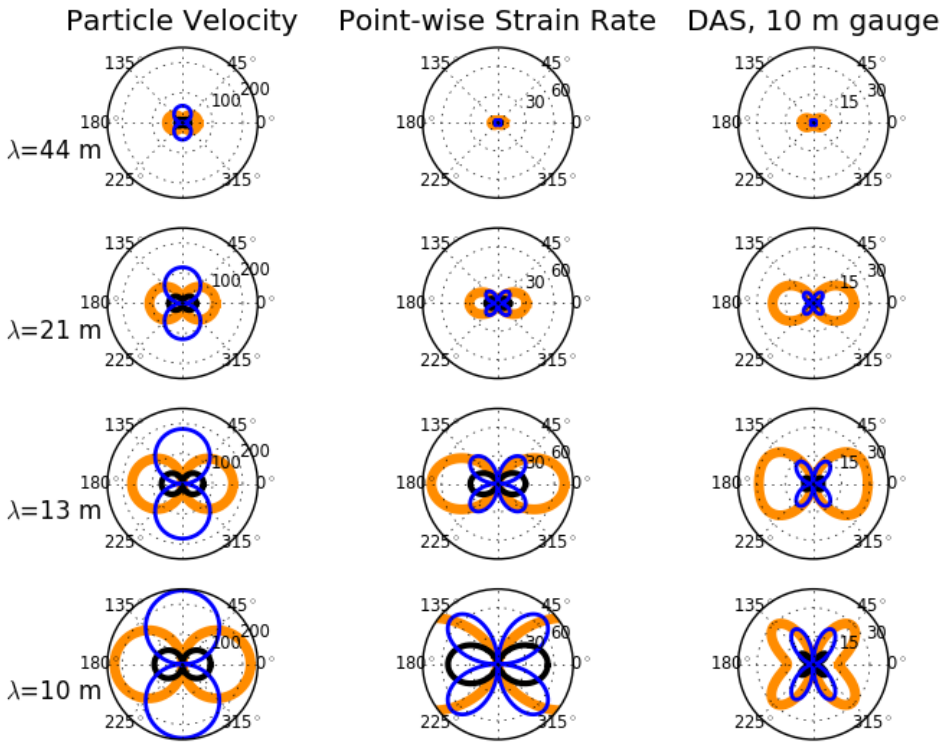

Figure 2.6: The radius of each line represents the sensitivity of geophones (left), point-wise strain measurements (middle) and DAS with a 10 meter gauge length (right) to a different wavelengths in a 400 m/s velocity material for both P (orange), SH (blue) and SV (black) plane waves coming from each horizontal angle $\phi_1 - \theta$ and vertical angle $\phi_2 = \pi/8$. The plots represent sensitivities for 9 Hz (top), 19 Hz (2nd row), 29 Hz (3rd row), and 39 Hz (bottom). **ER**

Love wave components [33], but as we only observe one component of the strain tensor with fiber, we cannot do the same with a horizontal fiber array. Thus, we calculate cross-correlations between a sensor at (x_1, y_1, z_1) oriented in the $(C_{\theta_1}, \mathcal{S}_{\theta_1}, 0)$ direction and a second sensor at (x_2, y_2, z_2) oriented in the $(C_{\theta_2}, \mathcal{S}_{\theta_2}, 0)$ direction. These cross-correlations are summarized in Table 2.3, as derived in Appendix B.

Say we have two sensors at two surface locations $\mathbf{x}_1$ and $\mathbf{x}_2$ such that $\frac{\mathbf{x}_1 - \mathbf{x}_2}{\|\mathbf{x}_1 - \mathbf{x}_2\|} = (1, 0, 0)$. A plane surface wave coming in from angle $\phi = 0$ or π would hit $\mathbf{x}_1$ and $\mathbf{x}_2$ at what appears to be the true velocity, but a plane wave coming in from angle $\phi = \pm\pi/2$ would arrive at $\mathbf{x}_1$ and $\mathbf{x}_2$ at the same time at an infinitely fast velocity, and any angle in between will have some fast biased apparent velocity, so ideally, we want whichever wave type we are trying to detect, to be emphasized close to $\phi = 0, \pi$.

Ignoring the oscillatory terms and exponentially decaying depth-dependent surface wave terms, we have plotted cross-correlation sensitivities for $\mathbf{x}_1$ and $\mathbf{x}_2$ if they were geophones, point-wise strain rates, and DAS responding to surface waves in Figures 2.7 and 2.8, which show their radial-radial ($\theta_1 = \theta_2 = 0$) and transverse-transverse ($\theta_1 = \theta_2 = \pi/2$) cross-correlation sensitivities respectively. These are the cross-correlations we use for extracting Rayleigh waves and Love waves, respectively from geophones, and as expected, the radial-radial cross-correlation in Figure 2.7 is very sensitive to Rayleigh waves at $\phi = 0, \pi$, and the transverse-transverse cross-correlation in Figure 2.8 is very sensitive to Love waves at $\phi = 0, \pi$. However, when we look at the point-wise strain rate diagrams (the same as DAS when the gauge length is chosen appropriately), the radial-radial correlations in Figure 2.7 are very sensitive to Rayleigh waves at $\phi = 0, \pi$, but the transverse-transverse correlations in Figure 2.8 are not very sensitive to any waves at $\phi = 0, \pi$, and in fact are very sensitive to Rayleigh waves that would yield a very fast (even infinite) velocity.

So how to we detect any Love waves from cross-correlations? The transverse-transverse cross-correlations are sensitive to Love waves coming from $\phi = \pm\pi/4, \pm 3\pi/4$, just not as sensitive as they are to Rayleigh waves near $\phi = \pm\pi/2$ which would appear to have an extremely fast velocity. If we have reason to believe that Love waves dominate the wavefield, then transverse-transverse cross-correlations will result in an apparent velocity that is $c/\cos(\Phi)$, where c is the true Love wave velocity at that frequency, and Φ is the peak Love wave cross-correlation sensitivity angle within the frequency band of interest

($\Phi = \pi/4$ for longer wavelengths relative to the gauge length).

2.3 Simple Ambient Noise Models

A simple thought experiment to understand why hydrophone (pressure) and vertical geophone ambient noise cross-correlations averaged over many sources yield a signal with its peak around the Green's function arrival time of one of the receivers responding to a virtual source at the other can be found in [65]. Here, I recreate that thought experiment at the same scale, but study the cross-correlations of the particle velocity and point-wise axial strain response to random sources that travel either like Rayleigh waves or Love Waves (although at a faster velocity than surface waves and without dispersion). Further, I test a range of geometries encountered in the experiments examined in this thesis: a virtual source that is a fiber optic channel cross-correlated with a set of receivers on a parallel cable, and a fiber optic virtual source cross-correlated with a set of receivers on an orthogonal cable.

Here, I assume a simple model of surface wave point sources: a Ricker wavelet set off at a point that either has particle motion in the direction of propagation (Rayleigh wave) or horizontal and orthogonal to the direction of propagation (Love wave). This is described in detail in Appendix C along with the derivations of the expected response of the x- and y-components of the particle velocity and axial strain rate to these point sources, which represent idealized horizontal geophones and DAS cables. These responses are summarized in Table 2.4

2.3.1 Radial-radial Cross-correlations

Prior work has shown in practice that it is possible to retrieve reasonable geology from surface wave inversion using cross-correlations of data recorded on collinear DAS channels [21]. This section aims to better understand why this works. Following the thought experiment of [65], imagine two receivers at $\mathbf{x}_1 = (-600, 0, 0)$ and $\mathbf{x}_2 = (600, 0, 0)$ surrounded by 5000 point sources randomly distributed on an annulus with inner and outer radii of 2000 and 3000 m (uniformly distributed azimuth in $[0, 2\pi]$ and uniformly distributed radius in $[2000, 3000]$). While the original experiment studied a scalar response (pressure), in this

Table 2.3: Cross-correlations of measurements at $\mathbf{x}_1 = (x_1, y_1, z)$ in the $(C_{\theta_1}, S_{\theta_1}, 0)$ direction with those at $\mathbf{x}_2 = (x_2, y_2, z)$ in the $(C_{\theta_2}, S_{\theta_2}, 0)$ direction. I denote oscillatory terms by $o^{\tau}_{RL} = e^{-ik(c\tau+(x_1-x_2)C_{\phi}+(y_1-y_2)S_{\phi})}$ and $o^{\tau}_{PS} = e^{-ik(c\tau+(x_1-x_2)C_{\phi_1}C_{\phi_2}+(y_1-y_2)S_{\phi_1}C_{\phi_2})}$

Wave	quantity	value
Rayleigh	prop. dir.	$(C_{\phi}, S_{\phi}, 0)$
	$\dot{u}_{\theta_1}(\mathbf{x}_1) \star \dot{u}_{\theta_2}(\mathbf{x}_2)$	$c^2k^2 C_{(\phi-\theta_1)}C_{(\phi-\theta_2)} \left(A^2 e^{-2\gamma_\alpha kz} + B^2\gamma_\beta^2 e^{-2\gamma_\beta kz}\right) o^{\tau}_{RL}$
	$\dot{\sigma}_{\theta_1}(\mathbf{x}_1) \star \dot{\sigma}_{\theta_2}(\mathbf{x}_2)$	$c^2k^4 C^2_{(\phi-\theta_1)} C^2_{(\phi-\theta_2)} \left(A^2 e^{-2\gamma_\alpha kz} + B^2\gamma_\beta^2 e^{-2\gamma_\beta kz}\right) o^{\tau}_{RL}$
	$\dot{\sigma}_{\theta_1,g}(\mathbf{x}_1) \star \dot{\sigma}_{\theta_2,g}(\mathbf{x}_2)$	$\frac{4c^2k^2}{g^2} C_{(\phi-\theta_1)}C_{(\phi-\theta_2)} \sin\left(\frac{kg}{2} C_{(\phi-\theta_1)}\right) \left(A^2 e^{-2\gamma_\alpha kz} + B^2\gamma_\beta^2 e^{-2\gamma_\beta kz}\right) o^{\tau}_{RL}$
Love	prop. dir.	$(C_{\phi}, S_{\phi}, 0)$
	$\dot{u}_{\theta_1}(\mathbf{x}_1) \star \dot{u}_{\theta_2}(\mathbf{x}_2)$	$c^2k^2 S_{(\phi-\theta_1)}S_{(\phi-\theta_2)}(A^2 + AB(e^{2i\eta_1 kz} + e^{-2i\eta_1 kz}) + B^2) o^{\tau}_{RL}$
	$\dot{\sigma}_{\theta_1}(\mathbf{x}_1) \star \dot{\sigma}_{\theta_2}(\mathbf{x}_2)$	$\frac{c^2k^4}{4} S_{2(\phi-\theta_1)}S_{2(\phi-\theta_2)}(A^2 + 2AB\cos(2\eta_1 kz) + B^2) o^{\tau}_{RL}$
	$\dot{\sigma}_{\theta_1,g}(\mathbf{x}_1) \star \dot{\sigma}_{\theta_2,g}(\mathbf{x}_2)$	$\frac{4c^2k^2}{g^2} S_{(\phi-\theta_1)}S_{(\phi-\theta_2)} \sin\left(\frac{kg}{2} C_{(\phi-\theta_1)}\right) \sin\left(\frac{kg}{2} C_{(\phi-\theta_2)}\right) (A^2 + 2AB\cos(2\eta_1 kz) + B^2) o^{\tau}_{RL}$
P	prop. dir.	$(C_{\phi_1}C_{\phi_2}, S_{\phi_1}C_{\phi_2}, S_{\phi_2})$
	$\dot{u}_{\theta_1}(\mathbf{x}_1) \star \dot{u}_{\theta_2}(\mathbf{x}_2)$	$c^2k^2 C_{(\phi_1-\theta_1)}C_{(\phi_1-\theta_2)}C^2_{\phi_2} A^2 o^{\tau}_{PS}$
	$\dot{\sigma}_{\theta_1}(\mathbf{x}_1) \star \dot{\sigma}_{\theta_2}(\mathbf{x}_2)$	$c^2k^4 C^2_{(\phi_1-\theta_1)}C^2_{(\phi_1-\theta_2)}C^4_{\phi_2} A^2 o^{\tau}_{PS}$
	$\dot{\sigma}_{\theta_1,g}(\mathbf{x}_1) \star \dot{\sigma}_{\theta_2,g}(\mathbf{x}_2)$	$\frac{4c^2k^2}{g^2} C_{(\phi_1-\theta_1)}C_{(\phi_1-\theta_2)}C^2_{\phi_2} \sin\left(\frac{kg}{2} C_{(\phi_1-\theta_1)}C_{\phi_2}\right) \sin\left(\frac{kg}{2} C_{(\phi_1-\theta_2)}C_{\phi_2}\right) A^2 o^{\tau}_{PS}$
SV	prop. dir.	$(C_{\phi_1}C_{\phi_2}, S_{\phi_1}C_{\phi_2}, S_{\phi_2})$
	$\dot{u}_{\theta_1}(\mathbf{x}_1) \star \dot{u}_{\theta_2}(\mathbf{x}_2)$	$c^2k^2 C_{(\phi_1-\theta_1)}C_{(\phi_1-\theta_2)}S^2_{\phi_2} A^2 o^{\tau}_{PS}$
	$\dot{\sigma}_{\theta_1}(\mathbf{x}_1) \star \dot{\sigma}_{\theta_2}(\mathbf{x}_2)$	$\frac{c^2k^4}{4} C^2_{(\phi_1-\theta_1)}C^2_{(\phi_1-\theta_2)}S^2_{2\phi_2} A^2 o^{\tau}_{PS}$
	$\dot{\sigma}_{\theta_1,g}(\mathbf{x}_1) \star \dot{\sigma}_{\theta_2,g}(\mathbf{x}_2)$	$\frac{c^2k^2}{g^2} \cdot \frac{C_{(\phi_1-\theta_1)}C_{(\phi_1-\theta_2)}S^2_{2\phi_2}}{C^2_{\phi_2}} \sin\left(\frac{kg}{2} C_{(\phi_1-\theta_1)}C_{\phi_2}\right) \sin\left(\frac{kg}{2} C_{(\phi_1-\theta_2)}C_{\phi_2}\right) A^2 o^{\tau}_{PS}$
SH	prop. dir.	$(C_{\phi_1}C_{\phi_2}, S_{\phi_1}C_{\phi_2}, S_{\phi_2})$
	$\dot{u}_{\theta_1}(\mathbf{x}_1) \star \dot{u}_{\theta_2}(\mathbf{x}_2)$	$c^2k^2 S_{(\phi_1-\theta_1)}S_{(\phi_1-\theta_2)}A^2 o^{\tau}_{PS}$
	$\dot{\sigma}_{\theta_1}(\mathbf{x}_1) \star \dot{\sigma}_{\theta_2}(\mathbf{x}_2)$	$\frac{c^2k^4}{4} S_{2(\phi_1-\theta_1)}S_{2(\phi_1-\theta_2)}C^2_{\phi_2} A^2 o^{\tau}_{PS}$
	$\dot{\sigma}_{\theta_1,g}(\mathbf{x}_1) \star \dot{\sigma}_{\theta_2,g}(\mathbf{x}_2)$	$\frac{4c^2k^2}{g^2} S_{(\phi_1-\theta_1)}S_{(\phi_1-\theta_2)} \sin\left(\frac{kg}{2} C_{(\phi_1-\theta_1)}C_{\phi_2}\right) \sin\left(\frac{kg}{2} C_{(\phi_1-\theta_2)}C_{\phi_2}\right) A^2 o^{\tau}_{PS}$

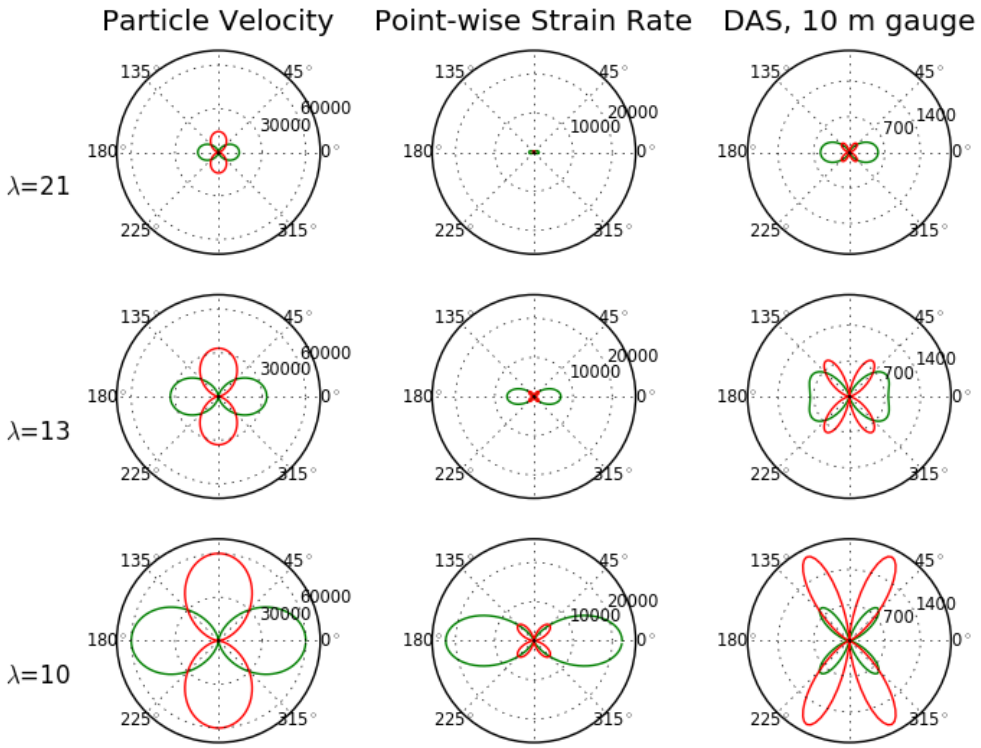

Figure 2.7: The radius of each line represents the sensitivity of radial-radial ($\theta_1 = \theta_2 = 0$) cross-correlations geophones (left), point-wise strain measurements (middle) and DAS with a 10 meter gauge length (right) to a range of wavelengths in a 400 m/s velocity material for both Rayleigh (green) and Love (red) plane waves coming from each angle. The plots represent sensitivities for 19 Hz (top), 29 Hz (2nd row), and 39 Hz (bottom). 9 Hz was not pictured because the responses are too small to see. **ER**

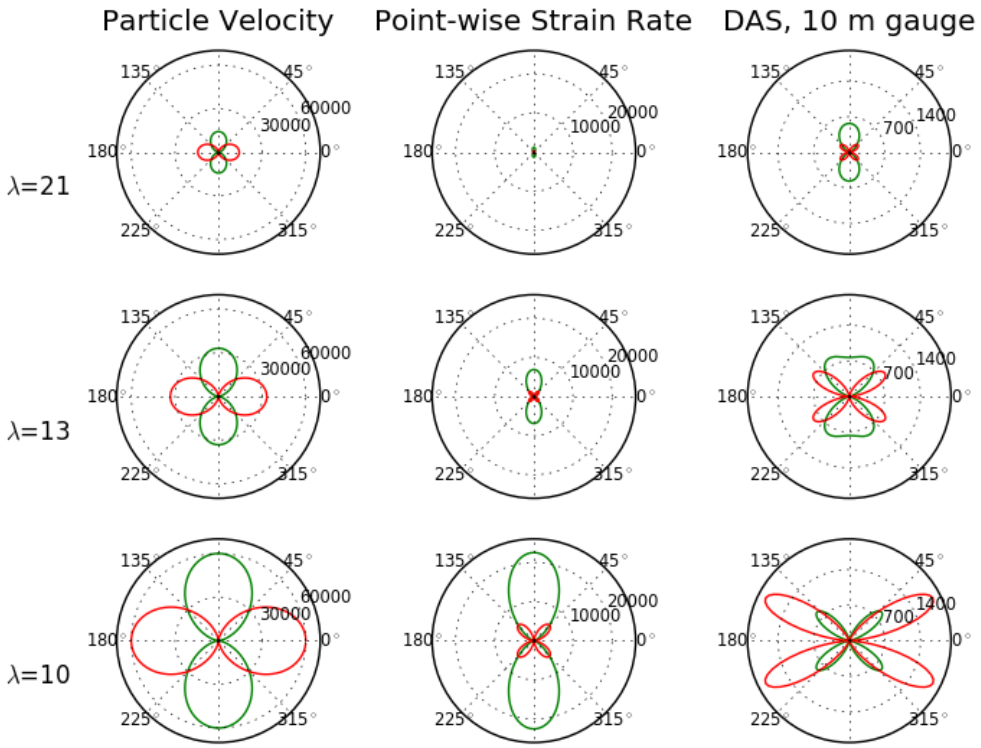

Figure 2.8: The radius of each line represents the sensitivity of transverse-transverse ($\theta_1 = \theta_2 = \pi/2$) cross-correlations geophones (left), point-wise strain measurements (middle) and DAS with a 10 meter gauge length (right) to a range of wavelengths in a 400 m/s velocity material for both Rayleigh (green) and Love (red) plane waves coming from each angle. The plots represent sensitivities for 19 Hz (top), 29 Hz (2nd row), and 39 Hz (bottom). 9 Hz was not pictured because the responses are too small to see. **ER**

Table 2.4: Horizontal particle velocity and point-wise axial strain rate responses at $\mathbf{x}$ to a simplified model of Rayleigh and Love wave point sources at $\mathbf{x}_s$ that emit a Ricker wavelet at frequency f. To keep notation short, let $R = \|\mathbf{x} - \mathbf{x}_s\|$, $\tau = t - \frac{R}{C}$, and $o_f = e^{-\pi^2 f^2 (t-\frac{R}{c})^2}$.

Wave	Quantity	Value
Rayleigh	$\dot{u}_0(\mathbf{x}, t)$	$o_f \frac{x-x_s}{R^2}\left(-6\pi^2 f^2 \tau + 4\pi^4 f^4 \tau^3\right)$
	$\dot{u}_{\pi/2}(\mathbf{x}, t)$	$o_f \frac{y-y_s}{R^2}\left(-6\pi^2 f^2 \tau + 4\pi^4 f^4 \tau^3\right)$
	$\dot{\sigma}_0(\mathbf{x}), t$	$o_f \frac{(x-x_s)^2}{R^3}\left(\frac{6\pi^2 f^2}{c} + \frac{12\pi^2 f^2}{R}\tau - \frac{24\pi^4 f^4}{c}\tau^2 - \frac{8\pi^4 f^4}{R}\tau^3 + \frac{8\pi^6 f^6}{c}\tau^4\right)$
	$\dot{\sigma}_{\pi/2}(\mathbf{x}, t)$	$o_f \frac{(y-y_s)^2}{R^3}\left(\frac{6\pi^2 f^2}{c} + \frac{12\pi^2 f^2}{R}\tau - \frac{24\pi^4 f^4}{c}\tau^2 - \frac{8\pi^4 f^4}{R}\tau^3 + \frac{8\pi^6 f^6}{c}\tau^4\right)$
Love	$\dot{u}_0(\mathbf{x}, t)$	$o_f \frac{y-y_s}{R^2}\left(-6\pi^2 f^2 \tau + 4\pi^4 f^4 \tau^3\right)$
	$\dot{u}_{\pi/2}(\mathbf{x}, t)$	$o_f \frac{x_s-x}{R^2}\left(-6\pi^2 f^2 \tau + 4\pi^4 f^4 \tau^3\right)$
	$\dot{\sigma}_0(\mathbf{x}), t$	$o_f \frac{(y-y_s)(x-x_s)}{R^3}\left(\frac{6\pi^2 f^2}{c} + \frac{12\pi^2 f^2}{R}\tau - \frac{24\pi^4 f^4}{c}\tau^2 - \frac{8\pi^4 f^4}{R}\tau^3 + \frac{4\pi^6 f^6 2}{c}\tau^4\right)$
	$\dot{\sigma}_{\pi/2}(\mathbf{x}, t)$	$o_f \frac{(x_s-x)(y-y_s)}{R^3}\left(\frac{6\pi^2 f^2}{c} + \frac{12\pi^2 f^2}{R}\tau - \frac{24\pi^4 f^4}{c}\tau^2 - \frac{8\pi^4 f^4}{R}\tau^3 + \frac{8\pi^6 f^6}{c}\tau^4\right)$

section I am interested in the radial-radial cross-correlations of geophones or DAS channels oriented following the geometries shown in Figure 2.9, so $\theta_1 = \theta_2 = \pi/2$.

The recordings of these sources (every eighth source for visualization) on both sensors acting as geophones (particle velocity) and as DAS channels (point-wise strain rate) is shown in Figure 2.10. Both the geophones and the fiber optics emphasize sources with ϕ_{Src} close to 0 and π (i.e. sources that aren't observed with any apparent velocity bias), and in fact, the relative emphasis of these sources by the fiber channels is stronger than the relative emphasis observed by the geophone. This is also seen in the cross-correlations for each source. As in [65], even though the initial recordings had random time lags due to their radius being chosen over a range between 2000 and 3000 meters, their relative arrival times at $\mathbf{x}_1$ and $\mathbf{x}_2$ are consistent, so the cross-correlations show a clear trend. When we average the source-wise cross-correlations we get a clear signal with a peak at ± 0.6 seconds for both the geophone and DAS experiments. Because $\mathbf{x}_1$ and $\mathbf{x}_2$ are 1200 meters apart in a 2000 m/s medium, that is the arrival time we would expect for a source emitted from one receiver's location and recorded at the other receiver.

While the average of single-source cross-correlations can start to give some intuition about why ambient noise interferometry works, in reality, each window of noise contains the responses to many sources. If a finite number, N, of point sources go off during a

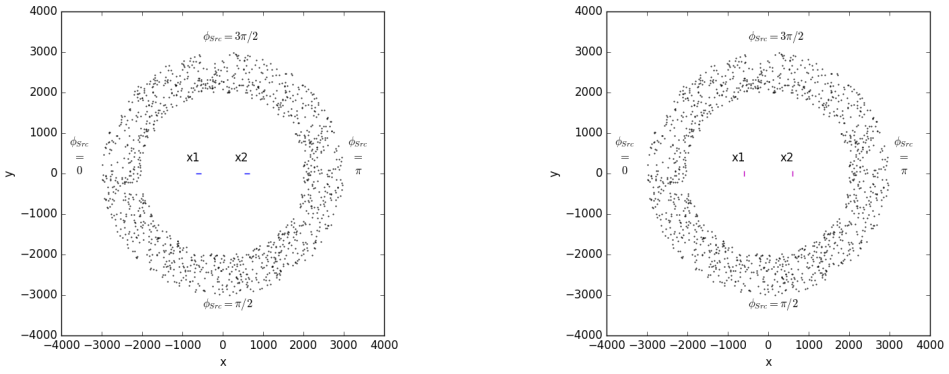

Figure 2.9: I study the cross-correlation response of two sensors at $\mathbf{x}_1 = (-600, 0, 0)$ and $\mathbf{x}_2 = (600, 0, 0)$ oriented in a (left) radial-radial $\theta_1 = \theta_2 = 0$ and (right) transverse-transverse $\theta_1 = \theta_2 = \pi/2$ configuration to sources randomly distributed in an azimuth at azimuth ϕ_{Src} and radius between 2000 and 3000 m. Only one fourth of the sources are shown for clarity. This figure is adapted from [65]. **ER**

particular time window, then the cross-correlation of two traces (denoted by u) recording these sources would include both single-source cross-correlations and cross-terms between different sources. This is apparent when the cross-correlations are written as a product of Green's functions, G, and source functions f:

$$
\begin{aligned}
C(\tau) &= \int_{-T}^{T} u(\mathbf{x}_1, t) u^*(\mathbf{x}_2, t+\tau) dt \\
&= \int_{-T}^{T} \sum_{i=1}^{N} G(\mathbf{x}_1, t; \mathbf{x}_i^s) f(\mathbf{x}_i^s, t) \sum_{j=1}^{N} G^*(\mathbf{x}_2, t+\tau; \mathbf{x}_j^s) f^*(\mathbf{x}_j^s, t+\tau) dt \\
&= \sum_{i=1}^{N} \int_{-T}^{T} G(\mathbf{x}_1, t; \mathbf{x}_i^s) f(\mathbf{x}_i^s, t) G^*(\mathbf{x}_2, t+\tau; \mathbf{x}_i^s) f^*(\mathbf{x}_i^s, t+\tau) dt \\
&\quad + \sum_{j=1}^{N} \sum_{i \neq j} \int_{-T}^{T} G(\mathbf{x}_1, t; \mathbf{x}_i^s) f(\mathbf{x}_i^s, t) G^*(\mathbf{x}_2, t+\tau; \mathbf{x}_j^s) f^*(\mathbf{x}_j^s, t+\tau) dt
\end{aligned}
$$

Only the first term (single source cross-correlations) are explained by Figure 2.10. Thus, [65] performed a slightly more realistic test case to ensure that these cross-source-terms did not add up to make coherent changes in the extracted velocity. The test is to take a long time

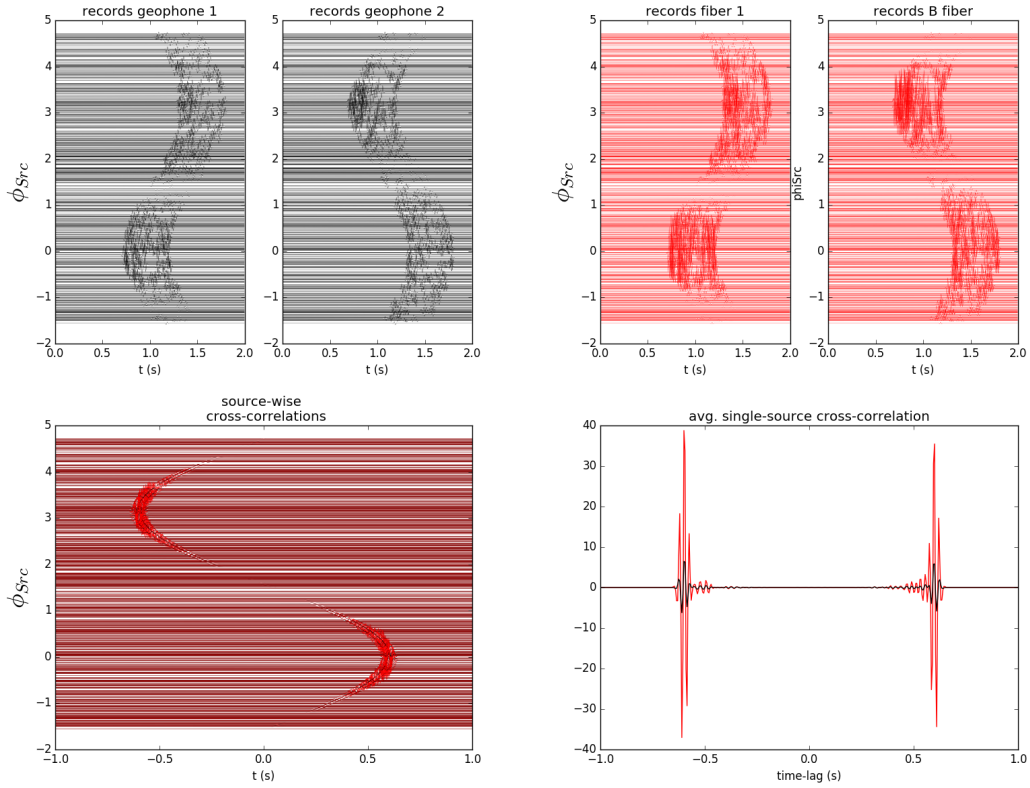

Figure 2.10: Random synthetic point sources emitting Rayleigh waves were recorded via particle velocity and strain rate at $\mathbf{x}_1$ and $\mathbf{x}_2$ in the $(1, 0, 0)$ direction. Only every eighth source is shown. (Top left) The geophones and (top right) fiber channels both respond strongly to Rayleigh waves coming from the $\phi_{Src} = 0, \pi$ directions. (Bottom left) For each source, the geophone cross-correlation is plotted in black and the fiber cross-correlation is plotted in red, and the cross-correlations are very similar for both sensor types. (Bottom right) The average of these source-wise cross-correlations is plotted for the geophones in black and the fiber in red. **ER**

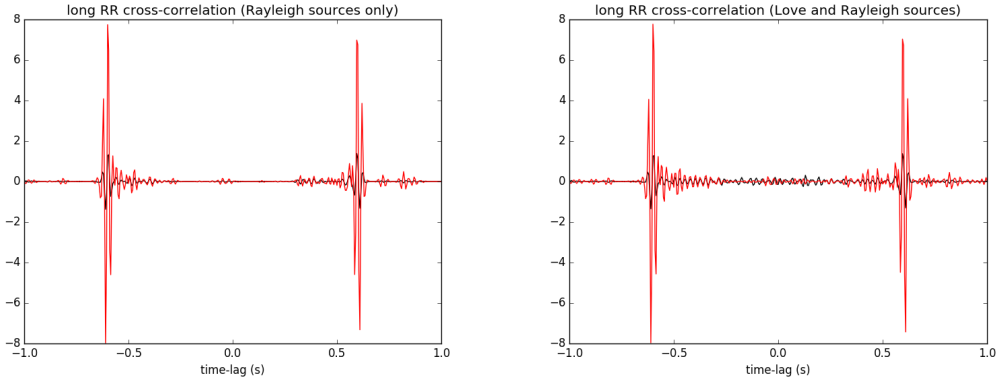

Figure 2.11: A single long radial-radial cross-correlation of synthetic geophone (black) data recorded in the presence of many Rayleigh wave point sources (left) yields a coherent signal the correct arrival time of ±0.6 seconds, and the same holds true for the process repeated with synthetic fiber (red) data. Even when Love wave sources are present at equal amplitudes to the Rayleigh wave sources (right), the correct arrival time can still be picked clearly. **ER**

period and record a single trace for each sensor while letting a number of random sources go off. These are recorded at both $\mathbf{x}_1$ and $\mathbf{x}_2$ (and I repeat this for both a particle velocity and a point-wise strain rate). Then a single cross-correlation is done between the long window of recording at $\mathbf{x}_1$ with the long window of recording at $\mathbf{x}_2$. The resulting single-window cross-correlations for both fiber and geophones responding to 1000 random Rayleigh wave point sources throughout a 40,000 second window are shown in Figure 2.11. Also shown are the cross-correlations of the same experiment repeated with 1000 random Rayleigh wave point sources and 1000 random Love wave point sources of the same amplitude. The signal extracted when both Rayleigh and Love waves are present is a bit noisier than when just Rayleigh waves are present, but the peak at ±0.6 seconds is easy to pick for both the fiber and geophone responses. The additional noise when both Rayleigh and Love wave sources are present is likely because these two channels are both more sensitive to Love waves around at $\pm\pi/4$ and $\pm 3\pi/4$ than to Love waves at 0 and π.

2.3.2 Transverse-transverse Cross-correlations

While the radial-radial cross-correlations yield a clear peak at the correct ±0.6 second time lags for both geophones and DAS. Radial-radial cross-correlations were already observed to be a simpler situation in that they both respond strongly to Rayleigh wave sources at $\phi = 0, \pi$ (the azimuths corresponding to true velocity sources). The same does not hold true for transverse-transverse cross-correlations in the setup pictured in Figure 2.9. To better understand transverse-transverse cross-correlations, I repeated the exercise from [65] but with just Love wave sources, and the results can be seen in Figure 2.12. While the geophones emphasize Love wave sources at $\phi_{Src} = 0, \pi$, the fiber channels emphasize Love wave sources at $\phi_{Src} = -\pi/4, \pi/4, 3\pi/4, 5\pi/4$. This relative difference is even more pronounced in the cross-correlations of the records for each of these sources. As has already been confirmed in practice [33], the average geophone cross-correlation has a strong peak at ±0.6 seconds which is the correct arrival time. The average fiber cross-correlation is much more spread out, which may be in part because wavelets don't cancel as cleanly away from peak sensitivity angles, but also due to the amplitude difference predicted in Table 2.8. As predicted, the peak of the average fiber cross-correlation is between ±0.4 and ±0.5 seconds (since 0.42 seconds = 0.6 seconds $/\sqrt{2}$).

I also repeated the exercise from [65] recording 1000 random Love wave point sources spanning a 40000 second-long trace for each location in both particle velocity and strain rate measurements, then doing a single cross-correlation for each type of measurement, pictured in Figure 2.13. Again, because there is only a single window with cross-terms due to many sources rather than averaging over multiple windows that each have a single source, the resulting cross-correlations are noisier than in Figure 2.12. The geophone cross-correlation again yields correct peaks at ±0.6 seconds, but again, the fiber signal is spread out with a peak somewhere less than ±0.5 seconds.

I repeated this exercise in the presence of 1000 Love wave sources and 1000 Rayleigh wave sources of equal amplitude, also shown in Figure 2.13. There might be some hope of recovering a Love wave signal (that can be corrected) from this receiver geometry when only in the presence of Love wave sources, but it appears that the sensitivity to very apparently fast Rayleigh wave sources near $\phi_{Src} = \pi/2, 3\pi/2$ dominates the signal too much to recover

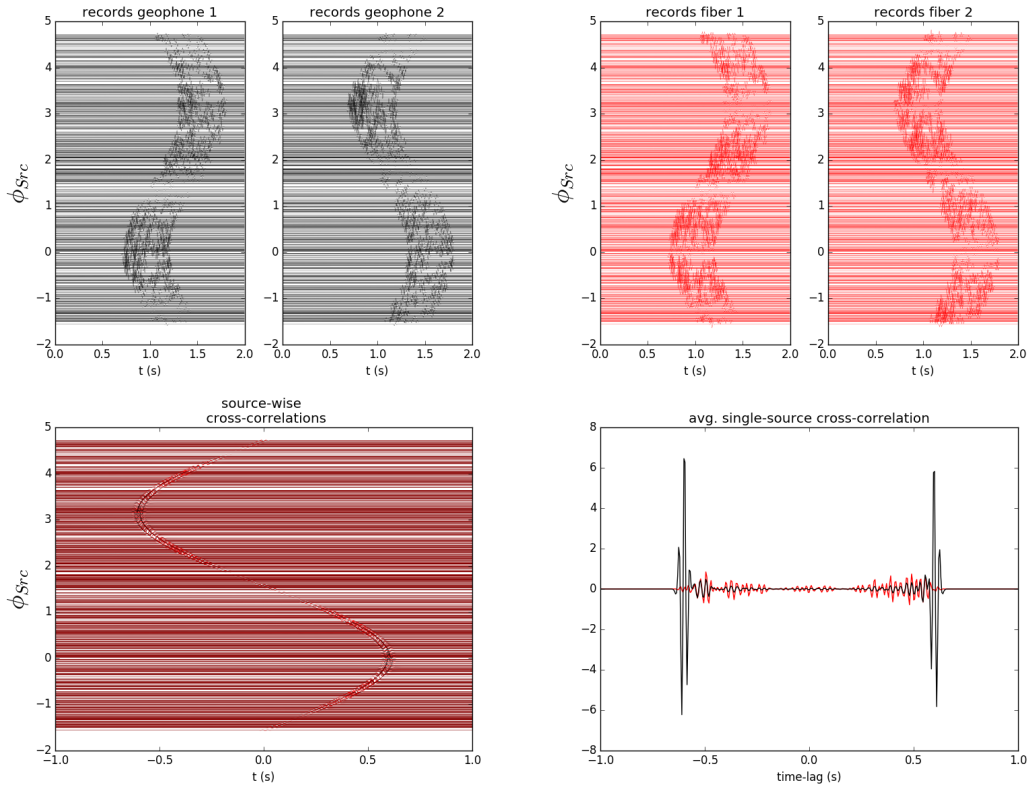

Figure 2.12: Random synthetic point sources emitting Love waves were recorded via particle velocity and strain rate at $\mathbf{x}_1$ and $\mathbf{x}_2$ in the $(0, 1, 0)$ direction. (Top left) The geophones respond strongly to Love waves coming from the $\phi_{Src} = 0, \pi$ directions. (Top right) The fiber channels respond strongly to Love waves coming from the $\phi_{Src} = -\pi/4, \pi/4, 3\pi/4, 5\pi/4$ directions. (Bottom left) For each source, the geophone cross-correlation is plotted in black and the fiber cross-correlation is plotted in red. (Bottom right) The average of these source-wise cross-correlations is plotted for the geophones in black and the fiber in red. The peak geophone signal is around ±0.6 seconds, and the peak fiber signal is more spread in time with a peak in the ±0.4 to ±0.5 second range. **ER**

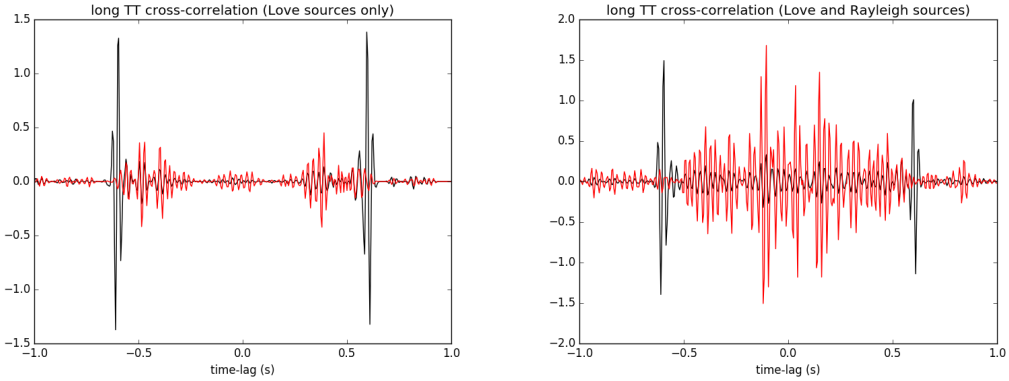

Figure 2.13: (Left) A single long transverse-transverse cross-correlation of strain rate data (red) recorded in the presence of many Love wave point sources yields a coherent signal at an apparently fast velocity by a factor of $\sqrt{2}$, while the . (Right) No discernible arrival can be picked when both Love and Rayleigh wave point sources of equal amplitude and number are recorded as strain rate data (red), but the particle velocity cross-correlation (black) still shows the correct arrival time in the presence of both types of sources. **ER**

a Love wave signal.

2.3.3 Virtual Source Parallel to Receiver Line

Although the transverse-transverse fiber geometry does not appear to yield a clear signal, it seems reasonable that cross-correlations of parallel channels such that $\mathbf{x}_1 - \mathbf{x}_2$ is in a direction close to $(C_{\pi/4}, \mathcal{S}_{\pi/4}, 0)$ would have a Love wave signal since this is the direction that is most sensitive to Love waves. However, these sensors also have significant sensitivity to Rayleigh waves, so it seems plausible that the cross-correlations might include both a Rayleigh wave and Love wave signal. I put this to a test similar to the single cross-correlation over a long recording window in the previous section.

I again use a 30 Hz Ricker wavelet (same expressions as in previous section) with 10000 random Love wave and 10000 random Rayleigh wave sources uniformly distributed over an annulus with inner radius 2000 m and outer radius 3000 m. These are recorded during a 400,000 second record. The Rayleigh wave velocity is again 2000 m/s, but the Love wave is 20% faster: 2400 m/s. This way it will be possible to distinguish the Rayleigh and Love

wave signals from each other easily, and if the Love wave signal is apparently fast it will just lead to better separation from any Rayleigh wave signal. As pictured in Figure 2.14, the virtual source is a point-wise axial strain measurement oriented in the $(0, 1, 0)$ direction and sits at $(425, 425, 0)$, and there are 7 other point-wise axial strain receivers on a parallel line, each oriented in the $(0, 1, 0)$ direction and evenly spaced between $(-425, -850, 0)$ and $(-425, 425, 0)$ (so this last receiver is in the transverse-transverse setup with the virtual source).

The cross-correlations of these long records for each receiver against the virtual source are shown in Figure 2.14. For the receivers within a 15^o offset of the transverse-transverse orientation (i.e. the two bluest receivers) there is a lot of energy from the very apparently fast velocity Rayleigh wave sources from $\phi_{Src} = \pm\pi/2$, so there is no clear arrival at the true Love and Rayleigh wave arrival times. Moving down to the third receiver, about a 25^o offset, there is still quite a bit of this fast energy, but there is also a strong peak at the true Love wave velocity and a smaller peak (although not nearly as clear) at the true Rayleigh wave velocity. All of the receivers farther down have both clear Rayleigh and Love arrivals and less of the early arrival energy. The Rayleigh wave arrivals get increasingly strong moving down the line because the orientation between the receivers and the virtual source gets closer to the two channels being collinear (like a radial-radial setup).

2.3.4 Virtual Source Perpendicular to Receiver Line

At corners of arrays where one fiber line is orthogonal to another, it would be ideal to be able to use the ray paths between those two lines. To better understand this situation, I test a virtual source on one line at $(425, 425, 0)$ oriented in the $(1, 0, 0)$ direction, and seven equally spaced receivers oriented in the $(0, 1, 0)$ direction between $(-425, -800, 0)$ and $(-425, 425, 0)$, as pictured in Figure 2.15. The same velocities and same configuration of Rayleigh and Love wave point sources were used as in the previous section.

The cross-correlation results are seen in Figure 2.15. No clear signal is visible in the cross-correlation with the top receiver that is directly across from the virtual source, but for all other offsets, both the Rayleigh and Love wave signals are clearly visible. While the relative amplitudes between the Rayleigh and Love wave signal peaks varied significantly

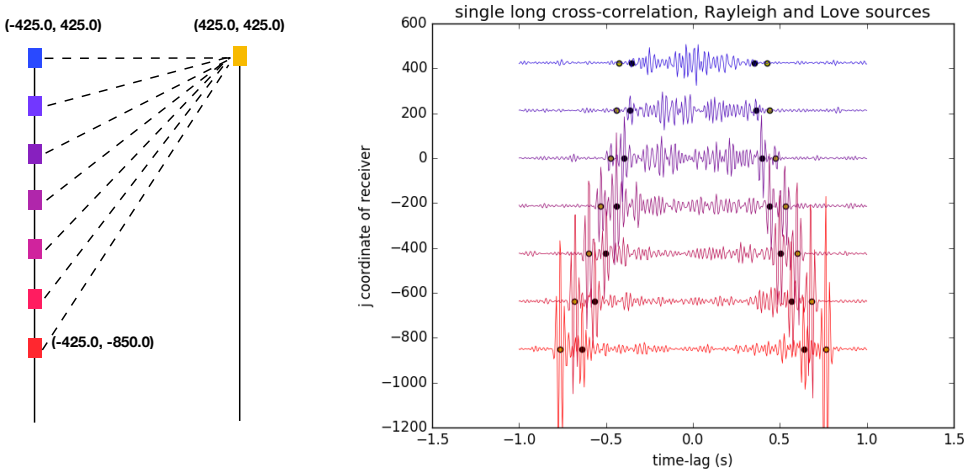

Figure 2.14: (Left) A virtual source is marked in yellow along one fiber line, and along a parallel cable are other receivers marked in blues, purples and reds. (Right) Some of the receiver-color-coded cross-correlations show clear peaks at the correct positive and negative arrival time lags, where Rayleigh waves are marked with yellow dots and Love waves are marked with blue dots. Left: **NR**, Right: **ER**

with offset in the parallel lines setup, the relative amplitudes of the Rayleigh and Love wave peaks stay consistent over offsets in this orthogonal lines setup. Overall, it appears that the orthogonal lines setup is actually more reliable for simultaneously extracting both Rayleigh and Love wave signals than the parallel lines setup, but the parallel lines setup can be used for a limited range of offsets.

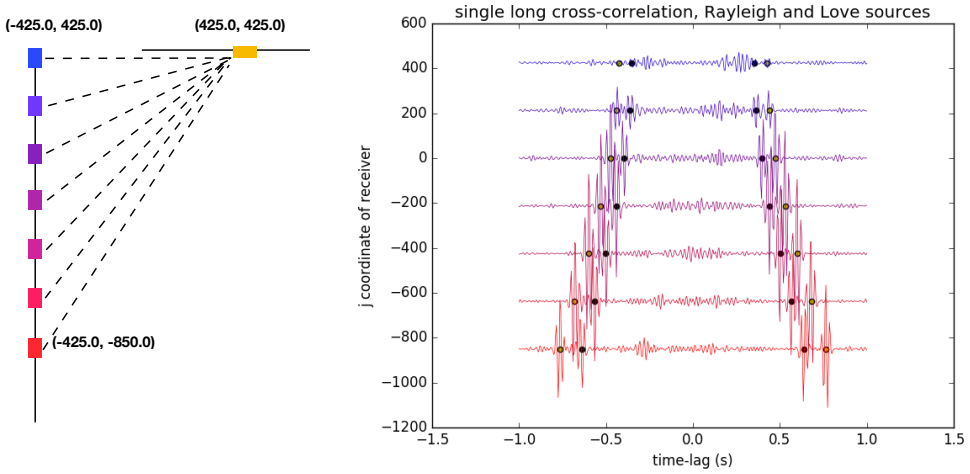

Figure 2.15: (Left) A virtual source is marked in yellow along one fiber line, and along an orthogonal cable are other receivers marked in blues, purples and reds. (Right) Some of the receiver-color-coded cross-correlations show clear peaks at the correct positive and negative arrival time lags, where Rayleigh waves are marked with yellow dots and Love waves are marked with blue dots. Left: **NR**, Right: **ER**

Chapter 3

Experimental Data Overview

Throughout this thesis, I will show examples from four surface DAS array installations: three with fiber optic cables directly coupled to the ground, and one with fiber optic cables run through existing telecommunications conduits. The three directly buried fiber optic arrays were supported through a SERDP grant to develop a fiber optic monitoring system to detect precursor V_S drops indicating permafrost thaw before the point of failure. In a separate experiment occurring after the first two SERDP experimental phases, we installed fiber optics in existing telecommunications conduits under the Stanford University Campus. The goal of this installation is to evaluate the data quality recorded by a DAS system when the coupling between the ground and fiber relies only on gravity and friction. Although the data quality is expected to be better in the backfilled trenched installations, positive results in the telecommunications installation would reveal the possibility of using existing telecommunications infrastructure for recording seismic data at low cost and under urban areas.The goals of the Stanford DAS Array were earthquake analysis and estimation of near surface soil properties by seismic interferometry. The experiments, in chronological order, are:

1. December 2014, SERDP Pilot Test at Richmond Field Station in Richmond, CA
2. Summer 2015, SERDP Roadside Array at Farmer's Loop Site in Fairbanks, AK
3. Summer 2016, SERDP Active Thaw Test at Farmer's Loop Site in Fairbanks, AK

4. Sep. 2016 - present (continues upon writing, June 2018), Stanford Fiber Optic Seismic Observatory in Stanford, CA

Previous work on DAS has emphasized the importance of installation technique and cable-to-formation coupling, but the experiments in this thesis help demonstrate that the results of horizontal DAS arrays are relatively robust to installation technique. The first three experiments were installed such that the fiber optic cables were laid in trenches then buried (either backfilled soil or wood chips) to ensure coupling to the ground. However, the trenching process can be costly and requires permitting that can be difficult to obtain at a large scale, particularly in environmentally sensitive regions or urban areas. One experiment was conducted in the SERDP Active Thaw Test to test a fiber pinned on the surface to cut costs for temporary deployments. To further reduce the manual labor required for installation I organized the installation of fibers in existing telecommunications conduits at the Stanford Fiber Optic Seismic Observatory. This required several days of work for a couple of technicians installing the fiber optics following the same installation technique as they use for all other telecommunications projects, although writing down a bit more detail including marking location and lengths of slack fiber spooled up in manholes, and marking small jobs in the conduit paths. For each experimental site, I show some summaries of the data distribution, their spectra, and how continuous the data are in space and time. These analyses are only intended to give the reader a sense of what the data are like and not intended as a comparison of interrogator units; such statements would require controlled 'shoot-out' experiments with units attached to fibers in the same cable at a single site.

3.1 SERDP Richmond Field Station Pilot

The goals of the December 2014 Richmond Field Station Pilot test were to demonstrate that passive noise can be recorded by trenched and buried fiber optics, that virtual source response estimates can be extracted from that noise through cross-correlation, and to compare the signal quality and cost trade-offs of multiple types of cable jackets. These tests were conducted at Richmond Field Station because it is near infrastructure, is a well-characterized site with known simple geology (layers of bay muds), and it is near Lawrence Berkeley National Laboratory providing easy access to additional experimental equipment.

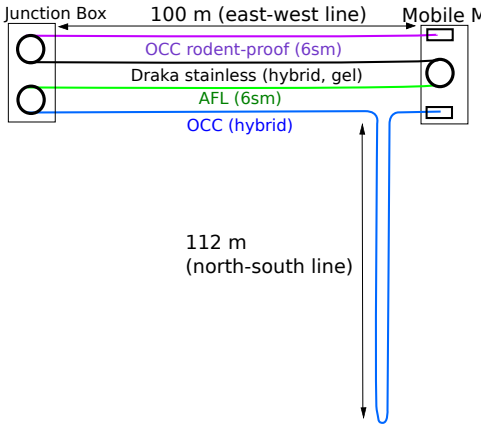

Figure 3.1: A diagram of the DAS deployment at Richmond Field Station. We tested four types of straight fiber optic cable, and these cables were spliced end to end. The DAS control unit and recording system are located in the Mobile Mini. We ran a 112 m North-South line and 100 m East-West line of an OCC hybrid 6 sm cable (blue), an East-West line of an AFL 6 sm cable (green), an East-West line of a Draka stainless-steel encased hybrid cable (black), and an East-West line of an OCC rodent-proof 6 sm cable (purple). This figure was adapted from the splice design diagram of Nate Lindsey (LBL/UC Berkeley). **NR**

We deployed an L-shaped trenched DAS array made up of several types of fiber optic cables attached to a Silixa iDAS system at the Richmond Field Station (RFS) in Richmond, CA as shown in Figure 3.1. The East-West trench was 2 ft deep and 15 in wide, the North-South trench was 2 ft deep and 8 in wide, and all cables were laid flat along the bottom before the trench was backfilled. There was a heavy storm the day after cable installation, which may have had some effect on the cables' coupling. Alongside the trench, we installed a series of three component geophones for comparison purposes. We conducted a number of active source (hammer) tests as a means of calibrating the sensors, then began passive recording tests.

The RFS is an ideal location for passive recording. There is a train that passes by the field station (< 100 m away) approximately hourly, the San Francisco Bay is less than a kilometer away to the South and West, a road that frequently has 18 wheelers driving on it is less than 50 m North and runs parallel to the East-West segment of the cable, and highway 580 is less than half a kilometer away to the North and East. The data were collected in one

minute traces at a rate of 2000 samples per second, with a 1 m channel spacing and 10 m gauge length (so nearby channels overlapped).

3.2 SERDP Fairbanks, AK DAS Roadside Array

In summer 2015 researchers from Lawrence Berkeley National Laboratory and the U.S. Army Corps of Engineers installed 2+ km of trenched fiber optics on Corps of Engineers Land along Farmer's Loop Road near Fairbanks, AK, a patchy permafrost zone. As shown in Figure 3.2, it has a 638 meter segment running within 10 m of Farmer's Loop Rd, and loops back as a mostly parallel line. A highway runs mostly parallel to the array about 400 m east. Ambient noise was recorded by a Silixa iDAS system with a 1 m channel spacing, 10 m gauge length, and a 1 kHz sample rate. DAS recording was limited to roughly 20 hrs of daytime data recorded between Aug. 5 and Aug. 10. After the fibers were laid in the trenches, they were backfilled with a mix of soil and woodchips.

Vehicular traffic on Farmer's Loop Rd, seen in Figure 3.4, is the defining feature of this dataset. Spectral stacks like the one seen in Figure 3.3 help pin down which channels correspond to each part of the array geometry. Channels 134-525 lie between the field house and the south end of the array with roughly 200 m running next to the long mostly straight line closest to the road. We consider channel 535 on the south end up to channel 1135 in the north.

3.3 SERDP Fairbanks, AK DAS Active Thaw Grid Array

Following the roadside tests at the Farmer's Loop Site, a grid of trenched fiber was installed to the east of the field house, seen in Figure 3.5. The trenches were 30 cm deep, and the fibers were in an OCC hybrid tactical cable. One line, was pinned on the surface instead of trenched. This was to test the potential for temporary deployments of fiber. Within the fiber grid, a 10 m x 13 m array of heaters were installed to actively warm a section of permafrost over a two month period. The data were collected at a rate of 1000 samples per second with a 1 m channel spacing and 10 m gauge length [2].

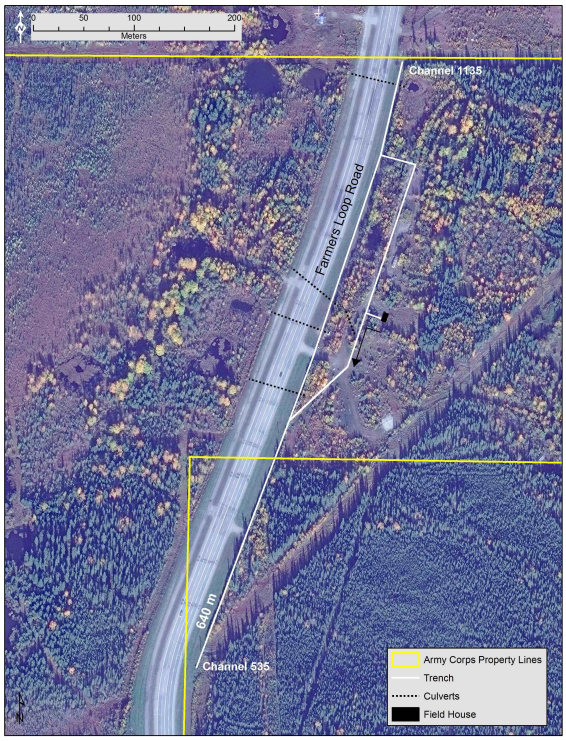

Figure 3.2: An overhead view of the 2015 fiber layout (white line). Channel numbering starts at the field house and continues in the direction of the arrow. This figure was created by Anna Wagner (US Army Corps of Engineers Cold Regions Research and Engineering Laboratory). **NR**

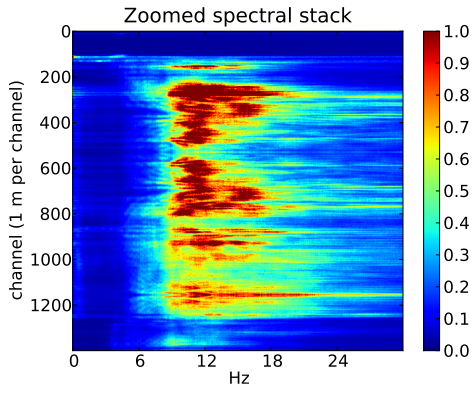

Figure 3.3: The spectrum for each channel stacked over a two hour daytime recording shows that the majority of the noise content is between 5 and 25 Hz. **CR**

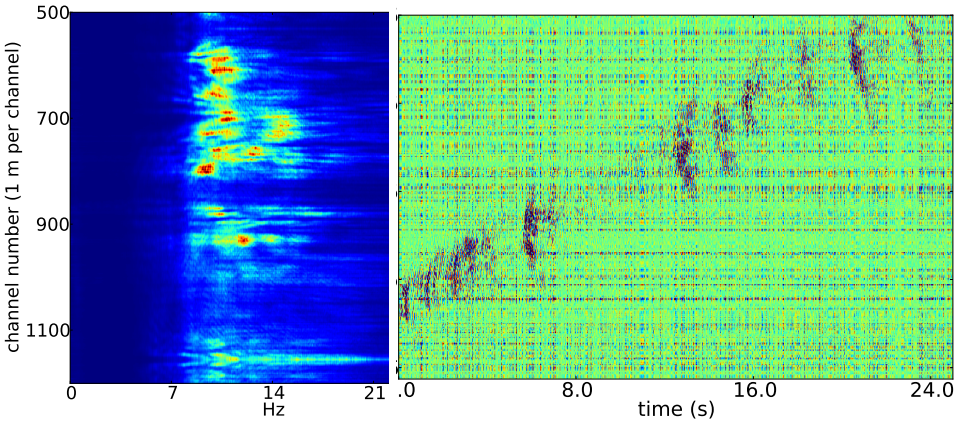

Figure 3.4: (Left) A stack of the Figure 3.3 spectrum squared enhances channels with strong responses. Many points with strong spectral response roughly correspond to points that are excited as a car drives by (right), emphasized with a high clip. **CR**

To further characterize the passive data recorded on a typical day I analyzed the distribution of strain rate amplitudes, jumps between time steps for each channel, jumps between channels, the amplitude distribution and spectrum of the mean and median throughout the array, and the distribution of average energy per channel. I only considered data between channels 3001 and 3624, the channels trenched in a straight line alongside the road. I studied continuous data between 00:00:29 and 07:00:29 as well as data between 10:09:29 and 12:00:29 (UTC). There was an interruption in the data for a few hours, as their are occasionally in this data set, so it gives an opportunity to understand any changes that occur when restarting the interrogator unit. For the time-lapse thaw study, I used data that I had first anti-aliased to 50 Hz Nyquist then downsampled to 100 samples per second, so here I analyze the distribution of these downsampled data (note: this almost certainly would change the statistics in the following figures when compared to raw data, but should give the reader better context for understanding results in Chapter 7).

The overall distribution of values of this data can be seen in the histogram in Figure 3.6, which has bins set based on the distribution of data in the first minute of recording of the day. The data are distributed symmetrically centered around 0 and smoothly decaying away from 0 with the majority of values within ±50. Note that these are not absolute strain rate

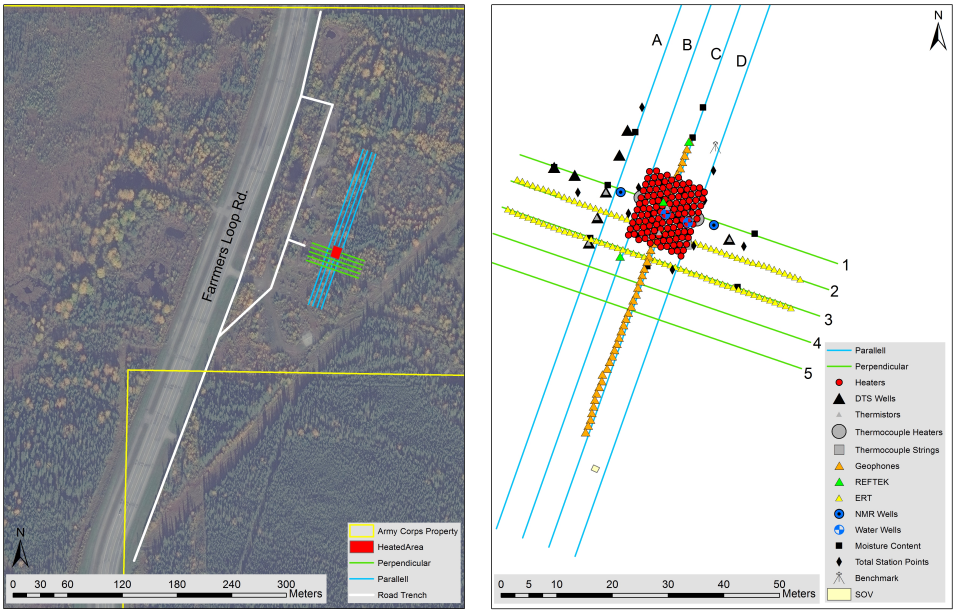

Figure 3.5: (Left) In 2016 a grid of trenched fiber was deployed east of the 2015 roadside array. Although the fibers are shown as separate lines, all fibers are spliced end-to-end so a single interrogator unit probes the entire 7 km of fiber throughout the array (both roadside and grid). (Right) Heaters were installed within the grid of fiber, marked as red dots. This figure was created by Anna Wagner (US Army Corps of Engineers Cold Regions Research and Engineering Laboratory). **NR**

measurements, just proportional to strain rate. I also wondered about the distribution of jumps between time steps, which appears as vertical striping in Figure 3.4, so I calculated its distribution which is also pictured in Figure 3.6. These temporal jumps are also distributed symmetrically centered at 0, although their values are spread more than the strain rate data by roughly a factor of 100. To study spatial continuity of the data, I calculated first-order finite-difference approximations of the spatial derivative of strain rate along the fiber (change rate of neighboring channels at each time step). This channel-jump distribution can be seen in Figure 3.7. The jumps from one channel to the next channel along the fiber are symmetrically distributed around 0 and most of the time have an amplitude smaller than 5 (keeping in mind that the data are typically amplitudes less than 50).

To further understand the differences between channels, I plot the distribution of two-norms for each minute and each channel (that is, 6000 samples per channel for each channel for each minute of the day) in Figure 3.7. The trenched installation keeps the energy detected between nearby channels relatively close, although there are some channels (perhaps near road joints or in areas with different near-surface conditions) that are lower or higher amplitudes. There can be an order of magnitude difference in energy from one minute to the next on the same channel. There is a clear and significant drop in energy after the first 7 hours of data when the interrogator unit was turned off for several hours, then turned back on. However, the horizontal striping indicating which channels tend to detect the most energy is relatively consistent even after the energy drop. This could be due to either decreased traffic alongside the road during the period it was turned off, but could also indicate a slight change in recording settings. Either way, this suggests normalizing the average energy within each file would be sensible before any passive data analysis.

There is a further interesting feature of this data: laser noise. One possible explanation for laser drift in some interrogator units is that noises in the interrogator unit itself cause issues in the optical measurement system, showing up as jumps in energy on all channels simultaneously. I wondered whether these jumps in energy were distributed randomly around 0, so I calculated the mean reading throughout the array at each time step and the median reading throughout the array at each time step. I show the distribution of the mean and median data values throughout the roadside array at each time step as well as the spectra of the array-wide mean and median throughout the day in Figures 3.8 and 3.9. As

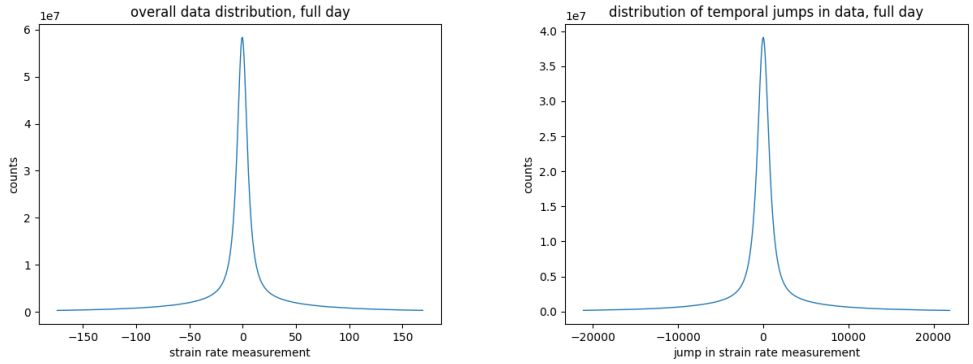

Figure 3.6: These histograms show the (left) distribution of strain-rate data along the roadside line and (right) the distribution of temporal jumps in the strain-rate data. These jumps are calculated by a first-order finite-difference derivative of each channel's strain-rate data. The strain rate distribution plot does not show 5.7% of the samples that are most extreme. The jump in strain rate histogram does not show 3.6% of the most extreme samples. Compared to a Gaussian distribution, these are relatively heavy tails. **CR**

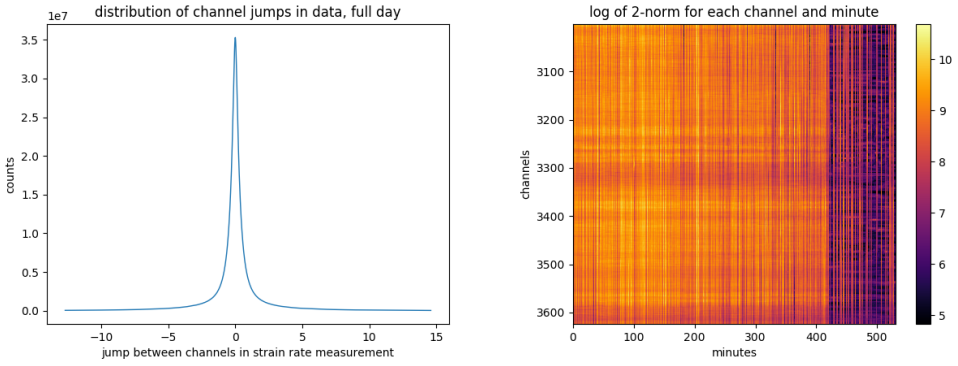

Figure 3.7: (Left) this histogram shows the distribution of jumps between strain rate data of neighboring channels along the roadside line. The histogram does not show 1.6% of the most extreme jumps. (Right) For each channel along the road, the log of the two-norm of that channel's data for each minute is plotted. There is a major drop in energy at 420 minutes when the box was turned off then turned on again, but there was also a 3 hour gap in data. **CR**

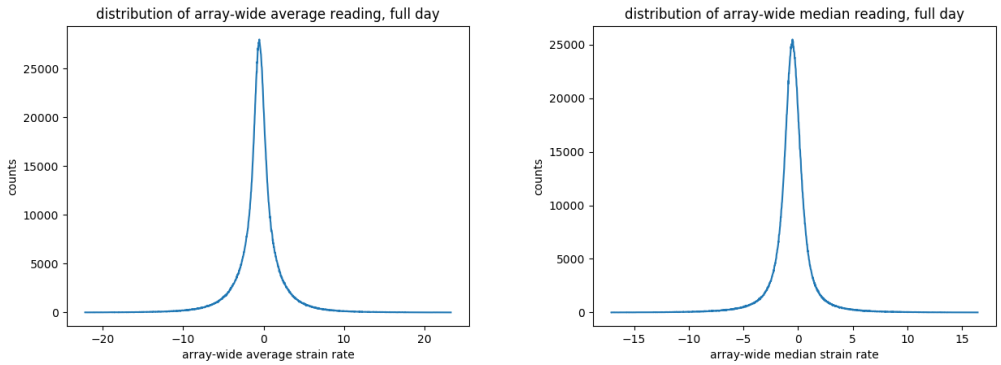

Figure 3.8: These histograms show the distribution of the (left) median and (right) mean strain rate data throughout the roadside line at each time sample. The histogram of the array-wide mean does not show 0.09% of the most extreme values, and the histogram of the median does not show 0.06% of the most extreme values. **CR**

seen in Figure 3.8, both the mean and the median of this roadside fiber line are distributed symmetrically and decaying smoothly away from their peaks. Interestingly, both the mean and median values have a slight negative bias. This is more than an order of magnitude smaller than the strain rate amplitudes recorded, and any changes that appear on all channels at once can easily be removed from ambient noise interferometry by filtering out infinite velocity events. While it is unlikely to cause problems, it was unexpected. In Figure 3.9, the drop in energy after the interrogator unit was reset can be seen again, although it is less extreme than the drop in each channel's two-norm. The spectra of the mean reading has a strong effect from the anti-alias filter used on the data, but the median only has a slight drop in energy, suggesting that the median may tend to jump around more than the mean in this case (more high frequency energy). Both the mean and median tend to have the most energy in the 5-15 Hz range.

3.4 Stanford Fiber Optic Seismic Observatory

While the arrays in Richmond, CA and Fairbanks, AK were well-suited to their objectives for high-resolution study of near-surface geophysical processes, the trenching and backfilling process to install cables was labor intensive. The desire to reduce the man-hours required

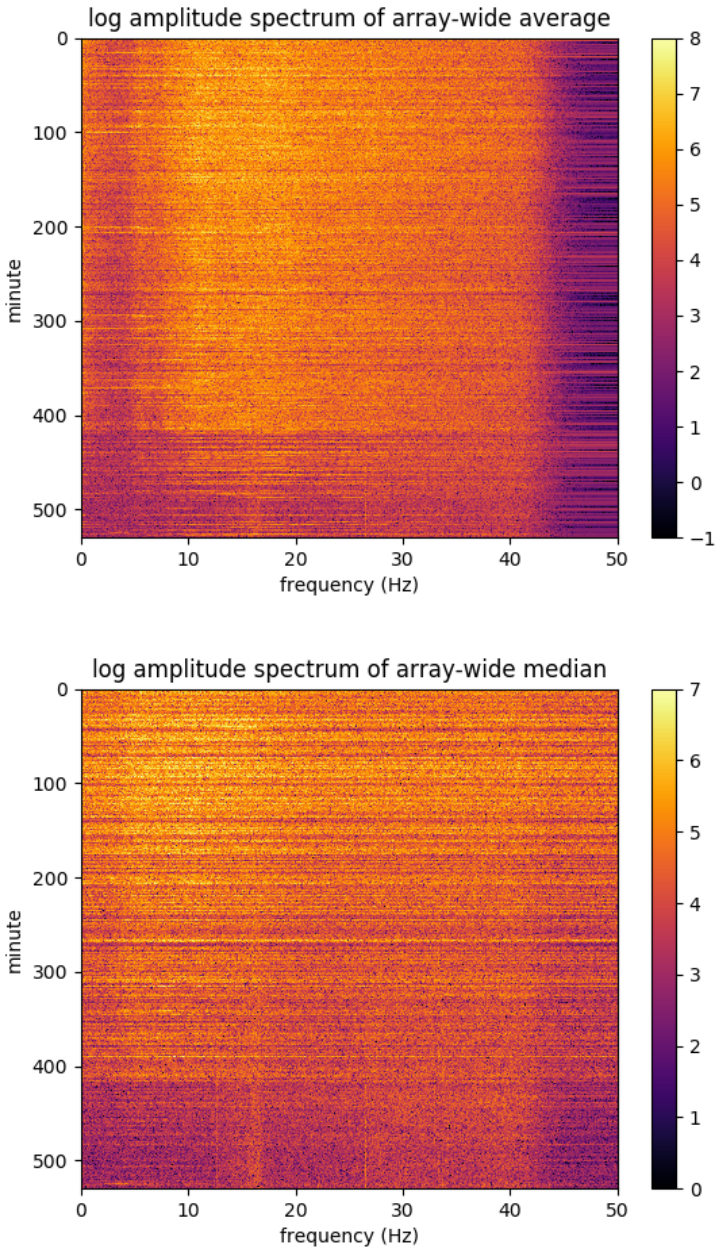

Figure 3.9: For each minute of data, these histograms show the spectrum of the (left) median and (right) mean of the strain rate data at each time sample throughout the roadside line. **CR**

for array installation sparked the design of a novel experiment to investigate the potential for fibers run through existing telecommunications conduits underneath the Stanford Campus. The experiment has three primary goals: ambient noise interferometry, earthquake detection, and recording active seismic shooting. In August 2016, 2.4 km of fiber optic cable was deployed in a two-dimensional array in existing telecommunications conduits underneath the Stanford University campus. This array has been continuously recording since September 3, 2016, and continues to record data at the present (Spring 2018). In this thesis I refer to it as the Stanford Fiber Optic Seismic Observatory, but previously the same experiment has also been called the Stanford DAS Array (SDASA).

After discussions with Stanford IT, we decided it would be more cost effective in this particular case for us to run a new fiber in the existing telecommunications conduits rather than leasing several fiber lines that had previously been installed by Stanford IT, then splicing those lines together. This array was installed in the same way that all other fiber optic cables are installed in telecommunications conduits around campus, as diagrammed in Figure 3.10. The fibers were spooled up and brought down into manholes, then pulled either by hand or with a machine along narrow (10-15 cm wide) conduits connected between the manholes. The fibers sit loosely in the conduits, and where they are inside manholes (small underground rooms roughly 8 feet high and 3-4 ft by 6-9 ft wide) the fibers are zip-tied to a bracket on the side of the wall. There were two locations with 150 feet of fiber spooled up and strapped to the wall (with a vertical and horizontal component): one at Campus Dr. and Via Ortega, and another just south of Allen on Via Pueblo.

The array has two recording modes currently configured: active and passive.

- **Active** mode records 2500 samples per second at a gauge length of 7.14 m and channel spacing of 1.02 m.
- **Passive** mode records 50 samples per second at a gauge length of 7.14 m and channel spacing of 8.16 m.

Note that the gauge length is the length of the subset of fiber over which average strains are reported. The vast majority of the time, the array is recording in passive mode so as to keep the data size manageable. When we do active tests (including geometry calibration tap tests), we switch to active recording mode. The switch between these two configured modes

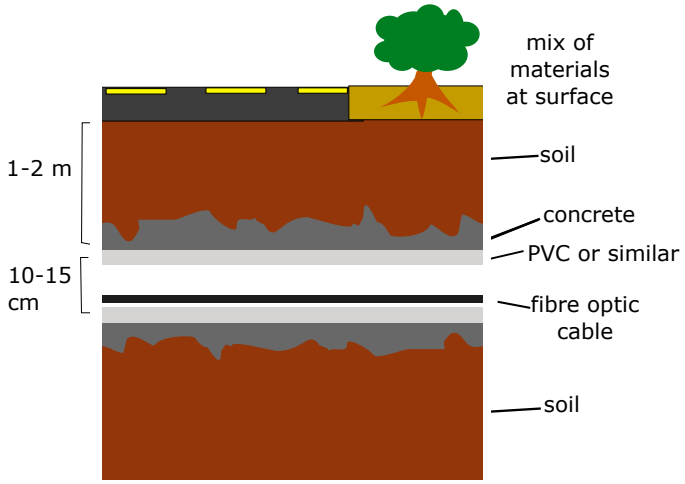

Figure 3.10: The campus has a mix of near surface materials, both natural and manmade. One to two meters below the surface sit conduits for telecommunications. These are generally 10-15 cm in diameter, and usually made of PVC or similar materials, and in some parts of campus are surrounded by concrete or cement slurry before being buried. Our fiber optic cable is roughly 1 cm in diameter and rests in the conduits loosely. **NR**

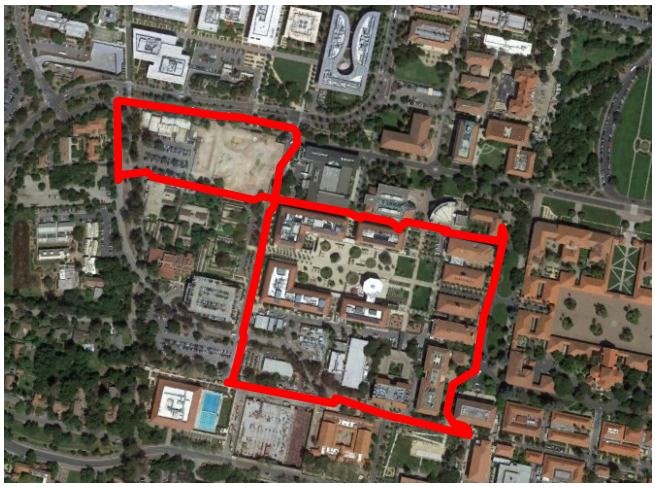

Figure 3.11: The layout of the fiber following telecommunications conduits overlaid on the map. The longest linear section is roughly 600 meters wide. Some deviations from straight lines had to occur due to existing conduit geometry constraints. **NR**

can be handled remotely and no physical access to the box is required after installation. Although their gauge length is the same, the active mode data can have more options to add together neighboring channels to simulate a variety of gauge lengths (and thus, a variety of wavenumber sensitivity profiles, which can be beneficial).

On instance that required active mode recording was assigning spatial locations to each channel number along the fiber (the passive channel numbering was 1 channel per 8 active channels). Unfortunately, there is currently no easy way to tie the data recorded on each channel to specific spatial locations without some manual labor. Stanford IT provided a scale map of manhole locations along our path, so used many of these points for calibration. The channels in manholes tended to have poorer coupling since the fiber was strung partially along the side of a wall instead of sitting on the bottom of the conduit with gravity assisting it, so I looked for weakly responding channels to align with known manhole locations. Ethan Williams, Chris Castillo and I also did many sledgehammer tests, as well as a few betsy gun shots. Both types of tests can be seen in Figure 3.12 and 3.13. We recorded these

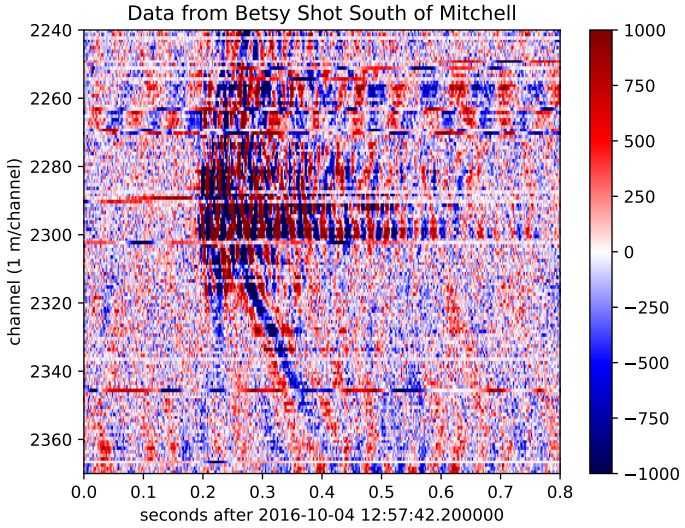

Figure 3.12: A betsy gun shot south of Mitchell on 2016-10-04 as recorded on channels 2240 to 2370 in active recording mode starting 1016-10-04 12:57:42.2 UTC shows both a fast (likely body wave) event and a slower surface wave propagating across the array along Panama Street from Mitchell Building towards Green Earth Sciences Building. **CR**

in active mode, so we had to scale distances by roughly a factor of 8 for the passive channel points. By manually inspecting these data, then comparing to a map in Google Earth of the fiber path, I settled on the approximate geometry in Table 3.1.

To further characterize the passive data recorded on a typical day I analyzed the distribution of strain rate amplitudes, jumps between time steps for each channel, jumps between channels, the amplitude distribution and spectrum of the mean and median throughout the array, and the distribution of average energy per channel. I studied continuous data between channels 15 and 305 (avoiding channels in Green building) on Sep. 12, 2016 from 00:00:00 to 23:59:59 (UTC) because there were no interruptions in recording, and it was a relatively quiet seismic day (aside from one M2.1 earthquake at 11:28:45 UTC at 1.6 km depth roughly 23 km southeast of campus).

Because the data are recorded with some DC offset that varies greatly between channels, I analyzed data with the small preprocessing step of a first-order forward finite difference estimate of the strain rate (just finite difference in time for each channel). I only considered

Label	Channel Number	East UTM	North UTM
Start S. of Green	14	573088.0	4142497.0
Between Roble & HEPL	25	573000.58	4142531.35
Arrillaga Corner Start	48	572851.00	4142560.00
Arrillaga Corner End	49	572851.00	4142560.0
Via Ortega & Panama	58	572871.35	4142626.52
Via Ortega By Y2E2	70	572889.00	4142710.00
Via Ortega & Via Pueblo NS	83	572920.19	4142817.00
NW Corner of Allen	96	572961.29	4142909.74
Campus Dr. Coil Start	100	572942.64	4142936.69
Campus Dr. Coil End	107	572942.64	4142936.69
Panama & Campus	138	572694.11	4142985.43
Panama Near Pine	155	572693.26	4142866.36
Panama Curve Start	157	572695.88	4142872.24
Panama Curve End	165	572736.10	4142875.45
NW Corner of Pine	167	572740.38	4142868.55
Via Ortega & Via Pueblo EW	184	572922.4	4142826.52
Coil by Allen Start	203	573047.61	4142791.85
Coil by Allen End	209	573047.61	4142791.85
S of Hewlett Start	225	573172.14	4142767.36
S of Hewlett End	228	573172.14	4142767.36
Sequoia Jog Start	240	573249.00	4142746.00
Sequoia Jog Top	245	573258.00	4142770.00
Moore	261	573221.45	4142639.24
Bike Racks By Skilling	269	573205.43	4142563.1
NW Corner of Mitchell	274	573173.9	4142544.07
W Side of Mitchell	280	573161.0	4142501.0
S of Mitchell Start	283	573188.0	4142468.0
S of Mitchell End	288	573188.0	4142468.0
End S. of Green	302	573088.84	4142497.62

Table 3.1: List of physical points used to compare signals from particular passive channels to geometric locations

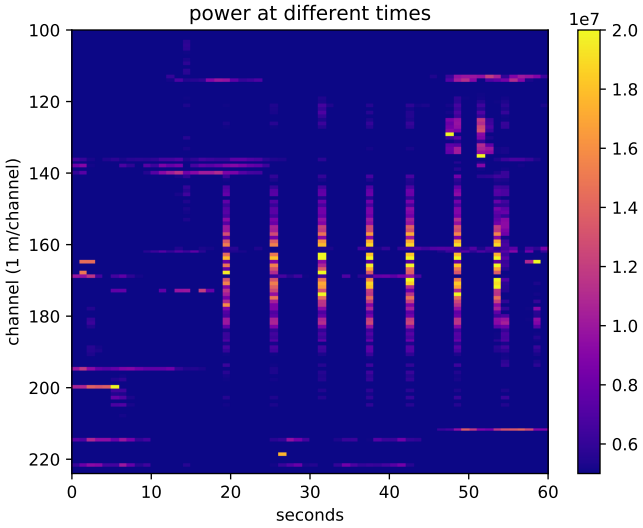

Figure 3.13: The power of small windows of time on each channel during 8 lbs. sledge-hammer tests west of Green Building from 2016-10-04 starting at 12:36:43 UTC. **CR**

data between channels 15 and 305 to exclude channels in the walls of Green building (these channels tend to be outliers in their behavior). The overall distribution of values of this data can be seen in the histogram in Figure 3.14, which has bins set based on the distribution of data in the first minute of recording of the day (mid-afternoon local time). The data are distributed symmetrically centered around 0 with the majority of values within ±5. Since I always use data with a finite difference first applied, I also wondered about the distribution of jumps between time steps, also pictured in Figure 3.14. These data are also distributed symmetrically centered at 0, although their values are spread more than the strain rate data by roughly a factor of 100. To study spatial continuity of the data, I calculated first-order finite-difference approximations of the spatial derivative of strain rate along the fiber (change rate of neighboring channels at each time step). This channel-jump distribution can be seen in Figure 3.15. The jumps from one channel to the next channel along the fiber are symmetrically distributed around 0 and most of the time have an amplitude smaller than 1 (keeping in mind that the data are typically amplitudes less than 5). To further understand the differences between channels, I plot the distribution of two-norms for each minute and

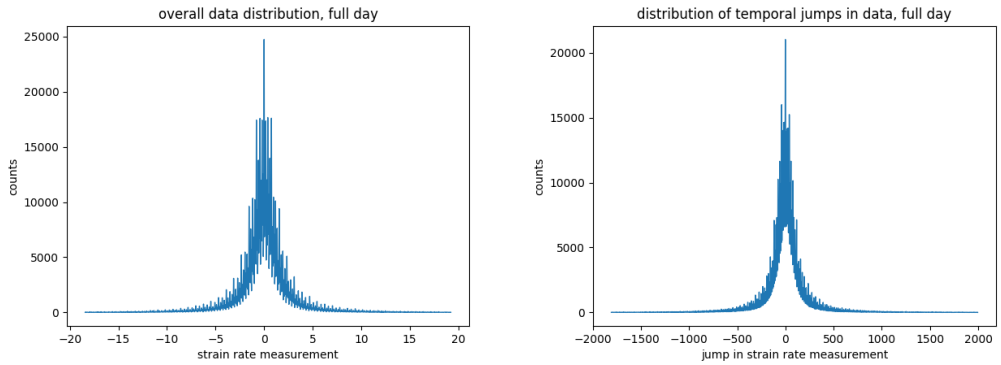

Figure 3.14: These histograms show the (left) distribution of strain-rate data from channels 15 to 305 and (right) the distribution of temporal jumps in the strain-rate data. These jumps are calculated by a first-order finite-difference derivative of each channel's strain-rate data. The strain rate distribution plot does not show 1.5% of the samples that are most extreme. The jump in strain rate histogram does not show 0.9% of the most extreme samples. **CR**

each channel (that is, 3000 samples per channel for each channel for each minute of the day) in Figure 3.15. From one minute to the next, there is not a great deal of variability for any channel, although between nearby channels the difference in energy can be stark, sometimes varying by a factor of e^5 between nearby channels.

There is a further interesting feature of this data: laser drift and low-frequency content. One possible explanation for laser drift in some interrogator units is that noises in the interrogator unit itself vibrate the optical interferometry reference fiber, showing up as strains on all channels simultaneously. However, if there are low-frequency seismic vibrations that propagate throughout the array (as we know there are due to primary and secondary microseism), these signals may stretch or compress the whole array simultaneously as well. I do not separate these two causes of array-wide signals, but do show the distribution of the mean and median data values throughout the array as well as the spectra of the array-wide mean and median throughout the day in Figures 3.16 and 3.17. Both histograms show that the mean and median signal throughout the array at any time step is distributed centered around 0. The mean has a greater spread of distribution and a smoother distribution, while the median tends to stay within ±0.2 and has a distribution with small concentrated spikes. However, the envelope of the distribution of the array-wide median is reasonably

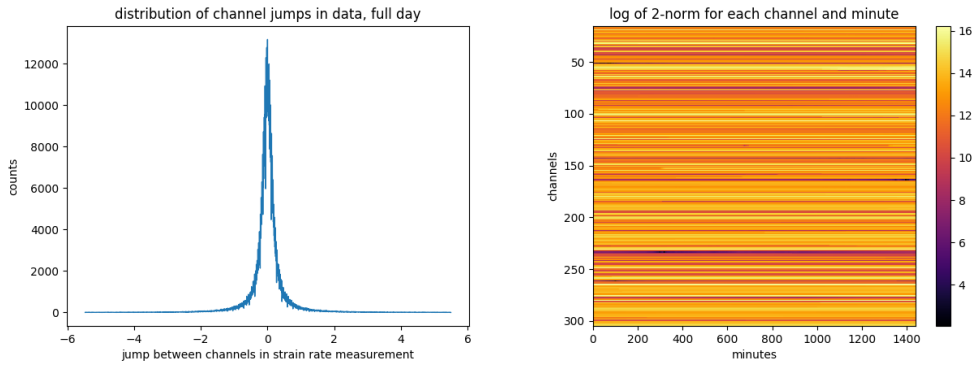

Figure 3.15: (Left) this histogram shows the distribution of jumps between strain rate data of neighboring channels along the roadside line. The histogram of jumps between channels does not show 0/7% of the most extreme jumps. (Right) For each channel along the road, the log of the two-norm of that channel's data for each minute is plotted. **CR**

well described by a decaying single-mode distribution like a Gaussian. The spectra of the mean and the median both show an gradual increase in energy during daytime hours (minutes 0 to 200 and 800 to 1400), and both show some striping with peaks in energy below 1 Hz, around 9 Hz, 13 Hz, and a peak between 16 and 17 Hz, as well as an energy decrease between 1 and 5 Hz and a drop with the anti-alias filter near the 25 Hz Nyquist frequency. However, the mean distribution shows that several minutes have some extreme outliers (leading to bright horizontal stripes), while the median is more resilient to this and overall shows more similarity in spectral distribution from minute-to-minute. The median does have much more energy concentrated below 1 Hz.

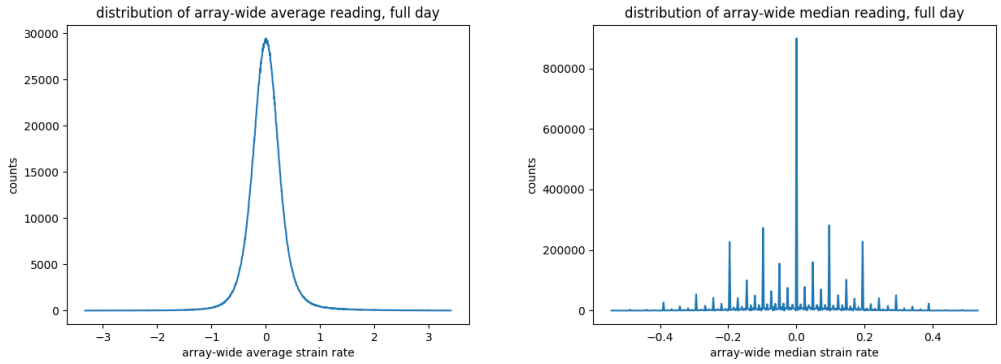

Figure 3.16: These histograms show the distribution of the (left) median and (right) mean strain rate data throughout the array at each time sample. The histogram of the array-wide mean does not show 0.2% of the most extreme values, and the histogram of the median does not show 0.1% of the most extreme values. **CR**

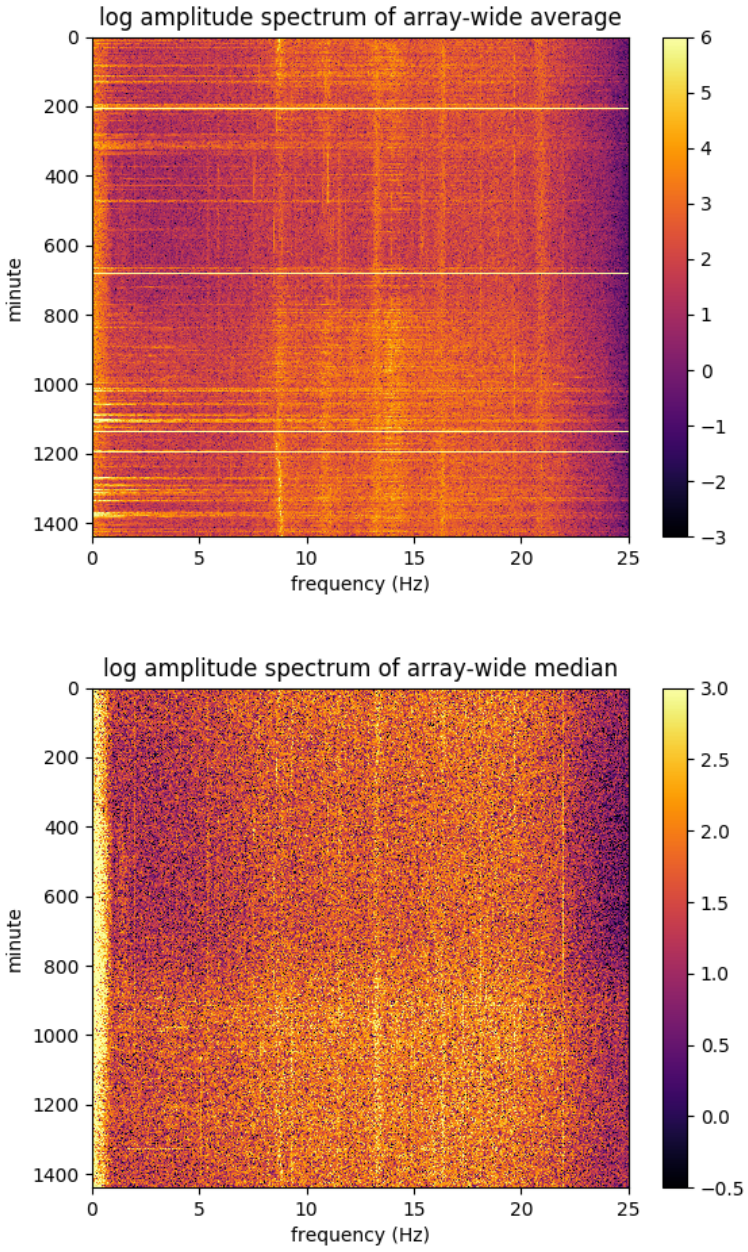

Figure 3.17: For each minute of data, these histograms show the spectrum of the array-wide (left) median and (right) mean of the strain rate data at each time sample. **CR**

Chapter 4

Observations of Earthquakes at Stanford

To verify whether the Stanford Fiber Optic Seismic Observatory was recording signals, I checked whether there were strong responses throughout the array during times when the USGS catalog reported earthquakes. The ability to see a strong response during earthquakes would suggest that the data recorded in those frequency bands are somewhat reliable. Concurrently with the array under Stanford, I compared and interpreted results with researchers at UC Berkeley and Lawrence Berkeley National Lab that were recorded at Richmond Field Station and Fairbanks, AK. The summary of our findings can be found in [35]. Quantifying the detection capabilities of the DAS array under Stanford is a subject of ongoing research. In this chapter, I show examples of a variety of earthquake observations and a simple explanation for some features of the data tied to the array geometry.

4.1 Nearby Small Earthquakes

One potential future application of DAS is for early earthquake warning, a field currently limited primarily by limited sensor coverage even in seismically active areas like California. To this end, I checked whether we could see a number of small earthquakes reported by the IRIS tool Wilbur3 Northern California, ranging from a couple of miles to a couple hundred miles away [25]. Of particular interest was whether we could detect any array-wide signal during P-wave arrivals (because this necessary for early earthquake warning). In the second week of recording at the Stanford Fiber Optic Seismic Observatory, a magnitude 3.5

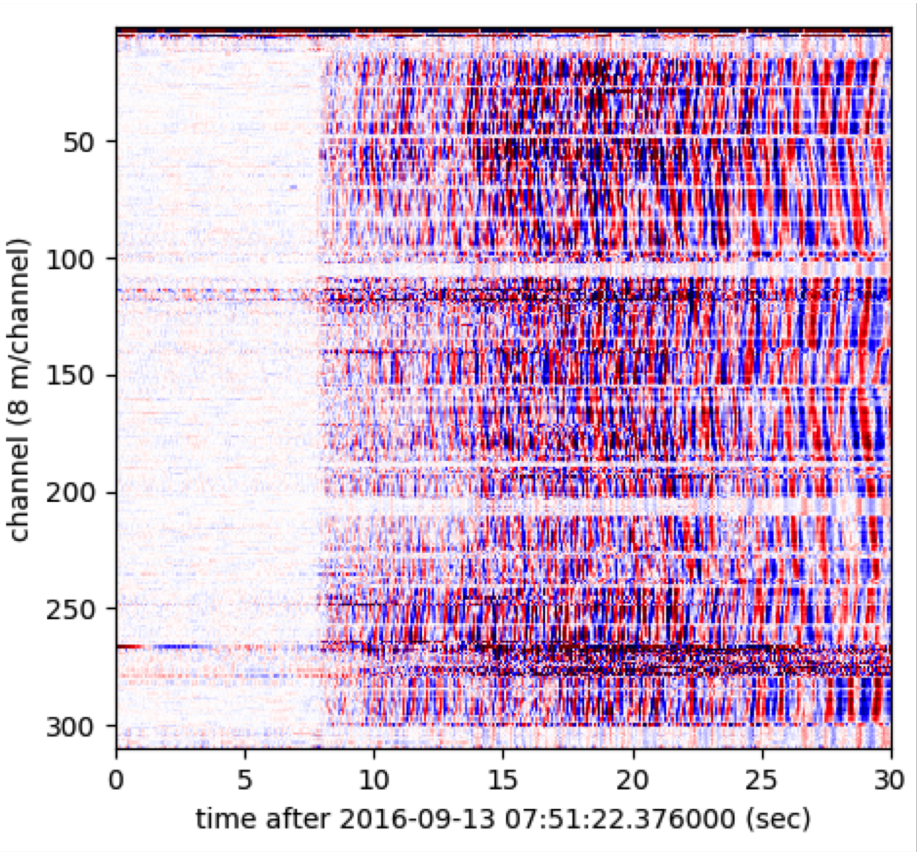

Figure 4.1: The 2016-09-13 M 3.5 earthquake in Piedmont, CA as recorded on the first loop of the Stanford array shows clear P arrivals at 7 seconds after the quake starts and S arrivals at 13 seconds. The zig-zag appearance of these arrivals is due to the angular figure-eight geometry of the array. **CR**

earthquake occurred at a depth of 4 km in Piedmont, CA which is roughly 45 km north of Stanford. The relatively large size and close proximity led to clear signals during both the P- and S-wave arrivals throughout the array, seen in Figure 4.1.

One interesting feature of Figure 4.1 is the horizontal striping indicating that certain channels respond very weakly to the earthquake. In particular just after channel 100 and after 200 there are blocks of 7-8 channels with weak responses. These locations correspond to two locations marked by the fiber install team as having 150 ft. of slack fiber coiled up and strapped to the side of manholes. There are a handful of one to two channel subsets that

respond weakly, which correlating to geometry and known manhole locations indicates that these fiber channels are at least partially in a manhole but there is not extra fiber spooled up at those locations. There are also many channels close to channel 1 and channel 310 that are either constantly very loud or very quiet because they are running through the walls of Green Building where the interrogator unit its. Additionally the southeast corner of the array (around channel 275) reverberates any noise. I hypothesize this is due to noises bouncing between the basements of Durand and Mitchell acting similar to a bell, but further investigation could be useful to better understand the ground motion in this part of campus during earthquakes.

While the Piedmont event was recorded loud and clear on the array, I also wished to get some rough idea of what magnitudes and distances were visible. A full quantitative analysis of distance versus magnitude sensitivity is the subject of ongoing research. In Table 4.1 I list the times, locations and magnitudes of nine Northern California events that were clearly visible when the data were plotted as in Figure 4.1. These are just example events that were clearly recorded, and do not serve to quantify sensitivity bounds. To summarize these data, I selected subsets of channels that did not have any cars or other unusual signals (for instance, channels between Durand and Mitchell or inside of Green building were excluded), then I plotted the average response of the array along northeast-southwest oriented lines in Figure 4.2. So that the events of small magnitudes and far away events are equally visible, the amplitudes in the figure are scaled to have equal peak amplitudes.

Of course, signals are weaker for small events than large events, particularly during the daytime when there is more anthropogenic noise present. A small, nearby example is a M 2.03 earthquake that occurred in Woodside, CA on Jan. 11, 2017, pictured in Figure 4.3. Several cars can be seen crossing by the array's northwest corner (near Panama St. and Campus Dr.) during the earthquake, but the quake signal is still clearly visible throughout most of the array. One interesting feature of this, and many other earthquake recordings is that much of the time, data at corners appears to flip polarity.

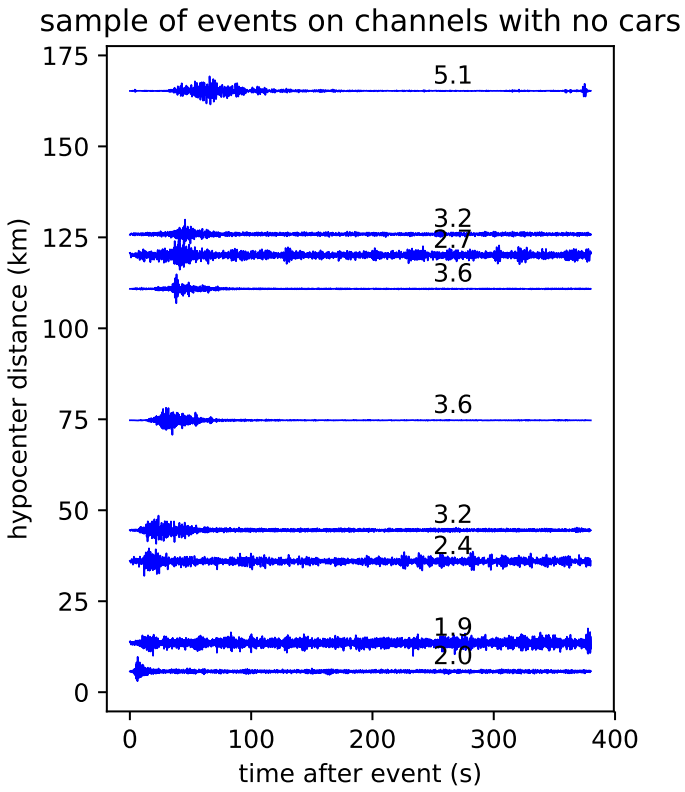

Figure 4.2: Stacks of data in the northeast direction (ignoring channels with cars) responding to a selection of recordings of regional earthquakes listed in Table 4.1. Each event is labeled with its magnitude, the vertical axis sorts events by their distance (in kilometers) from Stanford, and the horizontal axis is seconds from the start of each earthquake. **CR**

Table 4.1: Examples of nine events in Northern California that could be clearly in array-wide recordings. Average northeast and southwest array responses of each event can be seen in Figure 4.2.

Name	UTC Time	Latitude	Longitude	Depth (km)	Magnitude
Woodside	2017-01-11 23:04:40	37.406333	122.209833	4.15	2.0
Perman. quarry	2017-02-09 21:43:08	37.322167	122.1035	-0.26	1.9
Mt. Hamilton	2016-09-28 15:26:51	37.336333	121.695333	8.13	3.2
Lake Berryessa	2017-02-11 09:00:55	38.559167	122.28733	4.81	3.2
Salinas	2016-10-18 22:09:07	36.713	121.311333	7.59	3.6
Geysers	2016-12-14 16:41:05	38.822167	122.841333	1.48	5.1
Gilroy	2017-02-26 14:58:40	36.959	121.575667	4.46	3.6
San Benito	2016-10-10 08:32:15	36.638667	121.259833	9.31	2.7
Calaveras Reservoir	2016-10-10 05:09:00	37.456333	121.783167	8.78	2.4

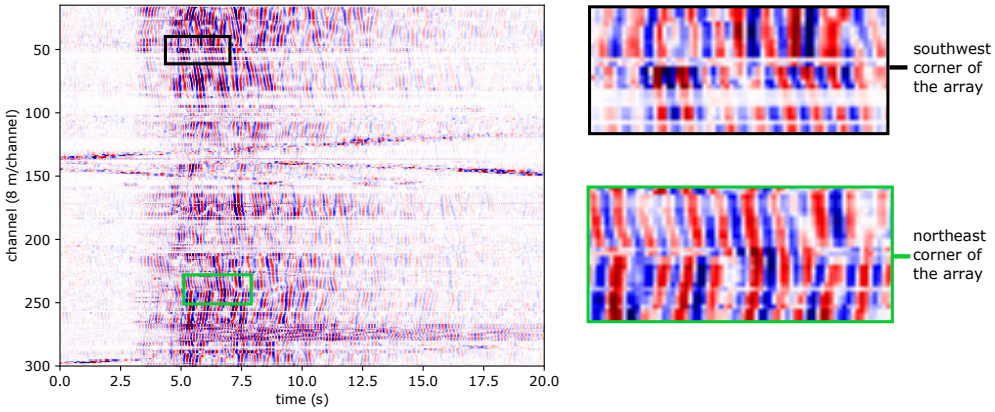

Figure 4.3: (Left) A clear signal was recorded throughout the array during the 2017-01-11 M 2.03 earthquake under Woodside, CA. The slow angled events are cars driving near the array which are recorded with slightly higher amplitude than S-waves. Zoom-ins of the (top right) southwest corner and (bottom right) northeast corner of the array show that often the data reverses polarity at corners of the array. **NR**

4.1.1 Inhomogeneities in Sensor-to-ground Coupling

One potential source of noise that changes between channels is the coupling of the fiber to the ground. It is reasonable to assume a constant friction coefficient between the fiber and cable jacket throughout this array because it is all cable from the same manufacturer, so the questions left are how much friction is there between the conduit wall and the cable jacket? And how well is the conduit coupled into the ground? We know that some parts of the campus network have conduits surrounded by a cement slurry, while other parts do not. The near surface on campus is a patchwork of cement, asphalt, gardens with loose soil, and walkways of packed soil. At a number of channels throughout the array, the fiber hangs loosely zip-tied to the wall of a manhole between two conduits.

One possibility for approximately quantifying the overall cable-to-ground coupling would be to compare relative amplitudes from our geometry calibration mallet tap tests, but their source strengths would be too inconsistent and die off at relatively short distances (sometimes they are invisible at less than 20 meters away) to estimate receiver response. However, we do get strong responses throughout the array from some earthquakes in our frequency bands of interest. I chose a M3.5 earthquake originating in Piedmont, CA (roughly 45 km north of the array) at a depth of 4 km, seen in Figure 4.4, to estimate receiver response. Here, we just use the first loop through the cable, so channel 50 is around the southwest corner of the array and 100 is at the corner of Via Ortega and Campus Dr. This response is estimated based on the ratios of the amplitude spectrum within small bands of each channelâĂŹs bandpassed (0.2-24 HZ) data within a window of 17 seconds starting at the P-arrival and continuing past the S-arrival. For each frequency band, the ratio of its amplitude is calculated relative to the median response. Here, I show results from channels 50 to 100, which sit along the straight middle segment pointing mostly north-south [38], but a similar procedure could incorporate more earthquakes from different azimuths to account for sensitivity differences of receivers oriented in different directions.

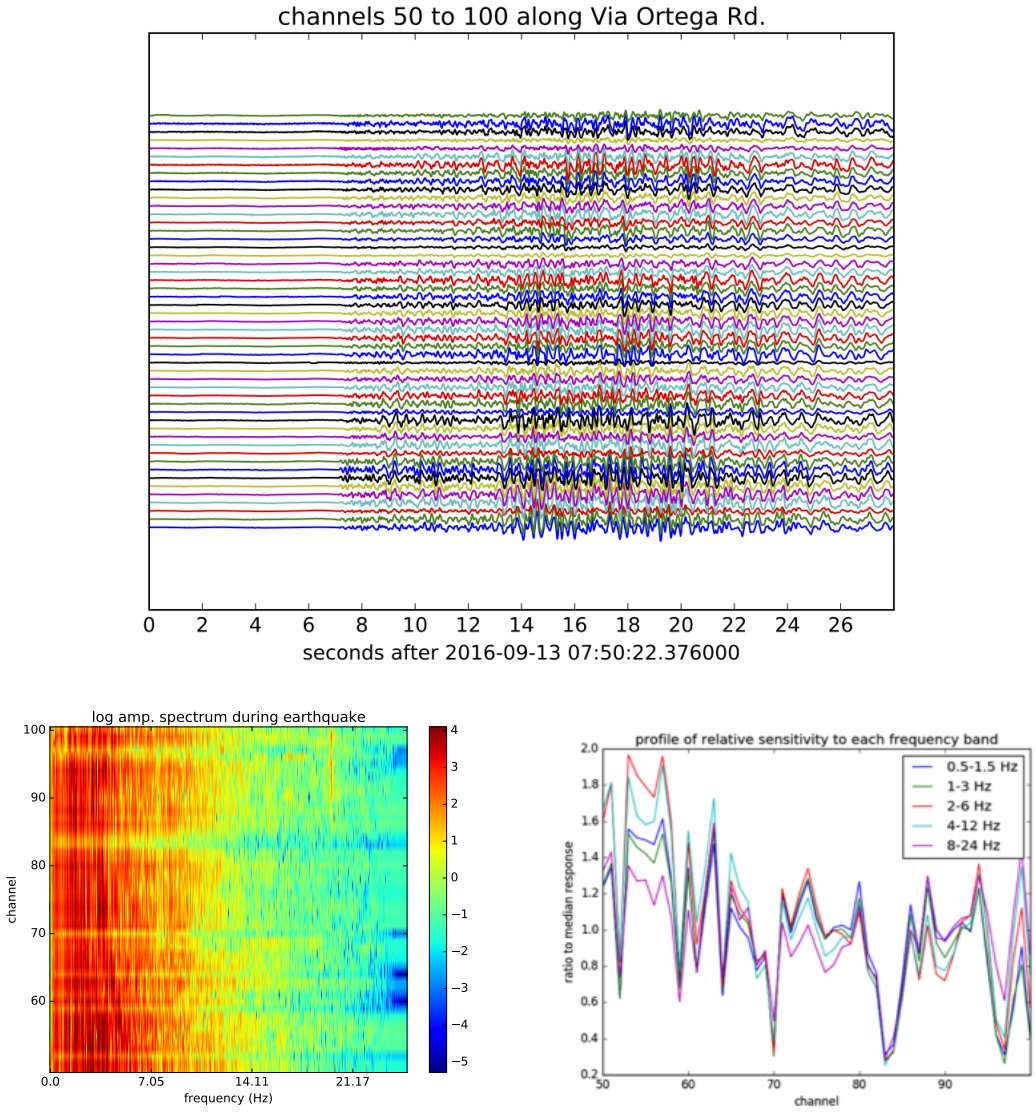

Figure 4.4: (Top) This is a recording of the Piedmont earthquake along channels 50 at the bottom (south) to 100 at the top (north). The P-arrival is about 7 seconds after the earthquake starts, and the S-arrival is around 13 seconds. (Left) A plot of the log of the amplitude spectrum for each channel during the earthquake shows a great deal of energy at low frequencies. (Right) The response of these channels relative to their median response varies significantly along the line in multiple frequency bands. The dip at channel 83 is a manhole at the middle crossing point of the array, and the dip around channel 70 is a manhole roughly 100 m south of that crossing point. **CR**

4.2 Teleseismic Events

Because active seismic surveys rarely contain reliable signals below 3 Hz, and many interrogator units are developed for best performance in active surveys, I wondered whether the interrogator would reliably record much low frequency data. However, the interrogator unit under Stanford was configured to return data with minimal pre-processing, so I wondered whether the different recording settings and interrogator unit would record strong responses to low frequencies. Reliable low frequency recording is necessary if the global seismology community is ever to take advantage of DAS data.

On just the second day of recording at Stanford 2016-09-03, there was the ideal opportunity to test sensitivity to teleseismic events when the Pawnee, OK M 5.8 earthquake occurred. This historically large earthquake for the region has been linked to human activity [69]. The epicenter was more than 2000 km southeast of the array, putting it in the range of teleseismic events. The time-series strain rate data recorded by 290 channels (the first loop through the array) is shown in Fig. 4.5 after a bandpass from 0.02 to 2 Hz. I compare this data with a long period recording rotated into the same direction from Jasper Ridge Seismic Station, a Northern California Seismic Network long period station located just 6 km away so it should have similar arrival times. The long period recording is tailored to viewing distant earthquakes at low frequencies, unlike the DAS array, but the P and S arrivals can be picked at the same times on both recordings. In particular, the P-arrival shows up on the DAS recording in the short-time Fourier Transform as a jump in in energy between 0.5 and 1 Hz. Such an indicator is not clear in the horizontal JRSC spectrum, and is only slightly more apparent on the vertical JRSC spectrum. Note that channels oriented in orthogonal directions show a polarity flip following the S-arrival.

Since that first teleseismic detection, several more teleseismic events have been recorded clearly at the Stanford array. In Figure 4.6 I show another example, a magnitude 8.1 earthquake at 57 km depth that occurred off the coast of Chiapas, Mexico on 2017-09-08 at 04:49:20 UTC. Interestingly, the DAS response to the direct S arrival around 800 seconds is much weaker than its response to the P arrival around 400 seconds, but the opposite is true for the Jasper Ridge Seismic Station horizontal component recording. This is particularly surprising given that the P arrival should be traveling almost vertically when it arrives in

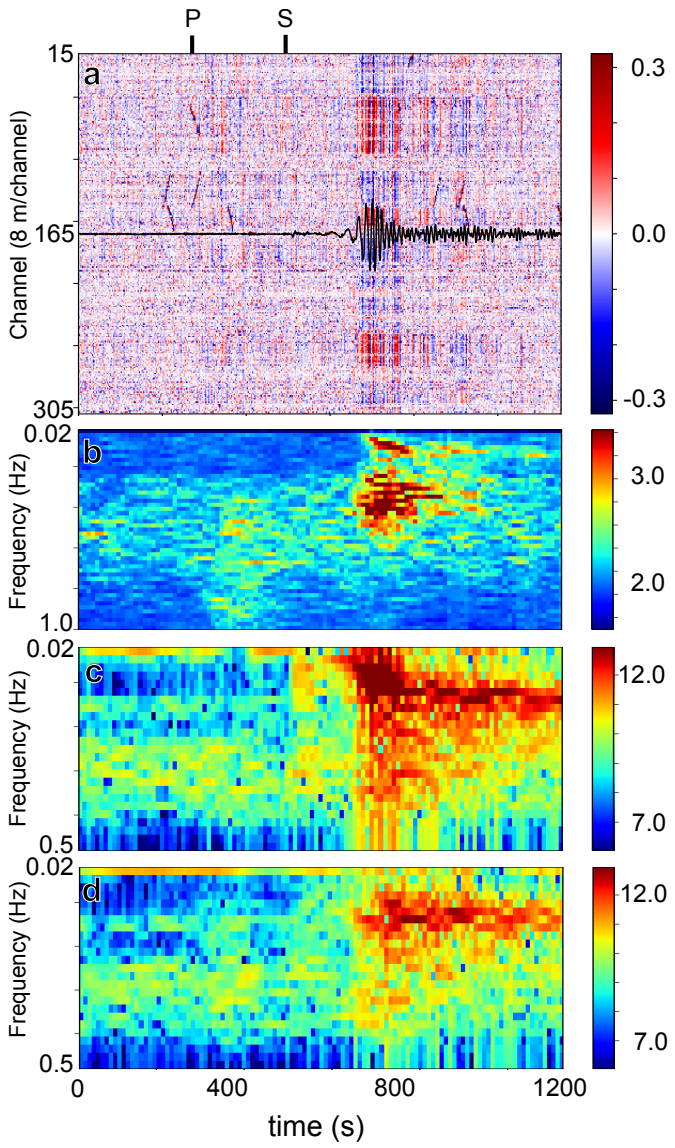

Figure 4.5: (A) DAS recordings with Jasper Ridge Seismic Station (JRSC) horizontal signal overlaid, (B) log of average of DAS amplitude spectra for channels without car signals, and JRSC long period (C) horizontal and (d) components' log amplitude spectra during the Pawnee, OK earthquake. The long period recordings have a Nyquist frequency of 0.5 Hz. The Stanford DAS array shows recordings from 290 continuous channels spanning the whole array's extent, and the JRSC horizontal data are rotated so the component in-line with DAS channels 50-100 is shown. **CR**

California, and this horizontal DAS array should be totally insensitive to P waves that hit the whole array at roughly the same time with a vertical displacement.

By zooming in on the data starting at 400 seconds, as in Figure 4.6, the polarity swap imprint of the geometry is clearly visible in the data. As explained in the next section of this chapter, that polarity swap should only be present in waves with particle motion orthogonal to their propagation direction, suggesting that these are S waves when they are recorded. However, the timing is consistent with a P arrival [25]. Thus, I hypothesize that this may be energy that traveled through the earth as a P wave, but converted to an S wave in the outer crust so that the P-S timing difference only mattered for a relatively short proportion of the distance traveled. This observation suggests that before full waveforms of DAS data are incorporated into global seismic imaging workflows that use horizontal waveform data, seismologists must modify algorithms to account for the change from particle velocities to strain rates.

4.3 Data at Corners of the Array

In many teleseismic low frequency earthquake recordings, we noticed a recurring pattern, particularly after the arrival of S-waves: fibers that were parallel would have be extending whenever fibers in the orthogonal direction were compressing. For nearby earthquakes this trend also appeared in a higher frequency band for S-waves and surface wave arrivals, but immediately following P-wave arrivals, it was less clear whether this behavior was observed. This trend was observed not just at the Stanford Fiber Optic Seismic Observatory, but also at the L-shaped Richmond Field Station array, the trenched fiber grid in the Fairbanks active thaw experiment [35], and has been observed recently at a shallow trenched array at Brady Hot Springs in Nevada [64].

We can gain some basic intuition about why this behavior should be expected by deriving the expected strains observed by two orthogonal fibers reacting to 2D monochromatic plane waves in two cases: particle motion in the same direction as propagation (similar to nearby events' P-waves or Rayleigh waves), and particle motion orthogonal to the direction of propagation (similar to nearby events' S-waves or Love waves) as in [35]. When wave motion is orthogonal to the direction of propagation (as in Love and SH-waves), we expect

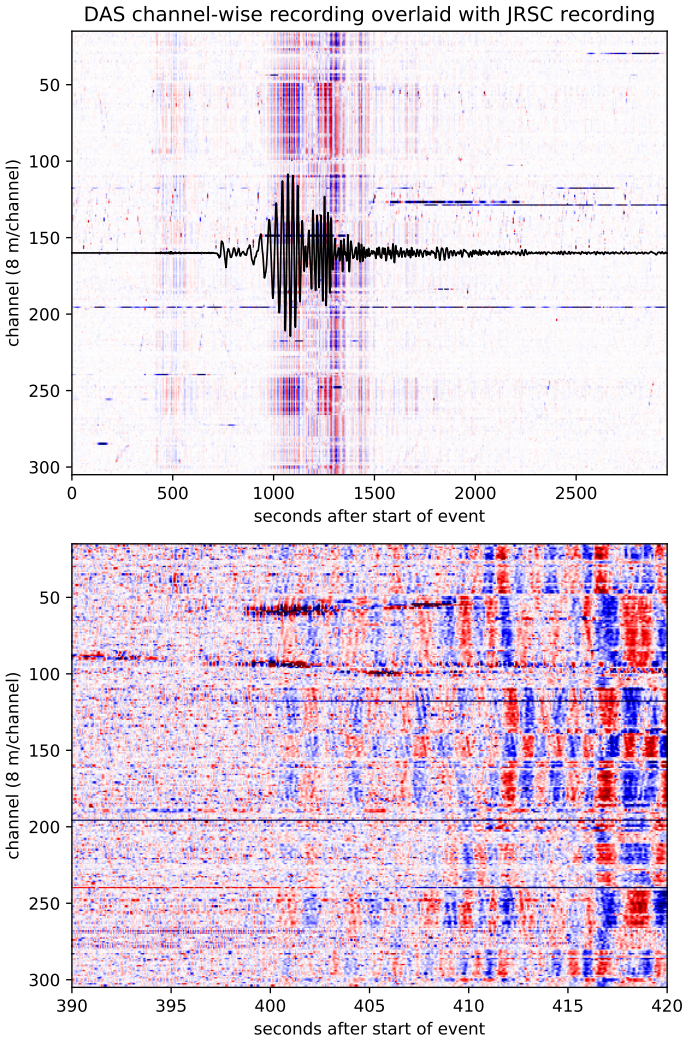

Figure 4.6: The Stanford array recorded a clear response to the magnitude 8.1 earthquake off the coast of Chiapas, Mexico on 2017-09-08 at 04:49:20 (marked as 0 seconds in the plots above). The array recorded multiple wave modes in the first 50 minutes following the earthquake (top) including a visible P and PP response, a weak S response, a strong SS and surface wave responses. Also overlaid is a horizontal component of the Jasper Ridge Seismic Station's simultaneous response. By zooming in on the P arrival (top) it is clear that fibers in orthogonal directions had opposite polarity responses, suggesting the particle motion was orthogonal to the propagation direction. **CR**

to see any two orthogonal fibers at the same location to have data of equal amplitude and opposite polarity, no matter what the incoming wave's incident angle is. When wave motion is in the direction of propagation (as in Rayleigh, P and SV-waves), we expect the ratio between two collocated orthogonal fibers' recordings to be $\tan^2(\theta)$ if θ is the horizontal angle of incidence of the earthquake. The extension showing that these results hold true in 3D for body waves with some vertical motion can be found in Appendix D.

Chapter 5

Anthropogenic Effects on Noise Correlation Functions

The theory behind extracting Green's function estimates from ambient noise interferometry of a pair of receivers relies heavily on the assumption of uniformly distributed, uncorrelated noise sources [67], [65]. Naturally occurring frequencies, like the primary and secondary microseism band, are often below 1 Hz and tend to mostly satisfy these theoretical assumptions, so the vast majority of ambient seismic noise analysis has been done in this frequency range for regional studies [1], [57], [7], [33]. In recent years, reservoir scale and city scale ambient noise interferometry has been applied up to a few Hz [16], [11], [49].

At the slightly higher frequencies needed for reservoir or city scale characterization, careful processing is needed to ensure reliability of the noise correlation functions. When extracting a single noise correlation function, it is ideal to have a correlation function that is compact in time so that an arrival time can be easily picked for use in tomography. However, noise sources near the array, or repeating noise sources can cause energy to spread over a wider range of times [51], or even cause apparently early arrivals due to noise sources within the array [11].

Even if a noise correlation function appears to be converged on a short time scale, it may still have some incorrect velocities, and this can become especially apparent when doing time-lapse ambient noise interferometry. Changes in the amplitude spectrum of the ambient noise distribution over time can cause spurious changes in velocities estimated

from ambient noise cross-correlations [72]. This effect has been documented when tides and storm patterns change the directional distribution of the amplitude spectra at sub-2 Hz frequencies in volcano monitoring applications, but a simple fix to avoid these changes can be to whiten data before cross-correlation [15], but whitening does reduce the utility of the noise correlation functions as amplitudes are no longer reliable. There have been some recent developments towards estimating the ambient noise field [22] and using noise correlation functions accounting for these non-ideal noise fields to retrieve reliable amplitudes and phases [24], but these methods are beyond the scope of this thesis as they are untested at higher frequencies and expect 3C geophones spanning a 2D region.

In this thesis, I work with frequencies from a few Hz to tens of Hz for geotechnical characterization, meaning that it is particularly important to understand spatially or temporally varying noise sources and any dependencies or correlations between noise sources. In this chapter, I show an example of noise correlation function artifacts at the Fairbanks, AK roadside array that look a bit like time-lagged copies of a noise correlation function governed by the wave equation, explain how these artifacts could be caused by time-correlated noise sources, and show how the noise processing workflow affects the strength of these artifacts. I also characterize a variety of noises at the Stanford array and show how these noises affect the convergence of noise correlation functions both temporally and spatially. These results suggest that although individual autocorrelation convergence and compactness are a common quality control metric, in populated areas or near infrastructure, they not a useful indicator of the reliability of noise correlation function picks as estimates of Green's function arrival times.

5.1 Exploring Correlation Artifacts at the Fairbanks, AK Roadside Array

Vehicular traffic on Farmer's Loop Rd, seen in Figure 3.4, is the defining feature of this dataset. Spectral stacks like the one seen in Figure 3.3 help pin down which channels correspond to each part of the array geometry. Channels 134-525 lie between the field house and the south end of the array with roughly 200 m running next to the long mostly

straight line closest to the road. We consider channel 535 on the south end up to channel 1135 in the north. Another feature in the time domain is a striping effect seen in Figure 3.4, which has been previously observed and is likely due to differences in the laser over time [3], [37].

We performed beamforming on raw data from the main line to characterize the source distribution. The formula used was based on [56]

$$b(v_y) = \left| \sum_t \sum_r d_r(t + (y_r - y_c)v_y) \right|, \tag{5.1}$$

where v_y is an apparent wave speed of interest in the north-to-south direction (negative if it is south-to-north), y_c the center of the array, d_r the data recorded at position y_r, t time, and b the beamformed energy. This formula results in high b values for velocities at which there appears to be significant seismic energy propagation. For broadband (no filtering) and bandpassed signals, results in Figure 5.1 show slightly more energy approached the array from the south.

5.1.1 Examples of Cross-correlations

A standard tool to estimate virtual source responses is cross-correlation of filtered data recorded at all receivers against a receiver acting as a virtual source. The resulting time series is called a noise-correlation function. Standard filters to improve cross-correlations include bandpassing, spectral whitening, and temporal normalization prior to the correlation procedure [7], but despite attempting many combinations and variations of pre-processing, all noise correlation functions showed unusual features that had apparent copies of the expected Green's functions at non-zero time-lags. These extra copies were coherent, and have increased S/N ratio as more time was stacked.

We hypothesized the copies were due to cars, so I hand-picked an hour of noise split into 5 second windows with no more than one car at any point in time. One procedure involved despiking the data to reduce optical noise, 3-50 Hz bandpassing, spectral whitening, and temporal normalization (by average amplitude in a moving window twice the longest period of interest). A result of this procedure followed by cross-correlation followed by damping

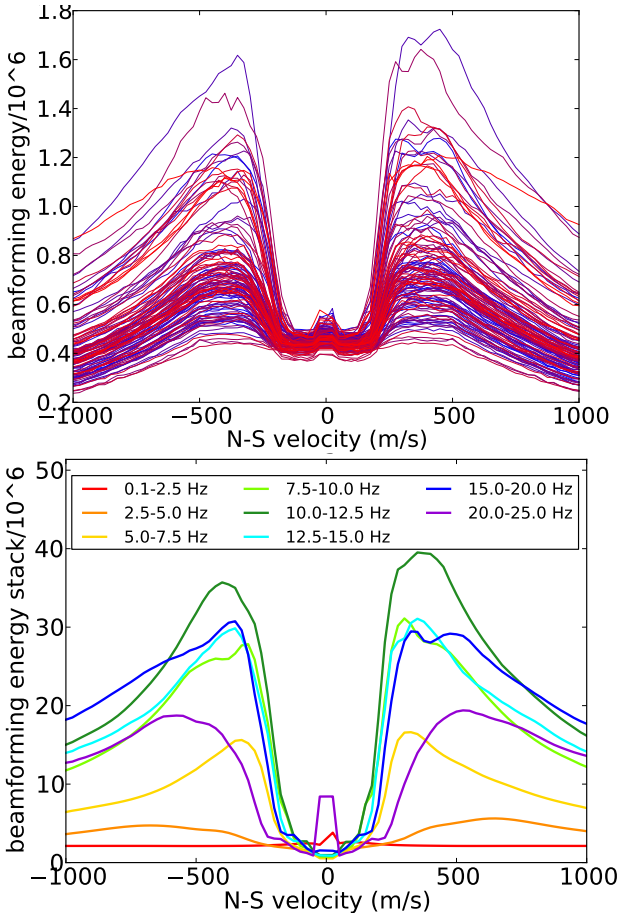

Figure 5.1: (Top) Beamforming on broadband one minute recordings over 1 hour 45 minutes are shown as separate lines. Later recordings are red and earlier recordings are blue to emphasize variation over time. (Bottom) Beamforming results on 2 hours of bandpassed recordings are shown with separate lines for each frequency band. Slightly more energy comes from the south in 2.5-15 Hz frequency bands. **CR**

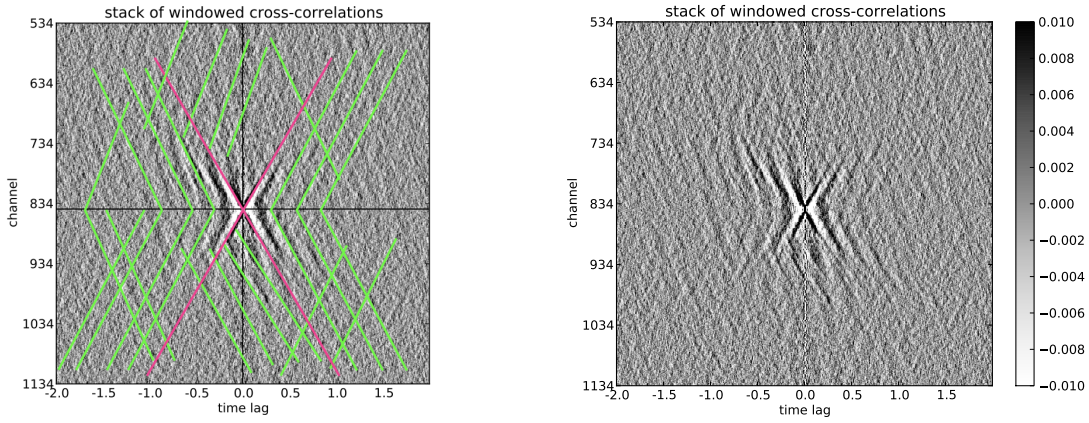

Figure 5.2: Cross-correlations are shown that should ideally approximate responses to a virtual source at channel 845 (middle of array) with relatively aggressive clipping. This is shown (left) with and (right) without the artifacts picked in green. The expected signal is marked in pink. Top is **CR**, and bottom is **NR**.

of infinite velocity events (vertical striping in raw data) is shown in Figure 5.2, and it is only a slight improvement over using all recordings, even those with more car noise.

5.1.2 Thought Experiment: Vehicles Repeatedly Drive Over Bumps

Cars are a dominant noise source in the data, and even more dominant than the car responses are points that appear to get excited as cars drive by as in Figure 3.4. The same points are repeatedly hit by many cars, indicating bumps or joints in the road acting like point sources. More importantly, the cars tend to have a distribution of velocities concentrated around 20-25 m/s, so any two bumps have a typical time between excitation, which may cause coherent artifacts.

A simple synthetic model simulating bumps as point sources excited in series (1D acoustic constant density wave equation, no dispersion) supports this hypothesis, as seen in Figure 5.3. To roughly simulate realistic spacings, the model has 6 bumps spread over 400 m of a 620 m array. A car travels one way at 25 m/s. The bumps act as point sources that send out a square pulse when the car hits them. The wave speed is uniformly 320 m/s. Cross-correlations of the synthetic recordings have some features that vary with the

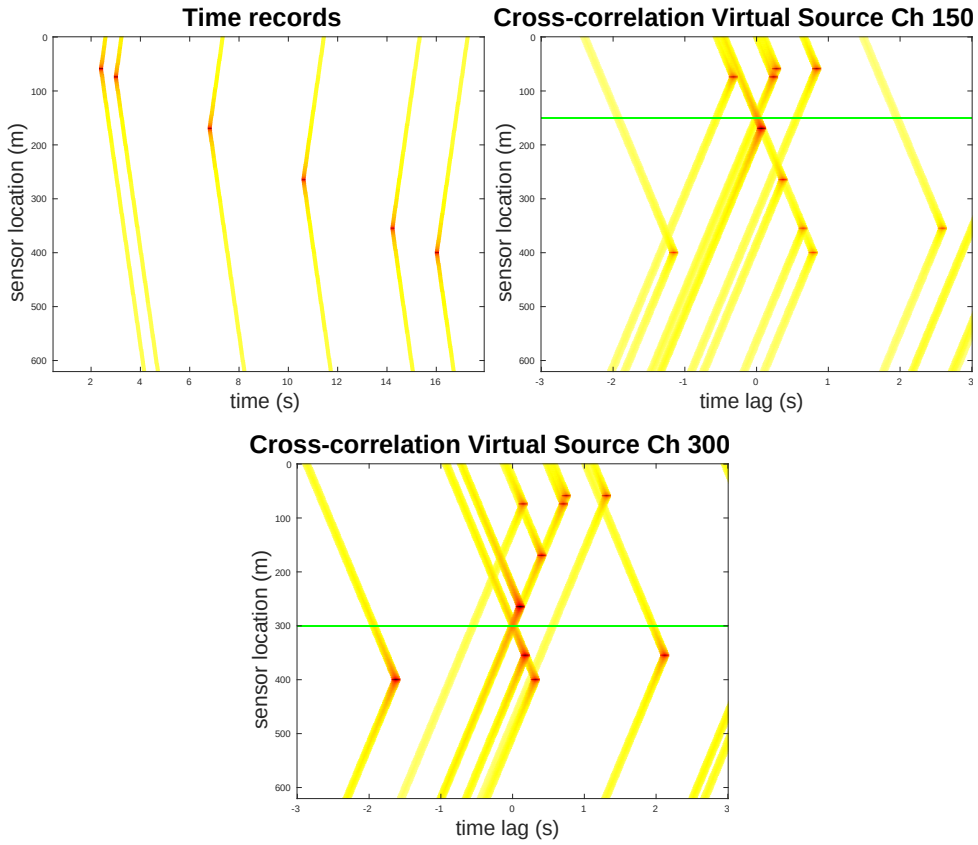

Figure 5.3: (Top) Time records of the bumps being excited by a single car. (Bottom left) Cross-correlations with a virtual source (green line) between the 2nd and 3rd bumps, and (bottom right) between the 4th and 5th bumps. The cross-correlation signals intersect the virtual source line at stationary time-lags. **CR**

virtual source, but we see non-zero time-lag events on stations near the virtual source that are constant for all virtual sources. These stationary events grow stronger as we stack over more time if car speeds are concentrated around some average speed for the road.

The nonzero time-lag events appear at long enough lags to reasonably explain the apparent copies in our field data Green's function estimates. This synthetic only showed the result of a car going in one direction, but it is easy to image V-shapes in the cross-correlations for cars hitting bumps traveling the other way. Artifacts in the real data cross-correlations have similar directionality.

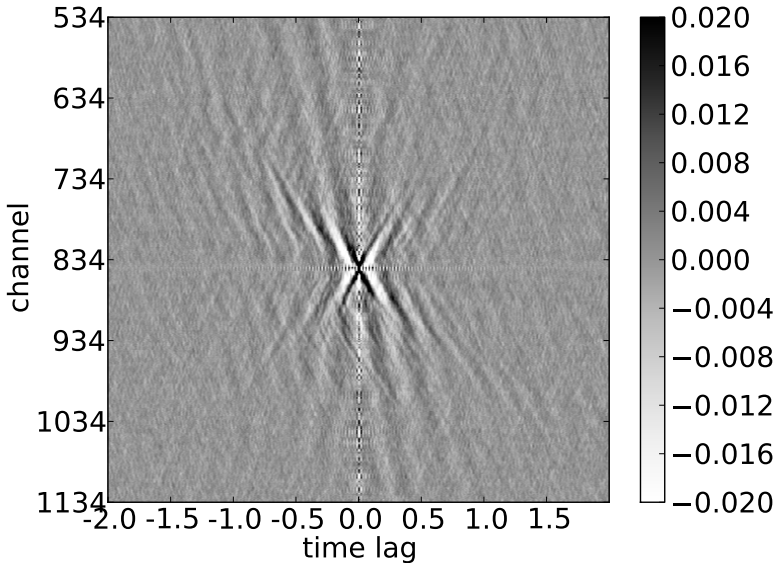

Figure 5.4: A cross-coherence estimate of the Green's function at channel 845 is shown. Some nonzero time-lag events remain, but are small enough we can see a fast asymmetrical event. **CR**

5.1.3 Cross-correlation Versus Cross-coherence at Fairbanks, AK

Although cross-correlations are a more common tool in ambient noise, and we were able to improve results by reducing the amount of car energy parallel to the array, there are other methods including cross-coherence and deconvolution that can be used to estimate virtual source responses. The results in [51], which studied a 1D array collecting ambient noise generated in the 12-16 Hz band from roads perpendicular to the array, suggested that cross-coherence might be a better tool for Green's function estimation when we have difficulties filtering the data to compensate for unknown ill-behaved sources. Our cross-coherence results for the same hour of data (with no bandpass or other filtering besides infinite velocity event removal) seen in Figure 5.4 were an improvement over our cross-correlations. The apparent copies were reduced, but more importantly we can detect a faster asymmetric event traveling south to north at over 600 m/s not visible in the cross-correlations.

As input to surface wave inversion in the dispersion domain [20] , we calculate dispersion images by calculating a $\tau - p$ transform (slant stacking at many time-lags) of a Green's

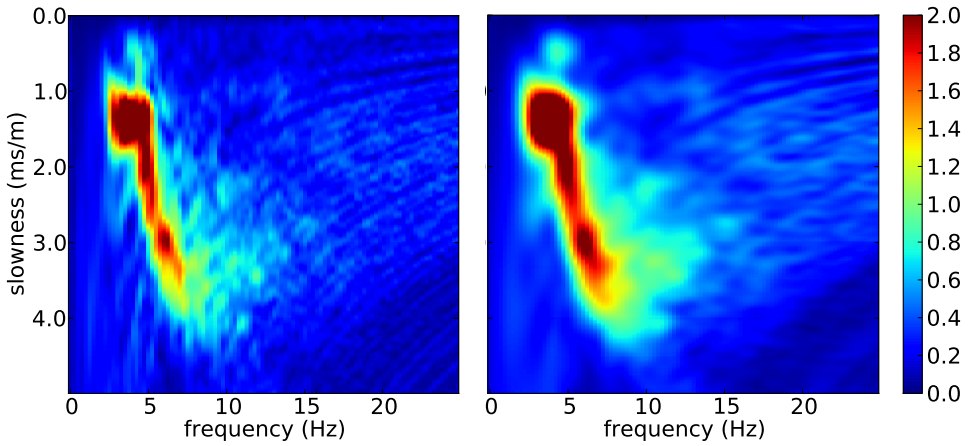

Figure 5.5: Dispersion images from cross-coherences in Figure 5.4 (left) without τ weighting, and (right) downweighting large τ events with a Gaussian mask. Slowness is one divided by velocity measured in milliseconds per meter. **CR**

function estimate, then taking the Fourier transform along the τ axis. Much of the energy from artifacts like those in Figure 5.3 would contribute to the τ-p transform at τ far from 0. One simple solution to this is to weight the τ-p transform to be small at large τ values with a Gaussian function centered at $\tau = 0$ with inflection points at ± 0.3 s (since little noise is observed below 3 Hz). A Gaussian in τ-p is equivalent to a Gaussian in the dispersion image, which leads to a smoother dispersion image (our ultimate goal for monitoring) in Figure 5.5. However, it is still possible that there could be amplitude issues in the small τ events, and this dispersion image solution will not necessarily help with tomography. We are investigating other strategies of artifact removal, particularly deconvolution applied to the cross-coherences.

5.2 Noises at the Stanford DAS Array

Here, I show some examples of noise recorded by the Stanford Fiber Optic Seismic Observatory, an environment with even more anthropogenic and mechanical noises than the Fairbanks Permafrost Thaw Site. As seen in Figures 5.6 and 5.7, the array detects a wide variety of seismic noise sources, some of which do not conform to the white, uncorrelated,

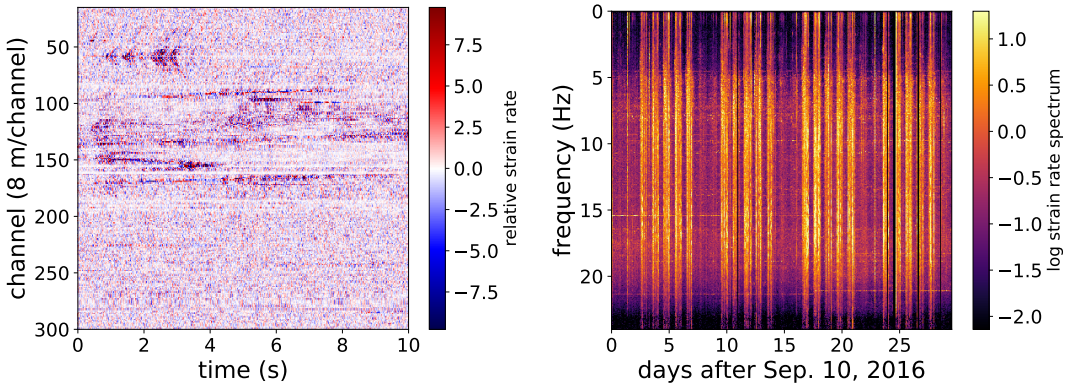

Figure 5.6: (Left) In just ten seconds of noise collected around noon local time we can see significant variation throughout the array. (Right) The amplitude spectrum, normalized to have a mean value of 1, of 80 meters of fiber just south of the array's crossing point is shown on a log scale. Weekday traffic noise above 5 Hz causes strong variability over time. **CR**

spatially uniform ideals of existing ambient noise theory: it sits in a seismically active region, 20 km from the Pacific Ocean, 7 km from the San Francisco Bay, with major highways on either side, a variety of roads with differing levels of traffic near the fiber, regular quarry blasts within 15 km, plumbing and HVAC systems throughout the site, multiple construction sites near the array, and foot and bicycle traffic throughout. With several hundred sensors continuously recording 50 samples per second, manual inspection of most data is difficult, so there have been efforts to automate this inspection [41]. Here, we just focus on manual interpretation of noises.

5.2.1 Effect of Noises on Cross-correlation Convergence

We split 30 days of data starting after the clustering training set into 5 minute windows, with a new window starting every 2.5 minutes, as the use of overlapping windows can improve the rate of convergence for virtual-source response estimates [58]. A first-order estimate of the strain rate was estimated from the data, then the strain rates were bandpassed from 0.5 to 24 Hz, and data were compressed to their sign bit (all positive values replaced with +1, all negative values with -1).

The cross-correlations for virtual sources throughout the array were then performed.

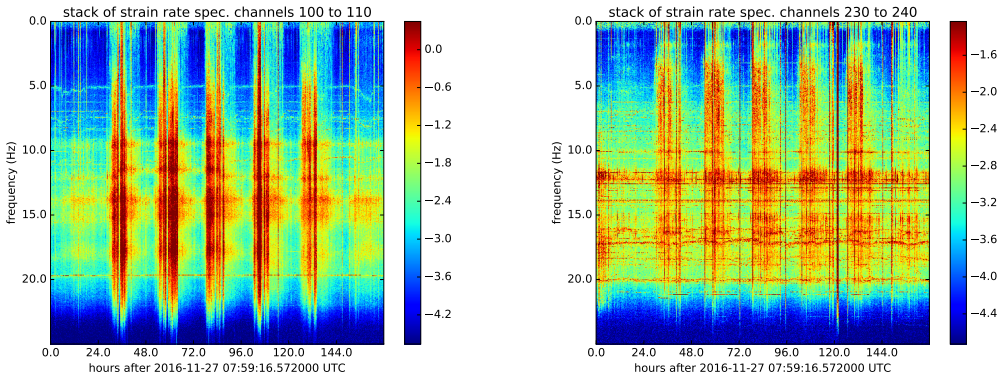

Figure 5.7: The strain rate spectrum averaged over 80 meter segments is shown over one week in Sep. 2016 (Left) near Campus Dr. and (Right) along a service road, Via Pueblo near its intersection with Lomita Mall, which has little automobile traffic. In addition to the five weekday trend during the daytime likely caused by vehicular traffic, there are consistent frequency peaks, although some peaks do have slight variation over time. **CR**

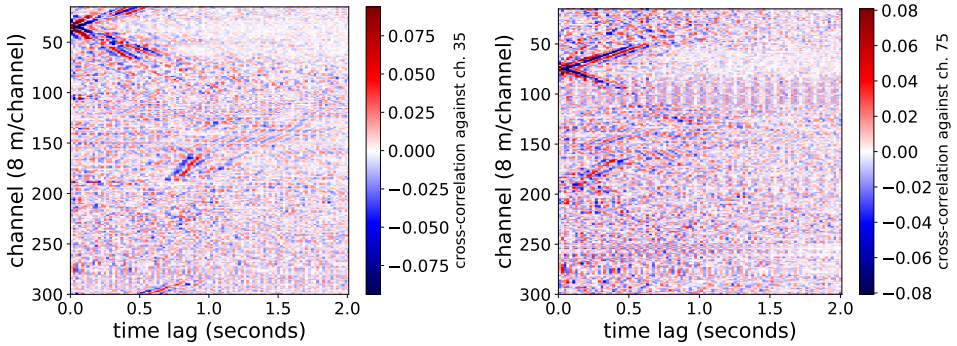

Figure 5.8: 30-day average beginning in September 2016 of symmetrized noise correlation functions estimating the array response to virtual sources at (Left) channel 35, and (right) channel 75 show multiple events from fiber sections in different directions. Each channel's cross-correlation is normalized so its L1 norm is 1.0. **CR**

Two examples with virtual sources along orthogonal lines are seen in Figure 5.8. Virtual response estimates along the same lines as the virtual sources primarily show a strong, slow event around 400 m/s, presumably a Rayleigh wave. For channel 35 this event is also picked up around channel 300 because of the figure-eight array shape looping back to the interrogator unit in line with earlier numbered channels. Channel 35's virtual source is also detected along channels 150-200 at an arrival time of 0.6 to 1 seconds corresponding to a 400 m/s velocity event's arrival. Channels 150-200 are across from and parallel to channel 35, so this is most likely a Love wave event. Starting at the southwestern corner of the array, channel 50 to 80 show a response to channel 35 that appears to have two distinct velocities, which would be consistent with predictions that orthogonal channels that don't line up should have a mix of Love waves, Rayleigh waves, and scattered energy. The response of the line parallel to channel 75 shows the strong slow event, but also a fast event traveling at roughly 1100 m/s. Channel 75 is close to but orthogonal to channel 180 (the crossing point of the array), and as expected we see an event arrive between channels 160 and 210 a little after zero time lag, although this event is somewhat weaker and less focused, it should primarily represent scattering between Rayleigh and Love waves.

To understand the convergence throughout the array, I studied the similarity of short-term to long-term averages. Improving convergence does not necessarily mean a more accurate signal, just a more repeatable one. As in [58], for any virtual source v receiver r pair, we use the normalized zero time-lag correlation between the long term average virtual-source response estimate, $l(v, r, \tau)$, and any shorter virtual-source response estimate, $s(v, r, \tau; t, t + w)$ averaging cross-correlations for windows that start and end between time t and $t + w$. Thus, if the virtual-source response estimates are compactly supported on $(-\tau, \tau)$, their correlation coefficient is:

$$R_C(v, r; t, t + w) = \frac{\int_{-\tau}^{\tau} l(v, r, \tau') \cdot s(v, r, \tau'; t, t + w) d\tau'}{\left(\int_{-\tau}^{\tau} l^2(v, r, \tau') d\tau'\right)^{1/2} \left(\int_{-\tau}^{\tau} s^2(v, r, \tau'; t, t + w) d\tau'\right)^{1/2}} \tag{5.2}$$

If $R_C(v, r; t, t + w) \approx 1$ for nearly all window start times, t, this suggests little is gained by continuing to average (v, r) cross-correlations averaged over a longer window, w.

As seen in figure 5.9, I calculated R_C to see how it varied throughout our 30 days of

cross-correlations. We calculated s for all receivers responding to channel 75 as a virtual source for each contiguous subset of w hours throughout the 30 days. This was tested for $w = 1, 6, 24$, and 96 hour windows. Note that windows with $w > 1$ overlap, so when $w = 6$, there is a window from midnight to 6 am on the first day, a window from 1 am to 7 am on the first day, and so on. The horizontal stripes in R_C plots for 1 and 6 hour windows repeatedly show lower R_C values during the daytime, even in parts of the array farther from roads. These daily variations are barely picked up by the auto-correlation of channel 75, indicating that processing decisions based on convergence require a measure of convergence throughout the array, not just auto-correlations. Overall improvement could be quantified by a higher entropy R_C matrix (more even convergence throughout the array and over time), higher average values, or higher minimum values. One possibility is not using any daytime noise, but this increases the recording time required (which could be important if multiple sites must share an interrogator unit).

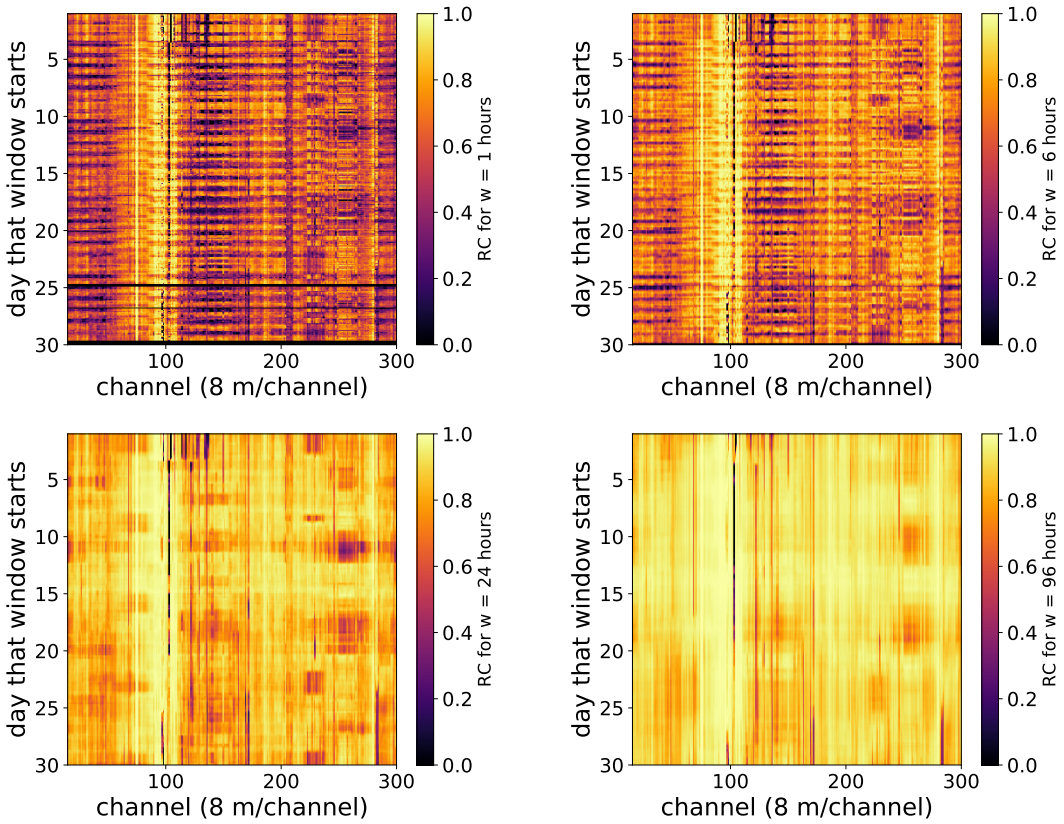

Figure 5.9: For each continuous window of length w = (top left) 1 hr, (top right) 6 hrs, (bottom left) 24 hrs, (bottom right) 96 hrs, R_C is plotted for one-bit cross-correlations between each channel and a virtual source at channel 75 as compared to the 30-day average cross-correlation of that source-receiver pair. The horizontal striping indicates that the monthly average is much less correlated with daytime data than nighttime data. **CR**

Chapter 6

Fast, Scalable Dispersion Image Calculation

To calculate dispersion curves, the amount of energy traveling at each phase velocity vs. frequency, from ambient seismic noise, many researchers calculate noise correlation functions in the time domain through cross-correlations, perform slant stacks across virtual source gathers at many initial time-lags, and take a Fourier transform along the time-lag axis. This algorithm scales as $O(n^2)$, where n is the number of sensors, due to the need for calculating $\frac{n(n+1)}{2}$ cross-correlations per time window. If the data are regularly sampled in space, an existing $O(n \log n)$ algorithm involves an F-K transform of the data cube followed by a transform into velocity vs frequency. This has previously been accepted because scientists were either using sparse networks over long periods of time at relatively low frequencies, or if they were using dense networks, those networks were only temporarily deployed.

I propose a new $O(n)$ algorithm which only takes the Fourier transform of the data in time. The new algorithm is conceptually simple, parallelizes easily, and does not require regular spacing between sensors. I show similar results for dispersion curves resulting from both the $O(n)$ algorithm and the $O(n^2)$ algorithm applied to data collected in a field trial of a trenched distributed acoustic sensing array at the Richmond Field Station. There are fewer opportunities for accumulating numerical error in the new $O(n)$ algorithm, so it yields a sharper image than the $O(n^2)$ algorithm.

6.1 Introduction

Dispersion curves are a simple way to analyze ambient seismic noise data. Dispersion images roughly show how much surface wave energy is traveling at any given frequency and velocity. Dispersion curves are the result of picking curves along the peaks in frequency and velocity in these images. They sometimes allow us to see not only fundamental surface wave modes, but also higher order modes [16].

Let n be the number of sensors in a linear array that passively records seismic data. In this thesis, I am interested in continuous monitoring applications over large regions with many sensors (ideally, n should scale well into the 10,000's). In particular, scaling with the number of sensors of interest when processing ambient seismic noise data collected by a distributed acoustic sensing (DAS) array due to the dense sensor spacing. I assume ambient seismic noise is processed in small chunks (on the order of 1-5 minutes).

I can reduce the communication and computation cost of calculating dispersion images (sometimes the peaks of these images are referred to as dispersion curves) from many sensors acting as virtual sources from $O(n^2)$ to $O(n)$ by solving this problem in the temporal Fourier domain instead of the time domain. Following the derivation of this new algorithm, I show dispersion images on a small field dataset collected by a distributed acoustic sensing array.

6.2 Summary of Previous Methods for Dispersion Image Calculation

A common and conceptually simple algorithm to calculate dispersion curves requires calculating source responses in the time domain then slant-stacking, but this method scales as $O(n^2)$. A slightly less intuitive but more efficient $O(n \log n)$ algorithm involves a Fourier transform of the data in both space and time, followed by a transform into slowness vs. frequency. The new $O(n)$ algorithm is inspired by an $O(n^2)$ algorithm, so I describe this existing $O(n^2)$ in detail before moving to the derivation of the $O(n)$ algorithm.

Let $d(x_r, t)$ be an ambient seismic noise trace recorded for some time period at a sensor in position x_r, perhaps with some filtering and preprocessing applied (see [7] for general

outline of preprocessing). Then let

$$u_s(x_r, t) = d(x_s, t) \times d(x_r, t)$$

be a cross-correlation that is some realization of a random variable with a mean that is the response to a virtual source placed at x_s (this is sometimes loosely referred to as an empirical Green's function, or a noise correlation function). Let p represent slowness (if v is the velocity then $p = 1/v$). One conceptually simple method for calculating the dispersion image, I_s, from the response to a virtual source at x_s, would be to calculate slant stacks along the responses of all sensors to the virtual source at x_s as is done in [10]:

$$I_s(p, t) = \sum_{r=1}^{n} u_s(x_r, t + p(x_r - x_s))$$
$$\hat{I}_s(p, \omega) = \mathcal{F}_t(c_s(p, t))$$

I use the notation that $\hat{u}(\omega)$ and $\mathcal{F}_t(u(t))$ are the Fourier transform of a function $u(t)$ throughout this report. Clearly, this slant-stack approach requires calculating $O(n)$ noise correlation functions per virtual source, and must be carried out for $O(n)$ virtual sources to get an understanding of spatial variability across the array, leading to an overall complexity of $O(n^2)$. The calculation of these dispersion images by slant-stacking of each virtual source gather underlies the Multichannel Analysis of Surface Waves (MASW) method commonly used in geotechnical characterization [53], [36].

6.3 Refactoring the Frequency Domain Equation of a Dispersion Image for $O(n)$ Serial Processing

Here, I use basic facts about cross-correlations and the Fourier transform to rewrite the dispersion image I_s for the response to a virtual source at x_s:

$$\begin{aligned}
\hat{I}_s(p,\omega) &= \mathcal{F}_t\left(\sum_{r=1}^{n} u_s(x_r, t + p(x_r - x_s))\right) \\
&= \sum_{r=1}^{n} \mathcal{F}_t(u_s(x_r, t + p(x_r - x_s))) \\
&= \sum_{r=1}^{n} \hat{u_s}(x_r,\omega) e^{2\pi i p(x_r - x_s)\omega} \\
&= \sum_{r=1}^{n} \hat{d}^*(x_s,\omega)\hat{d}(x_r,\omega) e^{2\pi i p(x_r - x_s)\omega} \\
&= \hat{d}^*(x_s,\omega) \sum_{r=1}^{n} \hat{d}(x_r,\omega) e^{2\pi i p(x_r - x_s)\omega} \\
&= \hat{d}^*(x_s,\omega) e^{-2\pi i p x_s \omega} \sum_{r=1}^{n} \hat{d}(x_r,\omega) e^{2\pi i p x_r \omega}
\end{aligned}$$

Let $\sigma := \sum_{r=1}^{n} \hat{d}(x_r,\omega) e^{2\pi i p x_r \omega}$. Clearly, σ can be reused in calculating the dispersion images for all sources $\hat{I}_s(p,\omega)$, and it only takes $O(n)$ calculations in serial. In the first step, the common factor σ is calculated as a slant-stack over the data, and in the second step each virtual source is time-lagged according to its position, then multiplied by σ. Thus, I can calculate dispersion curves for n sensors in $O(n)$ time in serial. In addition to being cheaper at $O(n)$ serial calculations, this method is highly parallelizable over the number of sensors, scaling as $O(n/m)$ calculations per machine if m machines are available (with the limiting communication factor being a single gather/scatter step for the small array σ). Only a single round of communication is required for the reduction to calculate σ. A point-wise multiplication in the frequency domain must be calculated for each source, but that is a constant.

Algorithm 1 $O(n)$ algorithm:

Given a short chunk of traces $d(x_i, t)$ from receivers at $x_1, x_2, \ldots, x_n$
Initialize $\sigma(p, \omega) = 0$
Calculate σ, the sum of phase shifted data spectra
for $i = 1, \ldots, n$ **do**
  Preprocessing and filtering of $d(x_r, t)$ and $\hat{d}(x_r, \omega)$
  $\sigma(p, \omega) += \hat{d}(x_r, \omega) e^{2\pi i p x_r \omega}$
end for
for $i = 1, \ldots, n$ **do**
  If stored, make filtered version of $\hat{d}(x_s, \omega)$ available. If not stored, do any filtering needed to calculate $\hat{d}(x_s, \omega)$
  Dispersion curve for virtual source at x_s is $\hat{c}_s(p, \omega) = \hat{d}^*(x_s, \omega) e^{-2\pi i p x_r \omega} \sigma(p, \omega)$
end for

Algorithm 2 Parallelized $O(n/m)$ algorithm:

Machines $j = 1, 2, \ldots, m$ each have a subset of short chunks of traces $d(x_{m,i}, t)$ from receivers at $x_{j,1}, x_{j,2}, \ldots, x_{j,n/m}$
On each machine initialize $\sigma_j(p, \omega) = 0$
Calculate σ_j, the sum of phase shifted data spectra
for $i = 1, \ldots, n/m$ **do**
  Preprocessing and filtering of $d(x_{j,i}, t)$ and $\hat{d}(x_{j,i}, \omega) = FFT(d(x_{j,i}, t))$
  $\sigma_j(p, \omega) += \hat{d}(x_{j,i}, \omega) e^{2\pi i p x_{j,i} \omega}$
end for
Gather $\sigma(p, \omega) = \sum_{j=1}^{m} \sigma_j(p, \omega)$
Scatter a copy of $\sigma(p, \omega)$ to all j machines
for $i = 1, \ldots, n/m$ **do**
  If stored, make filtered version of $\hat{d}(x_{j,i}, \omega)$ available on machine j. If not stored, do any filtering needed to calculate $\hat{d}(x_{j,i}, \omega)$
  Dispersion curve for virtual source at $x_{j,i}$ is $\hat{c}_{j,i}(p, \omega) = \hat{d}^*(x_{j,i}, \omega) e^{-2\pi i p x_{j,i} \omega} \sigma(p, \omega)$
end for

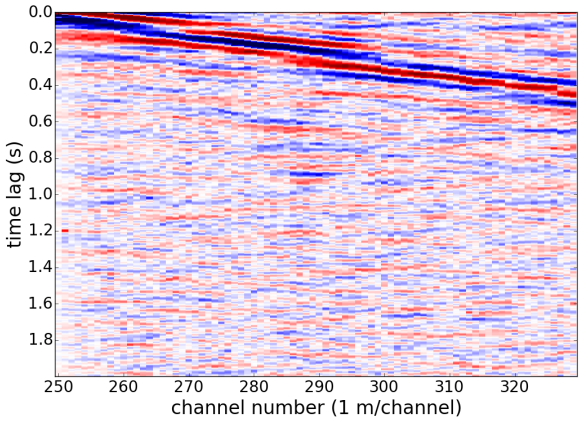

Figure 6.1: Estimated response to virtual source at channel 250 from 10 minutes of data filtered in the 5 to 50 Hz range. Noise correlation functions such as this one must be calculated for each virtual source in the $O(n^2)$ algorithm, but can be avoided in the $O(n)$ algorithm. **CR**

6.4 Demonstration on Data from Richmond Field Station

In the $O(n^2)$ algorithm, the first step is to calculate noise correlation functions for each channel acting as a virtual source. I show these response estimates (folded over zero time lag) in Figure 6.1 for one virtual source at the end of the array based on only ten minutes of ambient data. The next step in the $O(n^2)$ algorithm is to stack the response estimates over a variety of time lags and velocities, as seen in Figure 6.2.

In the end, the quantity of interest is the dispersion curve picked from the peaks of the dispersion image at each frequency. For this data set one can see the dispersion image that only includes a virtual source at channel 250 in Figure 6.3. In the $O(n^2)$ algorithm, one calculates this dispersion image by taking the FFT of the $\tau - p$ transform along the τ direction. However, in the $O(n)$ algorithm one can skip calculating the noise correlation functions and the $\tau - p$ transforms, and directly calculate the dispersion image. Both algorithms yield two strong modes at approximately the same velocity and frequency.

There are some significant differences in these results due to numerical error despite the results being equivalent in theory for exact arithmetic. Switching between the time and frequency domains multiple times in the $O(n^2)$ algorithm leads to small nonzero values

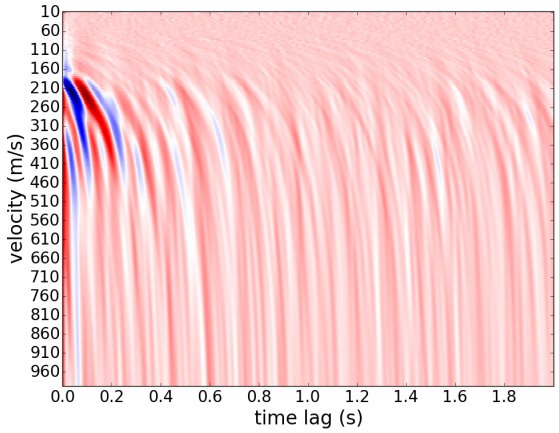

Figure 6.2: Velocity versus time lag resulting from $\tau - p$ transform of response estimate to virtual source at channel 250. This is a necessary step in the $O(n^2)$ algorithm, but can be avoided in the $O(n)$ algorithm. **CR**

below 5 Hz, despite the bandpass filter, which should cut out energy below 5 Hz. However, the new $O(n)$ algorithm respects the bandpass filter. The new $O(n)$ algorithm results in a much sharper dispersion image, most likely because it has fewer Fourier transforms and fewer opportunities for numerical error to accumulate.

There are some features visible in the $O(n)$ algorithm's dispersion image that are not apparent in the $O(n^2)$ algorithm's dispersion image. Between the two most readily apparent modes in the $O(n)$ algorithm's dispersion image, there appears to be another smaller peak for each frequency. It is possible this is another mode, but more data must be included before a conclusion on this mode can be drawn.

In the $O(n)$ algorithm's dispersion curve, there are some faint lines running from the low velocity and low frequency regime up to the high velocity and high frequency regime. The slope of these lines is approximately 10 meters. More data need to be incorporated before I can draw any more conclusions about whether this is a coherent feature, and what the interpretation of this feature could be. Further, a more detailed error analysis could help build understanding of any potential differences in numerical errors and boundary tapers between these two algorithms.

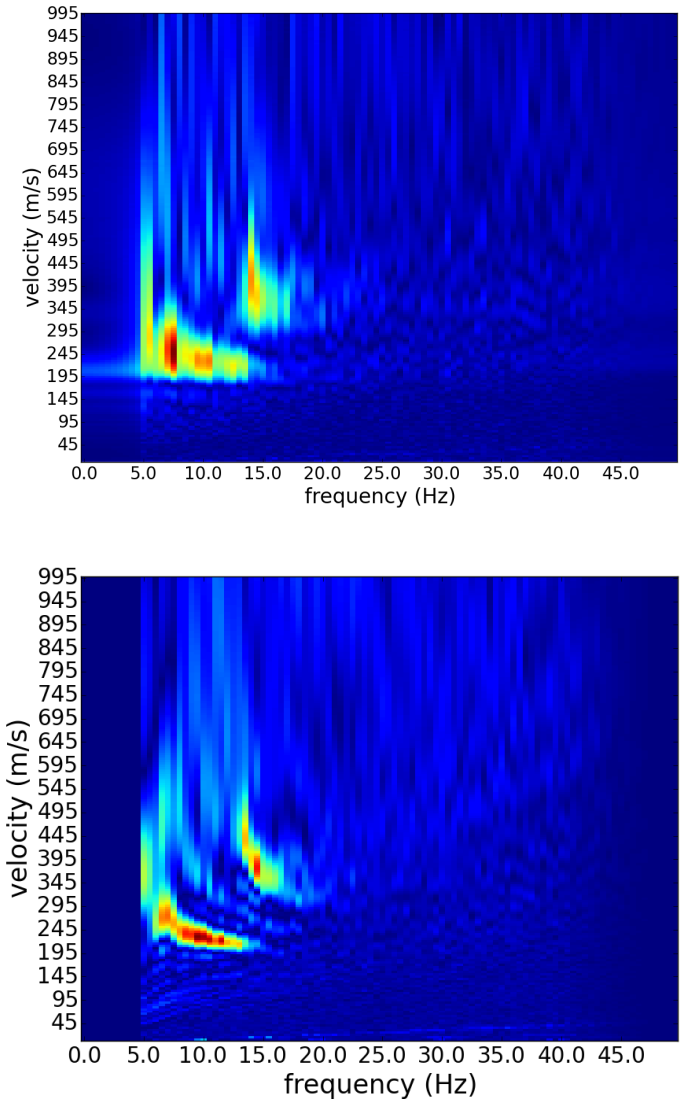

Figure 6.3: (Top) Velocity versus frequency dispersion image calculated by the $O(n^2)$ algorithm which takes an FFT of the $\tau - p$ transform in the τ direction. (Bottom) Dispersion image calculated by the $O(n)$ algorithm directly from the data spectra, then binned into 1 Hz intervals with a hard cutoff of any noise below 5 Hz, which was selected due to small array size. Both plots show the two strongest modes at approximately the same velocity and frequency, but the $O(n)$ algorithm results in a much sharper image. **CR**

6.5 Extensions: 2D Arrays and Alternative Processing

The 1D algorithm can be modified slightly to a 2D method, which can be parallelized the 1D case, although the gathered and scattered σ factor must now have an additional slowness dimension. I implemented this 2D code and it is available publicly. Further, I tested the 2D serial code for the new and old algorithms on up to 512 sensors, a subset of the Long Beach passive data set courtesy of Nodal Seismic. Frequently, ambient noise practitioners do not just use cross-correlation, but also may use deconvolution [62], so I point out the minor modifications needed for these common processing techniques.

6.5.1 2D Arrays

Let $\mathbf{p}$ represent slowness (note that if $\mathbf{v}$ is the velocity in two dimensions then $p_1 = 1/v_1$, and $p_2 = 1/v_2$). One conceptually simple method for calculating the dispersion image, I_s, from the response to virtual source, s, would be to calculate slant stacks along the responses of all sensors to the virtual source at $\mathbf{x}_s$ is:

$$I_s(\mathbf{p}, t) = \sum_{r=1}^{n} u_s(\mathbf{x}_r, t + \mathbf{p} \cdot (\mathbf{x}_r - \mathbf{x}_s))$$
$$\hat{I}_s(\mathbf{p}, \omega) = \mathcal{F}_t(I_s(\mathbf{p}, t))$$

In the same way as in 1D, I can factor out a common factor to create an $O(n)$ serial

algorithm yielding a dispersion image theoretically equivalent to frequency domain cross-correlations followed by slant-stacking:

$$\begin{aligned}
\hat{I}_s(\mathbf{p},\omega) &= \mathcal{F}_t\left(\sum_{r=1}^{n} u_s(\mathbf{x}_r, t+\mathbf{p}\cdot(\mathbf{x}_r-\mathbf{x}_s))\right) \\
&= \sum_{r=1}^{n} \mathcal{F}_t(u_s(\mathbf{x}_r, t+\mathbf{p}\cdot(\mathbf{x}_r-\mathbf{x}_s))) \\
&= \sum_{r=1}^{n} \hat{u_s}(\mathbf{x}_r,\omega)e^{2\pi i\mathbf{p}\cdot(\mathbf{x}_r-\mathbf{x}_s)\omega} \\
&= \sum_{r=1}^{n} \hat{d}^*(\mathbf{x}_s,\omega)\hat{d}(\mathbf{x}_r,\omega)e^{2\pi i\mathbf{p}\cdot(\mathbf{x}_r-\mathbf{x}_s)\omega} \\
&= \hat{d}^*(\mathbf{x}_s,\omega)\sum_{r=1}^{n} \hat{d}(\mathbf{x}_r,\omega)e^{2\pi i\mathbf{p}\cdot(\mathbf{x}_r-\mathbf{x}_s)\omega} \\
&= \hat{d}^*(\mathbf{x}_s,\omega)e^{-2\pi i\mathbf{p}\cdot\mathbf{x}_s\omega}\sum_{r=1}^{n} \hat{d}(\mathbf{x}_r,\omega)e^{2\pi i\mathbf{p}\cdot\mathbf{x}_r\omega}
\end{aligned}$$

In this case, $\sigma := \sum_{r=1}^{n} \hat{d}(\mathbf{x}_r,\omega)e^{2\pi i\mathbf{p}\cdot\mathbf{x}_r\omega}$, which is a (number of frequencies) x (number of x-velocities) x (number of y-velocities) array. The size of σ is independent of the number of sensors, so the parallelizability of this method over m machines is basically independent of the number of sensors (aside from the fact that you're more likely to use more machines if you have more sensors).

6.5.2 Scalability tested on Data from Long Beach, CA

To test the scalability of this algorithm on a larger ambient noise experiment, I tested the 2D $O(n)$ against the traditional $O(n^2)$ method on up to 512 of the vertical geophones at the Long Beach, CA array deployed by Nodal Seismic. These data were previously analyzed in [10]. For n = 1, 2, 4, 8, 16, and 32 sensors I tested cross-correlating $\frac{n(n+1)}{2}$ pairs followed by slant stacking of each pair with the new proposed method. My experiments with the $O(n)$ algorithm took a little bit less time to process up to 512 sensors of data as did the $n = 32$ experiments for the $O(n^2)$ experiment. The timing of each algorithm's experiments were scaled by the average timing of $n = 1$ autocorrelation experiments for the new $O(n)$

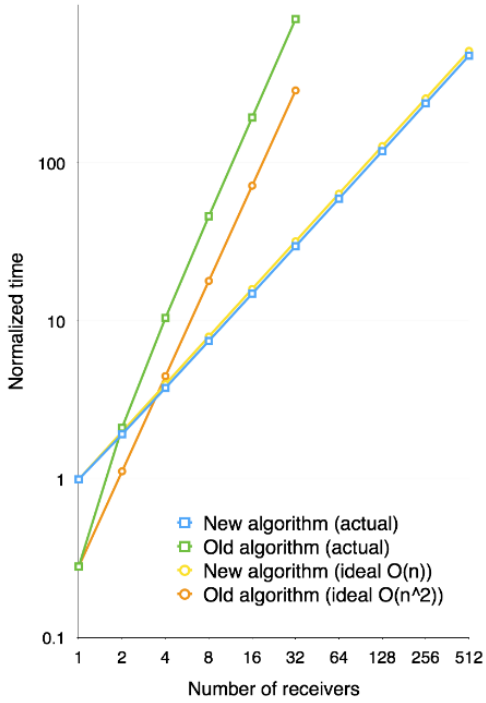

Figure 6.4: Timing of both the new $O(n)$ serial algorithm and the typical $O(n^2)$ algorithm for subsets of the Long Beach Array shows that the typical algorithm scales slightly worse than $O(n^2)$ while the new $O(n)$ algorithm scales almost perfectly linearly. All timing is relative, scaled by the time it took for an $n = 1$ experiment of the new algorithm. **CR**

algorithm. The results, seen in Figure 6.4, show that indeed the predicted linear trend holds true, even with many sensors (so more likely that data must be transferred from lower cache levels or main memory). Further, they show that the $O(n^2)$ algorithm actually scales just slightly worse than $O(n^2)$. I hypothesize that this may be due to an increased number of lower level cache and main memory hits as more sensors are considered.

6.5.3 Modifications: Cross-coherence and Deconvolution

In areas with non-ideal noise sources, the robustness of noise correlation functions estimated with cross-correlation can be supported by achieving similar results with multiple types of processing. In particular, cross-coherence tends to be more robust to noise sources in the array

$$\frac{\hat{d}(x_r,\omega)\hat{d}^*(x_s,\omega)}{|\hat{d}(x_r,\omega)||\hat{d}(x_s,\omega)|}. \tag{6.1}$$

The modification of Algorithm 1 and its parallelized version for cross-coherence is as simple as including whitening in the preprocessing/filtering of individual traces. This is true both for the first (receiver) and second (virtual source) round of calculations. Another option is deconvolution, which was tested in [51]:

$$\frac{\hat{d}(x_r,\omega)\hat{d}^*(x_s,\omega)}{|\hat{d}(x_s,\omega)|^*}. \tag{6.2}$$

With deconvolution, the whitening should not occur before the first (receiver) round of calculations, but in the second (virtual source) round of calculations filtering is required to scale each frequency sample by the square of its amplitude, so loud frequencies are more relatively damped and quiet frequencies are boosted even more than would be done for typical whitening. This differs from the cross-correlation and cross-coherence algorithm in that the second stage of filtering differs from the first stage, but it is expected to scale similarly.

Chapter 7

Time-lapse Interferometry Throughout DAS Arrays

Typically, ambient noise analysis is performed on dense, temporary arrays deployed for a few days to a few months [11], or sparse, permanent arrays [1], and it is expected that the velocity model stays the same throughout that time period. However, there has been some examples of velocity model changes detected by ambient noise interferometry. A velocity drop of roughly 0.08% immediately following a large earthquake were detected by seismic stations in California [60]. Over several decades, seismic noise recorded by four stations in Germany was used to detect changes in groundwater storage indicated by a roughly 0.01% velocity change [32]. Many previous examples of time lapse monitoring have been on sparse arrays measuring shifts in event picks between individual sensor pairs, but there has been at least one example of a before/after time-lapse ambient noise survey throughout a full array showing changes at a subsiding reservoir [16]. A benefit of DAS is that for environmental or geotechnical surveys it allows us to permanently install a dense array with low maintenance cost (besides the interrogator unit rental). In this chapter I explore time-lapse near-surface characterization in two cases: testing whether I detect seasonal saturation and temperature effects in Rayleigh wave interferometry at Stanford over 18 months, and observations of changes in waveforms in cross-correlations between orthogonal lines throughout the Fairbanks permafrost thaw test.

7.1 Dispersion Analysis at Stanford DAS Array Throughout Eighteen Months

I use ambient noise interferometry on data recorded by a distributed acoustic sensing (DAS) array to extract signals mimicking active source surveys without the cost and permitting requirements of a traditional active survey for geotechnical characterization. Between September 2016 and March 2018, I passively recorded DAS data on an array of fibers in existing telecommunications conduits under the Stanford University campus. I analyze time-lapse changes in the ambient noise field throughout campus and observe diurnal, weekday/weekend, and some annual variation trends. I calculate noise correlation functions (NCFs) throughout the 18 months of recording to test whether the array's NCFs were sensitive to near-surface velocity changes tied to seasonal saturation cycles. During rainier winter months, the NCFs have a higher signal-to-noise ratios (SNR) in one-bit cross-correlations, particularly at farther offsets. To understand whether temporal changes in the ambient noise field could cause spurious changes in NCFs, I compare two methods for calculating monthly NCFs (cross-correlation and cross-coherence) and their resulting dispersion images. Evidence does not suggest that the array detects a velocity shift correlated to saturation changes, but it is possible SNR of NCFs at far offsets may provide a qualitative indicator of saturation.

7.1.1 Background and Prior Work

For the purpose of near-surface characterization, including earthquake hazard analysis, on the Stanford campus, I am interested in processing ambient noise to avoid the cost, time and permitting requirements involved in active surveys. However, the Stanford campus displays a wide range of natural and anthropogenic noise sources which may not always be ideally distributed. Here, I analyze changes in the ambient noise field and NCFs throughout the first 555 days of data.

Ambient noise interferometry has successfully been used with point sensors to create data mimicking active surveys at the scale of a city [11] and time-lapse surveys at the reservoir scale [16]. Further, groundwater changes in California have been observed

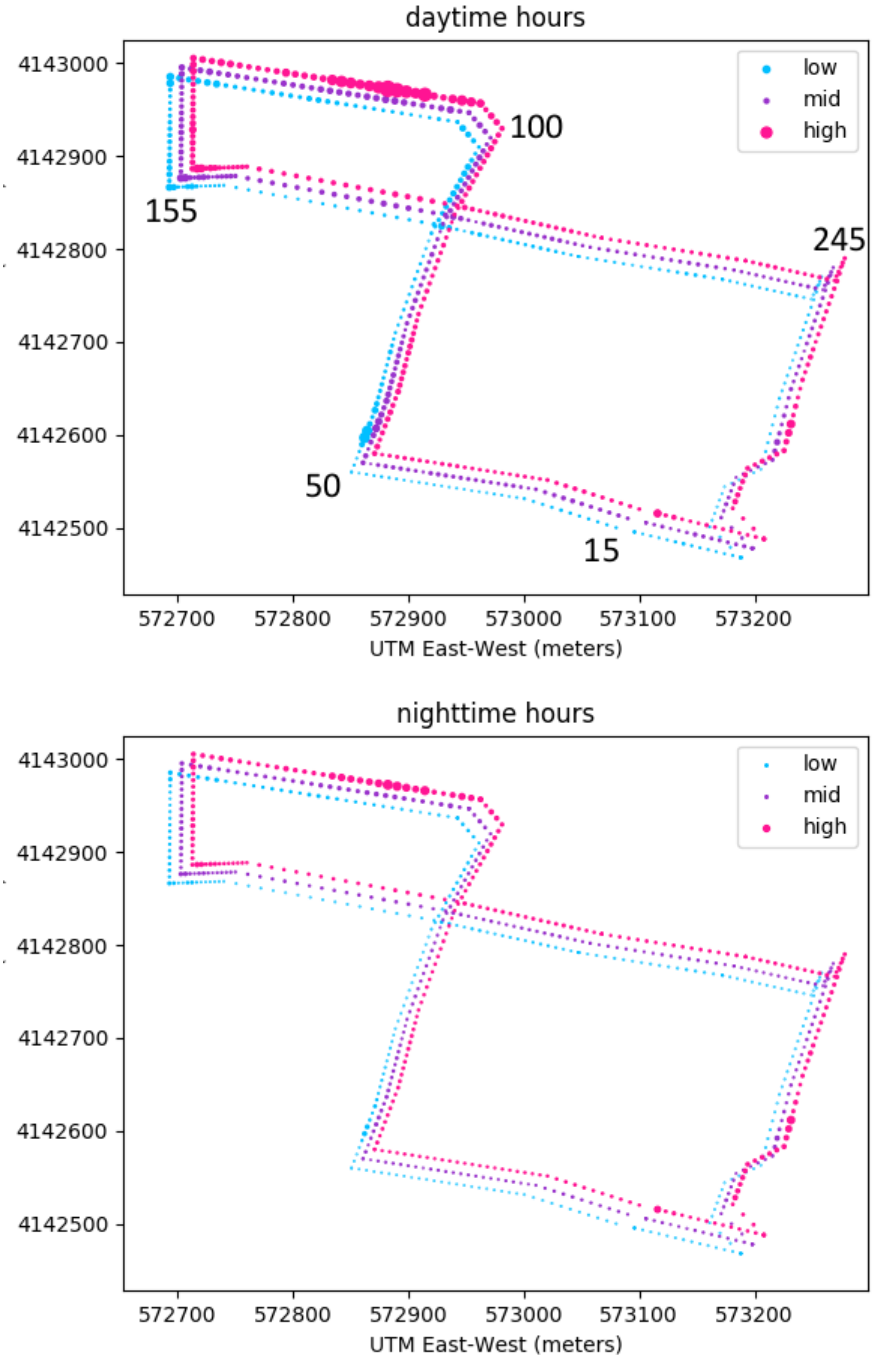

Figure 7.1: At each channel, the marker radius is proportional to the average spectral amplitude within three frequency ranges: 0.5-2.0 Hz (low, blue), 2.0-8.0 Hz (mid, violet) and 8.0-24.0 Hz (high, pink) average spectral amplitude. These are averaged over 18 months, separated into (top) daytime UTC 14:00 to 05:59, and (bottom) nighttime UTC 06:00 to 13:59. Several channel numbers are marked for reference. **CR**

over a larger scale using frequencies below 2 Hz through ambient noise interferometry of broadband seismometer data [12]. Cross-correlations of data from a trenched DAS array recording a repeatable active source have indicated velocity changes on rainy days [2]. Further, ambient noise interferometry at a trenched DAS array crossing a section of permafrost during an active thaw experiment shows a drop in velocities of NCFs as thawing occurred [34]. Previously at the Stanford array, it has been observed that coherent NCFs can be extracted even between non-collinear channels, and those NCFs converge in most places within approximately one week [41]. Given these studies, it is natural to wonder whether it is possible to observe velocity shifts tied to annual variations in saturation using ambient noise recorded here, and whether changes in the ambient noise field complicate reliable estimation of virtual source responses.

Inferring time-lapse velocity changes from ambient noise interferometry in an urban area is difficult because: NCF artifacts may be introduced by repeating noise sources that are not independent of each other [42], and changes in the amplitude spectrum or spatial distribution of the ambient noise field between epochs may introduce false apparent velocity changes in NCFs [72]. In both cases, the use of cross-coherence can reduce these effects [42, 15]. However, the whitening process in cross-coherence may keep us from studying the dependence of NCF sensitivity on geometry within different frequency bands [39], and one-bit cross-correlations should have a simpler invertible transformation corresponding to true correlations corresponding to more ideal noise source distributions [26], so I have previously focused on analysis of one-bit cross-correlations [42]. In this study, I analyze changes in the ambient noise field, and compare time-lapse changes in NCFs calculated through one-bit cross-correlation and cross-coherence, as well as tracking the stability of dispersion curve picks.

7.1.2 Spatio-temporal Variation of Ambient Noise

For each minute of data, I calculated each channel's amplitude spectrum, then averaged over each hour. As seen in Figure 7.1, there is more energy in the frequency ranges above 2 Hz, which tends to be anthropogenic noise. This can potentially cause issues because anthropogenic noise sometimes violates the assumption underlying ambient noise

theory: that the ambient noise field is made of independent, uniformly distributed noise sources. The loudest area of the array, the north edge, is along a main campus road, and particularly during the daytime this area suffers from increased traffic, and construction activity. Daily traffic patterns are not necessarily a problem in monthly time-lapse ambient noise interferometry if they are consistent month-to-month.

In addition to diurnal trends, there is a secondary trend: weekend days are much quieter than weekend days, as evidenced by the regular dips in energy above 2 Hz in Figure 7.2. The typical trend is that areas with more vehicular traffic, including channel 75, show stronger diurnal and weekly trends and less change over the course of the year. Channels in quieter pedestrian-only alreas, including channel 255, show significant annual variability in energy above 2 Hz: quietest in the summer months and loudest in the winter (peak is around February each year). Because the farthest north and west lines (channels 100 to 165) are particularly affected by vehicle noise, and the southeast corner (channels 270 to 287) are particularly affected by reverberations of waves off two large building basements [40], it is unclear whether a coherent signal can be extracted so the treatment of these receivers is beyond the scope of this effort.

7.1.3 Processing Noise Correlation Functions

One-bit cross-correlation should theoretically converge to NCFs that reflect information about attenuation and frequency-dependent geometric sensitivity of DAS NCFs. But these NCFs can demonstrate artifacts due to our non-ideal ambient noise field. Thus, I decided to calculate both the one-bit cross-correlation and the cross-coherence to understand whether velocity changes were robust to processing decisions, particularly in the presence of changing anthropogenic noise sources near the array. The aim of cross-coherence is reducing false velocity changes due to spectral amplitude shape differences over time [72]. Further, when dispersion analysis of cross-coherence results matches one-bit cross-correlation results, it may support the use of those one-bit cross-correlation NCFs for attenuation and frequency-related geometry sensitivity analysis.

For each one-minute window, I performed one-bit cross-correlation and cross-coherence

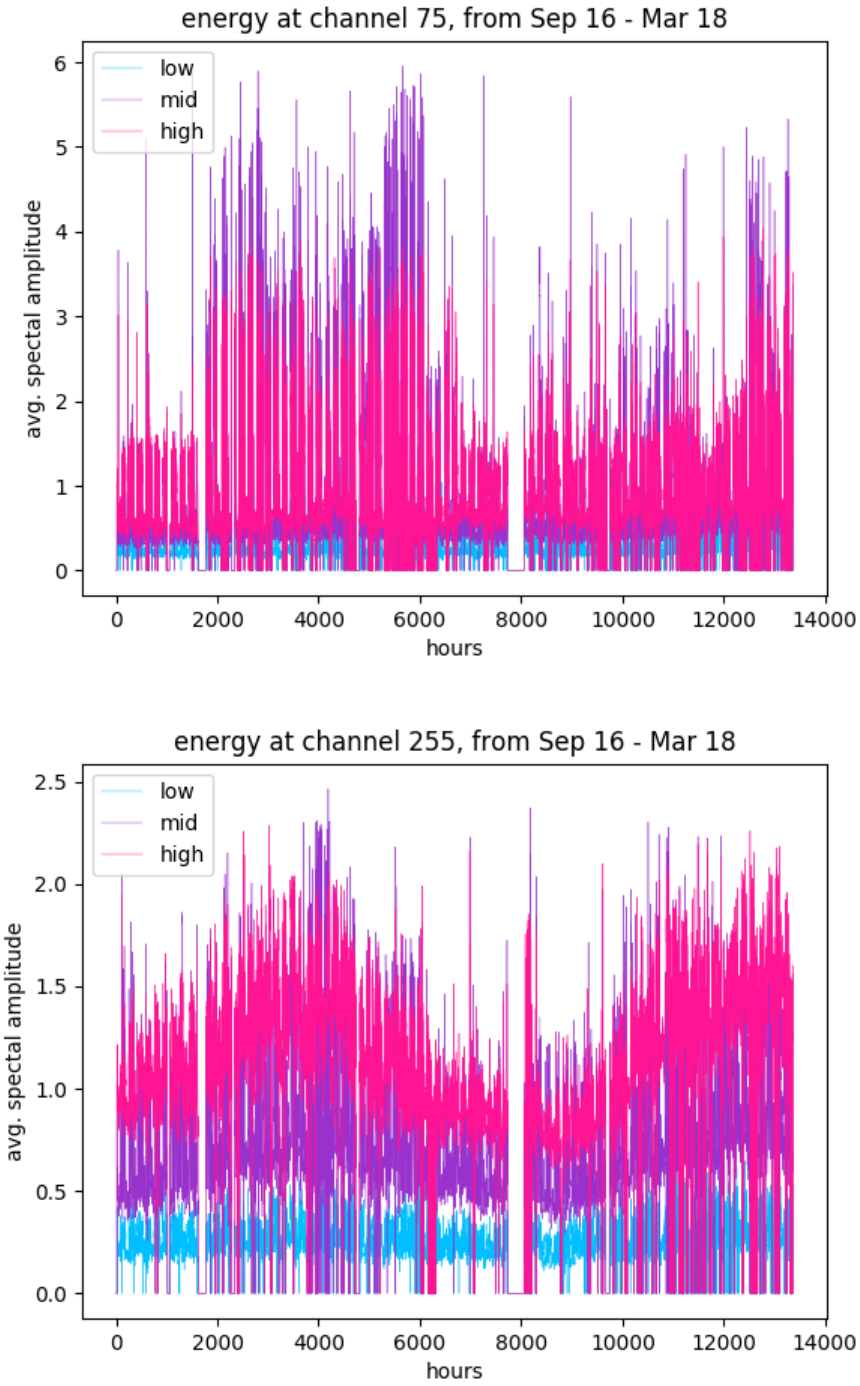

Figure 7.2: The hourly average spectral amplitudes are plotted for channels 75 (top) and 255 (bottom) in three frequency bands: 0.5-2.0 Hz (low, blue), 2.0-8.0 Hz (mid, violet) and 8.0-24.0 Hz (high, pink). In areas with more cars, including ch. 75, there is little seasonal variability, but pedestrian-only areas like ch. 255 show loud winters and quiet summers. **CR**

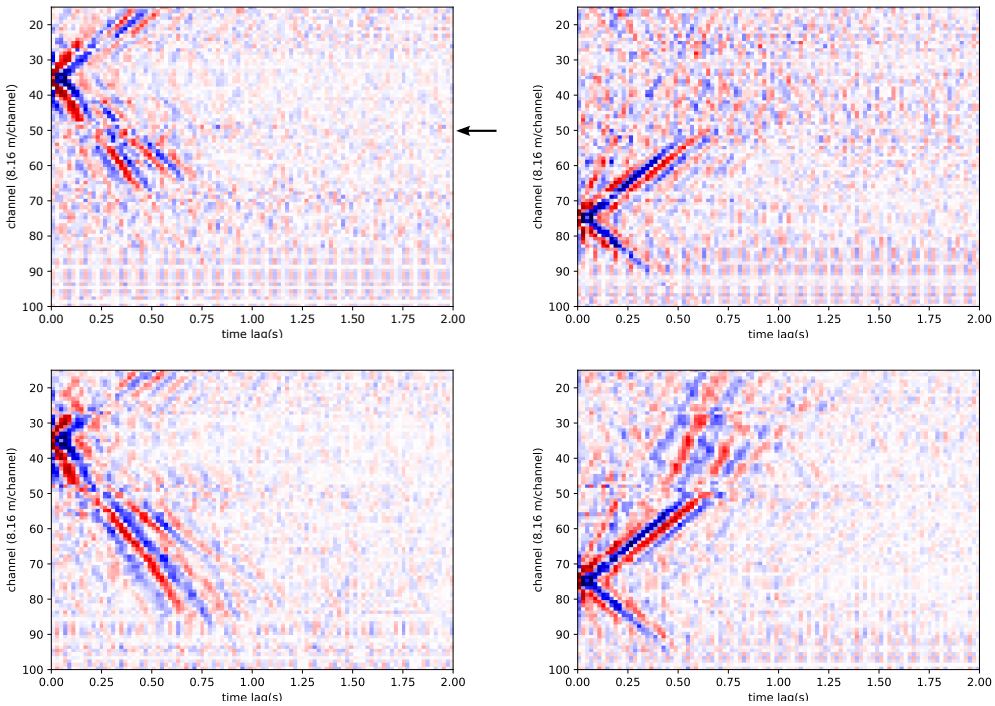

Figure 7.3: One-bit cross-correlations of ch. 15-100 with 35 (left) and 75 (right) in Sep. 2016 (top) and Mar. 2017 (bottom) show better SNR in March when the ground is more saturated. Each trace is normalized by its L2 norm. In the top-left diagram an arrow was added to mark the southwest corner of the array. **CR**

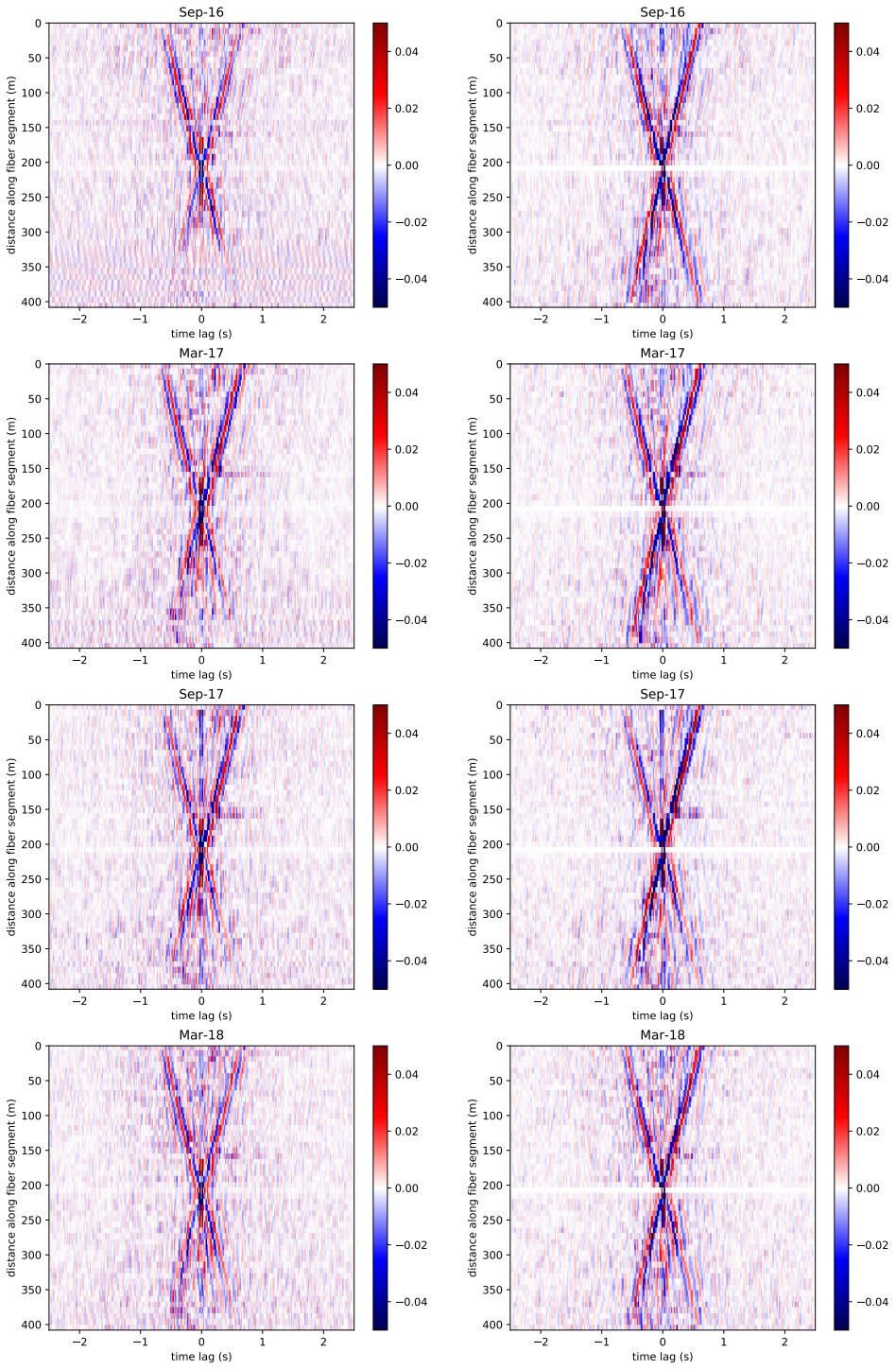

Figure 7.4: One-bit cross-correlations (left) and cross-coherences (right) of channel 75 with channels 50 to 100, at distances 0 to 400 meters, respectively, from the southwest corner of the array. Each trace is normalized by its L1 norm. From top to bottom: Sep. 2016, Mar. 2017, Sep. 2017, Mar. 2018. **CR**

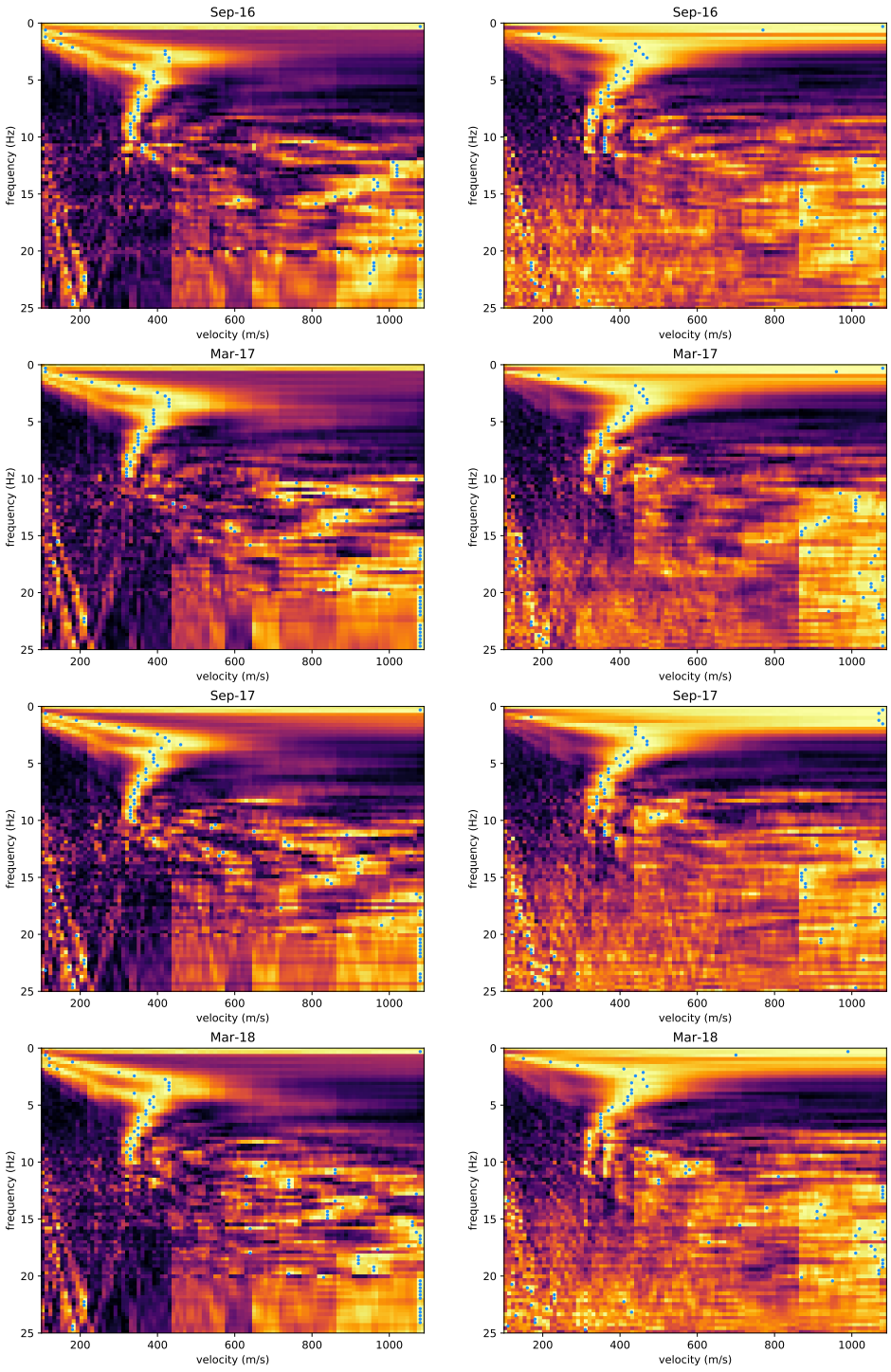

Figure 7.5: Dispersion images of monthly one-bit cross-correlations (left) and cross-coherences (right) in Figure 7.4. Yellow denotes more energy traveling at a particular frequency and velocity. Dark areas have less energy. Dots mark frequency-wise peak velocities. **CR**

for each receiver pair. For each hour, I stored the average one-bit cross-correlation and cross-coherence for each channel pair. I then calculated the monthly averages. First, I averaged the one-bit cross-correlations normalized by their L2 norms. The resulting NCFs appear to have stronger extracted signals during the rainy winter months than dry summer and early fall months, as seen in Figure 7.3 for two orthogonal fiber lines reacting to two different virtual sources (one on each line) averaged over one week. This change is clearer at distances longer than 200 meters.

By using the L2 norm, I de-emphasize hourly correlations with a concentrated wavelet and strong peak, making all monthly estimates noisier. Thus, in Figure 7.4 I show NCFs normalized by their L1 norm before monthly averaging to reduce this noise-quality difference and focus primarily on any velocity changes that may be present. To simplify their interpretation, I show results every six months for a straight line of fiber at offsets shorter than 200 meters responding to a virtual source at channel 75. These signals represent only Rayleigh wave arrival times (as opposed to the mix of Rayleigh and Love waves in Figure 7.3).

7.1.4 Dispersion Analysis

For each month I calculated the dispersion images for both types of NCF calculation, seen in Figure 7.5. The one-bit cross-correlation dispersion images split from 1-5 Hz into a higher and lower velocity. It is likely the higher velocity peak consistent with the coherence dispersion image (which is more robust to noise sources in the array) is reliable. The faster one-bit correlation peak is stronger and more consistent over all months, shown in Figure 7.6. There is not clear evidence of a velocity shift tied to saturation. Both types of dispersion image are coherent from 2-10 Hz, but vary at the high and low frequency ends by month (possibly due to changing noise levels), sometimes appearing to continue up to 12 Hz or down to 1 Hz. In the 9-11 Hz range, there is some hind of a possible first overtone in addition to the main fundamental mode Rayleigh wave peak, particularly in the cross-coherence dispersion images, but it is not consistently strong over all months. One-bit cross-correlations have more consistent dispersion curve picks in the 1-2 Hz range for more months than do cross-coherences, but even if these are coherent signals, they are likely to be

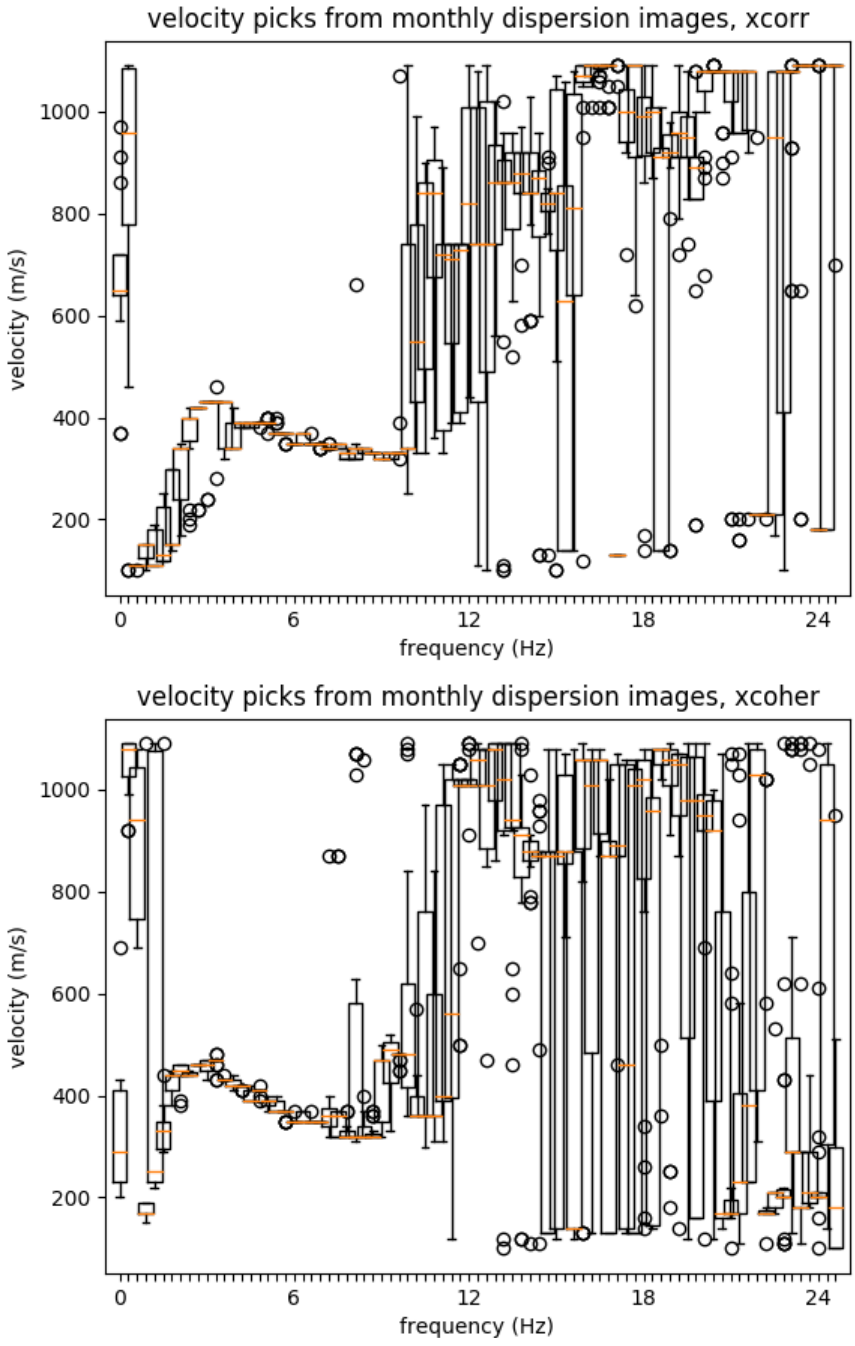

Figure 7.6: These plots show the distribution of the channel 75 virtual source gathers' 18 monthly dispersion images' peak velocity picks for each frequency. This was repeated for both one-bit cross-correlation (top) and cross-coherence (bottom). **CR**

biased due to the small array size. Further, phase velocity typically increases as frequency decreases. These picked velocities for frequencies above 2 Hz are typical of Rayleigh waves in geotechnical MASW studies, and given with the stability of these picks month-to-month this suggests ambient noise interferometry of DAS data is an effective tool for geotechnical surveys, even in urban areas.

A more complete picture of this variability can be seen when plotting the distribution of picks from monthly cross-coherences' dispersion images of multiple virtual source gathers. These distributions are seen in Figure 7.7 for virtual sources throughout the Via Ortega line (channels 55, 65, 75, 85, and 95, each approximately 80 m spaced), along with the distribution of each pick's wavelength versus frequency and wavelength versus velocity plots. These plots show very stable frequency versus wavelength curves for frequencies from 1 Hz up to 8-12 Hz, depending on the virtual source. In particular, channel 95 which is near the high traffic Campus Dr. and Via Ortega intersection is much less stable, showing a greater spread in the frequency/wavelength and frequency/velocity curves over time. While there is greater spread, it does not show any clear trend in summer versus winter months. at virtual sources on the south end (channels 55 and 65) there is a bit of a jump in wavelength at 6 Hz, suggesting a possible change around the area of parking structure 2 and Y2E2.

While the dispersion curves in Figure 7.7 are relatively coherent from 1 to 8-12 Hz for receiver pairs along Via Ortega, the virtual source gathers along the south side of the array, yield much less consistent dispersion picks. Figure 7.8 shows the same plots but for channels along the south edge of the array: channels 290 and 300 along Panama St. just south of Mitchell and Durand, channel 15 along Panama St. just south of Green building, and channels 25, 35, and 45 which are all between Roble and Arrillaga Gyms to the south of Panama St. In particular, channels 290 and 300 near Durand and Mitchell are particularly incoherent, even in the range of a few Hz. This may be an effect of being so close to the Durand and Mitchell basements, which cause large reverberations of vibrations, particularly seen during earthquakes. It could also be normal modes of these large buildings. The rest of the virtual source locations seems to have some coherency in the 2-6 Hz range with wavelengths in the 50-150 meter range (so sensitive to thicknesses of 15-75 meters depth).

The dispersion curves for Rayleigh wave interferometry along the south side of the array are clearly less consistent than the curves for channels along Via Ortega. One possible

explanation is that traffic on Panama St. and Campus Dr. would travel perpendicularly to Via Ortega, creating vibrations that would travel mostly parallel to Via Ortega (and thus be in the most sensitive zone for Rayleigh wave interferometry, yielding true Green's function velocities). Meanwhile that same traffic would travel mostly parallel to the south side of the array, creating waves that hit the southern channels mostly broadside at angles outside the zone most important for Rayleigh wave interferometry. This is somewhat similar to difficulties encountered in the road-parallel line of the Richmond Field Station experiment [21]. In theory, Rayleigh wave interferometry of a linear DAS array should be less effected by noises hitting the array broadside than a linear geophone array, so further experimentation should be done to determine whether this is the case at the Stanford Array.

When compared to active source data from multiple surveys throughout the north-central campus region [61], the dispersion curves calculated along the Via Ortega line are within the range of what is expected. To get an estimate of expected Rayleigh wave dispersion curves on campus, I made a four-layer model based roughly on the 1D V_s profiles estimated in north-central campus in [61]. Within the set of seven V_s profiles throughout north-central campus, there is up to 20% variability from the (lognormal) average speed at any depth. I assumed 1850 kg/m^3 density of the soil, a 2:1 V_p : V_s ratio, and a four layer model from top to bottom described by depth and V_s: 10 ft of 700 ft/s, 50 ft of 1000 ft/s, 110 ft of 1400 ft/s, and a half space of 1700 ft/s. Using the Matlab code MASWaves [52], I calculated the theoretical dispersion curve in Figure 7.9.

It is unclear whether the phase velocity picks below 2 Hz in the ambient noise data along Via Ortega are reliable given the small array size (and deviation from the typical trend of velocity increase with decreasing frequency), so here I compare the synthetic dispersion curve to the ambient noise dispersion curves in the 2-10 Hz range. I compare the synthetic curve to the ambient noise dispersion curve from virtual source channel 55 pictured in Figure 7.7 because it is the location closest to the Roble Field active source survey line and Escondido Mall active source survey line. Note however, that it is still a few hundred meters away from either of the nearest active source lines, so we do not expect exactly the same results. The ambient noise data dispersion curve peaks around 2 Hz at around 500 m/s phase velocity, while the synthetic curve shows a 440 m/s phase velocity. At 5 Hz, the synthetic dispersion curve has a phase velocity of 355 m/s while the ambient noise curve

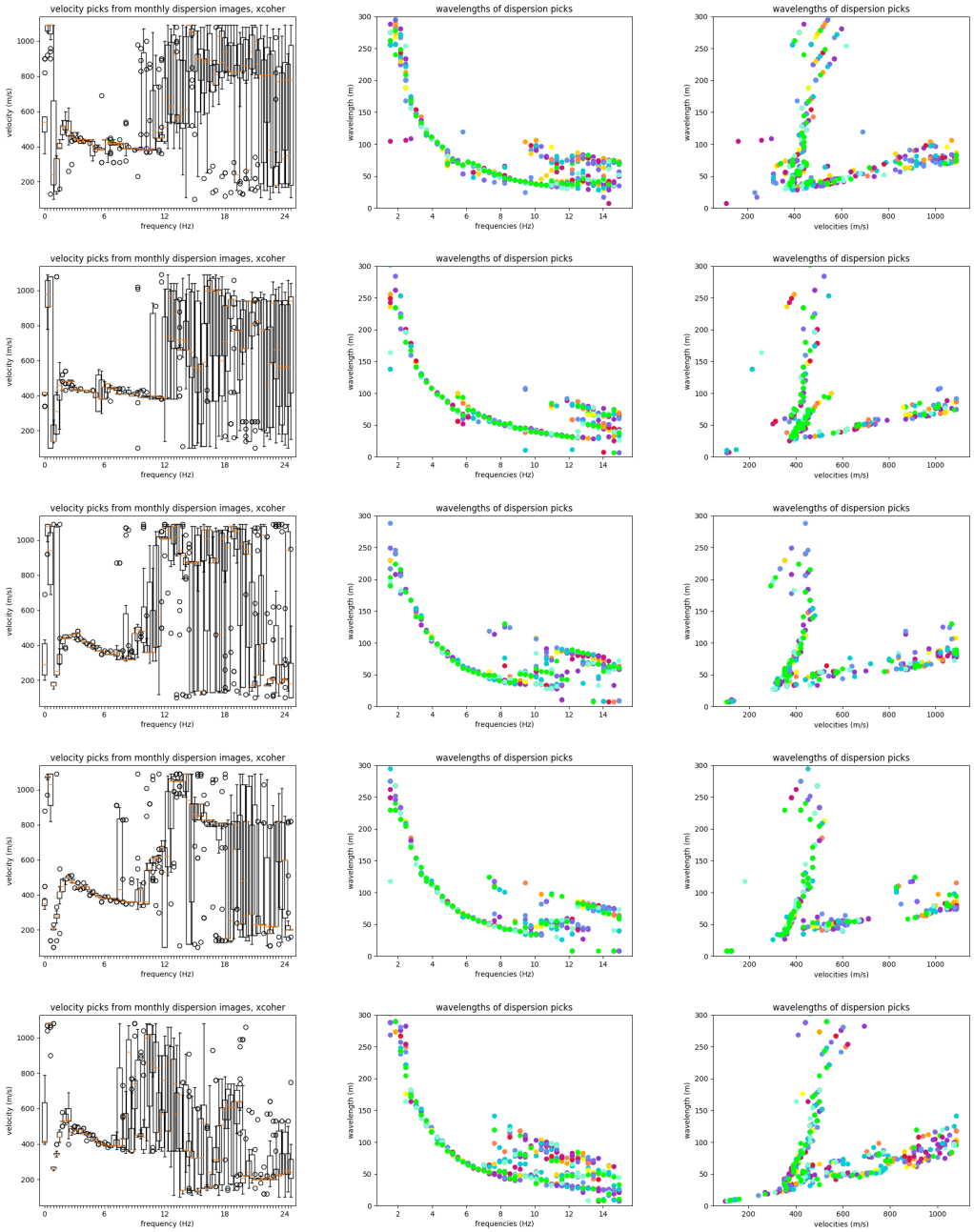

Figure 7.7: (Left) box plots of Rayleigh wave cross-coherence dispersion image picks, (center) corresponding picked wavelengths, and (right) velocities at those wavelengths plotted over all months (blues/greens are winter months, and reds/yellows are summer months) for virtual sources along Via Ortega at channels 55 (top), 65 (2nd row), 75 (3rd row), 85 (4th row) and 95 (bottom row). **CR**

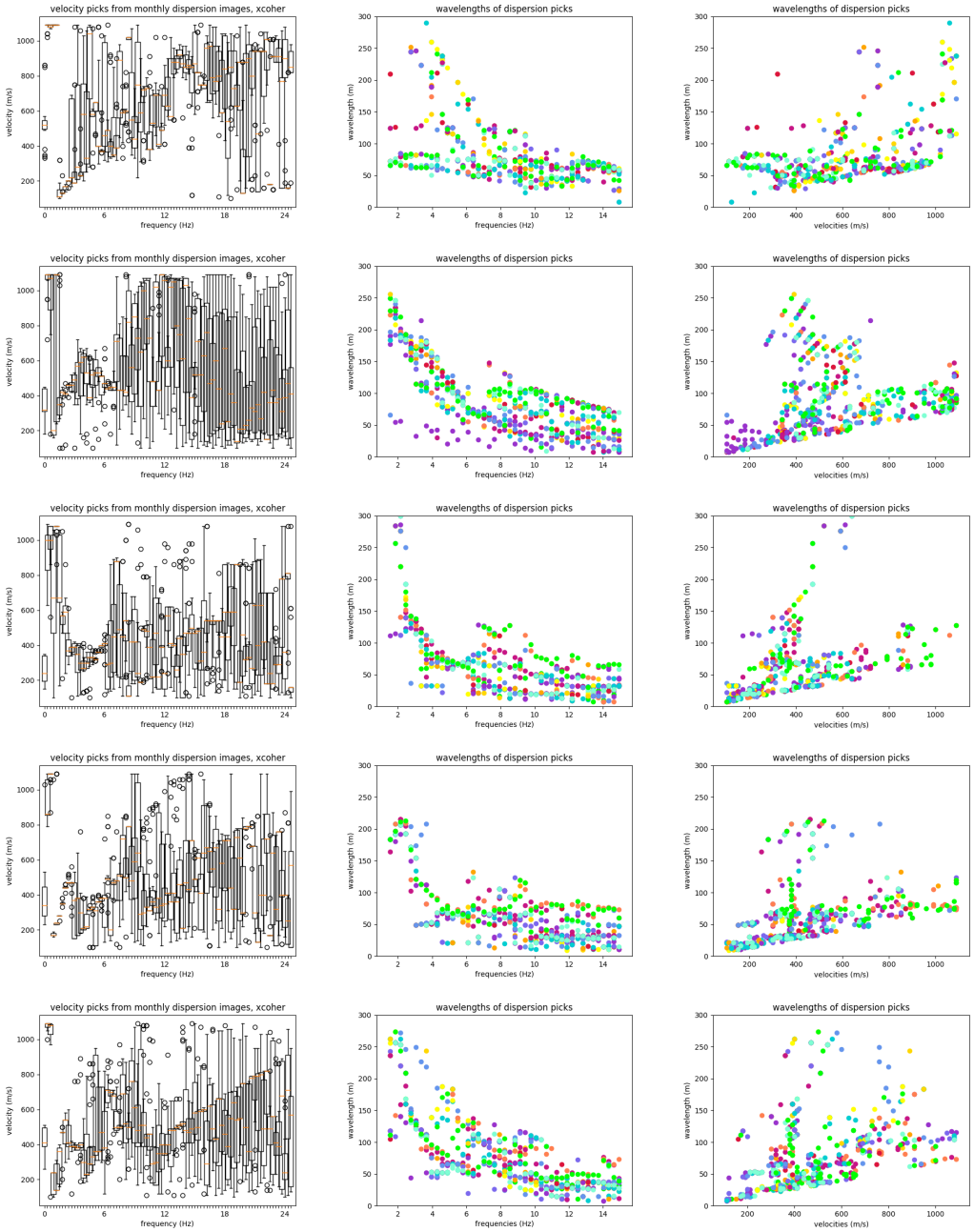

Figure 7.8: (Left) box plots of Rayleigh wave cross-coherence dispersion image picks, (center) corresponding picked wavelengths, and (right) velocities at those wavelengths plotted over all months (blues/greens are winter months, and reds/yellows are summer months) for virtual sources along the farthest south edge at channels 300 (top), 15 (2nd row) every 10 channels to 45 (bottom row). **CR**

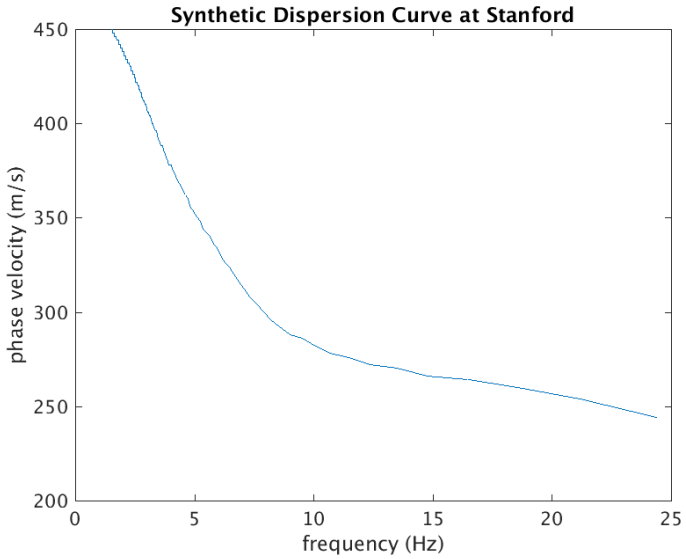

Figure 7.9: This plot shows the phase velocity versus frequency plot estimated by the code MASWaves for a four-layer model based on typical velocities measured with active source surveys in other parts of the Stanford University campus. This dispersion curve is slower than the ambient noise interferometry results along the 400 meter long Via Ortega line, but only by 50-100 m/s, which is within the range of variability for both the active source estimates on campus, and the ambient noise interferometry results along Via Ortega. **CR**

from channel 55 has a phase velocity around 400 m/s. Just slightly above, at 6 Hz is where the ambient noise dispersion curves in the southern end of the Via Ortega line show a sudden jump to higher phase velocities of 440 m/s, but the synthetic curve continues to decrease to 340 m/s. 6 Hz shows the largest deviation between the synthetic and real curves, 100 m/s, and that continues to be the difference up to 10 Hz, where the synthetic curve is roughly 280 m/s and the ambient noise curve is roughly 380 m/s. The difference between the ambient noise dispersion curves and the synthetic curve are reasonable, given that throughout the Via Ortega fiber line's ambient noise dispersion curves we see Rayleigh wave phase velocity varying up to 50 m/s, and amongst the active source results in north-central campus we see V_s profiles in the top 100 meters varying by up to 100 m/s from the average.

7.1.5 Conclusions

I analyzed 18 months of ambient noise from a DAS array in an urban area. The data show large spatial variability, diurnal patterns, weekday/weekend patterns, and an annual winter increase in noise levels. Monthly one-bit cross-correlations show an SNR drop for NCFs in summer months, which may be a qualitative proxy for saturation (this deserves further investigation). One-bit cross-correlation dispersion images show two peaks 1-5 Hz, one of which continues from 1-10 Hz and is consistent with cross-coherence results that are more robust to non-ideal ambient noise, suggesting it is reliable. While this analysis does not show evidence of significant velocity change with seasonal rain patterns, the stability of these dispersion curves suggests DAS with careful noise analysis is appropriate for urban geotechnical surveys in some urban areas, but this may depend in large part on fiber geometry relative to noise sources including roads, and our ability to automatically remove nearby traffic noise. Comparison to active source geotechnical surveys in other parts of campus confirms that the phase velocities estimated from ambient noise interferometry along the Via Ortega line are reasonable.

7.2 Time-lapse interferometry during permafrost thaw test at Fairbanks

I use ambient noise interferometry on data recorded by orthogonal fiber lines at the Fairbanks permafrost thaw experiment site throughout the thaw process to monitor changes in the noise correlation functions. Between August 6, 2016 and October 1, 2016 scientists from Lawrence Berkeley Lab and The Army Corps of Engineers Cold Regions Research and Engineering Laboratory recorded passive seismic data each day while an array of subsurface heaters actively thawed an 11 m x 13 m section of permafrost, moving the interface of the permafrost table down by 1 meter as measured by temperature sensing and mechanical deformation (subsidence) [63]. Permafrost thaw is tied to significant drops in both P- and S-wave velocities [73]. Previously, noise correlation functions between the roadside line and parallel lines near the heater grid have shown at least a 9% drop in apparent seismic velocity for some phases traveling near body-wave speeds [34], although further investigation must

be done to identify the mechanism by which these waves are excited. In this section, I test the sensitivity of noise correlation functions between the roadside line and orthogonal cables in the grid around the heater section, which is expected to yield different wave modes than the parallel lines. I first study the convergence rates of these noise correlation functions, and find that it is useful to average results from entire days of data. There are clear changes in these noise correlation functions, starting with the emergence of two clear arrivals: one at a slower velocity and one at a faster apparent velocity, as well as some energy that appears to be scattered or reflected. These results suggest that noise correlation functions from orthogonal DAS channels are sensitive enough to detect waveform changes when permafrost thaw occurs. This result expands the possibilities for which array geometries may be used for permafrost thaw monitoring when surface obstacles prevent parallel lines from being installed.

7.2.1 Processing

For each road-orthogonal line (1, 2, 3, 4, 5 in Figure 3.5), I calculated the cross-coherence of every other receiver with every tenth receiver in the roadside line. Between channels 3200 and 3300 I also correlated against every fifth receiver in the roadside line because these are the channels nearest to the road-orthogonal line, and thus the most likely to benefit from increased density. As shown in Chapter 5, cross-coherence of Rayleigh wave interferometry along the roadside line was helpful in reducing artifacts potentially due to cars driving over road joints, producing loud pops at repeating time intervals. The data were separated into 1 minute non-overlapping windows before I calculated their cross-coherence, then scaled by their L2 norms, then I calculated the mean of the cross-correlations within each set of 15 minutes of data and saved this to a file. I repeated this for every minute recorded of every fourth day throughout the experiment (days 1, 5, 9, ..., 57 spanning August 6 through October 1).

7.2.2 Effect of DAS sensitivity patterns on orthogonal correlations

As predicted in Chapter 2, the intensity and focus of the cross-coherence of any pair of channels in the array depend on their relative geometry and distance. When there are two

orthogonal channels, they are most sensitive to longitudinal (Rayleigh) waves coming from opposite azimuths, but they may both be slightly sensitive to four small ranges of common azimuths. The azimuths at which they are most sensitive to transverse (Love) waves could line up, and would yield the strongest signals if those angles also lined up well with the vector between the two sensors. Thus, it is predicted that a virtual source gather with the virtual source orthogonal to the receivers should appear to have a weak-strong-weak-strong-weak pattern due to: far offset and sensitivity angles do not line up, shorter offset and sensitivity angles do line up, shortest offset but sensitivity angles do not line up, and the same in the opposite direction.

An example of this trend can be seen in Figure 7.10 for a gather with virtual source 2006 on the eastern side of line 1 (the farthest north road-orthogonal line). Similar to Figure 2.15, at the closest offset roadside channels, 3200 to 3280, the wavelet gets very spread out. However, the signal extracted from this real data does appear to have some reasonable arrival time, whereas Figure 2.15 shows no usable signals at the shortest offsets, indicating that more realistic modeling may yield better theoretical understanding of these geometries. At slightly longer offsets, channels 3280-3350 to the southwest and 3100-3200 to the northwest, the signals remain strong but become more compact. I hypothesize this is due to better alignment of the approximately 45 degree peak sensitivity angles with the radial vectors between sensor pairs. As expected, there is a signal die-off with distance. To quantify these trends, I have calculated the ratio between the peak of each cross-coherence to its root-mean-square (RMS) average. A similar trend has been observed on parallel-line correlations [34], although the difference between that case and the cross-coherences shown in this chapter is how longitudinal wave sensitivities align.

This is not just a trend observed on a single virtual source gather. To give the reader a better sense of this weak-strong-weak-strong-weak trend, I show receiver gathers for six channels spread out along the roadside line against the channels in line 1 (the farthest north road-orthogonal line) with their ray-paths marked in Figure 7.11 and corresponding virtual source gathers in Figure 7.12. As shown with the annotations in Figure 7.13, in most cases there appears to be a fast event arriving around 600 m/s, and a slow event traveling around 100 m/s.

For all virtual sources, this signal dies off in the 15-20 channels on the eastern side

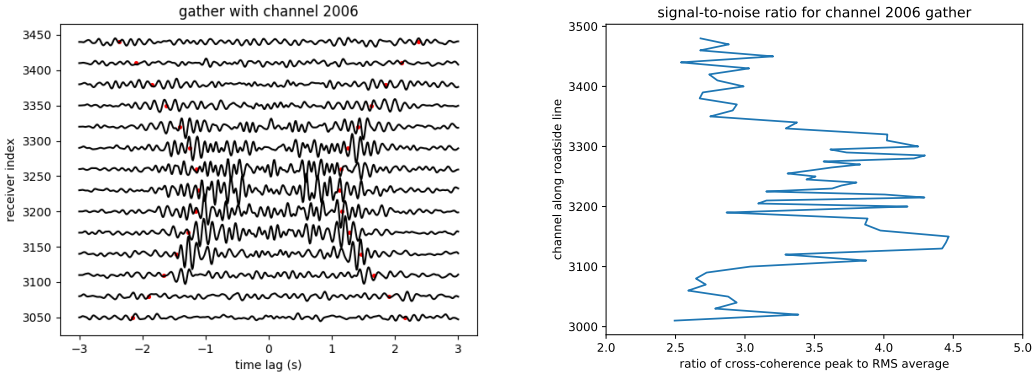

Figure 7.10: (Left) Cross-coherences of virtual source channel 2006 on the eastern half of line 1 with a subset of receivers along the roadside line shows the strongest responses are between channels 3350 and 3100. Red markers are added at expected arrival times of a 100 m/s moveout for visual reference. The closest receivers, between channels 3180 and 3280, have wavelets spread out over one second wide, making it difficult to pick arrival times. (Right) The spread or sharpness of cross-coherences, quantified by the ratio of the peak to RMS average of each pair, shows a weak-strong-weak-strong-weak pattern. **CR**

of each road-perpendicular line, even when averaging cross-coherences over an entire day. Because this is consistent across many receivers along the road-parallel lines acting as virtual sources, it is most likely that this phenomenon cannot be explained by geometry and DAS angular sensitivity alone, but rather that there may additionally be some velocity contrast or near-surface conditions that prevent much surface wave energy from traveling into this part of the array. Just after the 100 m/s slow event passes by most of the line, there is a wave of lower amplitude that travels back in the opposite direction, further supporting the hypothesis that there may be a large velocity contrast in this area. From synthetic tests in chapter 2, it is clear that compared to parallel cross-correlations, orthogonal cross-correlations have a wider range of offset angles that record more equal amplitudes of Rayleigh and Love waves, something that would be useful in extracting Rayleigh-Love converted energy in the presence of a high contrast reflector. I believe further modeling studies of ambient noise interferometry in the presence of a high velocity contrast are necessary before it can be adopted more widely in patchy permafrost zones.

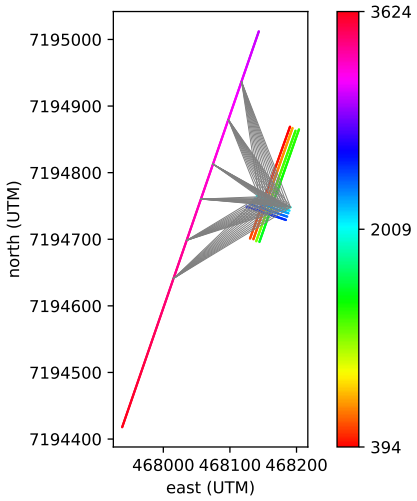

Figure 7.11: Each channel's location in the roadside line and grid is plotted with a marker colored according to its channel number in the data. Ray paths of a subset of the (virtual source, receiver) pairs included in Figures 7.12 and 7.13 are denoted with gray lines. Line 1 is the northern-most road-orthogonal line. **CR**

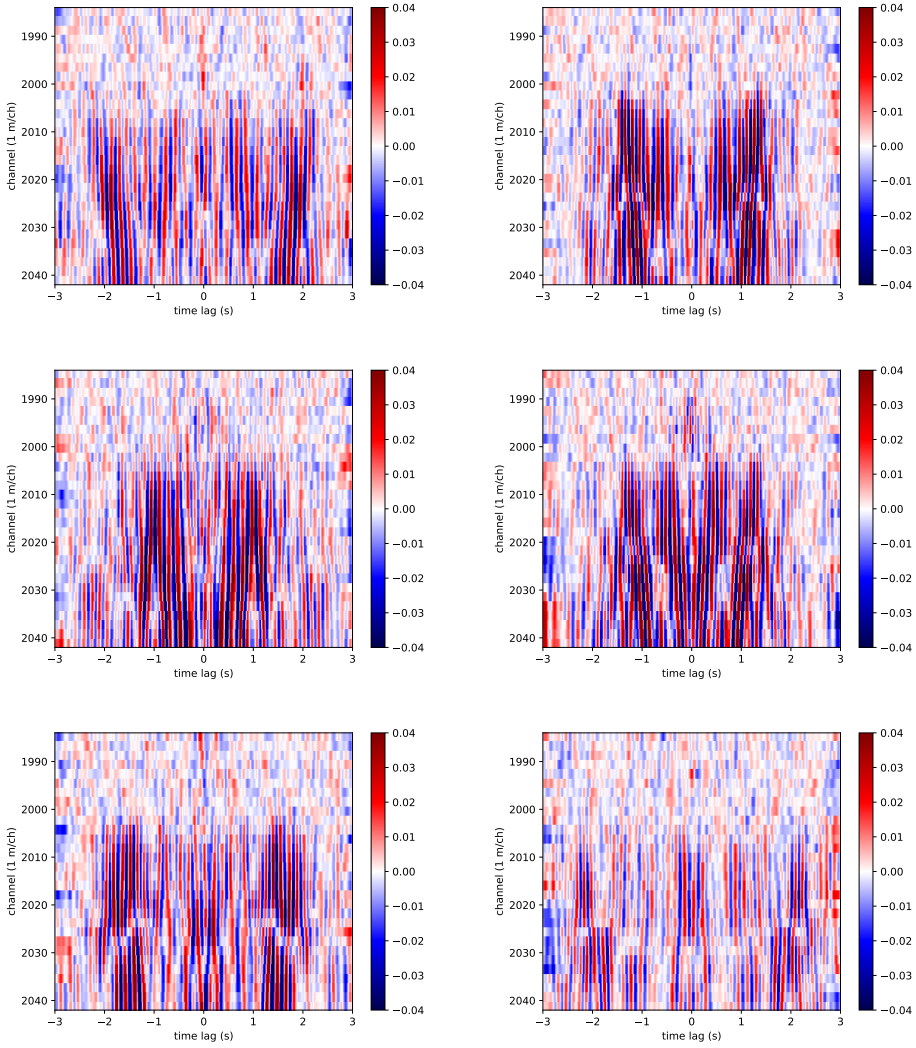

Figure 7.12: The noise correlation function average on August 6 is shown between virtual sources along the roadside line with the entirety of line 1: (top left) channel 3080, (top right) 3140, (middle left) 3210 which is close to line 1, (middle right) 3265, (bottom left) 3330, (bottom right) 3390. At very far offsets (channel 3390) the signal is too weak to pick, at far offsets (channels 3080 and 3330) amplitudes are slightly stronger and there is some signal that can be picked but a great deal of energy spread close to 0 arrival time. As offsets get closer (channels 3140 and 3265) the signals get stronger and there may even be two distinct events that can be picked. At very close offsets (channel 3210) the waveforms are much less compact although amplitudes are still high. Here, NCFs are bandpassed from 0.5-8 Hz. **CR**

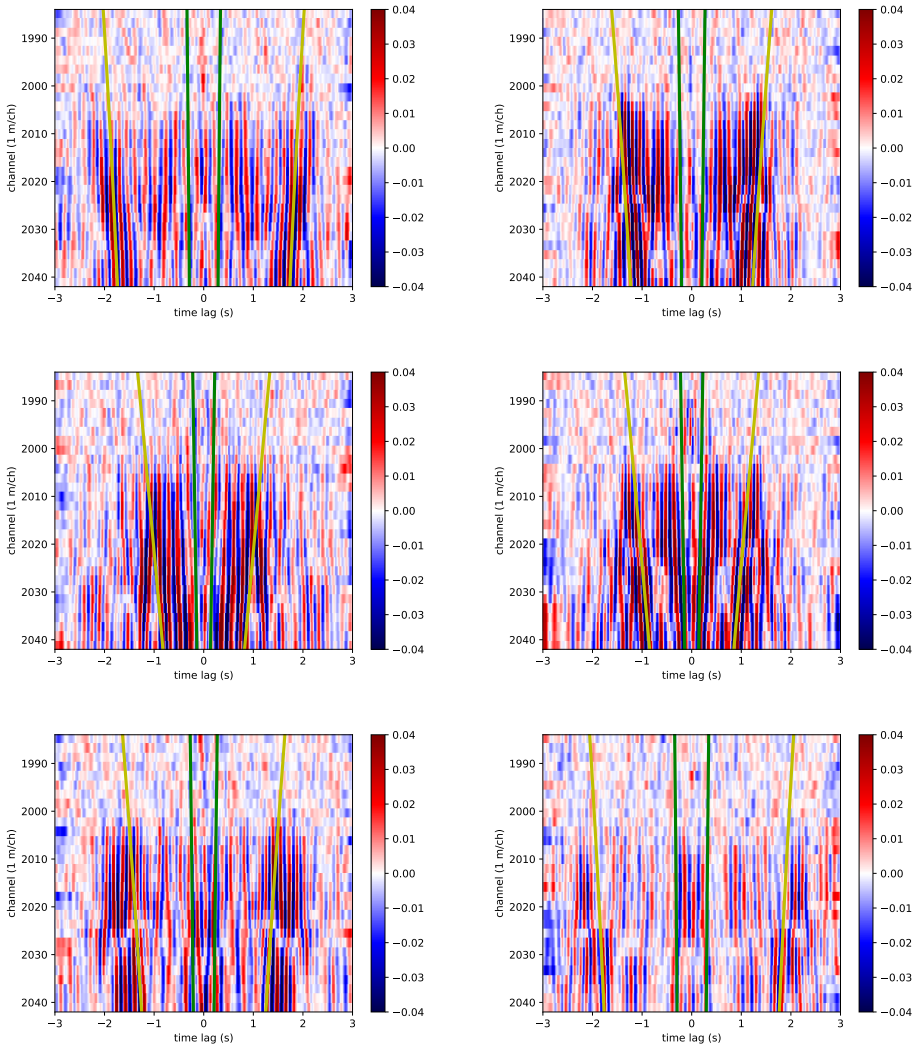

Figure 7.13: The same plots as in Figure 7.12: the noise correlation function average on August 6 between virtual sources along the roadside line with the entirety of line 1: (top left) channel 3080, (top right) 3140, (middle left) 3210 which is close to line 1, (middle right) 3265, (bottom left) 3330, (bottom right) 3390. Most gathers show one fast arrival and one slow arrival, which I have overlaid with the expected arrival times of 600 m/s waves (green) and 100 m/s waves (yellow). **CR**

7.2.3 Convergence of cross-coherences

Before interpreting results of ambient noise interferometry, it is important to understand the convergence of (virtual source, receiver) pairs. Previously it was shown using the same interrogator unit at the Richmond Field Station that roughly 8 hours of data were needed to recover similar V_s distributions [21]. At the Fairbanks site, the parallel-line cross-correlations required roughly 16 hours of noise to yield converged signals [34]. Since ambient noise interferometry signals between orthogonal lines may be weaker at some offsets than parallel lines, I tested the convergence of cross-coherences between many orthogonal pairs of receivers over full days (typically 24 hours, but some days have breaks in the data). I did not test windows longer than 1 day because it is possible some parts of the subsurface may show thaw changes at the scale of a day. There is a trade-off in temporal resolution and convergence that must be made.

In Figure 7.14, I plot cross-coherences adding increasingly more data for receivers 2004 and 3290 (a pair that crosses the heating plot with 2004 on the eastern side of line 1 and 3290 along the roadside line), as well as for receivers 2034 and 3250 (a pair that does not cross the heating plot with 2034 on the western side of line 1 and 3250 along the roadside line). The 2004-3290 pair does not have any clear signal even after a full day of recording before the thaw, but after the thaw it has a few arrivals that can be clearly picked from the same length of recording. The 2034-3250 pair are closer together, and have a strong signal before the thaw, although after the thaw the wavelets at a couple of arrivals become much sharper so it is easier to pick their arrival times. Most (virtual source, receiver) pairs exhibited the trend of clearer, more focused signals or required less recording time to converge to a clear signal after the thaw took place. This trend continues even when using virtual sources within the observation grid on line A. While the 2004-3290 pair has a more intense change after the thaw, it is interesting that 2034-3250 has a noticeable change despite not crossing the heating plot. Given the high velocity contrast between thawed and frozen permafrost, it is possible there could be enough energy scattering off the heating plot to affect receiver pairs whose straight-ray paths do not cross the plot. Further modeling is needed to determine whether the changes seen in 2034-3250 could be explained by increased scattering off a low velocity anomaly at the heater plot.

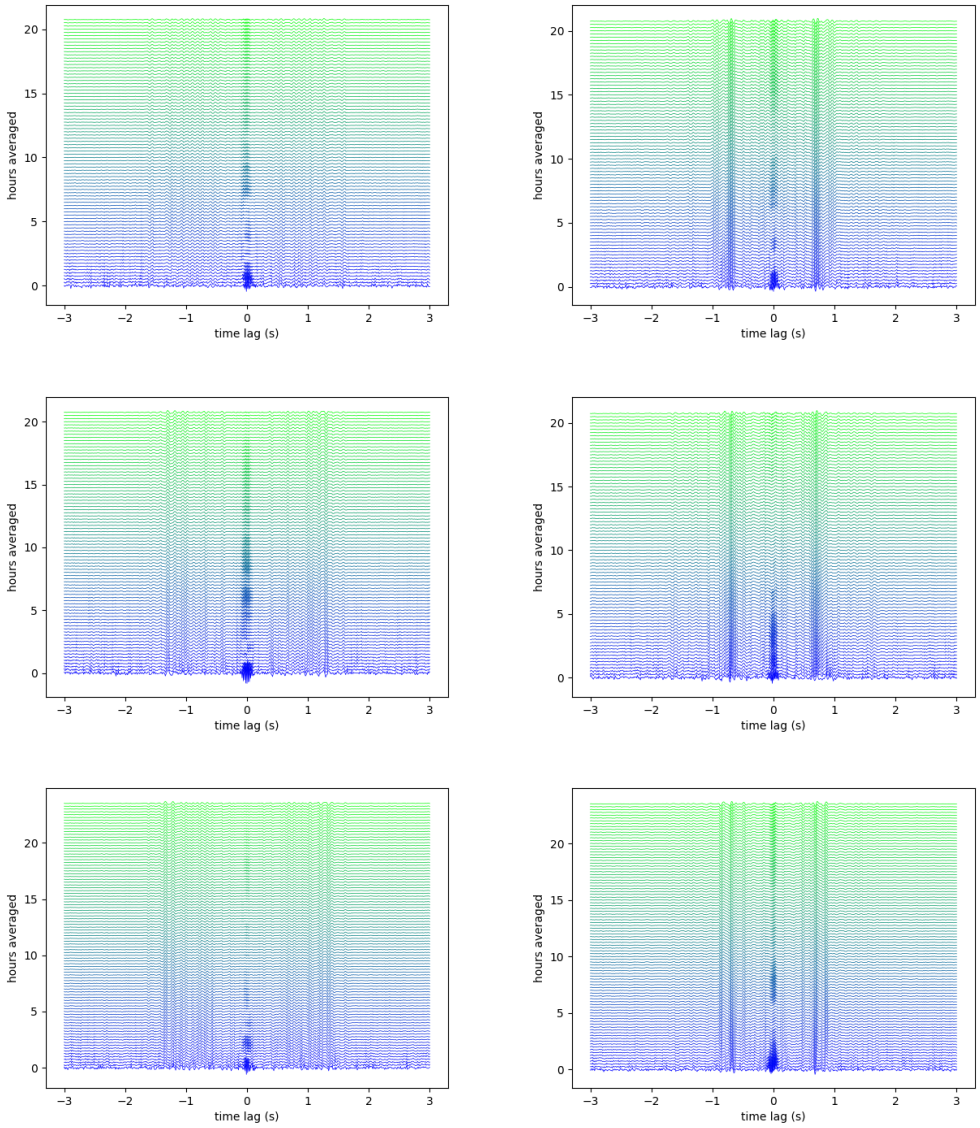

Figure 7.14: These plots show the cross-coherence averaged over increasingly longer windows between receiver (left) 2004 on the eastern side of line 1 with receiver 3290 on the roadside line and (right) between 2034 on the western side of line 1 with 3250 on the roadside line (top) August 6, (middle) September 3, (bottom) October 1. All amplitudes are relative, normalized so the average peak amplitude for any day and pair would be the same size. Previous days are not averaged into later days, so blue wiggles have just 15 minutes of data used, and green wiggles have a full day of data used. **CR**

As in Chapter 5, I calculated the correlation coefficient between short-term cross-coherence averages and long-term averages over a full day. The results for a single source gather with a source on the roadside line and receivers along line 1 are shown in Figure 7.15 for August 8, September 3, and October 1 for all windows of 1, 2, 4, and 8 hours. A value of 1 indicates that the cross-coherence for that receiver pair in that time window is the same (up to a scale factor) as the full-day average of that cross-coherence for that receiver pair. There is a dip in the correlation coefficient during windows primarily between 9:00 and 15:00 UTC due to daily variation in traffic patterns. On all days, the correlation coefficients are particularly low on the eastern side of line 1 (channels 1984 to 2005). These receivers are particularly important because many of the receivers with ray paths likely to cross the heater plot are in this section. Over the course of the thaw experiment there is some improvement in the correlation coefficients between 1994 and 2005. This trend holds true also when comparing short and long-term cross-coherences with virtual sources closer to the receivers on line A. These results justify the use of all data collected in a day.

7.2.4 Time-lapse changes

To understand changes in the extracted signals over time, I calculated the cross-coherences on every fourth day between the roadside line and all road-orthogonal lines, as well as line A (which is road-parallel) with all road-orthogonal lines. An example of one virtual source gather, channel 3290 with receivers along line 1 is shown in Figure 7.17. Just as the correlation coefficients for channels 1994 to 2005 improved as the thaw progressed in Figure 7.15, these gathers show stronger sharper peaks. These gathers have two clear events, one that starts on the west side close to 0 seconds, and one that starts on the west wide around ± 1 second. The earlier arriving event gets significantly more coherent over time. Further, there appears to be an even later event that starts around channel 2015 and travels to the west, arriving at channel 2043 at roughly ± 2 seconds. The changes between the days shown in the plot are gradual, so it is likely that these changes are due near-surface velocity changes (as opposed to diurnal or weekday/weekend ambient noise source distribution changes).

To better view these changes, I plot the daily cross-coherences between channel 3290 and two of the channels in the eastern half of line 1 in Figure 7.18. These cross-coherences

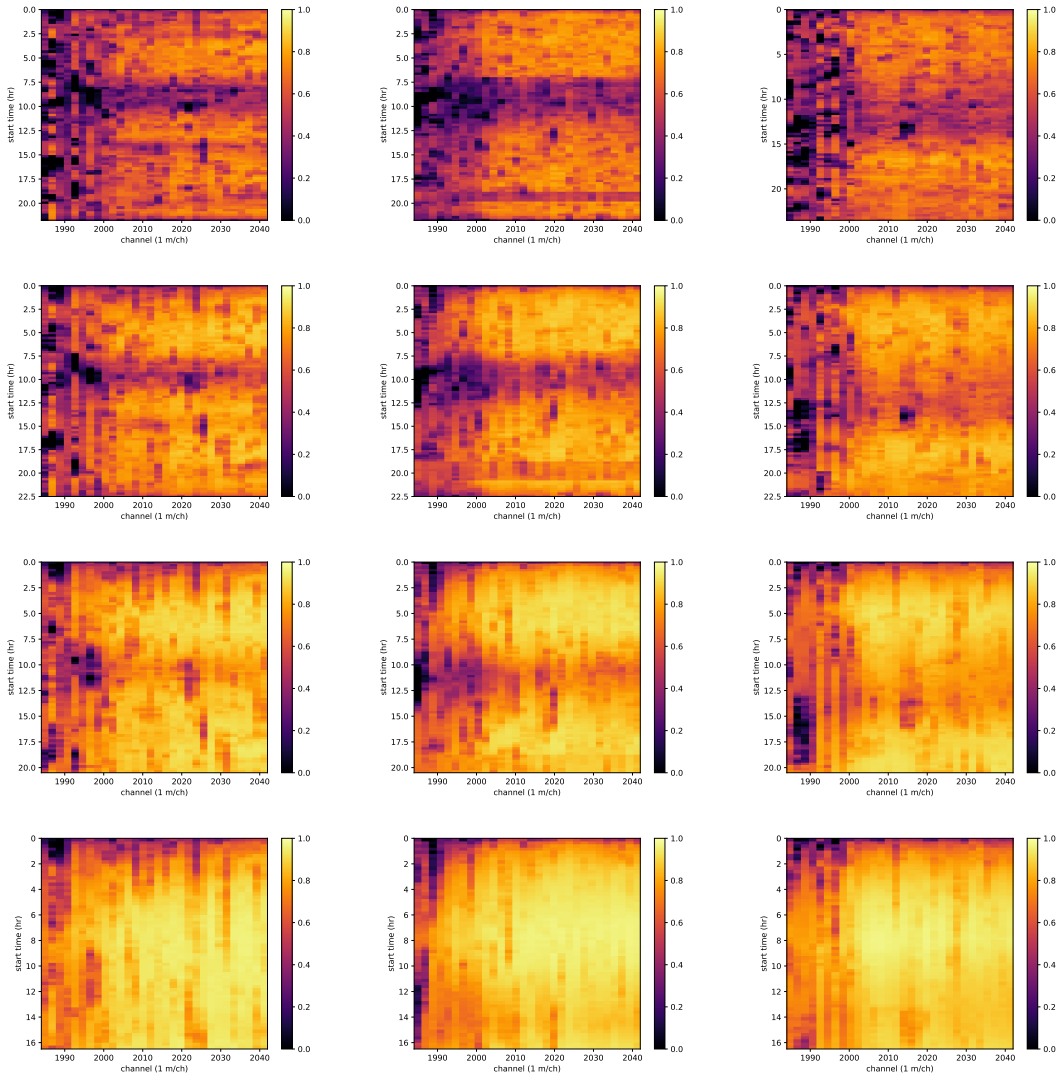

Figure 7.15: For the cross-coherence of each receiver in line 1 with receiver 3290 on the roadside line, I stacked over each consecutive window of (top) 1 hour, (2nd row)2 hours, (3rd row) 4 hours, and (bottom) 8 hours, then calculated the correlation coefficient (normalized dot product) between the short-time cross-coherence average and the full-day cross-coherence average. I repeated this exercise on (left) August 6, (middle) September 3, and (right) October 1. **CR**

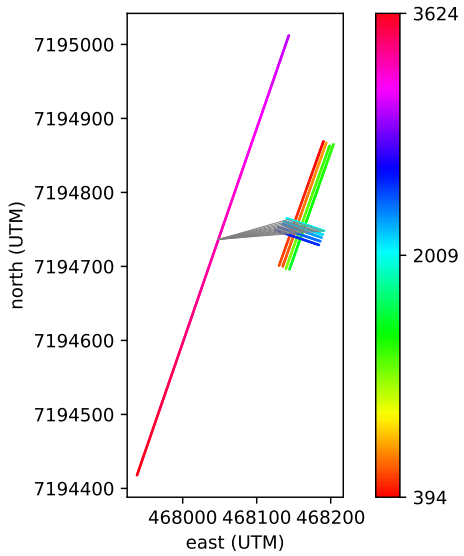

Figure 7.16: Each channel's location in the roadside line and grid is plotted with a marker colored according to its channel number in the data. Ray paths of a subset of the (virtual source, receiver) pairs included in Figure 7.17 are denoted with gray lines. Line 1 is the northern-most road-orthogonal line. Most of the ray paths with receivers in the eastern half of line 1 cross the heater plot, while the rays in the western half do not. **CR**

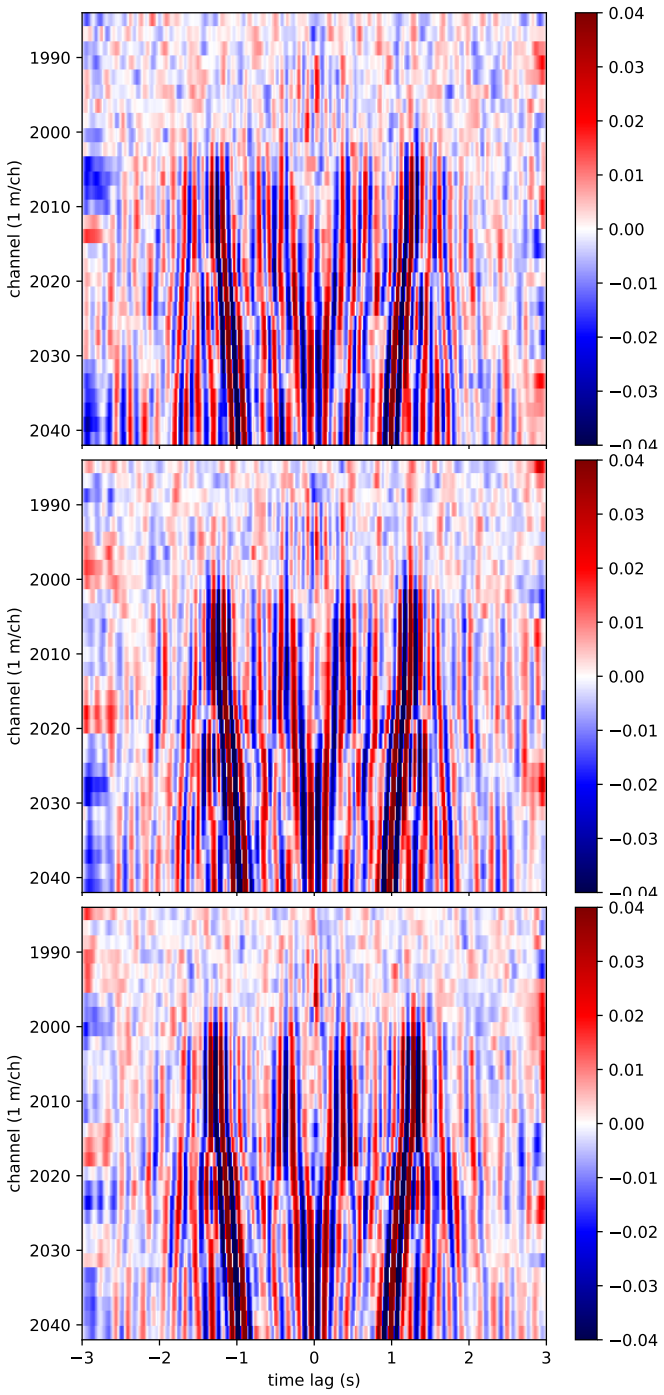

Figure 7.17: Daily cross-coherences between receiver 3290 on the roadside line with line 1 show significant change from (top) August 8 to (middle) September 3 to (bottom) October 1, particularly east of channel 2035 (channels in or east of the thaw plot). **CR**

show the development of a stronger early arrival event(about 1/4 second time-lag), a sharper peak around 1 second time lag, and a stronger late event just after 2 seconds time lag. There are not clear arrival-time shifts in either of these plots for any phase, but the formation of clearer signals with more defined peaks is visible.

While the longer offsets between the roadside line and the lines in the grid make different phases easier to pick, they may not be available in all installations. Thus, I also wondered whether orthogonal channels at shorter offsets, less than 150 meters, could yield any indication of subsurface change. I calculated the cross-coherence of channels on line A with line 1, and one example of a virtual source gather can be seen in Figure 7.20. There is a great deal of energy close to 0 time lag on channels 2020-2025 because this is where the two lines cross. However, there are also later arrivals, energy around ± 1 second on these channels which appears to travel away from the eastern side of line 1. It is surprising that these later signals are quite clear, as the signal expected based on the laterally homogeneous velocity model in Chapter 2 would be that these channels should have no clear signal to pick. One signal becomes particularly weak as the thaw progresses: the arrival around ±1.2 seconds around channel 2040. As the thaw progresses, the wavelets in this case actually get more spread out (the opposite behavior as what was observed between line 1 and the roadside line). However, like the line 1 to roadside line correlations, the signals between channels 1994 and 2005 become stronger as the thaw progresses.

7.2.5 Conclusions

These tests show that strong signals can be obtained from ambient noise interferometry of orthogonal lines, even at relatively short offsets. It appears that a day of data is sufficient to obtain a converged noise correlation function for many (virtual source, receiver) pairs. Some days show signals that are are clearer than others, and in particular, most noise correlation functions show sharper, more compact peaks as the thaw progresses. These orthogonal line noise-correlation functions do show significant changes throughout the thaw process at both short and long offset signals, but I did not locate a clear peak signal to pick that shows clear velocity change consistently across all channel pairs with ray paths crossing the heater plot.

Some of the events in the noise correlation functions, particularly just after the later

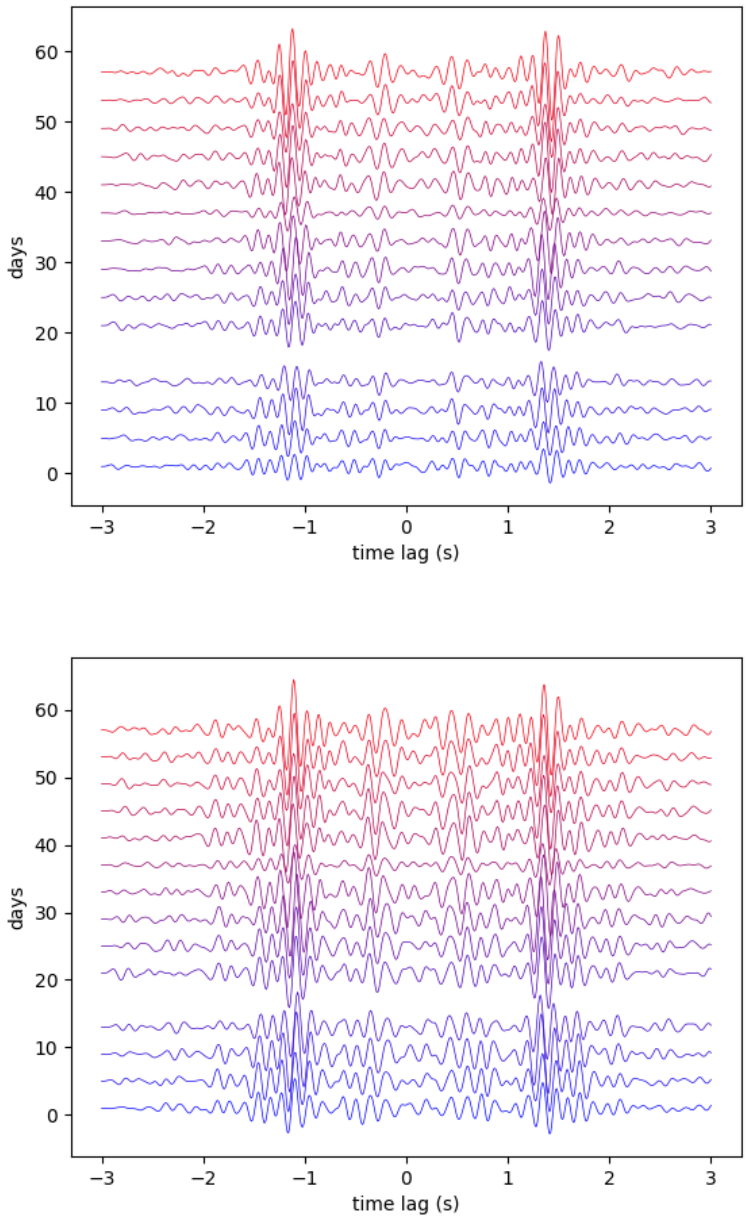

Figure 7.18: These plots show cross-coherences every four days from Figure 7.17 of channel 3290 with (top) channel 2004, and (bottom) channel 2014. The cross-coherences span August 8 (blue) through October 1 (red). **CR**

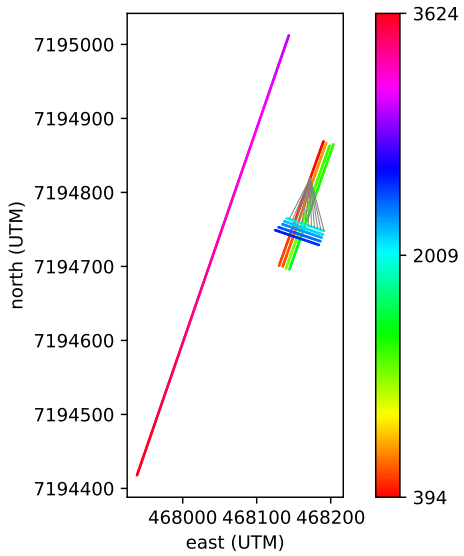

Figure 7.19: Each channel's location in the roadside line and grid is plotted with a marker colored according to its channel number in the data. Ray paths of a subset of the (virtual source, receiver) pairs included in Figure 7.20 are denoted with gray lines. Line 5 is the southern-most road-orthogonal line, and line A is the western-most road-parallel line within the grid. **CR**

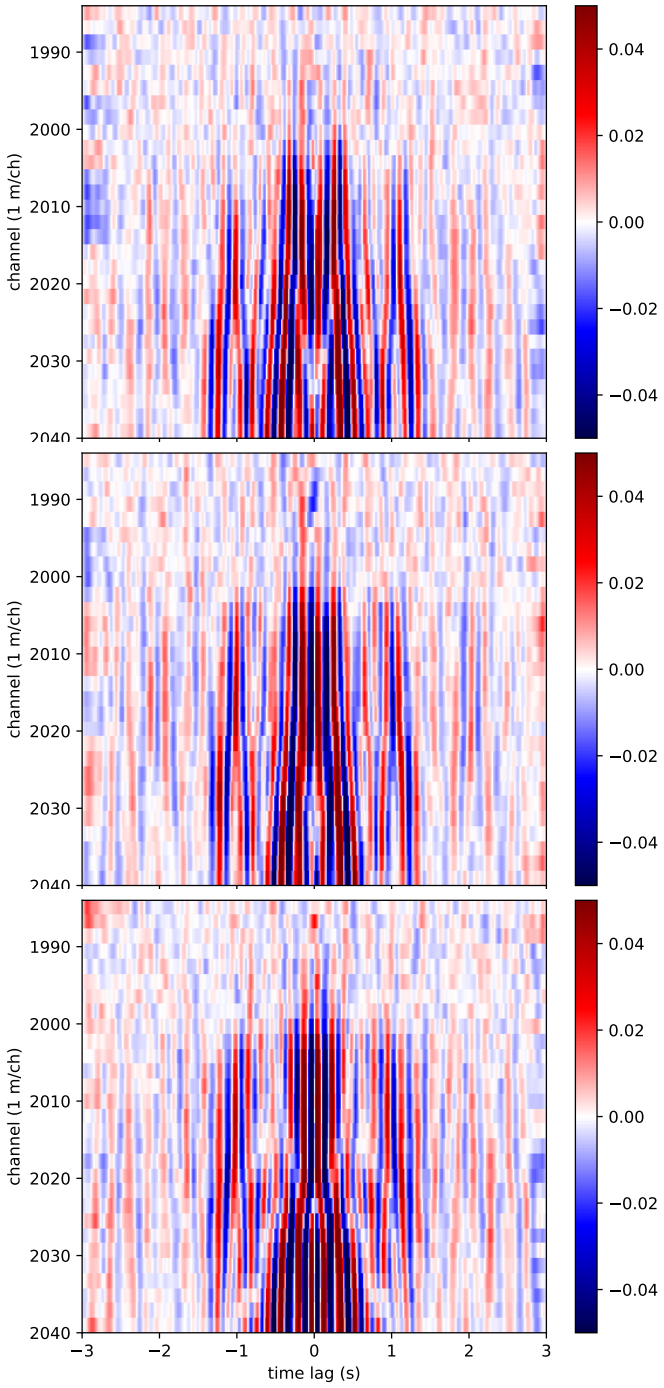

Figure 7.20: Daily cross-coherences between receiver 443 on line A, which is parallel to the road but in the grid, with line 1 show significant change from (top) August 8 before thaw to (middle) September 3 to (bottom) October 1 after thaw. **CR**

100 m/s arrivals, may be related to waves scattering at high-contrast velocity changes. Orthogonal cross-coherences are somewhat analogous to radial-transverse cross-coherences of 3C geophones, which would be expected to emphasize energy scattered between Rayleigh and Love wave motion, so it is not totally unexpected that orthogonal lines would emphasize scattered energy more than parallel line noise correlation functions would. The question of investigating the cause of these late arrivals deserves further modeling to understand expected features in the noise correlation functions during and after thaw. Further work will include combining these results with the changes observed in parallel-line noise correlation functions [34].

Appendix A

Review of particle velocity and strain rate rotations

Most seismologists do not use strain measurements, so here, I provide a brief review of the basics of working with particle velocity and strain rate measurements in rotated coordinate systems. Particle velocity is a vector quantity, $\dot{\mathbf{u}}$, meaning that if one wants to rotate their observation coordinate system counter-clockwise by an angle θ around the z-axis from (x, y, z) to (x', y', z') (for instance, by rotating a 3C geophone's two horizontal components), the particle velocity vector observed in that rotated coordinate system, $\dot{\mathbf{u}}'$, is calculated by applying a single rotation matrix, R:

$$\dot{\mathbf{u}}' = \begin{bmatrix} \dot{u}'_x \\ \dot{u}'_y \\ \dot{u}'_z \end{bmatrix} = \begin{bmatrix} C_\theta & \mathcal{S}_\theta & 0 \\ -\mathcal{S}_\theta & C_\theta & 0 \\ 0 & 0 & 1 \end{bmatrix} \begin{bmatrix} \dot{u}_x \\ \dot{u}_y \\ \dot{u}_z \end{bmatrix} = R\dot{\mathbf{u}} \tag{A.1}$$

using the short notation $C_{|theta} = \cos(\theta)$ and $\mathcal{S}_\theta = \sin(\theta)$. However, strain rate is a tensor quantity, so any strain rate measurements observed in a rotated coordinate system actually behave differently than particle velocity. Here, I show how that difference crops up for axial strain rate measurements. As a reminder, using the notation that $\nabla = \left(\partial_x, \partial_y, \partial_z\right)^T$ (so ∇ is a column vector), and writing out the definition of our strain rate tensor, it is described in

terms of ∇ and $\dot{\mathbf{u}}$:

$$\begin{aligned}
\dot{\Sigma} &= \begin{bmatrix} \dot{\sigma}_{xx} & \dot{\sigma}_{xy} & \dot{\sigma}_{xz} \\ \dot{\sigma}_{xy} & \dot{\sigma}_{yy} & \dot{\sigma}_{yz} \\ \dot{\sigma}_{xz} & \dot{\sigma}_{yz} & \dot{\sigma}_{zz} \end{bmatrix} \\
&= \begin{bmatrix} \frac{\partial \dot{u}_x}{\partial x} & \frac{1}{2}\left(\frac{\partial \dot{u}_x}{\partial y} + \frac{\partial \dot{u}_y}{\partial x}\right) & \frac{1}{2}\left(\frac{\partial \dot{u}_x}{\partial z} + \frac{\partial \dot{u}_z}{\partial x}\right) \\ \frac{1}{2}\left(\frac{\partial \dot{u}_x}{\partial y} + \frac{\partial \dot{u}_y}{\partial x}\right) & \frac{\partial \dot{u}_y}{\partial y} & \frac{1}{2}\left(\frac{\partial \dot{u}_y}{\partial z} + \frac{\partial \dot{u}_z}{\partial y}\right) \\ \frac{1}{2}\left(\frac{\partial \dot{u}_x}{\partial z} + \frac{\partial \dot{u}_z}{\partial x}\right) & \frac{1}{2}\left(\frac{\partial \dot{u}_y}{\partial z} + \frac{\partial \dot{u}_z}{\partial y}\right) & \frac{\partial \dot{u}_z}{\partial z} \end{bmatrix} \\
&= \frac{1}{2}\left(\nabla \dot{\mathbf{u}}^T + (\nabla \dot{\mathbf{u}}^T)^T\right)
\end{aligned} \tag{A.2}$$

Now look at $\dot{\Sigma}'$, the strain tensor as observed in that same rotated coordinate system as $\dot{\mathbf{u}}'$. First, note that by taking derivatives in a rotated (denoted by ') coordinate system, $\nabla' = \left(\partial_{x'}, \partial_{y'}, \partial_{z'}\right)^T = R\nabla$. I start with the definition of the strain rate in the rotated coordinate system, similar to Equation A.2, then plug in the rotated expressions for ∇' and $\dot{\mathbf{u}}'$:

$$\begin{aligned}
\dot{\Sigma}' &= \frac{1}{2}\left(\nabla' \dot{\mathbf{u}}'^T + (\nabla' \dot{\mathbf{u}}'^T)^T\right) \\
&= \frac{1}{2}\left((R\nabla)(R\dot{\mathbf{u}})^T + ((R\nabla)(R\dot{\mathbf{u}})^T)^T\right) \\
&= R^T \frac{1}{2}\left(\nabla \dot{\mathbf{u}}^T + (\nabla \dot{\mathbf{u}}^T)^T\right) R \\
&= R\dot{\Sigma}R^T
\end{aligned} \tag{A.3}$$

so the strain rate tensor in the rotated coordinate system is just the strain rate tensor in the original coordinate system with a rotation matrix and its transpose applied to either side. Expanding out Equation A.3, one can see how each term of the rotated strain rate tensor can be expressed from the matrix multiplication:

$$\dot{\Sigma}' = \begin{bmatrix} \dot{\sigma}_{x'x'} & \dot{\sigma}_{x'y'} & \dot{\sigma}_{x'z'} \\ \dot{\sigma}_{x'y'} & \dot{\sigma}_{y'y'} & \dot{\sigma}_{y'z'} \\ \dot{\sigma}_{x'z'} & \dot{\sigma}_{y'z'} & \dot{\sigma}_{z'z'} \end{bmatrix} = \begin{bmatrix} C_\theta & \mathcal{S}_\theta & 0 \\ -\mathcal{S}_\theta & C_\theta & 0 \\ 0 & 0 & 1 \end{bmatrix} \begin{bmatrix} \dot{\sigma}_{xx} & \dot{\sigma}_{xy} & \dot{\sigma}_{xz} \\ \dot{\sigma}_{xy} & \dot{\sigma}_{yy} & \dot{\sigma}_{yz} \\ \dot{\sigma}_{xz} & \dot{\sigma}_{yz} & \dot{\sigma}_{zz} \end{bmatrix} \begin{bmatrix} C_\theta & -\mathcal{S}_\theta & 0 \\ \mathcal{S}_\theta & C_\theta & 0 \\ 0 & 0 & 1 \end{bmatrix} \tag{A.4}$$

The particular term of interest is $\dot{\sigma}_{x'x'}$ because it is the point-wise axial strain rate that would be detected by a fiber oriented in the direction $(C_\theta, S_\theta, 0)$ if the fiber interrogator unit could return an infinitely small gauge length measurement. Expanding out the top-left term of Equation A.4, the axial strain rate can be expressed in terms of strains observed the original $x - y$ coordinate system as:

$$\dot{\sigma}_{x'x'} = \begin{bmatrix} C_\theta & S_\theta & 0 \end{bmatrix} \begin{bmatrix} \dot{\sigma}_{xx} & \dot{\sigma}_{xy} & \dot{\sigma}_{xz} \\ \dot{\sigma}_{xy} & \dot{\sigma}_{yy} & \dot{\sigma}_{yz} \\ \dot{\sigma}_{xz} & \dot{\sigma}_{yz} & \dot{\sigma}_{zz} \end{bmatrix} \begin{bmatrix} C_\theta \\ S_\theta \\ 0 \end{bmatrix} = C_\theta^2 \dot{\sigma}_{xx} + 2C_\theta S_\theta \dot{\sigma}_{xy} + S_\theta^2 \dot{\sigma}_{yy} \quad \text{(A.5)}$$

As shorthand for this, I use the notation $\dot{\sigma}_\theta := \dot{\sigma}_{x'x'}$ throughout this thesis.

Appendix B

Deriving responses to plane waves

In this appendix, I investigate the response of several types of idealized sensors to plane waves of multiple types: Rayleigh, Love, P, SH and SV. We are interested in the response of an idealized geophone (that measures exact particle velocity response at all frequencies), a point-wise axial strain rate measurement in some horizontal direction, and an average axial strain rate measurement over a line segment of length g (the gauge length).

For each type of wave, I start with a displacement expression from [55], although I generalize the starting displacement expressions so that the plane wave propagation direction is not restricted to the $x-z$ plane. Thus, I can assume any fixed horizontal sensor orientation, θ, then consider the response of that sensor to signals approaching the sensor from different angles (ϕ for surface waves, or ϕ_1, ϕ_2 for body waves). Starting with those displacements, I derive the following responses for each type of wave:

1. Take a time derivative for 3D particle velocities $\dot{\mathbf{u}} = (\dot{u}_x, \dot{u}_y, \dot{u}_z)$, summarized in Table 2.1.

2. Applying a single rotation matrix to $\dot{\mathbf{u}}$ yields the particle velocity $\dot{u}_\theta$ as detected by a geophone in the $(\cos(\theta), \sin(\theta), 0)$ direction. These results are summarized in Table 2.2

3. I calculate horizontal spatial derivatives of $\dot{\mathbf{u}}$ then plug them into Equation A.5 to calculate the pointwise axial strain rate in the $(\cos(\theta), \sin(\theta), 0)$ direction, $\dot{\sigma}_\theta$. These results are summarized in Table 2.2.

4. Averaging $\dot{\sigma}_\theta$ over a horizontal line segment of length g, the gauge length, yields $\dot{\sigma}_{\theta,g}$, which mimics a DAS signal in the same location in the direction $(\cos(\theta), \sin(\theta), 0)$. These results are summarized in Table 2.2.

5. I verify that $\lim_{k\to 0} \frac{\dot{\sigma}_{\theta,g}}{\dot{\sigma}_\theta} = 1$, i.e. at long wavelengths, the average strain rate over a fixed gauge length acts like a point-wise axial strain rate measurement in the same direction.

6. I calculate the cross-correlation of two horizontal particle velocity measurements, $\dot{u}_{\theta_1}(x_1, y_1, z)$ and $\dot{u}_{\theta_2}(x_2, y_2, z)$, simultaneously recording the same plane wave. These results are summarized in Table 2.3.

7. I calculate the cross-correlation of two horizontal point-wise axial strain rate measurements, $\dot{\sigma}_{\theta_1}(x_1, y_1, z)$ and $\dot{\sigma}_{\theta_2}(x_2, y_2, z)$, simultaneously recording the same plane wave. These results are summarized in Table 2.3.

8. I calculate the cross-correlation of two horizontal average axial strain rate measurements over a gauge length, $\dot{\sigma}_{\theta_1,g}(x_1, y_1, z)$ and $\dot{\sigma}_{\theta_2,g}(x_2, y_2, z)$, simultaneously recording the same plane wave. These results are summarized in Table 2.3.

9. I verify that $\lim_{k\to 0} \frac{\dot{\sigma}_{\theta_1,g}(x_1,y_1,z) \star \dot{\sigma}_{\theta_2,g}(x_2,y_2,z)}{\dot{\sigma}_{\theta_1}(x_1,y_1,z) \star \dot{\sigma}_{\theta_2}(x_2,y_2,z)} = 1$, verifying that the behavior of interferometry of DAS measurements is the same as interferometry of point-wise axial strain rate measurements at long wavelengths.

B.1 Rayleigh waves

1. Take a time derivative for 3D particle velocities $\dot{\mathbf{u}} = (\dot{u}_x, \dot{u}_y, \dot{u}_z)$

$$\begin{aligned}
\ddot{\mathbf{u}} &= \partial_t \left[\left(C_\phi (A e^{-\gamma_\alpha k z} + iB\gamma_\beta e^{-\gamma_\beta k z}), \mathcal{S}_\phi (A e^{-\gamma_\alpha k z} + iB\gamma_\beta e^{-\gamma_\beta k z}), \dots \right. \right. \\
&\quad \left. \left. -i\gamma_\alpha A e^{-\gamma_\alpha k z} + B e^{-\gamma_\beta k z} \right) e^{ik(ct - xC_\phi - y\mathcal{S}_\phi)} \right] \\
&= \left(C_\phi (A e^{-\gamma_\alpha k z} + iB\gamma_\beta e^{-\gamma_\beta k z}), \mathcal{S}_\phi (A e^{-\gamma_\alpha k z} + iB\gamma_\beta e^{-\gamma_\beta k z}), \dots \right. \\
&\quad \left. -i\gamma_\alpha A e^{-\gamma_\alpha k z} + B e^{-\gamma_\beta k z} \right) \partial_t e^{ik(ct - xC_\phi - y\mathcal{S}_\phi)} \\
&= \left(C_\phi (A e^{-\gamma_\alpha k z} + iB\gamma_\beta e^{-\gamma_\beta k z}), \mathcal{S}_\phi (A e^{-\gamma_\alpha k z} + iB\gamma_\beta e^{-\gamma_\beta k z}), \dots \right. \\
&\quad \left. -i\gamma_\alpha A e^{-\gamma_\alpha k z} + B e^{-\gamma_\beta k z} \right) ikc e^{ik(ct - xC_\phi - y\mathcal{S}_\phi)}
\end{aligned}$$

2. By applying a single rotation matrix to $\dot{\mathbf{u}}$ we can calculate the particle velocity $\dot{u}_\theta$ as detected by a geophone in the in the $(\cos(\theta), \sin(\theta), 0)$ direction.

$$\begin{aligned}
\dot{u}_\theta &= C_\theta \dot{u}_x + \mathcal{S}_\theta \dot{u}_y \\
&= ikc(A e^{-\gamma_\alpha k z} + iB e^{-\gamma_\beta k z}) \left(C_\theta C_\phi + \mathcal{S}_\theta \mathcal{S}_\phi \right) e^{ik(ct - xC_\phi - y\mathcal{S}_\phi)} \\
&= ikc(A e^{-\gamma_\alpha k z} + iB e^{-\gamma_\beta k z}) C_{(\phi-\theta)} e^{ik(ct - xC_\phi - y\mathcal{S}_\phi)} \qquad \text{(B.1)}
\end{aligned}$$

3. We calculate horizontal spatial derivatives of $\dot{\mathbf{u}}$ then plug them into Equation A.5 to calculate the pointwise axial strain rate in the $(\cos(\theta), \sin(\theta), 0)$ direction, $\dot{\sigma}_\theta$.

$$
\begin{aligned}
\frac{\partial \dot{u}_x}{\partial x} &= C_\phi (A e^{-\gamma_\alpha k z} + iB\gamma_\beta e^{-\gamma_\beta k z}) ikc e^{ik(ct - xC_\phi - y\mathcal{S}_\phi)}(-ikC_\phi) \\
&= k^2 c C_\phi^2 (A e^{-\gamma_\alpha k z} + iB\gamma_\beta e^{-\gamma_\beta k z}) e^{ik(ct - xC_\phi - y\mathcal{S}_\phi)} \\
\frac{\partial \dot{u}_y}{\partial x} &= \mathcal{S}_\phi (A e^{-\gamma_\alpha k z} + iB\gamma_\beta e^{-\gamma_\beta k z}) ikc e^{ik(ct - xC_\phi - y\mathcal{S}_\phi)}(-ikC_\phi) \\
&= \frac{k^2 c}{2} \mathcal{S}_{2\phi} (A e^{-\gamma_\alpha k z} + iB\gamma_\beta e^{-\gamma_\beta k z}) e^{ik(ct - xC_\phi - y\mathcal{S}_\phi)} \\
\frac{\partial \dot{u}_x}{\partial y} &= C_\phi (A e^{-\gamma_\alpha k z} + iB\gamma_\beta e^{-\gamma_\beta k z}) ikc e^{ik(ct - xC_\phi - y\mathcal{S}_\phi)}(-ik\mathcal{S}_\phi) \\
&= \frac{k^2 c}{2} \mathcal{S}_{2\phi} (A e^{-\gamma_\alpha k z} + iB\gamma_\beta e^{-\gamma_\beta k z}) e^{ik(ct - xC_\phi - y\mathcal{S}_\phi)} \\
\frac{\partial \dot{u}_y}{\partial y} &= \mathcal{S}_\phi (A e^{-\gamma_\alpha k z} + iB\gamma_\beta e^{-\gamma_\beta k z}) ikc e^{ik(ct - xC_\phi - y\mathcal{S}_\phi)}(-ik\mathcal{S}_\phi) \\
&= k^2 c \mathcal{S}_\phi^2 (A e^{-\gamma_\alpha k z} + iB\gamma_\beta e^{-\gamma_\beta k z}) e^{ik(ct - xC_\phi - y\mathcal{S}_\phi)}
\end{aligned} \tag{B.2}
$$

Now we can plug these in for the point-wise axial strain in the θ direction:

$$
\begin{aligned}
&= \dot{\sigma}_\theta(x, y, z, t) \\
&= C_\theta^2 \frac{\partial \dot{u}_x}{\partial x} + C_\theta \mathcal{S}_\theta \left(\frac{\partial \dot{u}_x}{\partial y} + \frac{\partial \dot{u}_y}{\partial x} \right) + \mathcal{S}_\theta^2 \frac{\partial \dot{u}_y}{\partial y} \\
&= k^2 c \left[C_\theta^2 C_\phi^2 + C_\theta \mathcal{S}_\theta \left(\frac{\mathcal{S}_{2\phi}}{2} + \frac{\mathcal{S}_{2\phi}}{2} \right) + \mathcal{S}_\theta^2 \mathcal{S}_\phi^2 \right] (A e^{-\gamma_\alpha k z} + iB\gamma_\beta e^{-\gamma_\beta k z}) o_{RL} \\
&= k^2 c (C_\theta C_\phi + \mathcal{S}_\theta \mathcal{S}_\phi)^2 (A e^{-\gamma_\alpha k z} + iB\gamma_\beta e^{-\gamma_\beta k z}) o_{RL} \\
&= k^2 c C_{(\phi-\theta)}^2 (A e^{-\gamma_\alpha k z} + iB\gamma_\beta e^{-\gamma_\beta k z}) o_{RL}
\end{aligned} \tag{B.3}
$$

4. We average $\dot{\sigma}_\theta$ over a horizontal line segment of length g, the gauge length, yielding $\dot{\sigma}_{\theta,g}$, which mimics a DAS signal in the same location in the direction $(\cos(\theta), \sin(\theta), 0)$.

$$
\begin{aligned}
\dot{\sigma}_{\theta,g}(x,y,z,t) &= \\
ck^2 C^2_{(\phi-\theta)} \left(Ae^{-\gamma_\alpha kz} + iB\gamma_\beta e^{-\gamma_\beta kz} \right) \frac{1}{g} \int_{-g/2}^{g/2} o_{RL}(x+\nu C_\theta, y+\nu \mathcal{S}_\theta, z, t) d\nu &= \\
\frac{ck^2}{g} C^2_{(\phi-\theta)} \left(Ae^{-\gamma_\alpha kz} + iB\gamma_\beta e^{-\gamma_\beta kz} \right) \int_{-g/2}^{g/2} e^{ik(ct-(x+\nu C_\theta)C_\phi-(y+\nu \mathcal{S}_\theta)\mathcal{S}_\phi)} d\nu &= \\
\frac{ck^2}{g} C^2_{(\phi-\theta)} \left(Ae^{-\gamma_\alpha kz} + iB\gamma_\beta e^{-\gamma_\beta kz} \right) e^{ik(ct-xC_\phi-y\mathcal{S}_\phi)} \int_{-g/2}^{g/2} e^{-ik\nu C_{(\phi-\theta)}} d\nu &= \\
\frac{ck^2}{g} C^2_{(\phi-\theta)} \left(Ae^{-\gamma_\alpha kz} + iB\gamma_\beta e^{-\gamma_\beta kz} \right) e^{ik(ct-xC_\phi-y\mathcal{S}_\phi)} \left[\frac{e^{-ik\nu C_{(\phi-\theta)}}}{-ikC_{(\phi-\theta)}} \right]_{-g/2}^{g/2} &= \\
-\frac{2ck}{g} C_{(\phi-\theta)} \left(Ae^{-\gamma_\alpha kz} + iB\gamma_\beta e^{-\gamma_\beta kz} \right) e^{ik(ct-xC_\phi-y\mathcal{S}_\phi)} \left[\frac{e^{-ik\nu C_{(\phi-\theta)}}}{2i} \right]_{-g/2}^{g/2} &= \\
-\frac{2ck}{g} C_{(\phi-\theta)} \left(Ae^{-\gamma_\alpha kz} + iB\gamma_\beta e^{-\gamma_\beta kz} \right) e^{ik(ct-xC_\phi-y\mathcal{S}_\phi)} \sin\left(\frac{-kgC_{\phi-\theta}}{2} \right) &=
\end{aligned}
$$

5. We verify that $\lim_{k\to 0} \frac{\dot{\sigma}_{\theta,g}}{\dot{\sigma}_\theta} = 1$, i.e. at long wavelengths, the average strain rate over a fixed gauge length acts like a point-wise axial strain rate measurement in the same direction. This requires the use of L'Hospital's rule:

$$\begin{aligned}
\lim_{k\to 0}\frac{\dot{\sigma}_{\theta,g}}{\dot{\sigma}_{\theta}} &= \lim_{k\to 0}\frac{-\frac{2ck}{g}C_{(\phi-\theta)}(Ae^{-\gamma_\alpha kz}+iB\gamma_\beta e^{-\gamma_\beta kz})e^{ik(ct-xC_\phi-yS_\phi)}\sin\left(\frac{-kg}{2}C_{(\phi-\theta)}\right)}{k^2cC^2_{(\phi-\theta)}(Ae^{-\gamma_\alpha kz}+iB\gamma_\beta e^{-\gamma_\beta kz})e^{ik(ct-xC_\phi-yS_\phi)}} \\
&= \lim_{k\to 0}\frac{-\frac{2}{g}\sin\left(\frac{-kg}{2}C_{(\phi-\theta)}\right)}{kC_{(\phi-\theta)}} \\
&= \frac{\lim_{k\to 0}-\frac{2}{g}\partial_k\sin\left(\frac{-kg}{2}C_{(\phi-\theta)}\right)}{\lim_{k\to 0}\partial_k kC_{(\phi-\theta)}} \\
&= \frac{\lim_{k\to 0}-\frac{2}{g}(-\frac{g}{2}C_{(\phi-\theta)})\cos\left(\frac{-kg}{2}C_{(\phi-\theta)}\right)}{\lim_{k\to 0}1\cdot C_{(\phi-\theta)}} \\
&= \frac{C_{(\phi-\theta)}}{C_{(\phi-\theta)}} \\
&= 1 \qquad \text{(B.4)}
\end{aligned}$$

6. We calculate the cross-correlation of two horizontal particle velocity measurements, $\dot{u}_{\theta_1}(x_1, y_1, z)$ and $\dot{u}_{\theta_2}(x_2, y_2, z)$, simultaneously recording the same plane wave.

$$\begin{aligned}
\frac{1}{2T}\int_{-T}^{T}\dot{u}_{\theta_1}(x_1,y_1,z,t)\dot{u}^*_{\theta_2}(x_2,y_2,z,t+\tau)d\tau &= \\
\frac{1}{2T}c^2k^2\int_{-T}^{T}C_{(\phi-\theta_1)}\left(Ae^{-\gamma_\alpha kz}+iB\gamma_\beta e^{-\gamma_\beta kz}\right)e^{ik(ct-x_1C_\phi-y_1S_\phi)}\ldots & \\
\ldots C_{(\phi-\theta_2)}\left(Ae^{-\gamma_\alpha kz}-iB\gamma_\beta e^{-\gamma_\beta kz}\right)e^{-ik(c(t+\tau)-x_2C_\phi-y_2S_\phi)}dt &= \\
\frac{1}{2T}c^2k^2C_{(\phi-\theta_1)}C_{(\phi-\theta_2)}\left(A^2e^{-2\gamma_\alpha kz}+B^2\gamma_\beta^2e^{-2\gamma_\beta kz}\right)e^{-ik(c\tau+(x_1-x_2)C_\phi+(y_1-y_2)S_\phi)}\int_{-T}^{T}dt &= \\
c^2k^2C_{(\phi-\theta_1)}C_{(\phi-\theta_2)}e^{-ik(c\tau+(x_1-x_2)C_\phi+(y_1-y_2)S_\phi)}\left(A^2e^{-2\gamma_\alpha kz}+B^2\gamma_\beta^2e^{-2\gamma_\beta kz}\right) &=
\end{aligned}$$

7. We calculate the cross-correlation of two horizontal point-wise axial strain rate measurements, $\dot{sigma}_{\theta_1}(x_1, y_1, z)$ and $\dot{sigma}_{\theta_2}(x_2, y_2, z)$, simultaneously recording the same plane wave.

$$
\begin{aligned}
\frac{1}{2T}\int_{-T}^{T}\dot{\sigma}_{\theta_1}(x_1,y_1,z,t)\dot{\sigma}^{*}_{\theta_2}(x_2,y_2,z,t+\tau)dt &= \\
\frac{1}{2T}c^2k^4C^2_{(\phi-\theta_1)}C^2_{(\phi-\theta_2)}\int_{-T}^{T}\left(Ae^{-\gamma_\alpha kz}+iB\gamma_\beta e^{-\gamma_\beta kz}\right)e^{ik(ct-x_1C_\phi-y_1S_\phi)}\ldots & \\
\ldots\left(Ae^{-\gamma_\alpha kz}-iB\gamma_\beta e^{-\gamma_\beta kz}\right)e^{-ik(c(t+\tau)-x_2C_\phi-y_2S_\phi)}dt &= \\
\frac{1}{2T}c^2k^4C^2_{(\phi-\theta_1)}C^2_{(\phi-\theta_2)}e^{-ik(c\tau-x_2C_\phi-y_2S_\phi)}e^{ik(-x_1C_\phi-y_1S_\phi)}\ldots & \\
\times\left(A^2e^{-2\gamma_\alpha kz}+B^2\gamma^2_\beta e^{-2\gamma_\beta kz}\right)\int_{-T}^{T}dt &= \\
c^2k^4C^2_{(\phi-\theta_1)}C^2_{(\phi-\theta_2)}e^{-ik(c\tau+(x_1-x_2)C_\phi+(y_1-y_2)S_\phi)}\left(A^2e^{-2\gamma_\alpha kz}+B^2\gamma^2_\beta e^{-2\gamma_\beta kz}\right) &=
\end{aligned}
$$

8. We calculate the cross-correlation of two horizontal average axial strain rate measurements over a gauge length, $\dot{\sigma}_{\theta_1,g}(x_1,y_1,z)$ and $\dot{sigma}_{\theta_2,g}(x_2,y_2,z)$, simultaneously recording the same plane wave.

$$\begin{aligned}
\frac{1}{2T}\int_{-T}^{T}\dot{\sigma}_{\theta_1,g}(x_1,y_1,z,t)\dot{\sigma}^{*}_{\theta_2,g}(x_2,y_2,z,t+\tau)dt &= \\
\frac{1}{2Tg^2}4c^2k^2C_{(\phi-\theta_1)}C_{(\phi-\theta_2)}\sin\left(\frac{-kgC_{(\phi-\theta_1)}}{2}\right)\sin\left(\frac{-kgC_{(\phi-\theta_2)}}{2}\right)\int_{-T}^{T}e^{ik(ct-x_1C_\phi-y_2S_\phi)}\dots & \\
\dots\left(Ae^{-\gamma_\alpha kz}+iB\gamma_\beta e^{-\gamma_\beta kz}\right)\left(Ae^{-\gamma_\alpha kz}-iB\gamma_\beta e^{-\gamma_\beta kz}\right)e^{-ik(c(t+\tau)-x_2C_\phi-y_2S_\phi)}dt &= \\
\frac{1}{2Tg^2}4c^2k^2C_{(\phi-\theta_1)}C_{(\phi-\theta_2)}\sin\left(\frac{-kgC_{(\phi-\theta_1)}}{2}\right)\sin\left(\frac{-kgC_{(\phi-\theta_2)}}{2}\right)\dots & \\
\dots\left(A^2e^{-2\gamma_\alpha kz}+B^2\gamma_\beta^2e^{-2\gamma_\beta kz}\right)\int_{-T}^{T}e^{ik(ct-x_1C_\phi-y_2S_\phi)}e^{-ik(c(t+\tau)-x_2C_\phi-y_2S_\phi)}dt &= \\
\frac{1}{2Tg^2}4c^2k^2C_{(\phi-\theta_1)}C_{(\phi-\theta_2)}\sin\left(\frac{-kgC_{(\phi-\theta_1)}}{2}\right)\sin\left(\frac{-kgC_{(\phi-\theta_2)}}{2}\right)\dots & \\
\dots\left(A^2e^{-2\gamma_\alpha kz}+B^2\gamma_\beta^2e^{-2\gamma_\beta kz}\right)e^{-ik(c\tau+(x_1-x_2)C_\phi+(y_1-y_2)S_\phi)}\int_{-T}^{T}dt &= \\
\frac{4c^2k^2}{g^2}C_{(\phi-\theta_1)}C_{(\phi-\theta_2)}\sin\left(\frac{-kgC_{(\phi-\theta_1)}}{2}\right)\sin\left(\frac{-kgC_{(\phi-\theta_2)}}{2}\right)\dots & \\
\dots e^{-ik(c\tau+(x_1-x_2)C_\phi+(y_1-y_2)S_\phi)}\left(A^2e^{-2\gamma_\alpha kz}+B^2\gamma_\beta^2e^{-2\gamma_\beta kz}\right) &=
\end{aligned}$$

9. We verify that $\lim_{k\to 0}\frac{\dot{\sigma}_{\theta_1,g}(x_1,y_1,z)\star\dot{\sigma}_{\theta_2,g}(x_2,y_2,z)}{\dot{\sigma}_{\theta_1}(x_1,y_1,z)\star\dot{\sigma}_{\theta_2}(x_2,y_2,z)}=1$, verifying that the behavior of interferometry of DAS measurements is the same as interferometry of point-wise axial strain rate measurements at long wavelengths. This requires two applications of L'Hospital's rule for indeterminate forms:

$$
\begin{aligned}
& \lim_{k\to 0} \frac{\dot{\sigma}_{\theta_1,g}(x_1,y_1,z) \star \dot{\sigma}_{\theta_2,g}(x_2,y_2,z)}{\dot{\sigma}_{\theta_1}(x_1,y_1,z) \star \dot{\sigma}_{\theta_2}(x_2,y_2,z)} \\
= & \lim_{k\to 0} \frac{\frac{4c^2k^2}{g^2} C_{(\phi-\theta_1)} C_{(\phi-\theta_2)} \sin\left(\frac{-kgC_{(\phi-\theta_1)}}{2}\right) \sin\left(\frac{-kgC_{(\phi-\theta_2)}}{2}\right) o^{\tau}_{RL} \left(A^2 e^{-2\gamma_\alpha kz} + B^2\gamma_\beta^2 e^{-2\gamma_\beta kz}\right)}{c^2k^4 C^2_{(\phi-\theta_1)} C^2_{(\phi-\theta_2)} o^{\tau}_{RL} \left(A^2 e^{-2\gamma_\alpha kz} + B^2\gamma_\beta^2 e^{-2\gamma_\beta kz}\right)} \\
= & \lim_{k\to 0} \frac{\frac{4}{g^2}\partial_k \left[\sin\left(\frac{-kgC_{(\phi-\theta_1)}}{2}\right) \sin\left(\frac{-kgC_{(\phi-\theta_2)}}{2}\right)\right]}{\partial_k(k^2) C_{(\phi-\theta_1)} C_{(\phi-\theta_2)}} \\
= & \lim_{k\to 0} \frac{\frac{4}{g^2}\frac{-gC_{(\phi-\theta_1)}}{2} \cos\left(\frac{-kgC_{(\phi-\theta_1)}}{2}\right) \sin\left(\frac{-kgC_{(\phi-\theta_2)}}{2}\right)}{2kC_{(\phi-\theta_1)} C_{(\phi-\theta_2)}} \cdots \\
& + \lim_{k\to 0} \frac{\frac{4}{g^2} \sin\left(\frac{-kgC_{(\phi-\theta_1)}}{2}\right) \frac{-gC_{(\phi-\theta_2)}}{2} \cos\left(\frac{-kgC_{(\phi-\theta_2)}}{2}\right)}{2kC_{(\phi-\theta_1)} C_{(\phi-\theta_2)}} \\
= & \lim_{k\to 0} \frac{-\frac{1}{g} C_{(\phi-\theta_1)} \cos\left(\frac{-kgC_{(\phi-\theta_1)}}{2}\right) \sin\left(\frac{-kgC_{(\phi-\theta_2)}}{2}\right)}{kC_{(\phi-\theta_1)} C_{(\phi-\theta_2)}} \cdots \\
& + \lim_{k\to 0} \frac{-\frac{1}{g} \sin\left(\frac{-kgC_{(\phi-\theta_1)}}{2}\right) C_{(\phi-\theta_2)} \cos\left(\frac{-kgC_{(\phi-\theta_2)}}{2}\right)}{kC_{(\phi-\theta_1)} C_{(\phi-\theta_2)}} \\
= & \lim_{k\to 0} \frac{-\frac{1}{g} C_{(\phi-\theta_1)} \partial_k \left[\cos\left(\frac{-kgC_{(\phi-\theta_1)}}{2}\right) \sin\left(\frac{-kgC_{(\phi-\theta_2)}}{2}\right)\right]}{\partial_k k C_{(\phi-\theta_1)} C_{(\phi-\theta_2)}} \cdots \\
& - \lim_{k\to 0} \frac{C_{(\phi-\theta_2)} \partial_k \left[\sin\left(\frac{-kgC_{(\phi-\theta_1)}}{2}\right) \cos\left(\frac{-kgC_{(\phi-\theta_2)}}{2}\right)\right]}{\partial_k k C_{(\phi-\theta_1)} C_{(\phi-\theta_2)}} \\
= & \lim_{k\to 0} \frac{C_{(\phi-\theta_1)} C_{(\phi-\theta_2)} \cos\left(\frac{-kgC_{(\phi-\theta_1)}}{2}\right) \cos\left(\frac{-kgC_{(\phi-\theta_2)}}{2}\right)}{C_{(\phi-\theta_1)} C_{(\phi-\theta_2)}} \cdots \\
& - \lim_{k\to 0} \frac{\frac{1}{2}(C^2_{(\phi-\theta_1)} + C^2_{(\phi-\theta_2)}) \sin\left(\frac{-kgC_{(\phi-\theta_1)}}{2}\right) \sin\left(\frac{-kgC_{(\phi-\theta_2)}}{2}\right)}{C_{(\phi-\theta_1)} C_{(\phi-\theta_2)}} \\
= & \frac{C_{(\phi-\theta_1)} C_{(\phi-\theta_2)} \cdot 1 \cdot 1 - 0}{C_{(\phi-\theta_1)} C_{(\phi-\theta_2)}} \\
= & 1
\end{aligned}
$$

B.2 Love waves

1. We take a time derivative for 3D particle velocities $\dot{\mathbf{u}} = (\dot{u}_x, \dot{u}_y, \dot{u}_z)$

$$\begin{aligned} \dot{\mathbf{u}} &= \partial_t \left[\left(-\mathcal{S}_\phi, C_\phi, 0\right) \left(Ae^{i\eta_1 kz} + Be^{i\eta_1 kz}\right) e^{ik(ct - xC_\phi - y\mathcal{S}_\phi)} \right] \\ &= ikc \left(-\mathcal{S}_\phi, C_\phi, 0\right) \left(Ae^{i\eta_1 kz} + Be^{i\eta_1 kz}\right) e^{ik(ct - xC_\phi - y\mathcal{S}_\phi)} \end{aligned} \tag{B.5}$$

2. By applying a single rotation matrix to $\dot{\mathbf{u}}$ we can calculate the particle velocity $\dot{u}_\theta$ as detected by a geophone in the in the $(\cos(\theta), \sin(\theta), 0)$ direction.

$$\begin{aligned} \dot{u}_\theta &= C_\theta \dot{u}_x + \mathcal{S}_\theta \dot{u}_y \\ &= ick \left(-C_\theta \mathcal{S}_\phi + \mathcal{S}_\theta C_\phi\right) \left(Ae^{i\eta_1 kz} + Be^{i\eta_1 kz}\right) e^{ik(ct - xC_\phi - y\mathcal{S}_\phi)} \\ &= -ick\mathcal{S}_{(\phi-\theta)} \left(Ae^{i\eta_1 kz} + Be^{i\eta_1 kz}\right) e^{ik(ct - xC_\phi - y\mathcal{S}_\phi)} \end{aligned} \tag{B.6}$$

3. We calculate horizontal spatial derivatives of $\dot{\mathbf{u}}$ then plug them into Equation A.5 to calculate the pointwise axial strain rate in the $(\cos(\theta), \sin(\theta), 0)$ direction, $\dot{\sigma}_\theta$.

$$
\begin{aligned}
\frac{\partial \dot{u}_x}{\partial x} &= -ikc\mathcal{S}_\phi(Ae^{i\eta_1 kz} + Be^{i\eta_1 kz})e^{ik(ct-xC_\phi-y\mathcal{S}_\phi)}(-ikC_\phi) \\
&= -\frac{k^2 c}{2}\mathcal{S}_{2\phi}(Ae^{i\eta_1 kz} + Be^{i\eta_1 kz})e^{ik(ct-xC_\phi-y\mathcal{S}_\phi)} \\
\frac{\partial \dot{u}_y}{\partial x} &= ikcC_\phi(Ae^{i\eta_1 kz} + Be^{i\eta_1 kz})e^{ik(ct-xC_\phi-y\mathcal{S}_\phi)}(-ikC_\phi) \\
&= k^2 cC_\phi^2(Ae^{i\eta_1 kz} + Be^{i\eta_1 kz})e^{ik(ct-xC_\phi-y\mathcal{S}_\phi)} \\
\frac{\partial \dot{u}_x}{\partial y} &= -ikc\mathcal{S}_\phi(Ae^{i\eta_1 kz} + Be^{i\eta_1 kz})e^{ik(ct-xC_\phi-y\mathcal{S}_\phi)}(-ik\mathcal{S}_\phi) \\
&= -k^2 c\mathcal{S}_\phi^2(Ae^{i\eta_1 kz} + Be^{i\eta_1 kz})e^{ik(ct-xC_\phi-y\mathcal{S}_\phi)} \\
\frac{\partial \dot{u}_y}{\partial y} &= ikcC_\phi(Ae^{i\eta_1 kz} + Be^{i\eta_1 kz})e^{ik(ct-xC_\phi-y\mathcal{S}_\phi)}(-ik\mathcal{S}_\phi) \\
&= \frac{k^2 c}{2}\mathcal{S}_{2\phi}(Ae^{i\eta_1 kz} + Be^{i\eta_1 kz})e^{ik(ct-xC_\phi-y\mathcal{S}_\phi)}
\end{aligned}
$$

Now we can plug these in for the point-wise axial strain in the θ direction:

$$
\begin{aligned}
\dot{\sigma}_\theta(x,y,z,t) &= C_\theta^2\frac{\partial \dot{u}_x}{\partial x} + C_\theta\mathcal{S}_\theta\left(\frac{\partial \dot{u}_x}{\partial y} + \frac{\partial \dot{u}_y}{\partial x}\right) + \mathcal{S}_\theta^2\frac{\partial \dot{u}_y}{\partial y} \\
&= k^2 c\left(C_\theta^2(-\frac{1}{2})\mathcal{S}_{2\phi} + C_\theta\mathcal{S}_\theta\left(-\mathcal{S}_\phi^2 + C_\phi^2\right) + \mathcal{S}_\theta^2\frac{1}{2}\mathcal{S}_{2\phi}\right)\ldots \\
&\quad \ldots(Ae^{i\eta_1 kz} + Be^{i\eta_1 kz})e^{ik(ct-xC_\phi-y\mathcal{S}_\phi)} \\
&= k^2 c\left(-C_\theta^2 C_\phi\mathcal{S}_\phi + C_\theta\mathcal{S}_\theta\left(-\mathcal{S}_\phi^2 + C_\phi^2\right) + \mathcal{S}_\theta^2 C_\phi\mathcal{S}_\phi\right)\ldots \\
&\quad \ldots(Ae^{i\eta_1 kz} + Be^{i\eta_1 kz})e^{ik(ct-xC_\phi-y\mathcal{S}_\phi)} \\
&= k^2 c\left(\mathcal{S}_\theta C_\phi - C_\theta\mathcal{S}_\phi\right)\left(C_\theta C_\phi + \mathcal{S}_\theta\mathcal{S}_\phi\right)(Ae^{i\eta_1 kz} + Be^{i\eta_1 kz})e^{ik(ct-xC_\phi-y\mathcal{S}_\phi)} \\
&= -k^2 c\mathcal{S}_{(\phi-\theta)}C_{(\phi-\theta)}(Ae^{i\eta_1 kz} + Be^{i\eta_1 kz})e^{ik(ct-xC_\phi-y\mathcal{S}_\phi)} \\
&= -\frac{k^2 c}{2}\mathcal{S}_{2(\phi-\theta)}(Ae^{i\eta_1 kz} + Be^{i\eta_1 kz})e^{ik(ct-xC_\phi-y\mathcal{S}_\phi)} \qquad \text{(B.7)}
\end{aligned}
$$

4. We average $\dot{\sigma}_\theta$ over a horizontal line segment of length g, the gauge length, yielding $\dot{\sigma}_{\theta,g}$, which mimics a DAS signal in the same location in the direction $(\cos(\theta), \sin(\theta), 0)$.

$$
\begin{aligned}
&= \dot{\sigma}_{\theta,g}(x,y,z,t) \\
&= ck^2 C_{\theta-\phi}\mathcal{S}_{(\theta-\phi)}(Ae^{-i\eta_1 kz} + Be^{i\eta_1 kz})\frac{1}{g}\int_{-g/2}^{g/2} o_{RL}(x+\nu C_\theta, y+\nu\mathcal{S}_\theta, z, t)d\nu \\
&= ck^2 C_{(\theta-\phi)}\mathcal{S}_{(\theta-\phi)}(Ae^{-i\eta_1 kz} + Be^{i\eta_1 kz})\frac{1}{g}\int_{-g/2}^{g/2} e^{ik(ct-(x+\nu C_\theta)C_\phi-(y+\nu\mathcal{S}_\theta)\mathcal{S}_\phi)}d\nu \\
&= ck^2 C_{(\theta-\phi)}\mathcal{S}_{(\theta-\phi)}(Ae^{-i\eta_1 kz} + Be^{i\eta_1 kz})e^{ik(ct-xC_\phi-y\mathcal{S}_\phi)}\frac{1}{g}\int_{-g/2}^{g/2} e^{-ik\nu C_{(\theta-\phi)}}d\nu \\
&= \frac{ck^2}{g}C_{(\theta-\phi)}\mathcal{S}_{(\theta-\phi)}(Ae^{-i\eta_1 kz} + Be^{i\eta_1 kz})e^{ik(ct-xC_\phi-y\mathcal{S}_\phi)}\left[\frac{e^{-ik\nu C_{(\theta-\phi)}}}{-ikC_{(\theta-\phi)}}\right]_{-g/2}^{g/2} \\
&= -\frac{2ck}{g}\mathcal{S}_{(\theta-\phi)}(Ae^{-i\eta_1 kz} + Be^{i\eta_1 kz})e^{ik(ct-xC_\phi-y\mathcal{S}_\phi)}\left[\frac{e^{-ik\nu C_{(\theta-\phi)}}}{2i}\right]_{-g/2}^{g/2} \\
&= \frac{2ck}{g}\mathcal{S}_{(\phi-\theta)}(Ae^{-i\eta_1 kz} + Be^{i\eta_1 kz})e^{ik(ct-xC_\phi-y\mathcal{S}_\phi)}\sin\left(\frac{-kgC_{(\phi-\theta)}}{2}\right) \qquad \text{(B.8)}
\end{aligned}
$$

5. We verify that $\lim_{k\to 0}\frac{\dot{\sigma}_{\theta,g}}{\dot{\sigma}_\theta} = 1$, i.e. at long wavelengths, the average strain rate over a fixed gauge length acts like a point-wise axial strain rate measurement in the same direction.

$$
\begin{aligned}
\lim_{k\to 0}\frac{\dot{\sigma}_{\theta,g}}{\dot{\sigma}_\theta} &= \lim_{k\to 0}\frac{\frac{2ck}{g}\mathcal{S}_{(\phi-\theta)}(Ae^{-i\eta_1 kz} + Be^{i\eta_1 kz})e^{ik(ct-xC_\phi-y\mathcal{S}_\phi)}\sin\left(\frac{-kgC_{(\phi-\theta)}}{2}\right)}{-\frac{k^2c}{2}\mathcal{S}_{2(\phi-\theta)}(Ae^{i\eta_1 kz} + Be^{i\eta_1 kz})e^{ik(ct-xC_\phi-y\mathcal{S}_\phi)}} \\
&= \lim_{k\to 0}\frac{2\sin\left(\frac{-kgC_{(\phi-\theta)}}{2}\right)}{gkC_{(\phi-\theta)}} \\
&= \lim_{k\to 0}\frac{-gC_{(\phi-\theta)}\cos\left(\frac{-kgC_{(\phi-\theta)}}{2}\right)}{gC_{(\phi-\theta)}} \\
&= 1
\end{aligned}
$$

6. We calculate the cross-correlation of two horizontal particle velocity measurements, $\dot{u}_{\theta_1}(x_1, y_1, z)$ and $\dot{u}_{\theta_2}(x_2, y_2, z)$, simultaneously recording the same plane wave.

$$
\begin{aligned}
\frac{1}{2T}\int_{-T}^{T}\dot{u}_{\theta_1}(x_1,y_1,z,t)\dot{u}^{*}_{\theta_2}(x_2,y_2,z,t+\tau)dt &= \\
\frac{1}{2T}\int_{-T}^{T}ick\mathcal{S}_{(\theta_1-\phi)}(Ae^{-i\eta_1 kz}+Be^{i\eta_1 kz})e^{ik(ct-x_1C_\phi-y_1\mathcal{S}_\phi)}\dots & \\
(-i)ck\mathcal{S}_{(\theta_2-\phi)}(Ae^{i\eta_1 kz}+Be^{-i\eta_1 kz})e^{-ik(c(t+\tau)-x_2C_\phi-y_2\mathcal{S}_\phi)}dt &= \\
\frac{c^2k^2}{2T}\mathcal{S}_{(\theta_1-\phi)}\mathcal{S}_{(\theta_2-\phi)}(A^2+AB(e^{2i\eta_1 kz}+e^{-2i\eta_1 kz})+B^2)\dots & \\
\times e^{-ik(c\tau+(x_1-x_2)C_\phi+(y_1-y_2)\mathcal{S}_\phi)}\int_{-T}^{T}dt &= \\
c^2k^2\mathcal{S}_{(\theta_1-\phi)}\mathcal{S}_{(\theta_2-\phi)}e^{-ik(c\tau+(x_1-x_2)C_\phi+(y_1-y_2)\mathcal{S}_\phi)}(A^2+AB(e^{2i\eta_1 kz}+e^{-2i\eta_1 kz})+B^2) &=
\end{aligned}
\tag{B.9}
$$

7. We calculate the cross-correlation of two horizontal point-wise axial strain rate measurements, $\dot{\sigma}_{\theta_1}(x_1,y_1,z)$ and $\dot{\sigma}_{\theta_2}(x_2,y_2,z)$, simultaneously recording the same plane wave.

$$
\begin{aligned}
\frac{1}{2T}\int_{-T}^{T}\dot{\sigma}_{\theta_1}(x_1,y_1,z,t)\dot{\sigma}^{*}_{\theta_2}(x_2,y_2,z,t+\tau)dt &= \\
\frac{1}{2T}\int_{-T}^{T}ck^2C_{(\phi-\theta_1)}\mathcal{S}_{(\theta_1-\phi)}(Ae^{-i\eta_1 kz}+Be^{i\eta_1 kz})e^{ik(ct-x_1C_\phi-y_1\mathcal{S}_\phi)}\dots & \\
\times ck^2C_{(\phi-\theta_2)}\mathcal{S}_{(\theta_2-\phi)}(Ae^{i\eta_1 kz}+Be^{-i\eta_1 kz})e^{-ik(c(t+\tau)-x_2C_\phi-y_2\mathcal{S}_\phi)}dt &= \\
\frac{c^2k^4}{8T}\mathcal{S}_{2(\phi-\theta_1)}\mathcal{S}_{2(\phi-\theta_2)}(A^2+AB(e^{2i\eta_1 kz}+e^{-2i\eta_1 kz})+B^2)\dots & \\
\times e^{-ik(c\tau+(x_1-x_2)C_\phi+(y_1-y_2)\mathcal{S}_\phi)}\int_{-T}^{T}dt &= \\
\frac{c^2k^4}{4}\mathcal{S}_{2(\phi-\theta_1)}\mathcal{S}_{2(\phi-\theta_2)}e^{-ik(c\tau+(x_1-x_2)C_\phi+(y_1-y_2)\mathcal{S}_\phi)}(A^2+2AB\cos(2\eta_1 kz)+B^2) &=
\end{aligned}
\tag{B.10}
$$

8. We calculate the cross-correlation of two horizontal average axial strain rate measurements over a gauge length, $\dot{\sigma}_{\theta_1,g}(x_1,y_1,z)$ and $\dot{\sigma}_{\theta_2,g}(x_2,y_2,z)$, simultaneously

recording the same plane wave.

$$
\begin{aligned}
\frac{1}{2T}\int_{-T}^{T}\dot{\sigma}_{\theta_1,g}(x_1,y_1,z,t)\dot{\sigma}^{*}_{\theta_2,g}(x_2,y_2,z,t+\tau)dt &= \\
\frac{1}{2Tg^2}4c^2k^2\sin\left(\frac{-kgC_{(\theta_1-\phi)}}{2}\right)\sin\left(\frac{-kgC_{(\theta_2-\phi)}}{2}\right)\mathcal{S}_{(\theta_1-\phi)}\mathcal{S}_{(\theta_2-\phi)}\cdots & \\
\cdots\int_{-T}^{T}(Ae^{-i\eta_1 kz}+Be^{i\eta_1 kz})e^{ik(ct-x_1C_\phi-y_1\mathcal{S}_\phi)}(Ae^{i\eta_1 kz}+Be^{-i\eta_1 kz})e^{-ik(c(t+\tau)-x_2C_\phi-y_2\mathcal{S}_\phi)}dt &= \\
\frac{1}{2Tg^2}4c^2k^2\sin\left(\frac{-kgC_{(\theta_1-\phi)}}{2}\right)\sin\left(\frac{-kgC_{(\theta_2-\phi)}}{2}\right)\mathcal{S}_{(\theta_1-\phi)}\mathcal{S}_{(\theta_2-\phi)}\cdots & \\
\cdots(A^2+AB(e^{2i\eta_1 kz}+e^{-2i\eta_1 kz})+B^2)e^{-ik(c\tau+(x_1-x_2)C_\phi+(y_1-y_2)\mathcal{S}_\phi)}\int_{-T}^{T}dt &= \\
\frac{4c^2k^2}{g^2}\sin\left(\frac{-kgC_{(\theta_1-\phi)}}{2}\right)\sin\left(\frac{-kgC_{(\theta_2-\phi)}}{2}\right)\mathcal{S}_{(\theta_1-\phi)}\mathcal{S}_{(\theta_2-\phi)}\cdots & \\
\cdots e^{-ik(c\tau+(x_1-x_2)C_\phi+(y_1-y_2)\mathcal{S}_\phi)}(A^2+2AB\cos(2\eta_1 kz)+B^2) &= \qquad \text{(B.11)}
\end{aligned}
$$

9. We verify that $\lim_{k\to 0}\frac{\dot{\sigma}_{\theta_1,g}(x_1,y_1,z)\star\dot{\sigma}_{\theta_2,g}(x_2,y_2,z)}{\dot{\sigma}_{\theta_1}(x_1,y_1,z)\star\dot{\sigma}_{\theta_2}(x_2,y_2,z)}=1$, verifying that the behavior of interferometry of DAS measurements is the same as interferometry of point-wise axial strain rate measurements at long wavelengths.

$$
\begin{aligned}
\lim_{k\to 0} \frac{\dot{\sigma}_{\theta_1,g}(x_1,y_1,z) \star \dot{\sigma}_{\theta_2,g}(x_2,y_2,z)}{\dot{\sigma}_{\theta_1}(x_1,y_1,z) \star \dot{\sigma}_{\theta_2}(x_2,y_2,z)} &= \\
\lim_{k\to 0} \left[\frac{\frac{2ck}{g} \sin\left(\frac{-kgC_{(\theta_1-\phi)}}{2}\right) \mathcal{S}_{(\theta_1-\phi)} e^{-ik(c\tau+(x_1-x_2)C_\phi+(y_1-y_2)\mathcal{S}_\phi)}}{\frac{ck^2}{2}\mathcal{S}_{2(\phi-\theta_1)} e^{-ik(c\tau+(x_1-x_2)C_\phi+(y_1-y_2)\mathcal{S}_\phi)}} \cdots \right. & \\
\left. \times \frac{\frac{2ck}{g} \sin\left(\frac{-kgC_{(\theta_2-\phi)}}{2}\right) \mathcal{S}_{(\theta_2-\phi)} (A^2 + 2AB\cos(2\eta_1 kz) + B^2)}{\frac{ck^2}{2}\mathcal{S}_{2(\phi-\theta_2)} (A^2 + 2AB\cos(2\eta_1 kz) + B^2)} \right] &= \\
\lim_{k\to 0} \frac{4 \sin\left(\frac{-kgC_{(\theta_1-\phi)}}{2}\right) \sin\left(\frac{-kgC_{(\theta_2-\phi)}}{2}\right)}{g^2k^2 C_{(\phi-\theta_1)} C_{(\phi-\theta_2)}} &= \\
\lim_{k\to 0} \frac{2}{kgC_{(\phi-\theta_1)}C_{(\phi-\theta_2)}} \left[\frac{-C_{(\theta_1-\phi)}}{2} \cos\left(\frac{-kgC_{(\theta_1-\phi)}}{2}\right) \sin\left(\frac{-kgC_{(\theta_2-\phi)}}{2}\right) \cdots \right. & \\
\left. + \sin\left(\frac{-kgC_{(\theta_1-\phi)}}{2}\right) \frac{-C_{(\theta_2-\phi)}}{2} \cos\left(\frac{-kgC_{(\theta_2-\phi)}}{2}\right) \right] &= \\
\lim_{k\to 0} \frac{-2}{kgC_{(\phi-\theta_1)}C_{(\phi-\theta_2)}} \left[C_{(\theta_1-\phi)} \cos\left(\frac{-kgC_{(\theta_1-\phi)}}{2}\right) \sin\left(\frac{-kgC_{(\theta_2-\phi)}}{2}\right) \cdots \right. & \\
\left. + C_{(\theta_2-\phi)} \sin\left(\frac{-kgC_{(\theta_1-\phi)}}{2}\right) \cos\left(\frac{-kgC_{(\theta_2-\phi)}}{2}\right) \right] &= \\
\lim_{k\to 0} \frac{-1}{C_{(\phi-\theta_1)}C_{(\phi-\theta_2)}} \left[\sin\left(\frac{-kgC_{(\theta_1-\phi)}}{2}\right) \sin\left(\frac{-kgC_{(\theta_2-\phi)}}{2}\right) \left(C^2_{(\theta_1-\phi)} + C^2_{(\theta_2-\phi)}\right) \cdots \right. & \\
\left. - \cos\left(\frac{-kgC_{(\theta_1-\phi)}}{2}\right) \cos\left(\frac{-kgC_{(\theta_2-\phi)}}{2}\right) C_{(\theta_1-\phi)} C_{(\theta_2-\phi)} \right] &= \\
\lim_{k\to 0} \frac{-\left[0 - C_{(\theta_1-\phi)}C_{(\theta_2-\phi)}\right]}{C_{(\phi-\theta_1)}C_{(\phi-\theta_2)}} &= \\
1 &=
\end{aligned}
$$

B.3 P waves

1. We take a time derivative for 3D particle velocities $\dot{\mathbf{u}} = (\dot{u}_x, \dot{u}_y, \dot{u}_z)$:

$$\begin{aligned}\dot{\mathbf{u}} &= \partial_t \left[A(C_{\phi_1}C_{\phi_2}, \mathcal{S}_{\phi_1}C_{\phi_2}, \mathcal{S}_{\phi_2}) e^{ik(ct - xC_{\phi_1}C_{\phi_2} - y\mathcal{S}_{\phi_1}C_{\phi_2} - z\mathcal{S}_{\phi_2})} \right] \\ &= ikcA(C_{\phi_1}C_{\phi_2}, \mathcal{S}_{\phi_1}C_{\phi_2}, \mathcal{S}_{\phi_2}) e^{ik(ct - xC_{\phi_1}C_{\phi_2} - y\mathcal{S}_{\phi_1}C_{\phi_2} - z\mathcal{S}_{\phi_2})} \end{aligned} \tag{B.12}$$

2. By applying a single rotation matrix to $\dot{\mathbf{u}}$ we can calculate the particle velocity $\dot{u}_\theta$ as detected by a geophone in the in the $(\cos(\theta), \sin(\theta), 0)$ direction.

$$\begin{aligned}\dot{u}_\theta &= ikcA \left(C_\theta C_{\phi_1} C_{\phi_2} + \mathcal{S}_\theta \mathcal{S}_{\phi_1} C_{\phi_2} \right) o_{PS} \\ &= ikcA C_{(\theta - \phi_1)} C_{\phi_2} o_{PS} \end{aligned} \tag{B.13}$$

3. We calculate horizontal spatial derivatives of $\dot{\mathbf{u}}$ then plug them into Equation A.5 to calculate the pointwise axial strain rate in the $(\cos(\theta), \sin(\theta), 0)$ direction, $\dot{\sigma}_\theta$.

   First, let's calculate the point-wise axial strain of a horizontal fiber oriented in the $(C_\theta, \mathcal{S}_\theta, 0)$ direction at the point $(x, y.z)$. The first steps are to calculate our spatial derivatives of the particle velocity, keeping in mind that $\dot{u}_x = ikcAC_{\phi_1}C_{\phi_2}o_{PS}$ and $\dot{u}_y = ikcA\mathcal{S}_{\phi_1}C_{\phi_2}o_{PS}$, where $o_{PS} = e^{ik(ct - xC_{\phi_1}C_{\phi_2} - y\mathcal{S}_{\phi_1}C_{\phi_2} - z\mathcal{S}_{\phi_2})}$:

$$
\begin{aligned}
\frac{\partial \dot{u}_x}{\partial x} &= ikcAC_{\phi_1}C_{\phi_2}e^{ik(ct-xC_{\phi_1}C_{\phi_2}-y\mathcal{S}_{\phi_1}C_{\phi_2}-z\mathcal{S}_{\phi_2})}(-ikC_{\phi_1}C_{\phi_2}) \\
&= k^2cAC_{\phi_1}^2C_{\phi_2}^2e^{ik(ct-xC_{\phi_1}C_{\phi_2}-y\mathcal{S}_{\phi_1}C_{\phi_2}-z\mathcal{S}_{\phi_2})} \\
\frac{\partial \dot{u}_y}{\partial x} &= ikcA\mathcal{S}_{\phi_1}C_{\phi_2}e^{ik(ct-xC_{\phi_1}C_{\phi_2}-y\mathcal{S}_{\phi_1}C_{\phi_2}-z\mathcal{S}_{\phi_2})}(-ikC_{\phi_1}C_{\phi_2}) \\
&= \frac{k^2cA}{2}\mathcal{S}_{2\phi_1}C_{\phi_2}^2e^{ik(ct-xC_{\phi_1}C_{\phi_2}-y\mathcal{S}_{\phi_1}C_{\phi_2}-z\mathcal{S}_{\phi_2})} \\
\frac{\partial \dot{u}_x}{\partial y} &= ikcAC_{\phi_1}C_{\phi_2}e^{ik(ct-xC_{\phi_1}C_{\phi_2}-y\mathcal{S}_{\phi_1}C_{\phi_2}-z\mathcal{S}_{\phi_2})}(-ik\mathcal{S}_{\phi_1}C_{\phi_2}) \\
&= \frac{k^2cA}{2}\mathcal{S}_{2\phi_1}C_{\phi_2}^2e^{ik(ct-xC_{\phi_1}C_{\phi_2}-y\mathcal{S}_{\phi_1}C_{\phi_2}-z\mathcal{S}_{\phi_2})} \\
\frac{\partial \dot{u}_y}{\partial y} &= ikcA\mathcal{S}_{\phi_1}C_{\phi_2}e^{ik(ct-xC_{\phi_1}C_{\phi_2}-y\mathcal{S}_{\phi_1}C_{\phi_2}-z\mathcal{S}_{\phi_2})}(-ik\mathcal{S}_{\phi_1}C_{\phi_2}) \\
&= k^2cA\mathcal{S}_{\phi_1}^2C_{\phi_2}^2e^{ik(ct-xC_{\phi_1}C_{\phi_2}-y\mathcal{S}_{\phi_1}C_{\phi_2}-z\mathcal{S}_{\phi_2})}
\end{aligned}
$$

Now we can plug these in for the point-wise axial strain in the θ direction:

$$
\begin{aligned}
\dot{\sigma}_\theta(x,y,z,t) &= C_\theta^2\frac{\partial \dot{u}_x}{\partial x} + C_\theta\mathcal{S}_\theta\left(\frac{\partial \dot{u}_x}{\partial y} + \frac{\partial \dot{u}_y}{\partial x}\right) + \mathcal{S}_\theta^2\frac{\partial \dot{u}_y}{\partial y} \\
&= k^2cAC_{\phi_2}^2\left(C_\theta^2C_{\phi_1}^2 + C_\theta\mathcal{S}_\theta\left(\frac{\mathcal{S}_{2\phi_1}}{2} + \frac{\mathcal{S}_{2\phi_1}}{2}\right) + \mathcal{S}_\theta^2\mathcal{S}_{\phi_1}^2\right)o_{PS}(x,y,z,t) \\
&= k^2cAC_{\phi_2}^2\left(C_\theta^2C_{\phi_1}^2 + C_\theta\mathcal{S}_\theta\mathcal{S}_{2\phi_1} + \mathcal{S}_\theta^2\mathcal{S}_{\phi_1}^2\right)o_{PS}(x,y,z,t) \\
&= -ik^2c^2AC_{\phi_2}^2(C_\theta C_{\phi_1} + \mathcal{S}_\theta\mathcal{S}_{\phi_1})^2o_{PS}(x,y,z,t) \\
&= k^2cAC_{\theta-\phi_1}^2C_{\phi_2}^2o_{PS}(x,y,z,t) \qquad \text{(B.14)}
\end{aligned}
$$

4. We average $\dot{\sigma}_\theta$ over a horizontal line segment of length g, the gauge length, yielding $\dot{\sigma}_{\theta,g}$, which mimics a DAS signal in the same location in the direction $(\cos(\theta), \sin(\theta), 0)$.

$$\begin{aligned}
\dot{\sigma}_{\theta,g}(x,y,z,t) &= k^2 cAC^2_{(\theta-\phi_1)}C^2_{\phi_2}\frac{1}{g}\int_{-g/2}^{g/2} o_{PS}(x+\nu C_\theta, y+\nu \mathcal{S}_\theta, z, t)d\nu \\
&= \frac{k^2 cA}{g}C^2_{(\theta-\phi_1)}C^2_{\phi_2}\int_{-g/2}^{g/2} e^{ik(ct-(x+\nu C_\theta)C_{\phi_1}C_{\phi_2}-(y+\nu\mathcal{S}_\theta)\mathcal{S}_{\phi_1}C_{\phi_2}-z\mathcal{S}_{\phi_2})}d\nu \\
&= \frac{k^2 cA}{g}C^2_{(\theta-\phi_1)}C^2_{\phi_2}e^{ik(ct-xC_{\phi_1}C_{\phi_2}-y\mathcal{S}_{\phi_1}C_{\phi_2}-z\mathcal{S}_{\phi_2})}\left[\frac{e^{-ik\nu C_{(\theta-\phi_1)}C_{\phi_2}}}{ikC_{(\theta-\phi_1)}C_{\phi_2}}\right]_{g/2}^{-g/2} \\
&= \frac{2kcA}{g}C_{(\theta-\phi_1)}C_{\phi_2}e^{ik(ct-xC_{\phi_1}C_{\phi_2}-y\mathcal{S}_{\phi_1}C_{\phi_2}-z\mathcal{S}_{\phi_2})}\sin\left(\frac{gkC_{(\theta-\phi_1)}C_{\phi_2}}{2}\right)
\end{aligned}$$

5. We verify that $\lim_{k\to 0}\frac{\dot{\sigma}_{\theta,g}}{\dot{\sigma}_\theta} = 1$, i.e. at long wavelengths, the average strain rate over a fixed gauge length acts like a point-wise axial strain rate measurement in the same direction.

$$\begin{aligned}
\lim_{k\to 0}\frac{\dot{\sigma}_{\theta,g}}{\dot{\sigma}_\theta} &= \lim_{k\to 0}\frac{\frac{2kcA}{g}C_{(\theta-\phi_1)}C_{\phi_2}e^{ik(ct-xC_{\phi_1}C_{\phi_2}-y\mathcal{S}_{\phi_1}C_{\phi_2}-z\mathcal{S}_{\phi_2})}\sin\left(\frac{gkC_{(\theta-\phi_1)}C_{\phi_2}}{2}\right)}{k^2cAC^2_{\theta-\phi_1}C^2_{\phi_2}e^{ik(ct-xC_{\phi_1}C_{\phi_2}-y\mathcal{S}_{\phi_1}C_{\phi_2}-z\mathcal{S}_{\phi_2})}} \\
&= \lim_{k\to 0}\frac{2\sin\left(\frac{gkC_{(\theta-\phi_1)}C_{\phi_2}}{2}\right)}{kgC_{\theta-\phi_1}C_{\phi_2}} \\
&= \lim_{k\to 0}\frac{2\frac{gC_{(\theta-\phi_1)}C_{\phi_2}}{2}\cos\left(\frac{gkC_{(\theta-\phi_1)}C_{\phi_2}}{2}\right)}{gC_{\theta-\phi_1}C_{\phi_2}} \\
&= 1
\end{aligned}$$

6. We calculate the cross-correlation of two horizontal particle velocity measurements, $\dot{u}_{\theta_1}(x_1, y_1, z)$ and $\dot{u}_{\theta_2}(x_2, y_2, z)$, simultaneously recording the same plane wave.

$$\begin{aligned}
\frac{1}{2T}\int_{-T}^{T}\dot{u}_{\theta_1}(x_1,y_1,z,t)\dot{u}^{*}_{\theta_2}(x_2,y_2,z,t+\tau)dt &= \\
\frac{1}{2T}\int_{-T}^{T} ickAC_{(\theta_1-\phi_1)}C_{\phi_2}e^{ik(ct-x_1C_{\phi_1}C_{\phi_2}-y_1S_{\phi_1}C_{\phi_2}-zS_{\phi_2})}\dots & \\
\times(-ick)AC_{(\theta_2-\phi_1)}C_{\phi_2}e^{-ik(c(t+\tau)-x_2C_{\phi_1}C_{\phi_2}-y_2S_{\phi_1}C_{\phi_2}-zS_{\phi_2})}dt &= \\
\frac{k^2c^2A^2}{2T}C_{(\theta_1-\phi_1)}C_{(\theta_2-\phi_1)}C^2_{\phi_2}e^{-ik(c\tau+(x_1-x_2)C_{\phi_1}C_{\phi_2}+(y_1-y_2)S_{\phi_1}C_{\phi_2})}\int_{-T}^{T}dt &= \\
k^2c^2A^2C_{(\theta_1-\phi_1)}C_{(\theta_2-\phi_1)}C^2_{\phi_2}e^{-ik(c\tau+(x_1-x_2)C_{\phi_1}C_{\phi_2}+(y_1-y_2)S_{\phi_1}C_{\phi_2})} &= \quad \text{(B.15)}
\end{aligned}$$

7. We calculate the cross-correlation of two horizontal point-wise axial strain rate measurements, $\dot{\sigma}_{\theta_1}(x_1, y_1, z)$ and $\dot{\sigma}_{\theta_2}(x_2, y_2, z)$, simultaneously recording the same plane wave.

$$\begin{aligned}
\frac{1}{2T}\int_{-T}^{T}\dot{\sigma}_{\theta_1}(x_1,y_1,z,t)\dot{\sigma}^{*}_{\theta_2}(x_2,y_2,z,t+\tau)dt &= \\
\frac{1}{2T}\int_{-T}^{T} ck^2AC^2_{\theta_1-\phi_1}C^2_{\phi_2}e^{ik(ct-x_1C_{\phi_1}C_{\phi_2}-y_1S_{\phi_1}C_{\phi_2}-zS_{\phi_2})}\dots & \\
\times ck^2AC^2_{\theta_2-\phi_1}C^2_{\phi_2}e^{-ik(c(t+\tau)-x_2C_{\phi_1}C_{\phi_2}-y_2S_{\phi_1}C_{\phi_2}-zS_{\phi_2})}dt &= \\
\frac{k^4c^2A^2}{2T}C^2_{\theta_1-\phi_1}C^2_{\phi_2}C^2_{\theta_2-\phi_1}C^2_{\phi_2}e^{-ik(c\tau+(x_1-x_2)C_{\phi_1}C_{\phi_2}+(y_1-y_2)S_{\phi_1}C_{\phi_2})}\int_{-T}^{T}dt &= \\
k^4c^2A^2C^2_{\theta_1-\phi_1}C^2_{\theta_2-\phi_1}C^4_{\phi_2}e^{-ik(c\tau+(x_1-x_2)C_{\phi_1}C_{\phi_2}+(y_1-y_2)S_{\phi_1}C_{\phi_2})} &= \quad \text{(B.16)}
\end{aligned}$$

8. We calculate the cross-correlation of two horizontal average axial strain rate measurements over a gauge length, $\dot{\sigma}_{\theta_1,g}(x_1, y_1, z)$ and $\dot{\sigma}_{\theta_2,g}(x_2, y_2, z)$, simultaneously recording the same plane wave.

$$
\begin{aligned}
\frac{1}{2T}\int_{-T}^{T}\dot{\sigma}_{\theta_1,g}(x_1,y_1,z,t)\dot{\sigma}^{*}_{\theta_2,g}(x_2,y_2,z,t+\tau)dt &= \\
\frac{1}{2Tg^2}\int_{-T}^{T}2ckAC_{(\theta_1-\phi_1)}C_{\phi_2}\sin\left(\frac{kg}{2}C_{(\theta_1-\phi_1)}C_{\phi_2}\right)e^{ik(ct-x_1C_{\phi_1}C_{\phi_2}-y_1\mathcal{S}_{\phi_1}C_{\phi_2}-z\mathcal{S}_{\phi_2})}\dots & \\
\dots 2ckAC_{(\theta_2-\phi_1)}C_{\phi_2}\sin\left(\frac{kg}{2}C_{(\theta_2-\phi_1)}C_{\phi_2}\right)e^{-ik(c(t+\tau)-x_2C_{\phi_1}C_{\phi_2}-y_2\mathcal{S}_{\phi_1}C_{\phi_2}-z\mathcal{S}_{\phi_2})}dt &= \\
\frac{4k^2c^2A^2}{g^2}C_{(\theta_1-\phi_1)}C^2_{\phi_2}C_{(\theta_2-\phi_1)}\sin\left(\frac{kg}{2}C_{(\theta_1-\phi_1)}C_{\phi_2}\right)\dots & \\
\times\sin\left(\frac{kg}{2}C_{(\theta_2-\phi_1)}C_{\phi_2}\right)e^{-ik(c\tau+(x_1-x_2)C_{\phi_1}C_{\phi_2}+(y_1-y_2)\mathcal{S}_{\phi_1}C_{\phi_2})}\frac{1}{2T}\int_{-T}^{T}dt &= \\
\frac{4k^2c^2A^2}{g^2}C_{(\theta_1-\phi_1)}C^2_{\phi_2}C_{(\theta_2-\phi_1)}\sin\left(\frac{kgC_{(\theta_1-\phi_1)}C_{\phi_2}}{2}\right)\dots & \\
\times\sin\left(\frac{kgC_{(\theta_2-\phi_1)}C_{\phi_2}}{2}\right)e^{-ik(c\tau+(x_1-x_2)C_{\phi_1}C_{\phi_2}+(y_1-y_2)\mathcal{S}_{\phi_1}C_{\phi_2})} &= \\
\end{aligned}
\tag{B.17}
$$

9. We verify that $\lim_{k\to 0}\frac{\dot{\sigma}_{\theta_1,g}(x_1,y_1,z)\star\dot{\sigma}_{\theta_2,g}(x_2,y_2,z)}{\dot{\sigma}_{\theta_1}(x_1,y_1,z)\star\dot{\sigma}_{\theta_2}(x_2,y_2,z)} = 1$, verifying that the behavior of interferometry of DAS measurements is the same as interferometry of point-wise axial strain rate measurements at long wavelengths.

$$
\begin{aligned}
\lim_{k\to 0} \frac{\dot{\sigma}_{\theta_1,g}(x_1,y_1,z) \star \dot{\sigma}_{\theta_2,g}(x_2,y_2,z)}{\dot{\sigma}_{\theta_1}(x_1,y_1,z) \star \dot{\sigma}_{\theta_2}(x_2,y_2,z)} &= \\
\lim_{k\to 0} \left[\frac{\frac{4k^2c^2A^2}{g^2} C_{(\theta_1-\phi_1)} \sin\left(\frac{kgC_{(\theta_1-\phi_1)}C_{\phi_2}}{2}\right) e^{-ik(c\tau+(x_1-x_2)C_{\phi_1}C_{\phi_2}+(y_1-y_2)S_{\phi_1}C_{\phi_2})}}{k^4c^2A^2C^2_{\theta_1-\phi_1}C^2_{\theta_2-\phi_1}C^4_{\phi_2} e^{-ik(c\tau+(x_1-x_2)C_{\phi_1}C_{\phi_2}+(y_1-y_2)S_{\phi_1}C_{\phi_2})}} \cdots \right. & \\
\left. \times C^2_{\phi_2} C_{(\theta_2-\phi_1)} \sin\left(\frac{kgC_{(\theta_2-\phi_1)}C_{\phi_2}}{2}\right) \right] &= \\
\lim_{k\to 0} \frac{4 \sin\left(\frac{kgC_{(\theta_1-\phi_1)}C_{\phi_2}}{2}\right) \sin\left(\frac{kgC_{(\theta_2-\phi_1)}C_{\phi_2}}{2}\right)}{g^2k^2 C_{\theta_1-\phi_1} C_{\theta_2-\phi_1} C^2_{\phi_2}} &= \\
\lim_{k\to 0} \frac{1}{gkC_{\theta_1-\phi_1}C_{\theta_2-\phi_1}C_{\phi_2}} \left[C_{(\theta_1-\phi_1)} \cos\left(\frac{kgC_{(\theta_1-\phi_1)}C_{\phi_2}}{2}\right) \sin\left(\frac{kgC_{(\theta_2-\phi_1)}C_{\phi_2}}{2}\right) \cdots \right. & \\
\left. + \sin\left(\frac{kgC_{(\theta_1-\phi_1)}C_{\phi_2}}{2}\right) \cos\left(\frac{kgC_{(\theta_2-\phi_1)}C_{\phi_2}}{2}\right) C_{(\theta_2-\phi_1)} \right] &= \\
\lim_{k\to 0} \frac{1}{C_{\theta_1-\phi_1}C_{\theta_2-\phi_1}C_{\phi_2}} \left[-\frac{C_{\phi_2}}{2} (C^2_{\theta_1-\phi_1} + C^2_{\theta_2-\phi_1}) \sin\left(\frac{kgC_{(\theta_1-\phi_1)}C_{\phi_2}}{2}\right) \cdots \right. & \\
\left. + \sin\left(\frac{kgC_{(\theta_2-\phi_1)}C_{\phi_2}}{2}\right) C_{\phi_2}C_{\theta_1-\phi_1}C_{\theta_2-\phi_1} \cos\left(\frac{kgC_{(\theta_1-\phi_1)}C_{\phi_2}}{2}\right) \cos\left(\frac{kgC_{(\theta_2-\phi_1)}C_{\phi_2}}{2}\right) \right] &= \\
\lim_{k\to 0} \frac{0 + C_{\phi_2}C_{\theta_1-\phi_1}C_{\theta_2-\phi_1}}{C_{\theta_1-\phi_1}C_{\theta_2-\phi_1}C_{\phi_2}} &= \\
1 &=
\end{aligned}
$$

B.4 SV waves

1. We take a time derivative for 3D particle velocities $\dot{\mathbf{u}} = (\dot{u}_x, \dot{u}_y, \dot{u}_z)$

$$
\begin{aligned}
\dot{\mathbf{u}} &= \partial_t \left[A \left(-C_{\phi_1}S_{\phi_2}, -S_{\phi_1}S_{\phi_2}, C_{\phi_2}\right) e^{ik(ct - xC_{\phi_1}C_{\phi_2} - yS_{\phi_1}C_{\phi_2} - zS_{\phi_2})} \right] \\
&= ickA \left(-C_{\phi_1}S_{\phi_2}, -S_{\phi_1}S_{\phi_2}, C_{\phi_2}\right) e^{ik(ct - xC_{\phi_1}C_{\phi_2} - yS_{\phi_1}C_{\phi_2} - zS_{\phi_2})}
\end{aligned}
$$

2. By applying a single rotation matrix to $\dot{\mathbf{u}}$ we can calculate the particle velocity $\dot{u}_\theta$ as

detected by a geophone in the in the $(\cos(\theta), \sin(\theta), 0)$ direction.

$$\begin{aligned}\dot{u}_\theta &= -ickA\left(C_\theta C_{\phi_1}\mathcal{S}_{\phi_2} + \mathcal{S}_\theta \mathcal{S}_{\phi_1}\mathcal{S}_{\phi_2}\right) o_{PS} \\ &= -ickAC_{(\phi_1-\theta)}\mathcal{S}_{\phi_2} o_{PS}\end{aligned}$$

3. We calculate horizontal spatial derivatives of $\dot{\mathbf{u}}$ then plug them into Equation A.5 to calculate the pointwise axial strain rate in the $(\cos(\theta), \sin(\theta), 0)$ direction, $\dot{\sigma}_\theta$.
   First, let's calculate the point-wise axial strain of a horizontal fiber oriented in the $(C_\theta, \mathcal{S}_\theta, 0)$ direction at the point $(x, y.z)$. The first steps are to calculate our spatial derivatives of the particle velocity, keeping in mind that $\dot{u}_x = -ikcAC_{\phi_1}\mathcal{S}_{\phi_2} o_{PS}$ and $\dot{u}_y = -ikcA\mathcal{S}_{\phi_1}\mathcal{S}_{\phi_2} o_{PS}$, where $o_{PS} = e^{ik(ct - xC_{\phi_1}C_{\phi_2} - y\mathcal{S}_{\phi_1}C_{\phi_2} - z\mathcal{S}_{\phi_2})}$:

$$\begin{aligned}\frac{\partial \dot{u}_x}{\partial x} &= -ikcAC_{\phi_1}\mathcal{S}_{\phi_2} e^{ik(ct - xC_{\phi_1}C_{\phi_2} - y\mathcal{S}_{\phi_1}C_{\phi_2} - z\mathcal{S}_{\phi_2})}(-ikC_{\phi_1}C_{\phi_2}) \\ &= -\frac{k^2cA}{2} C_{\phi_1}^2 \mathcal{S}_{2\phi_2} e^{ik(ct - xC_{\phi_1}C_{\phi_2} - y\mathcal{S}_{\phi_1}C_{\phi_2} - z\mathcal{S}_{\phi_2})} \\ \frac{\partial \dot{u}_y}{\partial x} &= -ikcA\mathcal{S}_{\phi_1}\mathcal{S}_{\phi_2} e^{ik(ct - xC_{\phi_1}C_{\phi_2} - y\mathcal{S}_{\phi_1}C_{\phi_2} - z\mathcal{S}_{\phi_2})}(-ikC_{\phi_1}C_{\phi_2}) \\ &= -\frac{k^2cA}{4} \mathcal{S}_{2\phi_1}\mathcal{S}_{2\phi_2} e^{ik(ct - xC_{\phi_1}C_{\phi_2} - y\mathcal{S}_{\phi_1}C_{\phi_2} - z\mathcal{S}_{\phi_2})} \\ \frac{\partial \dot{u}_x}{\partial y} &= -ikcAC_{\phi_1}\mathcal{S}_{\phi_2} e^{ik(ct - xC_{\phi_1}C_{\phi_2} - y\mathcal{S}_{\phi_1}C_{\phi_2} - z\mathcal{S}_{\phi_2})}(-ik\mathcal{S}_{\phi_1}C_{\phi_2}) \\ &= -\frac{k^2cA}{4} C_{2\phi_1}\mathcal{S}_{2\phi_2} e^{ik(ct - xC_{\phi_1}C_{\phi_2} - y\mathcal{S}_{\phi_1}C_{\phi_2} - z\mathcal{S}_{\phi_2})} \\ \frac{\partial \dot{u}_y}{\partial y} &= -ikcA\mathcal{S}_{\phi_1}\mathcal{S}_{\phi_2} e^{ik(ct - xC_{\phi_1}C_{\phi_2} - y\mathcal{S}_{\phi_1}C_{\phi_2} - z\mathcal{S}_{\phi_2})}(-ik\mathcal{S}_{\phi_1}C_{\phi_2}) \\ &= -\frac{k^2cA}{2} \mathcal{S}_{\phi_1}^2 \mathcal{S}_{2\phi_2} e^{ik(ct - xC_{\phi_1}C_{\phi_2} - y\mathcal{S}_{\phi_1}C_{\phi_2} - z\mathcal{S}_{\phi_2})}\end{aligned}$$

Now we can plug these in for the point-wise axial strain in the θ direction:

$$\begin{aligned}
\dot{\sigma}_\theta(x,y,z,t) &= C_\theta^2 \frac{\partial \dot{u}_x}{\partial x} + C_\theta \mathcal{S}_\theta \left(\frac{\partial \dot{u}_x}{\partial y} + \frac{\partial \dot{u}_y}{\partial x} \right) + \mathcal{S}_\theta^2 \frac{\partial \dot{u}_y}{\partial y} \\
&= -\frac{k^2 cA}{2} \left(C_\theta^2 C_{\phi_1}^2 \mathcal{S}_{2\phi_2} + C_\theta \mathcal{S}_\theta \mathcal{S}_{2\phi_1} \mathcal{S}_{2\phi_2} + \mathcal{S}_\theta^2 \mathcal{S}_{\phi_1}^2 \mathcal{S}_{2\phi_2} \right) o_{PS} \\
&= -\frac{k^2 cA}{2} (C_\theta C_{\phi_1} + \mathcal{S}_\theta \mathcal{S}_{\phi_1})^2 \mathcal{S}_{2\phi_2} o_{PS} \\
&= -\frac{k^2 cA}{2} C_{(\phi_1-\theta)}^2 \mathcal{S}_{2\phi_2} o_{PS} \qquad \text{(B.18)}
\end{aligned}$$

4. We average $\dot{\sigma}_\theta$ over a horizontal line segment of length g, the gauge length, yielding $\dot{\sigma}_{\theta,g}$, which mimics a DAS signal in the same location in the direction $(\cos(\theta), \sin(\theta), 0)$.

$$\begin{aligned}
\dot{\sigma}_{\theta,g}(x,y,z,t) &= \frac{1}{g} \int_{-g/2}^{g/2} \dot{\sigma}_\theta(x + \nu C_\theta, y + \nu \mathcal{S}_\theta, z, t) d\nu \\
&= -\frac{k^2 cA}{2g} C_{(\phi_1-\theta)}^2 \mathcal{S}_{2\phi_2} \int_{-g/2}^{g/2} e^{ik(ct - (x+\nu C_\theta) C_{\phi_1} C_{\phi_2} - (y+\nu \mathcal{S}_\theta) \mathcal{S}_{\phi_1} C_{\phi_2} - z \mathcal{S}_{\phi_2})} d\nu \\
&= -\frac{k^2 cA}{2g} C_{(\phi_1-\theta)}^2 \mathcal{S}_{2\phi_2} e^{ik(ct - xC_{\phi_1} C_{\phi_2} - y \mathcal{S}_{\phi_1} C_{\phi_2} - z \mathcal{S}_{\phi_2})} \dots \\
&\quad \times \left[\frac{e^{-ik\nu(C_\theta C_{\phi_1} + \mathcal{S}_\theta \mathcal{S}_{\phi_1}) C_{\phi_2}}}{-ik(C_\theta C_{\phi_1} + \mathcal{S}_\theta \mathcal{S}_{\phi_1})} C_{\phi_2} \right]_{-g/2}^{g/2} \\
&= -\frac{kcA}{gC_{(\phi_1-\theta)} C_{\phi_2}} C_{(\phi_1-\theta)}^2 \mathcal{S}_{2\phi_2} e^{ik(ct - xC_{\phi_1} C_{\phi_2} - y \mathcal{S}_{\phi_1} C_{\phi_2} - z \mathcal{S}_{\phi_2})} \dots \\
&\quad \times \left[\frac{e^{-ik\nu C_{(\phi_1-\theta)} C_{\phi_2}}}{2i} \right]_{g/2}^{-g/2} \\
&= -\frac{kcA}{gC_{\phi_2}} C_{(\phi_1-\theta)} \mathcal{S}_{2\phi_2} \sin\left(\frac{kgC_{(\phi_1-\theta)} C_{\phi_2}}{2} \right) o_{PS} \qquad \text{(B.19)}
\end{aligned}$$

5. We verify that $\lim_{k \to 0} \frac{\dot{\sigma}_{\theta,g}}{\dot{\sigma}_\theta} = 1$, i.e. at long wavelengths, the average strain rate over a fixed gauge length acts like a point-wise axial strain rate measurement in the same direction.

$$\begin{aligned}
\lim_{k\to 0}\frac{\dot{\sigma}_{\theta,g}}{\dot{\sigma}_{\theta}} &= \lim_{k\to 0}\frac{-\frac{kcA}{gC_{\phi_2}}C_{(\phi_1-\theta)}\mathcal{S}_{2\phi_2}\sin\left(\frac{kgC_{(\phi_1-\theta)}C_{\phi_2}}{2}\right)o_{PS}}{-\frac{k^2cA}{2}C^2_{(\phi_1-\theta)}\mathcal{S}_{2\phi_2}o_{PS}} \\
&= \lim_{k\to 0}\frac{2\sin\left(\frac{kgC_{(\phi_1-\theta)}C_{\phi_2}}{2}\right)}{kgC_{\phi_2}C_{(\phi_1-\theta)}} \\
&= \lim_{k\to 0}\frac{2\cos\left(\frac{kgC_{(\phi_1-\theta)}C_{\phi_2}}{2}\right)\frac{gC_{(\phi_1-\theta)}C_{\phi_2}}{2}}{gC_{\phi_2}C_{(\phi_1-\theta)}} \\
&= 1
\end{aligned}$$

6. We calculate the cross-correlation of two horizontal particle velocity measurements, $\dot{u}_{\theta_1}(x_1, y_1, z)$ and $\dot{u}_{\theta_2}(x_2, y_2, z)$, simultaneously recording the same plane wave.

$$\begin{aligned}
\frac{1}{2T}\int_{-T}^{T}\dot{u}_{\theta_1}(x_1, y_1, z, t)\dot{u}^*_{\theta_2}(x_2, y_2, z, t+\tau)dt &= \\
\frac{1}{2T}\int_{-T}^{T}-ickAC_{\phi_1-\theta_1}\mathcal{S}_{\phi_2}e^{ik(ct-x_1C_{\phi_1}C_{\phi_2}-y_1\mathcal{S}_{\phi_1}C_{\phi_2}-z\mathcal{S}_{\phi_2})}\ldots & \\
\times ickAC_{\phi_1-\theta_2}\mathcal{S}_{\phi_2}e^{-ik(c(t+\tau)-x_2C_{\phi_1}C_{\phi_2}-y_2\mathcal{S}_{\phi_1}C_{\phi_2}-z\mathcal{S}_{\phi_2})}dt &= \\
\frac{c^2k^2A^2}{2T}C_{\phi_1-\theta_1}C_{\phi_1-\theta_2}\mathcal{S}^2_{\phi_2}e^{-ik(c\tau+(x_1-x_2)C_{\phi_1}C_{\phi_2}+(y_1-y_2)\mathcal{S}_{\phi_1}C_{\phi_2})}\int_{-T}^{T}dt &= \\
c^2k^2A^2C_{\phi_1-\theta_1}C_{\phi_1-\theta_2}\mathcal{S}^2_{\phi_2}e^{-ik(c\tau+(x_1-x_2)C_{\phi_1}C_{\phi_2}+(y_1-y_2)\mathcal{S}_{\phi_1}C_{\phi_2})} &= \quad \text{(B.20)}
\end{aligned}$$

7. We calculate the cross-correlation of two horizontal point-wise axial strain rate measurements, $\dot{\sigma}_{\theta_1}(x_1, y_1, z)$ and $\dot{\sigma}_{\theta_2}(x_2, y_2, z)$, simultaneously recording the same plane wave.

$$
\begin{aligned}
\frac{1}{2T}\int_{-T}^{T}\dot{\sigma}_{\theta_1}(x_1,y_1,z,t)\dot{\sigma}^{*}_{\theta_2}(x_2,y_2,z,t+\tau)dt &= \\
\frac{1}{2T}\int_{-T}^{T}-\frac{ck^2}{2}C^2_{(\phi_1-\theta_1)}\mathcal{S}_{2\phi_2}Ae^{ik(ct-x_1C_{\phi_1}C_{\phi_2}-y_1\mathcal{S}_{\phi_1}C_{\phi_2}-z\mathcal{S}_{\phi_2})}\dots & \\
\times\left(-\frac{ck^2}{2}\right)C^2_{(\phi_1-\theta_2)}\mathcal{S}_{2\phi_2}Ae^{ik(c(t+\tau)-x_2C_{\phi_1}C_{\phi_2}-y_2\mathcal{S}_{\phi_1}C_{\phi_2}-z\mathcal{S}_{\phi_2})}dt &= \\
\frac{c^2k^4A^2}{8T}C^2_{(\phi_1-\theta_1)}C^2_{(\phi_1-\theta_2)}\mathcal{S}^2_{2\phi_2}e^{-ik(c\tau+(x_1-x_2)C_{\phi_1}C_{\phi_2}+(y_1-y_2)\mathcal{S}_{\phi_1}C_{\phi_2})}\int_{-T}^{T}dt &= \\
\frac{c^2k^4A^2}{4}C^2_{(\phi_1-\theta_1)}C^2_{(\phi_1-\theta_2)}\mathcal{S}^2_{2\phi_2}e^{-ik(c\tau+(x_1-x_2)C_{\phi_1}C_{\phi_2}+(y_1-y_2)\mathcal{S}_{\phi_1}C_{\phi_2})} &= \quad \text{(B.21)}
\end{aligned}
$$

8. We calculate the cross-correlation of two horizontal average axial strain rate measurements over a gauge length, $\dot{\sigma}_{\theta_1,g}(x_1,y_1,z)$ and $\dot{\sigma}_{\theta_2,g}(x_2,y_2,z)$, simultaneously recording the same plane wave.

$$
\begin{aligned}
\frac{1}{2T}\int_{-T}^{T}\dot{\sigma}_{\theta_1,g}(x_1,y_1,z,t)\dot{\sigma}^{*}_{\theta_2,g}(x_2,y_2,z,t+\tau)dt &= \\
\frac{k^2c^2A^2\mathcal{S}^2_{2\phi_2}C_{(\phi_1-\theta_1)}C_{(\phi_1-\theta_2)}}{g^2C^2_{\phi_2}2T}\sin\left(\frac{kgC_{(\phi_1-\theta_1)}C_{\phi_2}}{2}\right)\sin\left(\frac{kgC_{(\phi_1-\theta_2)}C_{\phi_2}}{2}\right)\dots & \\
\dots\int_{-T}^{T}e^{ik(ct-x_1C_{\phi_1}C_{\phi_2}-y_1\mathcal{S}_{\phi_1}C_{\phi_2}-z\mathcal{S}_{\phi_2})}e^{-ik(c(t+\tau)-x_2C_{\phi_1}C_{\phi_2}-y_2\mathcal{S}_{\phi_1}C_{\phi_2}-z\mathcal{S}_{\phi_2})} &= \\
\frac{k^2c^2A^2\mathcal{S}^2_{2\phi_2}C_{(\phi_1-\theta_1)}C_{(\phi_1-\theta_2)}}{g^2C^2_{\phi_2}2T}\sin\left(\frac{kgC_{(\phi_1-\theta_1)}C_{\phi_2}}{2}\right)\dots & \\
\times\sin\left(\frac{kgC_{(\phi_1-\theta_2)}C_{\phi_2}}{2}\right)e^{-ik(c\tau+(x_1-x_2)C_{\phi_1}C_{\phi_2}+(y_1-y_2)\mathcal{S}_{\phi_1}C_{\phi_2})}\int_{-T}^{T}dt &= \\
\frac{k^2c^2A^2\mathcal{S}^2_{2\phi_2}C_{(\phi_1-\theta_1)}C_{(\phi_1-\theta_2)}}{g^2C^2_{\phi_2}}\sin\left(\frac{kgC_{(\phi_1-\theta_1)}C_{\phi_2}}{2}\right)\dots & \\
\times\sin\left(\frac{kgC_{(\phi_1-\theta_2)}C_{\phi_2}}{2}\right)e^{-ik(c\tau+(x_1-x_2)C_{\phi_1}C_{\phi_2}+(y_1-y_2)\mathcal{S}_{\phi_1}C_{\phi_2})} &= \\
& \quad \text{(B.22)}
\end{aligned}
$$

9. We verify that $\lim_{k\to 0} \frac{\dot{\sigma}_{\theta_1,g}(x_1,y_1,z)\star\dot{\sigma}_{\theta_2,g}(x_2,y_2,z)}{\dot{\sigma}_{\theta_1}(x_1,y_1,z)\star\dot{\sigma}_{\theta_2}(x_2,y_2,z)} = 1$, verifying that the behavior of interferometry of DAS measurements is the same as interferometry of point-wise axial strain rate measurements at long wavelengths.

$$\lim_{k\to 0} \frac{\dot{\sigma}_{\theta_1,g}(x_1,y_1,z)\star\dot{\sigma}_{\theta_2,g}(x_2,y_2,z)}{\dot{\sigma}_{\theta_1}(x_1,y_1,z)\star\dot{\sigma}_{\theta_2}(x_2,y_2,z)} =$$

$$\lim_{k\to 0} \frac{\frac{k^2c^2A^2\mathcal{S}^2_{2\phi_2}C_{(\phi_1-\theta_1)}C_{(\phi_1-\theta_2)}}{g^2C^2_{\phi_2}}\sin\left(\frac{kgC_{(\phi_1-\theta_1)}C_{\phi_2}}{2}\right)\sin\left(\frac{kgC_{(\phi_1-\theta_2)}C_{\phi_2}}{2}\right)o^\tau_{PS}}{\frac{c^2k^4A^2}{4}C^2_{(\phi_1-\theta_1)}C^2_{(\phi_1-\theta_2)}\mathcal{S}^2_{2\phi_2}o^\tau_{PS}} =$$

$$\lim_{k\to 0} \frac{4\sin\left(\frac{kgC_{(\phi_1-\theta_1)}C_{\phi_2}}{2}\right)\sin\left(\frac{kgC_{(\phi_1-\theta_2)}C_{\phi_2}}{2}\right)}{k^2g^2C^2_{\phi_2}C_{(\phi_1-\theta_1)}C_{(\phi_1-\theta_2)}} =$$

$$\lim_{k\to 0}\left[\frac{\left(\frac{gC_{(\phi_1-\theta_1)}C_{\phi_2}}{2}\right)\cos\left(\frac{kgC_{(\phi_1-\theta_1)}C_{\phi_2}}{2}\right)\sin\left(\frac{kgC_{(\phi_1-\theta_2)}C_{\phi_2}}{2}\right)}{\frac{1}{2}kg^2C^2_{\phi_2}C_{(\phi_1-\theta_1)}C_{(\phi_1-\theta_2)}}\cdots\right.$$

$$\left.+\frac{\sin\left(\frac{kgC_{(\phi_1-\theta_1)}C_{\phi_2}}{2}\right)\left(\frac{gC_{(\phi_1-\theta_2)}C_{\phi_2}}{2}\right)\cos\left(\frac{kgC_{(\phi_1-\theta_2)}C_{\phi_2}}{2}\right)}{\frac{1}{2}kg^2C^2_{\phi_2}C_{(\phi_1-\theta_1)}C_{(\phi_1-\theta_2)}}\right] =$$

$$\lim_{k\to 0}\left[\frac{C_{(\phi_1-\theta_1)}\cos\left(\frac{kgC_{(\phi_1-\theta_1)}C_{\phi_2}}{2}\right)\sin\left(\frac{kgC_{(\phi_1-\theta_2)}C_{\phi_2}}{2}\right)}{kgC_{\phi_2}C_{(\phi_1-\theta_1)}C_{(\phi_1-\theta_2)}}\cdots\right.$$

$$\left.+\frac{\sin\left(\frac{kgC_{(\phi_1-\theta_1)}C_{\phi_2}}{2}\right)C_{(\phi_1-\theta_2)}\cos\left(\frac{kgC_{(\phi_1-\theta_2)}C_{\phi_2}}{2}\right)}{kgC_{\phi_2}C_{(\phi_1-\theta_1)}C_{(\phi_1-\theta_2)}}\right] =$$

$$\lim_{k\to 0}\left[\frac{-\frac{g}{2}(C^2_{(\phi_1-\theta_1)}+C^2_{(\phi_1-\theta_2)})C_{\phi_2}\sin\left(\frac{kgC_{(\phi_1-\theta_1)}C_{\phi_2}}{2}\right)\sin\left(\frac{kgC_{(\phi_1-\theta_1)}C_{\phi_2}}{2}\right)}{gC_{\phi_2}C_{(\phi_1-\theta_1)}C_{(\phi_1-\theta_2)}}\cdots\right.$$

$$\left.+\frac{gC_{(\phi_1-\theta_1)}C_{(\phi_1-\theta_2)}C_{\phi_2}\cos\left(\frac{kgC_{(\phi_1-\theta_1)}C_{\phi_2}}{2}\right)\cos\left(\frac{kgC_{(\phi_1-\theta_1)}C_{\phi_2}}{2}\right)}{gC_{\phi_2}C_{(\phi_1-\theta_1)}C_{(\phi_1-\theta_2)}}\right] =$$

$$0+1 =$$

B.5 SH waves

1. We take a time derivative for 3D particle velocities $\dot{\mathbf{u}} = (\dot{u}_x, \dot{u}_y, \dot{u}_z)$

$$\begin{aligned} \dot{\mathbf{u}} &= \partial_t \left[A(\mathcal{S}_{\phi_1}, -\mathcal{C}_{\phi_1}, 0) e^{ik(ct - x\mathcal{C}_{\phi_1}\mathcal{C}_{\phi_2} - y\mathcal{S}_{\phi_1}\mathcal{C}_{\phi_2} - z\mathcal{S}_{\phi_2})} \right] \\ &= ikcA(\mathcal{S}_{\phi_1}, -\mathcal{C}_{\phi_1}, 0) e^{ik(ct - x\mathcal{C}_{\phi_1}\mathcal{C}_{\phi_2} - y\mathcal{S}_{\phi_1}\mathcal{C}_{\phi_2} - z\mathcal{S}_{\phi_2})} \end{aligned} \tag{B.23}$$

2. By applying a single rotation matrix to $\dot{\mathbf{u}}$ we can calculate the particle velocity $\dot{u}_\theta$ as detected by a geophone in the in the $(\cos(\theta), \sin(\theta), 0)$ direction.

$$\begin{aligned} \dot{u}_\theta &= ikcA(\mathcal{C}_\theta \mathcal{S}_{\phi_1} - \mathcal{S}_\theta \mathcal{C}_{\phi_1}) o_{PS} \\ &= ikcA\mathcal{S}_{(\phi_1 - \theta)} o_{PS} \end{aligned}$$

3. We calculate horizontal spatial derivatives of $\dot{\mathbf{u}}$ then plug them into Equation A.5 to calculate the pointwise axial strain rate in the $(\cos(\theta), \sin(\theta), 0)$ direction, $\dot{\sigma}_\theta$.

   First, let's calculate the point-wise axial strain of a horizontal fiber oriented in the $(\mathcal{C}_\theta, \mathcal{S}_\theta, 0)$ direction at the point $(x, y.z)$. The first steps are to calculate our spatial derivatives of the particle velocity, keeping in mind that $\dot{u}_x = ickA\mathcal{S}_{\phi_1} o_{PS}$ and

$\dot{u}_y = -ickAC_{\phi_1} o_{PS}$, where $o_{PS} = e^{ik(ct - xC_{\phi_1}C_{\phi_2} - y\mathcal{S}_{\phi_1}C_{\phi_2} - z\mathcal{S}_{\phi_2})}$:

$$\begin{aligned}
\frac{\partial \dot{u}_x}{\partial x} &= ickA\mathcal{S}_{\phi_1} e^{ik(ct - xC_{\phi_1}C_{\phi_2} - y\mathcal{S}_{\phi_1}C_{\phi_2} - z\mathcal{S}_{\phi_2})}(-ikC_{\phi_1}C_{\phi_2}) \\
&= \frac{ck^2A}{2}\mathcal{S}_{2\phi_1}C_{\phi_2} e^{ik(ct - xC_{\phi_1}C_{\phi_2} - y\mathcal{S}_{\phi_1}C_{\phi_2} - z\mathcal{S}_{\phi_2})} \\
\frac{\partial \dot{u}_y}{\partial x} &= -ickAC_{\phi_1} e^{ik(ct - xC_{\phi_1}C_{\phi_2} - y\mathcal{S}_{\phi_1}C_{\phi_2} - z\mathcal{S}_{\phi_2})}(-ikC_{\phi_1}C_{\phi_2}) \\
&= -ck^2AC_{\phi_1}^2 C_{\phi_2} e^{ik(ct - xC_{\phi_1}C_{\phi_2} - y\mathcal{S}_{\phi_1}C_{\phi_2} - z\mathcal{S}_{\phi_2})} \\
\frac{\partial \dot{u}_x}{\partial y} &= ickA\mathcal{S}_{\phi_1} e^{ik(ct - xC_{\phi_1}C_{\phi_2} - y\mathcal{S}_{\phi_1}C_{\phi_2} - z\mathcal{S}_{\phi_2})}(-ik\mathcal{S}_{\phi_1}C_{\phi_2}) \\
&= ck^2A\mathcal{S}_{\phi_1}^2 C_{\phi_2} e^{ik(ct - xC_{\phi_1}C_{\phi_2} - y\mathcal{S}_{\phi_1}C_{\phi_2} - z\mathcal{S}_{\phi_2})} \\
\frac{\partial \dot{u}_y}{\partial y} &= -ickAC_{\phi_1} e^{ik(ct - xC_{\phi_1}C_{\phi_2} - y\mathcal{S}_{\phi_1}C_{\phi_2} - z\mathcal{S}_{\phi_2})}(-ik\mathcal{S}_{\phi_1}C_{\phi_2}) \\
&= -\frac{ck^2A}{2}\mathcal{S}_{2\phi_1}C_{\phi_2} e^{ik(ct - xC_{\phi_1}C_{\phi_2} - y\mathcal{S}_{\phi_1}C_{\phi_2} - z\mathcal{S}_{\phi_2})}
\end{aligned}$$

Now we can plug these in for the point-wise axial strain in the θ direction:

$$\begin{aligned}
\dot{\sigma}_\theta(x, y, z, t) &= C_\theta^2 \frac{\partial \dot{u}_x}{\partial x} + C_\theta \mathcal{S}_\theta \left(\frac{\partial \dot{u}_x}{\partial y} + \frac{\partial \dot{u}_y}{\partial x} \right) + \mathcal{S}_\theta^2 \frac{\partial \dot{u}_y}{\partial y} \\
&= ck^2A \left(C_\theta^2 \frac{\mathcal{S}_{2\phi_1}}{2} + C_\theta \mathcal{S}_\theta \left(\mathcal{S}_{\phi_1}^2 - C_{\phi_1}^2 \right) + \mathcal{S}_\theta^2 (-\frac{\mathcal{S}_{2\phi_1}}{2}) \right) C_{\phi_2} o_{PS} \\
&= \frac{ck^2A}{2} \left((C_\theta^2 - \mathcal{S}_\theta^2)\mathcal{S}_{2\phi_1} - (C_{\phi_1}^2 - \mathcal{S}_{\phi_1}^2)\mathcal{S}_{2\theta} \right) C_{\phi_2} o_{PS} \\
&= \frac{ck^2A}{2} \left(C_{2\theta}\mathcal{S}_{2\phi_1} - C_{2\phi_1}\mathcal{S}_{2\theta} \right) C_{\phi_2} o_{PS} \\
&= \frac{ck^2A}{2} \mathcal{S}_{2(\phi_1 - \theta)} C_{\phi_2} o_{PS} \qquad \text{(B.24)}
\end{aligned}$$

4. We average $\dot{\sigma}_\theta$ over a horizontal line segment of length g, the gauge length, yielding $\dot{\sigma}_{\theta,g}$, which mimics a DAS signal in the same location in the direction $(\cos(\theta), \sin(\theta), 0)$.

$$
\begin{aligned}
\dot{\sigma}_{\theta,g}(x,y,z,t) &= \frac{1}{g}\int_{-g/2}^{g/2}\dot{\sigma}_{\theta}(x+\nu C_{\theta}, y+\nu S_{\theta}, z, t)d\nu \\
&= \frac{ck^2A}{2g}\int_{-g/2}^{g/2} S_{2(\phi_1-\theta)}C_{\phi_2}e^{ik(ct-(x+\nu C_{\theta})C_{\phi_1}C_{\phi_2}-(y+\nu S_{\theta})S_{\phi_1}C_{\phi_2}-zS_{\phi_2})}d\nu \\
&= \frac{ck^2A}{2g}S_{2(\phi_1-\theta)}C_{\phi_2}e^{ik(ct-xC_{\phi_1}C_{\phi_2}-yS_{\phi_1}C_{\phi_2}-zS_{\phi_2})}\int_{-g/2}^{g/2}e^{-ik\nu C_{(\phi_1-\theta)}C_{\phi_2}}d\nu \\
&= \frac{ck^2A}{2g}S_{2(\phi_1-\theta)}C_{\phi_2}e^{ik(ct-xC_{\phi_1}C_{\phi_2}-yS_{\phi_1}C_{\phi_2}-zS_{\phi_2})}\left[\frac{e^{-ik\nu C_{(\phi_1-\theta)}C_{\phi_2}}}{ikC_{(\phi_1-\theta)}C_{\phi_2}}\right]_{g/2}^{-g/2} \\
&= \frac{2ckA}{g}S_{(\phi_1-\theta)}\sin\left(\frac{kgC_{(\phi_1-\theta)}C_{\phi_2}}{2}\right)e^{ik(ct-xC_{\phi_1}C_{\phi_2}-yS_{\phi_1}C_{\phi_2}-zS_{\phi_2})} \quad \text{(B.25)}
\end{aligned}
$$

5. We verify that $\lim_{k\to 0}\frac{\dot{\sigma}_{\theta,g}}{\dot{\sigma}_{\theta}} = 1$, i.e. at long wavelengths, the average strain rate over a fixed gauge length acts like a point-wise axial strain rate measurement in the same direction.

$$
\begin{aligned}
\lim_{k\to 0}\frac{\dot{\sigma}_{\theta,g}}{\dot{\sigma}_{\theta}} &= \lim_{k\to 0}\frac{\frac{2ckA}{g}S_{(\phi_1-\theta)}\sin\left(\frac{kgC_{(\phi_1-\theta)}C_{\phi_2}}{2}\right)o_{PS}}{\frac{ck^2A}{2}S_{2(\phi_1-\theta)}C_{\phi_2}o_{PS}} \\
&= \lim_{k\to 0}\frac{2\sin\left(\frac{kgC_{(\phi_1-\theta)}C_{\phi_2}}{2}\right)}{kgC_{(\phi_1-\theta)}C_{\phi_2}} \\
&= \lim_{k\to 0}\frac{2\cos\left(\frac{kgC_{(\phi_1-\theta)}C_{\phi_2}}{2}\right)\left(\frac{gC_{(\phi_1-\theta)}C_{\phi_2}}{2}\right)}{gC_{(\phi_1-\theta)}C_{\phi_2}} \\
&= 1
\end{aligned}
$$

6. We calculate the cross-correlation of two horizontal particle velocity measurements, $\dot{u}_{\theta_1}(x_1, y_1, z)$ and $\dot{u}_{\theta_2}(x_2, y_2, z)$, simultaneously recording the same plane wave.

$$
\begin{aligned}
\frac{1}{2T}\int_{-T}^{T}\dot{u}_{\theta_1}(x_1,y_1,z,t)\dot{u}^{*}_{\theta_2}(x_2,y_2,z,t+\tau)dt &= \\
\frac{1}{2T}\int_{-T}^{T} ickAS_{(\phi_1-\theta_1)}e^{ik(ct-x_1C_{\phi_1}C_{\phi_2}-y_1S_{\phi_1}C_{\phi_2}-zS_{\phi_2})}\dots & \\
\times(-ickA)S_{(\phi_1-\theta_2)}e^{-ik(c(t+\tau)-x_2C_{\phi_1}C_{\phi_2}-y_2S_{\phi_1}C_{\phi_2}-zS_{\phi_2})}dt &= \\
c^2k^2A^2S_{(\phi_1-\theta_1)}S_{(\phi_1-\theta_2)}e^{-ik(c\tau+(x_1-x_2)C_{\phi_1}C_{\phi_2}+(y_1-y_2)S_{\phi_1}C_{\phi_2})}\frac{1}{2T}\int_{-T}^{T}dt &= \\
c^2k^2A^2S_{(\phi_1-\theta_1)}S_{(\phi_1-\theta_2)}e^{-ik(c\tau+(x_1-x_2)C_{\phi_1}C_{\phi_2}+(y_1-y_2)S_{\phi_1}C_{\phi_2})} &= \quad \text{(B.26)}
\end{aligned}
$$

7. We calculate the cross-correlation of two horizontal point-wise axial strain rate measurements, $\dot{\sigma}_{\theta_1}(x_1,y_1,z)$ and $\dot{\sigma}_{\theta_2}(x_2,y_2,z)$, simultaneously recording the same plane wave.

$$
\begin{aligned}
\frac{1}{2T}\int_{-T}^{T}\dot{\sigma}_{\theta_1}(x_1,y_1,z,t)\dot{\sigma}^{*}_{\theta_2}(x_2,y_2,z,t+\tau)dt &= \\
\frac{1}{2T}\int_{-T}^{T}\frac{ck^2A}{2}\mathcal{S}_{2(\phi_1-\theta_1)}C_{\phi_2}e^{ik(ct-x_1C_{\phi_1}C_{\phi_2}-y_1S_{\phi_1}C_{\phi_2}-zS_{\phi_2})}\dots & \\
\times\frac{ck^2A}{2}\mathcal{S}_{2(\phi_1-\theta_2)}C_{\phi_2}e^{-ik(c(t+\tau)-x_2C_{\phi_1}C_{\phi_2}-y_2S_{\phi_1}C_{\phi_2}-zS_{\phi_2})}dt &= \\
\frac{c^2k^4A^2}{4}\mathcal{S}_{2(\phi_1-\theta_1)}\mathcal{S}_{2(\phi_1-\theta_2)}C^2_{\phi_2}e^{-ik(c\tau+(x_1-x_2)C_{\phi_1}C_{\phi_2}+(y_1-y_2)S_{\phi_1}C_{\phi_2})}\frac{1}{2T}\int_{-T}^{T}dt &= \\
\frac{c^2k^4A^2}{4}\mathcal{S}_{2(\phi_1-\theta_1)}\mathcal{S}_{2(\phi_1-\theta_2)}C^2_{\phi_2}e^{-ik(c\tau+(x_1-x_2)C_{\phi_1}C_{\phi_2}+(y_1-y_2)S_{\phi_1}C_{\phi_2})} &= \\
& \quad \text{(B.27)}
\end{aligned}
$$

8. We calculate the cross-correlation of two horizontal average axial strain rate measurements over a gauge length, $\dot{\sigma}_{\theta_1,g}(x_1,y_1,z)$ and $\dot{\sigma}_{\theta_2,g}(x_2,y_2,z)$, simultaneously recording the same plane wave.

$$
\begin{aligned}
\frac{1}{2T}\int_{-T}^{T}\dot{\sigma}_{\theta_1,g}(x_1,y_1,z,t)\dot{\sigma}^{*}_{\theta_2,g}(x_2,y_2,z,t+\tau)dt &= \\
\frac{1}{2T}\int_{-T}^{T}\frac{2ckA}{g}\mathcal{S}_{(\phi_1-\theta_1)}\sin\left(\frac{kgC_{(\phi_1-\theta_1)}C_{\phi_2}}{2}\right)e^{ik(ct-x_1C_{\phi_1}C_{\phi_2}-y_1\mathcal{S}_{\phi_1}C_{\phi_2}-z\mathcal{S}_{\phi_2})}\dots & \\
\dots\frac{2ckA}{g}\mathcal{S}_{(\phi_1-\theta_2)}\sin\left(\frac{kgC_{(\phi_1-\theta_2)}C_{\phi_2}}{2}\right)e^{ik(c(t+\tau)-x_2C_{\phi_1}C_{\phi_2}-y_2\mathcal{S}_{\phi_1}C_{\phi_2}-z\mathcal{S}_{\phi_2})}dt &= \\
\frac{4c^2k^2A^2}{g^2}\mathcal{S}_{(\phi_1-\theta_1)}\mathcal{S}_{(\phi_1-\theta_2)}\sin\left(\frac{kgC_{(\phi_1-\theta_1)}C_{\phi_2}}{2}\right)\dots & \\
\times\sin\left(\frac{kgC_{(\phi_1-\theta_2)}C_{\phi_2}}{2}\right)e^{-ik(c\tau+(x_1-x_2)C_{\phi_1}C_{\phi_2}+(y_1-y_2)\mathcal{S}_{\phi_1}C_{\phi_2})}\frac{1}{2T}\int_{-T}^{T}dt &= \\
\frac{4c^2k^2A^2}{g^2}\mathcal{S}_{(\phi_1-\theta_1)}\mathcal{S}_{(\phi_1-\theta_2)}\sin\left(\frac{kgC_{(\phi_1-\theta_1)}C_{\phi_2}}{2}\right)\dots & \\
\times\sin\left(\frac{kgC_{(\phi_1-\theta_2)}C_{\phi_2}}{2}\right)e^{-ik(c\tau+(x_1-x_2)C_{\phi_1}C_{\phi_2}+(y_1-y_2)\mathcal{S}_{\phi_1}C_{\phi_2})} &= \\
\end{aligned}
\tag{B.28}
$$

9. We verify that $\lim_{k\to 0}\frac{\dot{\sigma}_{\theta_1,g}(x_1,y_1,z)\star\dot{\sigma}_{\theta_2,g}(x_2,y_2,z)}{\dot{\sigma}_{\theta_1}(x_1,y_1,z)\star\dot{\sigma}_{\theta_2}(x_2,y_2,z)} = 1$, verifying that the behavior of interferometry of DAS measurements is the same as interferometry of point-wise axial strain rate measurements at long wavelengths.

$$\lim_{k\to 0} \frac{\dot{\sigma}_{\theta_1,g}(x_1,y_1,z) \star \dot{\sigma}_{\theta_2,g}(x_2,y_2,z)}{\dot{\sigma}_{\theta_1}(x_1,y_1,z) \star \dot{\sigma}_{\theta_2}(x_2,y_2,z)} =$$

$$\lim_{k\to 0} \frac{\frac{4c^2k^2A^2}{g^2}\mathcal{S}_{(\phi_1-\theta_1)}\mathcal{S}_{(\phi_1-\theta_2)} \sin\left(\frac{kgC_{(\phi_1-\theta_1)}C_{\phi_2}}{2}\right) \sin\left(\frac{kgC_{(\phi_1-\theta_2)}C_{\phi_2}}{2}\right) o^{\tau}_{PS}}{\frac{c^2k^4A^2}{4}\mathcal{S}_{2(\phi_1-\theta_1)}\mathcal{S}_{2(\phi_1-\theta_2)}C^2_{\phi_2} o^{\tau}_{PS}} =$$

$$\lim_{k\to 0} \frac{4 \sin\left(\frac{kgC_{(\phi_1-\theta_1)}C_{\phi_2}}{2}\right) \sin\left(\frac{kgC_{(\phi_1-\theta_2)}C_{\phi_2}}{2}\right)}{k^2g^2C_{(\phi_1-\theta_1)}C_{(\phi_1-\theta_2)}C^2_{\phi_2}} =$$

$$\lim_{k\to 0} \left[\frac{4\cos\left(\frac{kgC_{(\phi_1-\theta_1)}C_{\phi_2}}{2}\right)\left(\frac{gC_{(\phi_1-\theta_1)}C_{\phi_2}}{2}\right)\sin\left(\frac{kgC_{(\phi_1-\theta_2)}C_{\phi_2}}{2}\right)}{2kg^2C_{(\phi_1-\theta_1)}C_{(\phi_1-\theta_2)}C^2_{\phi_2}} \cdots \right.$$

$$\left. + \frac{4\sin\left(\frac{kgC_{(\phi_1-\theta_1)}C_{\phi_2}}{2}\right)\cos\left(\frac{kgC_{(\phi_1-\theta_2)}C_{\phi_2}}{2}\right)\left(\frac{gC_{(\phi_1-\theta_2)}C_{\phi_2}}{2}\right)}{2kg^2C_{(\phi_1-\theta_1)}C_{(\phi_1-\theta_2)}C_{\phi_2}} \right] =$$

$$\lim_{k\to 0} \frac{-\frac{g}{2}(C^2_{(\phi_1-\theta_1)} + C^2_{(\phi_1-\theta_2)})C_{\phi_2} \sin\left(\frac{kgC_{(\phi_1-\theta_1)}C_{\phi_2}}{2}\right) \sin\left(\frac{kgC_{(\phi_1-\theta_2)}C_{\phi_2}}{2}\right)}{gC_{(\phi_1-\theta_1)}C_{(\phi_1-\theta_2)}C^2_{\phi_2}} \cdots$$

$$\cdots + \lim_{k\to 0} \frac{gC_{(\phi_1-\theta_1)}C_{(\phi_1-\theta_2)}C_{\phi_2} \cos\left(\frac{kgC_{(\phi_1-\theta_1)}C_{\phi_2}}{2}\right) \cos\left(\frac{kgC_{(\phi_1-\theta_2)}C_{\phi_2}}{2}\right)}{gC_{(\phi_1-\theta_1)}C_{(\phi_1-\theta_2)}C_{\phi_2}} =$$

$$0 + 1 =$$

Appendix C

Deriving Responses to Point Sources

Here, we derive analytical expressions for idealized geophones (particle velocity $\dot{u}_\theta$) and DAS channels (point-wise axial strain rate $\dot{\sigma}_\theta$) responding to a surface point source at $\mathbf{x_s}$ that emits a wave that spreads in a circle along the Earth's surface. This is the simplified model used in the exercises in Chapter 2, so I include its detailed description here so that it is easy for other researchers to reproduce and extend the exercises. These surface wave sources mimic either a Rayleigh wave with particle motion in the direction of propagation and vertically, or a Love wave with particle motion orthogonal to the direction of propagation. Like real surface waves, we assume a $1/R$ die-off of amplitudes as the waves propagate away from their source locations, but unlike real surface waves, we assume no dispersion for the sake of analyzing an extremely simple analytical expression.

C.1 Love waves

We assume a simple model of displacement $\mathbf{u}$ at any surface point $\mathbf{x} = (x, y, 0)$ responding to a surface Love wave point source at $\mathbf{x_s} = (x_s, y_s, 0)$: a frequency f Ricker wavelet with particle motion in the direction tangent to the circular spreading surface that decays as $1/\|\mathbf{x} - \mathbf{x_s}\|_2$. The equation describing this displacement is:

$$\mathbf{u}(\mathbf{x}, t; \mathbf{x_s}) = \hat{\mathbf{T}} \frac{1}{\|\mathbf{x} - \mathbf{x_s}\|} \left(1 - 2\pi^2 f^2 (t - \frac{\|\mathbf{x} - \mathbf{x_s}\|}{c})^2\right) \exp\left(-\pi^2 f^2 (t - \frac{\|\mathbf{x} - \mathbf{x_s}\|}{c})^2\right) \quad \text{(C.1)}$$

where c is the speed of propagation and $\mathbf{T} = (\mathbf{x} - \mathbf{x_s}) \times (0, 0, 1)$, so $\hat{\mathbf{T}} = \mathbf{T}/\|\mathbf{T}\|$ is the horizontal unit vector orthogonal to the direction of propagation, so $\mathbf{T} = (y - y_s, x_s - x, 0)/\|\mathbf{x} - \mathbf{x_s}\|_2$. Taking the time derivative of the displacement and using the short notation $R = \|\mathbf{x} = \mathbf{x_s}\|$ results in the particle velocity $\dot{\mathbf{u}}$:

$$\begin{aligned}
\dot{\mathbf{u}}(\mathbf{x}, t; \mathbf{x_s}) &= \frac{\hat{\mathbf{T}}}{R}\left[\left(-4\pi^2 f^2\left(t - \frac{R}{c}\right)\right)\exp\left(-\pi^2 f^2\left(t - \frac{R}{c}\right)^2\right)\ldots\right. \\
&\quad \left.\ldots + \left(1 - 2\pi^2 f^2\left(t - \frac{R}{c}\right)^2\right)\left(-\pi^2 f^2 2\left(t - \frac{R}{c}\right)\right)\exp\left(-\pi^2 f^2\left(t - \frac{R}{c}\right)^2\right)\right] \\
&= \frac{\hat{\mathbf{T}}}{R}\exp\left(-\pi^2 f^2\left(t - \frac{R}{c}\right)^2\right)\left(3 - 2\pi^2 f^2\left(t - \frac{R}{c}\right)^2\right)\left(-\pi^2 f^2 2\left(t - \frac{R}{c}\right)\right) \quad \text{(C.2)}
\end{aligned}$$

so the measurement detected by a geophone's x-component would be

$$\dot{u}_x(\mathbf{x}, t; \mathbf{x_s}) = \frac{y - y_s}{R^2}\exp\left(-\pi^2 f^2 (t - \frac{R}{c})^2\right)\left(-6\pi^2 f^2 (t - \frac{R}{c}) + 4\pi^4 f^4 (t - \frac{R}{c})^3\right) \quad \text{(C.3)}$$

and the measurement detected by a geophone's y-component would be

$$\dot{u}_y(\mathbf{x}, t; \mathbf{x_s}) = \frac{x_s - x}{R^2}\exp\left(-\pi^2 f^2 (t - \frac{R}{c})^2\right)\left(-6\pi^2 f^2 (t - \frac{R}{c}) + 4\pi^4 f^4 (t - \frac{R}{c})^3\right) \quad \text{(C.4)}$$

To calculate the point-wise strain axial strain rate detected by a fiber oriented in the i direction, we can use the chain rule with $\|\mathbf{x} - \mathbf{x_s}\|$ as an intermediate variable, $\frac{\partial \dot{u}_x(\mathbf{x},t;\mathbf{x_s})}{\partial x} = \frac{\partial \dot{u}_x(\mathbf{x},t;\mathbf{x_s})}{\partial R}\frac{\partial R}{\partial x}$ where the second term can be calculated as

$\frac{\partial R}{\partial x} = \partial_x\left(\sqrt{(x - x_s)^2 + (y - y_s)^2}\right) = \frac{x - x_s}{\sqrt{(x-x_s)^2+(y-y_s)^2}} = \frac{x - x_s}{R}$

and the first term can be calculated using the product rule:

$$\begin{aligned}
\frac{\partial \dot{u}_x(\mathbf{x},t;\mathbf{x_s})}{\partial R} &= \frac{-2(y-y_s)}{R^3}\exp\left(-\pi^2 f^2(t-\frac{R}{c})^2\right)\left(-6\pi^2 f^2(t-\frac{R}{c})+4\pi^4 f^4(t-\frac{R}{c})^3\right)\dots \\
&\quad +\frac{y-y_s}{R^2}\exp\left(-\pi^2 f^2(t-\frac{R}{c})^2\right)\left(\pi^2 f^2 2(t-\frac{R}{c})\frac{1}{c}\right)\left(-6\pi^2 f^2(t-\frac{R}{c})\dots\right. \\
&\quad \left.+4\pi^4 f^4(t-\frac{R}{c})^3\right)\dots \\
&\quad +\frac{y-y_s}{R^2}\exp\left(-\pi^2 f^2(t-\frac{R}{c})^2\right)\left(\frac{6\pi^2 f^2}{c}-\frac{12\pi^4 f^4}{c}(t-\frac{R}{c})^2\right) \\
&= \exp\left(-\pi^2 f^2(t-\frac{R}{c})^2\right)\frac{y-y_s}{R^2}\left[\frac{(-2)}{R}\left(-6\pi^2 f^2(t-\frac{R}{c})\dots\right.\right. \\
&\quad \left.+4\pi^4 f^4\left(t-\frac{R}{c}\right)^3\right)+\frac{\pi^2 f^2 2\left(t-\frac{R}{c}\right)}{c}\left(-6\pi^2 f^2(t-\frac{R}{c})\dots\right. \\
&\quad \left.\left.+4\pi^4 f^4\left(t-\frac{R}{c}\right)^3\right)+\frac{6\pi^2 f^2}{c}-\frac{12\pi^4 f^4}{c}\left(t-\frac{R}{c}\right)^2\right] \\
&= \exp\left(-\pi^2 f^2\left(t-\frac{R}{c}\right)^2\right)\frac{x_j-x_{sj}}{R^2}\left[\frac{6\pi^2 f^2}{c}+\frac{12\pi^2 f^2}{R}\left(t-\frac{R}{c}\right)\dots\right. \\
&\quad \left.-\frac{24\pi^4 f^4}{c}\left(t-\frac{R}{c}\right)^2-\frac{8\pi^4 f^4}{R}\left(t-\frac{R}{c}\right)^3+\frac{4\pi^6 f^6 2}{c}\left(t-\frac{R}{c}\right)^4\right]
\end{aligned}$$

so we can put the two terms together to get the i direction axial strain rate:

$$\begin{aligned}
\frac{\partial \dot{u}_x(\mathbf{x},t;\mathbf{x_s})}{\partial x} &= \exp\left(-\pi^2 f^2\left(t-\frac{R}{c}\right)^2\right)\frac{(y-y_s)(x-x_s)}{R^3}\left(\frac{6\pi^2 f^2}{c}+\frac{12\pi^2 f^2}{R}(t-\frac{R}{c})\dots\right. \\
&\quad \left.-\frac{24\pi^4 f^4}{c}(t-\frac{R}{c})^2-\frac{8\pi^4 f^4}{R}(t-\frac{R}{c})^3+\frac{4\pi^6 f^6 2}{c}(t-\frac{R}{c})^4\right) \qquad \text{(C.5)}
\end{aligned}$$

To calculate the point-wise strain axial strain rate detected by a fiber oriented in the y-direction, we again use the chain rule with $\|\mathbf{x}-\mathbf{x_s}\|$ as an intermediate variable $\frac{\partial \dot{u}_y(\mathbf{x},t;\mathbf{x_s})}{\partial y} = \frac{\partial \dot{u}_y(\mathbf{x},t;\mathbf{x_s})}{\partial \|\mathbf{x}-\mathbf{x_s}\|}\frac{\partial \|\mathbf{x}-\mathbf{x_s}\|}{\partial y}$ where the second term can be calculated as $\frac{\partial \|\mathbf{x}-\mathbf{x_s}\|}{\partial y} = \partial_y\left(\sqrt{(x-x_s)^2+(y-y_s)^2}\right) = \frac{y-y_s}{\sqrt{(x-x_s)^2+(y-y_s)^2}} = \frac{y-y_s}{\|\mathbf{x}-\mathbf{x_s}\|}$

and the first term can be calculated using the product rule

$$\begin{aligned}
\frac{\partial \dot{u}_y(\mathbf{x},t;\mathbf{x_s})}{\partial \|\mathbf{x}-\mathbf{x_s}\|} &= \frac{2(x-x_s)}{R^3}\exp\left(-\pi^2 f^2(t-\frac{R}{c})^2\right)\left(-6\pi^2 f^2(t-\frac{R}{c})+4\pi^4 f^4(t-\frac{R}{c})^3\right)\ldots \\
&\quad +\frac{x_s-x}{R^2}\exp\left(-\pi^2 f^2(t-\frac{R}{c})^2\right)(\pi^2 f^2 2(t-\frac{R}{c})\frac{1}{c})\left(-6\pi^2 f^2(t-\frac{R}{c})\ldots\right. \\
&\quad \left.+4\pi^4 f^4(t-\frac{R}{c})^3\right)+\frac{x_s-x}{R^2}\exp\left(-\pi^2 f^2(t-\frac{R}{c})^2\right)\left(\frac{6\pi^2 f^2}{c}\ldots\right. \\
&\quad \left.-\frac{12\pi^4 f^4}{c}(t-\frac{R}{c})^2\right) \\
&= \exp\left(-\pi^2 f^2(t-\frac{R}{c})^2\right)\frac{x_s-x}{R^2}\left[\frac{-2}{R}\left(-6\pi^2 f^2(t-\frac{R}{c})+4\pi^4 f^4(t-\frac{R}{c})^3\right)\ldots\right. \\
&\quad +\frac{\pi^2 f^2 2(t-\frac{R}{c})}{c}\left(-6\pi^2 f^2(t-\frac{R}{c})+4\pi^4 f^4(t-\frac{R}{c})^3\right)+\frac{6\pi^2 f^2}{c} \\
&\quad \left.-\frac{12\pi^4 f^4}{c}(t-\frac{R}{c})^2\right] \\
&= \exp\left(-\pi^2 f^2(t-\frac{R}{c})^2\right)\frac{x_s-x}{R^2}\left(\frac{6\pi^2 f^2}{c}+\frac{12\pi^2 f^2}{R}(t-\frac{R}{c})\ldots\right. \\
&\quad \left.-\frac{24\pi^4 f^4}{c}(t-\frac{R}{c})^2-\frac{8\pi^4 f^4}{R}(t-\frac{R}{c})^3+\frac{4\pi^6 f^6 2}{c}(t-\frac{R}{c})^4\right)
\end{aligned}$$

Then when we combine the two chain-rule terms to get the axial strain measurement in the y-direction, we get

$$\begin{aligned}
\frac{\partial \dot{u}_y(\mathbf{x},t;\mathbf{x_s})}{\partial y} &= \frac{(x_s-x)(y-y_s)}{R^3}\exp\left(-\pi^2 f^2(t-\frac{R}{c})^2\right)\left(\frac{6\pi^2 f^2}{c}+\frac{12\pi^2 f^2}{R}(t-\frac{R}{c})\ldots\right. \\
&\quad \left.-\frac{24\pi^4 f^4}{c}(t-\frac{R}{c})^2-\frac{8\pi^4 f^4}{R}(t-\frac{R}{c})^3+\frac{8\pi^6 f^6}{c}(t-\frac{R}{c})^4\right) \qquad \text{(C.6)}
\end{aligned}$$

C.2 Rayleigh waves

Assume the horizontal particle displacement, $\mathbf{u}$, at $\mathbf{x}$ to a point source at $\mathbf{x_s}$ will be a Ricker wavelet that decays as 1/distance:

$$\mathbf{u}(\mathbf{x}, t; \mathbf{x_s}) = \hat{\mathbf{R}} \frac{1}{\|\mathbf{x} - \mathbf{x_s}\|} \left(1 - 2\pi^2 f^2 (t - \frac{\|\mathbf{x} - \mathbf{x_s}\|}{c})^2\right) \exp\left(-\pi^2 f^2 (t - \frac{\|\mathbf{x} - \mathbf{x_s}\|}{c})^2\right) \quad \text{(C.7)}$$

where c is the speed of propagation, f is the peak frequency of the Ricker wavelet, and $\mathbf{R} = \mathbf{x} - \mathbf{x_s}$, so $\hat{\mathbf{R}} = \mathbf{R}/\|\mathbf{R}\|$ is the horizontal unit vector orthogonal to the direction of propagation. While a Rayleigh wave also has a vertical displacement component, we ignore that term because it would not mix with the horizontal components as observed either through a horizontal strain rate or velocity measurement. Taking the time derivative of the displacement, and using the notation $R = \|\mathbf{x} - \mathbf{x_s}\|$, we get the particle velocity $\dot{\mathbf{u}}$:

$$\begin{aligned} \dot{\mathbf{u}}(\mathbf{x}, t; \mathbf{x_s}) &= \frac{\hat{\mathbf{R}}}{\|\mathbf{x} - \mathbf{x_s}\|} \left[\left(-4\pi^2 f^2 \left(t - \frac{R}{c}\right)\right) \exp\left(-\pi^2 f^2 (t - \frac{R}{c})^2\right) \ldots \right. \\ &\quad \left. + \left(1 - 2\pi^2 f^2 \left(t - \frac{R}{c}\right)^2\right) \left(-\pi^2 f^2 2 \left(t - \frac{R}{c}\right)\right) \exp\left(-\pi^2 f^2 (t - \frac{R}{c})^2\right) \right] \\ &= \frac{\hat{\mathbf{R}}}{R} \exp\left(-\pi^2 f^2 \left(t - \frac{R}{c}\right)^2\right) \left(-6\pi^2 f^2 \left(t - \frac{R}{c}\right) + 4\pi^4 f^4 \left(t - \frac{R}{c}\right)^3\right) \quad \text{(C.8)} \end{aligned}$$

The measurement detected by a geophone's x- and y-components would be:

$$\begin{aligned} \dot{u}_x(\mathbf{x}, t; \mathbf{x_s}) &= \frac{x - x_s}{\|\mathbf{x} - \mathbf{x_s}\|^2} \exp\left(-\pi^2 f^2 (t - \frac{\|\mathbf{x} - \mathbf{x_s}\|}{c})^2\right) \ldots \\ &\quad \left(-6\pi^2 f^2 (t - \frac{\|\mathbf{x} - \mathbf{x_s}\|}{c}) + 4\pi^4 f^4 (t - \frac{\|\mathbf{x} - \mathbf{x_s}\|}{c})^3\right) \quad \text{(C.9)} \end{aligned}$$

$$\begin{aligned}\dot{u}_y(\mathbf{x}, t; \mathbf{x_s}) &= \frac{y - y_s}{\|\mathbf{x} - \mathbf{x_s}\|^2} \exp\left(-\pi^2 f^2 (t - \frac{\|\mathbf{x} - \mathbf{x_s}\|}{c})^2\right) \ldots \\ &\left(-6\pi^2 f^2 (t - \frac{\|\mathbf{x} - \mathbf{x_s}\|}{c}) + 4\pi^4 f^4 (t - \frac{\|\mathbf{x} - \mathbf{x_s}\|}{c})^3\right) \qquad \text{(C.10)}\end{aligned}$$

To calculate the point-wise strain axial strain rate detected by a fiber oriented in the i direction, we can use the chain rule with $\|\mathbf{x} - \mathbf{x_s}\|$ as an intermediate variable $\frac{\partial \dot{u}_x(\mathbf{x},t;\mathbf{x_s})}{\partial x} = \frac{\partial \dot{u}_x(\mathbf{x},t;\mathbf{x_s})}{\partial \|\mathbf{x}-\mathbf{x_s}\|} \frac{\partial \|\mathbf{x}-\mathbf{x_s}\|}{\partial x}$ so the second term can be calculated as

$$\frac{\partial \|\mathbf{x} - \mathbf{x_s}\|}{\partial x} = \partial_x \left(\sqrt{(x - x_s)^2 + (y - y_s)^2}\right) = \frac{x - x_s}{\sqrt{(x - x_s)^2 + (y - y_s)^2}} = \frac{x - x_s}{\|\mathbf{x} - \mathbf{x_s}\|}$$

and the first term can be calculated using the product rule (defining the notation $R := \|\mathbf{x} - \mathbf{x_s}\|$)

$$
\begin{aligned}
\frac{\partial \dot{u}_x(\mathbf{x},t;\mathbf{x_s})}{\partial \|\mathbf{x}-\mathbf{x_s}\|} &= \frac{2(x_s-x)}{R^3}\exp\left(-\pi^2 f^2(t-\frac{R}{c})^2\right)\left(-6\pi^2 f^2(t-\frac{R}{c})+4\pi^4 f^4(t-\frac{R}{c})^3\right)\dots \\
&\quad +\frac{x-x_s}{R^2}\exp\left(-\pi^2 f^2(t-\frac{R}{c})^2\right)\left(\pi^2 f^2 2\left(t-\frac{R}{c}\right)\frac{1}{c}\right)\left(-6\pi^2 f^2(t-\frac{R}{c})\dots\right. \\
&\quad \left.+4\pi^4 f^4\left(t-\frac{R}{c}\right)^3\right)+\frac{x-x_s}{R^2}\exp\left(-\pi^2 f^2(t-\frac{R}{c})^2\right)\left(\frac{6\pi^2 f^2}{c}\dots\right. \\
&\quad \left.-\frac{12\pi^4 f^4}{c}\left(t-\frac{R}{c}\right)^2\right) \\
&= \exp\left(-\pi^2 f^2\left(t-\frac{R}{c}\right)^2\right)\frac{x\_x_s}{R^2}\left[\frac{-2}{R}\left(-6\pi^2 f^2\left(t-\frac{R}{c}\right)\dots\right.\right. \\
&\quad \left.+4\pi^4 f^4\left(t-\frac{R}{c}\right)^3\right)+\frac{\pi^2 f^2 2\left(t-\frac{R}{c}\right)}{c}\left(-6\pi^2 f^2\left(t-\frac{R}{c}\right)\dots\right. \\
&\quad \left.\left.+4\pi^4 f^4\left(t-\frac{R}{c}\right)^3\right)+\frac{6\pi^2 f^2}{c}-\frac{12\pi^4 f^4}{c}\left(t-\frac{R}{c}\right)^2\right] \\
&= \exp\left(-\pi^2 f^2\left(t-\frac{R}{c}\right)^2\right)\frac{x-x_s}{R^2}\left(\frac{6\pi^2 f^2}{c}+\frac{12\pi^2 f^2}{R}\left(t-\frac{R}{c}\right)\dots\right. \\
&\quad \left.-\frac{24\pi^4 f^4}{c}\left(t-\frac{R}{c}\right)^2-\frac{8\pi^4 f^4}{R}\left(t-\frac{R}{c}\right)^3+\frac{4\pi^6 f^6 2}{c}\left(t-\frac{R}{c}\right)^4\right)
\end{aligned}
$$

When we combine the two derivative terms, we get point-wise axial strain rate in the i direction as:

$$
\begin{aligned}
\frac{\partial \dot{u}_x(\mathbf{x},t;\mathbf{x_s})}{\partial x} &= \exp\left(-\pi^2 f^2\left(t-\frac{R}{c}\right)^2\right)\frac{(x-x_s)^2}{R^3}\left(\frac{6\pi^2 f^2}{c}+\frac{12\pi^2 f^2}{R}(t-\frac{R}{c})\dots\right. \\
&\quad \left.-\frac{24\pi^4 f^4}{c}\left(t-\frac{R}{c}\right)^2-\frac{8\pi^4 f^4}{R}\left(t-\frac{R}{c}\right)^3+\frac{8\pi^6 f^6}{c}\left(t-\frac{R}{c}\right)^4\right) \qquad \text{(C.11)}
\end{aligned}
$$

To calculate the point-wise strain axial strain rate detected by a fiber oriented in the y-direction, we can use the chain rule with $\|\mathbf{x}-\mathbf{x_s}\|$ as an intermediate variable $\frac{\partial \dot{u}_y(\mathbf{x},t;\mathbf{x_s})}{\partial y} =$

$\frac{\partial \dot{u}_y(\mathbf{x},t;\mathbf{x_s})}{\partial \|\mathbf{x}-\mathbf{x_s}\|}\frac{\partial \|\mathbf{x}-\mathbf{x_s}\|}{\partial y}$, so the second term can be calculated as

$$\frac{\partial \|\mathbf{x}-\mathbf{x_s}\|}{\partial y} = \partial_y\left(\sqrt{(x-x_s)^2+(y-y_s)^2}\right) = \frac{y-y_s}{\sqrt{(x-x_s)^2+(y-y_s)^2}} = \frac{y-y_s}{\|\mathbf{x}-\mathbf{x_s}\|}$$

and the first term can be calculated using the product rule:

$$\begin{aligned}
\frac{\partial \dot{u}_y(\mathbf{x},t;\mathbf{x_s})}{\partial \|\mathbf{x}-\mathbf{x_s}\|} &= \frac{2(y_s-y)}{R^3}\exp\left(-\pi^2 f^2\left(t-\frac{R}{c}\right)^2\right)\left(-6\pi^2 f^2\left(t-\frac{R}{c}\right)\ldots\right.\\
&\quad \left.+4\pi^4 f^4\left(t-\frac{R}{c}\right)^3\right) + \frac{y-y_s}{R^2}\exp\left(-\pi^2 f^2\left(t-\frac{R}{c}\right)^2\right)\frac{\pi^4 f^4 2}{c}\ldots\\
&\quad \times\left(t-\frac{R}{c}\right)^2\left(-6+4\pi^2 f^2\left(t-\frac{R}{c}\right)^2\right)\ldots\\
&\quad +\frac{y-y_s}{R^2}\exp\left(-\pi^2 f^2\left(t-\frac{R}{c}\right)^2\right)\left(\frac{6\pi^2 f^2}{c}-\frac{12\pi^4 f^4}{c}\left(t-\frac{R}{c}\right)^2\right)\\
&= \exp\left(-\pi^2 f^2\left(t-\frac{R}{c}\right)^2\right)\frac{y-y_s}{R^2}\left(\frac{6\pi^2 f^2}{c}+\frac{12\pi^2 f^2}{R}\left(t-\frac{R}{c}\right)\ldots\right.\\
&\quad \left.-\frac{24\pi^4 f^4}{c}\left(t-\frac{R}{c}\right)^2-\frac{8\pi^4 f^4}{R}\left(t-\frac{R}{c}\right)^3+\frac{4\pi^6 f^6 2}{c}\left(t-\frac{R}{c}\right)^4\right)
\end{aligned}$$

and when we combine these two terms we get the yy-component of the strain rate:

$$\begin{aligned}
\frac{\partial \dot{u}_y(\mathbf{x},t;\mathbf{x_s})}{\partial y} &= \exp\left(-\pi^2 f^2\left(t-\frac{R}{c}\right)^2\right)\frac{(y-y_s)^2}{R^3}\left(\frac{6\pi^2 f^2}{c}+\frac{12\pi^2 f^2}{R}\left(t-\frac{R}{c}\right)\ldots\right.\\
&\quad \left.-\frac{24\pi^4 f^4}{c}\left(t-\frac{R}{c}\right)^2-\frac{8\pi^4 f^4}{R}\left(t-\frac{R}{c}\right)^3+\frac{8\pi^6 f^6}{c}\left(t-\frac{R}{c}\right)^4\right) \qquad \text{(C.12)}
\end{aligned}$$

Appendix D

3D Extension of Corner Data Analysis

As seen in Chapter 4, there often appear to be sign-flips in strain rate data recorded along orthogonal horizontal fiber lines, both at corners of the array where a fiber bends suddenly, and at locations where the fibers cross each others' paths in perpendicular directions. This feature has also been observed at the Fairbanks Array and Richmond Field Station [35]. An intuition for why this occurs comes from the 2D plane wave analysis in [35]. Here, I show how the 2D analysis extends to 3D, still assuming the fibers are constrained to lied at the 2D surface. The 2D analysis for wave motion orthogonal to propagation extends directly to 3D for Love waves and SH-waves. The analysis for wave motion in the same direction as propagation extends directly to 3D for Rayleigh waves, P-waves and SV-waves. I use the same notation here as in Chapter 2 for each type of wave considered.

D.1 Rayleigh waves

As noted in Table 2.2, the point-wise axial strain in the direction $(C_\theta, \mathcal{S}_\theta, 0)$ at location $(x, y, 0)$ and time t to a Rayleigh wave propagating in the direction $(C_\phi, \mathcal{S}_\phi, 0)$ is $\dot{\sigma}_\theta(x, y, 0, t) = ck^2 C^2_{(\phi-\theta)} \left(Ae^{-\gamma_\alpha kz} + iB\gamma_\beta e^{-\gamma_\beta kz}\right) e^{ik(ct - xC_\phi - y\mathcal{S}_\phi)}$. Thus, if I were to have a horizontal fiber at the same location rotated counterclockwise by $\pi/2$, its point-wise axial

strain at the same location would be

$$\begin{aligned}
\dot{\sigma}_{\theta+\pi/2}(x,y,0,t) &= ck^2 C^2_{(\phi-\theta-\pi/2)} \left(Ae^{-\gamma_\alpha kz} + iB\gamma_\beta e^{-\gamma_\beta kz} \right) e^{ik(ct-xC_\phi - yS_\phi)} \\
&= \dot{\sigma}_\theta(x,y,0,t) \frac{C^2_{(\phi-\theta-\pi/2)}}{C^2_{(\phi-\theta)}} \\
&= \dot{\sigma}_\theta(x,y,0,t) \left(\frac{C_{(\phi-\theta)}C_{\pi/2} + S_{(\phi-\theta)}S_{\pi/2}}{C_{(\phi-\theta)}} \right)^2 \\
&= \dot{\sigma}_\theta(x,y,0,t) \left(\frac{S_{(\phi-\theta)}S_{\pi/2}}{C_{(\phi-\theta)}} \right)^2 \\
&= \dot{\sigma}_\theta(x,y,0,t) \left(\frac{S_{(\phi-\theta)}}{C_{(\phi-\theta)}} \right)^2 \\
&= \dot{\sigma}_\theta(x,y,0,t) \tan^2(\phi-\theta)
\end{aligned}$$

We can also check on the relationship when rotated clockwise by $\pi/2$:

$$\begin{aligned}
\dot{\sigma}_{\theta-\pi/2}(x,y,0,t) &= ck^2 C^2_{(\phi-\theta-\pi/2)} \left(Ae^{-\gamma_\alpha kz} + iB\gamma_\beta e^{-\gamma_\beta kz} \right) e^{ik(ct-xC_\phi - yS_\phi)} \\
&= \dot{\sigma}_\theta(x,y,0,t) \frac{C^2_{(\phi-\theta+\pi/2)}}{C^2_{(\phi-\theta)}} \\
&= \dot{\sigma}_\theta(x,y,0,t) \left(\frac{C_{(\phi-\theta)}C_{-\pi/2} + S_{(\phi-\theta)}S_{-\pi/2}}{C_{(\phi-\theta)}} \right)^2 \\
&= \dot{\sigma}_\theta(x,y,0,t) \left(\frac{S_{(\phi-\theta)}S_{-\pi/2}}{C_{(\phi-\theta)}} \right)^2 \\
&= \dot{\sigma}_\theta(x,y,0,t) \left(\frac{S_{(\phi-\theta)}}{C_{(\phi-\theta)}} \right)^2 \\
&= \dot{\sigma}_\theta(x,y,0,t) \tan^2(\phi-\theta)
\end{aligned}$$

Of course the steps above don't all apply if $\phi - \theta = \pm\pi/2$. In that case, however, $\dot{\sigma}_\theta(x,y,0,t) = 0$, and $\dot{\sigma}_{\theta\pm\pi/2}(x,y,0,t) = ck^2 \left(Ae^{-\gamma_\alpha kz} + iB\gamma_\beta e^{-\gamma_\beta kz} \right) e^{ik(ct-xC_\phi - yS_\phi)}$ so their ratio is infinite, just as $\tan(\pm\pi/2)^2$ is also infinite. Thus, for all ϕ, θ combinations, the ratio between the point-wise axial strain measurements of two collocated horizonta but orthogonal fibers is $\tan^2(\phi-\theta)$. The trend from 2D analysis of wave motion in the direction of

propagation holds true in 3D for Rayleigh waves.

D.2 Love waves

As noted in Table 2.2, the point-wise axial strain in the direction $(C_\theta, \mathcal{S}_\theta, 0)$ at location $(x, y, 0)$ and time t to a Love wave propagating in the direction $(C_\phi, \mathcal{S}_\phi, 0)$ is $\dot{\sigma}_\theta(x, y, 0, t) = -\frac{ck^2}{2}\mathcal{S}_{2(\phi-\theta)}(Ae^{-i\eta_1 kz} + Be^{i\eta_1 kz})e^{ik(ct-xC_\phi-y\mathcal{S}_\phi)}$. Thus, if I were to have a horizontal fiber at the same location rotated counterclockwise by $\pi/2$, its point-wise axial strain at the same location would be

$$\begin{aligned}
\dot{\sigma}_{\theta+\pi/2}(x, y, 0, t) &= -\frac{ck^2}{2}\mathcal{S}_{2(\phi-\theta-\pi/2)}(Ae^{-i\eta_1 kz} + Be^{i\eta_1 kz})e^{ik(ct-xC_\phi-y\mathcal{S}_\phi)} \\
&= \dot{\sigma}_\theta(x, y, 0, t)\frac{\mathcal{S}_{2(\phi-\theta-\pi/2)}}{\mathcal{S}_{2(\phi-\theta)}} \\
&= \dot{\sigma}_\theta(x, y, 0, t)\frac{C_\pi\mathcal{S}_{2(\phi-\theta)} - \mathcal{S}_\pi C_{2(\phi-\theta)}}{\mathcal{S}_{2(\phi-\theta)}} \\
&= \dot{\sigma}_\theta(x, y, 0, t)\frac{-\mathcal{S}_{2(\phi-\theta)}}{\mathcal{S}_{2(\phi-\theta)}} \\
&= -\dot{\sigma}_\theta(x, y, 0, t)
\end{aligned}$$

Likewise, we could do the same with a clockwise rotation:

$$\begin{aligned}
\dot{\sigma}_{\theta-\pi/2}(x, y, 0, t) &= -\frac{ck^2}{2}\mathcal{S}_{2(\phi-\theta+\pi/2)}(Ae^{-i\eta_1 kz} + Be^{i\eta_1 kz})e^{ik(ct-xC_\phi-y\mathcal{S}_\phi)} \\
&= \dot{\sigma}_\theta(x, y, 0, t)\frac{\mathcal{S}_{2(\phi-\theta+\pi/2)}}{\mathcal{S}_{2(\phi-\theta)}} \\
&= \dot{\sigma}_\theta(x, y, 0, t)\frac{C_{-\pi}\mathcal{S}_{2(\phi-\theta)} - \mathcal{S}_{-\pi}C_{2(\phi-\theta)}}{\mathcal{S}_{2(\phi-\theta)}} \\
&= \dot{\sigma}_\theta(x, y, 0, t)\frac{-\mathcal{S}_{2(\phi-\theta)}}{\mathcal{S}_{2(\phi-\theta)}} \\
&= -\dot{\sigma}_\theta(x, y, 0, t)
\end{aligned}$$

These steps fall apart when $\phi = \theta$, but in that case both $\dot{\sigma}_\theta(x, y, 0, t) = 0$ and $\dot{\sigma}_{\theta\pm\pi/2}(x, y, 0, t) = 0$, so one is still the negative of the other. The 2D analysis of wave motion orthogonal to

propagation direction holds true in 3D for Love waves.

D.3 P-waves

As noted in Table 2.2, the point-wise axial strain in the direction $(C_\theta, S_\theta, 0)$ at location $(x, y, 0)$ and time t to a P-wave propagating in the direction $(C_{\phi_1}C_{\phi_2}, S_{\phi_1}C_{\phi_2}, S_{\phi_2})$ is $\dot{\sigma}_\theta(x, y, 0, t) = ck^2C^2_{(\phi_1-\theta)}C^2_{\phi_2}Ae^{ik(ct-xC_{\phi_1}C_{\phi_2}-yS_{\phi_1}C_{\phi_2}-zS_{\phi_2})}$. Thus, if I were to have a horizontal fiber at the same location rotated counterclockwise by $\pi/2$, its point-wise axial strain at the same location would be

$$\begin{aligned}
\dot{\sigma}_{\theta+\pi/2}(x, y, 0, t) &= ck^2C^2_{(\phi_1-\theta-\pi/2)}C^2_{\phi_2}Ae^{ik(ct-xC_{\phi_1}C_{\phi_2}-yS_{\phi_1}C_{\phi_2}-zS_{\phi_2})} \\
&= \dot{\sigma}_\theta(x, y, 0, t)\frac{C^2_{(\phi_1-\theta-\pi/2)}}{C^2_{(\phi_1-\theta)}} \\
&= \dot{\sigma}_\theta(x, y, 0, t)\left(\frac{C_{(\phi_1-\theta)}C_{\pi/2} + S_{(\phi_1-\theta)}S_{\pi/2}}{C_{(\phi_1-\theta)}}\right)^2 \\
&= \dot{\sigma}_\theta(x, y, 0, t)\left(\frac{S_{(\phi_1-\theta)}}{C_{(\phi_1-\theta)}}\right)^2 \\
&= \dot{\sigma}_\theta(x, y, 0, t)\tan^2(\phi_1 - \theta)
\end{aligned}$$

The relationship works out similarly for rotating the fiber clockwise by $\pi/2$. These steps fall apart when $\phi_1 - \theta = \pm\pi/2$, but in that case, $\dot{\sigma}_\theta(x, y, 0, t) = 0$, while $\dot{\sigma}_{\theta+\pi/2}(x, y, 0, t)$ is nonzero, so their ratio is inifinite, as is $\tan^2(\phi_1 - \theta)$. The 2D analysis of wave motion in the direction of propagation holds true in 3D for P waves.

D.4 SV-waves

As noted in Table 2.2, the point-wise axial strain in the direction $(C_\theta, S_\theta, 0)$ at location $(x, y, 0)$ and time t to an SV-wave propagating in the direction $(C_{\phi_1}C_{\phi_2}, S_{\phi_1}C_{\phi_2}, S_{\phi_2})$ is $\dot{\sigma}_\theta(x, y, 0, t) = -\frac{ck^2}{2}C^2_{(\phi_1-\theta)}S_{2\phi_2}Ae^{ik(ct-xC_{\phi_1}C_{\phi_2}-yS_{\phi_1}C_{\phi_2}-zS_{\phi_2})}$. Thus, if I were to have a horizontal fiber at the same location rotated counterclockwise by $\pi/2$, its point-wise axial

strain at the same location would be

$$\begin{aligned}
\dot{\sigma}_{\theta+\pi/2}(x,y,0,t) &= -\frac{ck^2}{2}C^2_{(\phi_1-\theta-\pi/2)}\mathcal{S}_{2\phi_2}Ae^{ik(ct-xC_{\phi_1}C_{\phi_2}-y\mathcal{S}_{\phi_1}C_{\phi_2}-z\mathcal{S}_{\phi_2})} \\
&= \dot{\sigma}_\theta(x,y,0,t)\left(\frac{C_{(\phi_1-\theta-\pi/2)}}{C_{(\phi_1-\theta)}}\right)^2 \\
&= \dot{\sigma}_\theta(x,y,0,t)\left(\frac{C_{(\phi_1-\theta)}C_{\pi/2)}+\mathcal{S}_{(\phi_1-\theta)}\mathcal{S}_{\pi/2)}}{C_{(\phi_1-\theta)}}\right)^2 \\
&= \dot{\sigma}_\theta(x,y,0,t)\left(\frac{\mathcal{S}_{(\phi_1-\theta)}}{C_{(\phi_1-\theta)}}\right)^2 \\
&= \dot{\sigma}_\theta(x,y,0,t)\tan^2(\phi_1-\theta)
\end{aligned}$$

Again, the relationship works out to be the same when the fiber is rotated clockwise by $\pi/2$. Again, these steps don't work when $\phi_1-\theta=\pm\pi/2$, but that's a case where $\dot{\sigma}_\theta(x,y,0,t)=0$ and $\dot{\sigma}_{\theta+\pi/2}(x,y,0,t)$ can be nonzero, while $\tan^2(\phi_1-\theta)$ goes to infinity. The trend from the 2D analysis holds true for SV waves in 3D.

D.5 SH-waves

As noted in Table 2.2, the point-wise axial strain in the direction $(C_\theta,\mathcal{S}_\theta,0)$ at location $(x,y,0)$ and time t to an SH-wave propagating in the direction $(C_{\phi_1}C_{\phi_2},\mathcal{S}_{\phi_1}C_{\phi_2},\mathcal{S}_{\phi_2})$ is $\dot{\sigma}_\theta(x,y,0,t)=\frac{ck^2}{2}\mathcal{S}_{2(\phi_1-\theta)}C_{\phi_2}Ae^{ik(ct-xC_{\phi_1}C_{\phi_2}-y\mathcal{S}_{\phi_1}C_{\phi_2}-z\mathcal{S}_{\phi_2})}$. Thus, if I were to have a horizontal fiber at the same location rotated counterclockwise by $\pi/2$, its point-wise axial strain at the same location would be

$$\begin{aligned}
\dot{\sigma}_{(\theta+\pi/2)}(x,y,0,t) &= \frac{ck^2}{2}\mathcal{S}_{2(\phi_1-\theta-\pi/2)}C_{\phi_2}Ae^{ik(ct-xC_{\phi_1}C_{\phi_2}-y\mathcal{S}_{\phi_1}C_{\phi_2}-z\mathcal{S}_{\phi_2})} \\
&= \dot{\sigma}_\theta(x,y,0,t)\frac{\mathcal{S}_{2(\phi_1-\theta-\pi/2)}}{\mathcal{S}_{2(\phi_1-\theta)}} \\
&= \dot{\sigma}_\theta(x,y,0,t)\frac{C_\pi\mathcal{S}_{2(\phi_1-\theta)}-\mathcal{S}_\pi C_{2(\phi_1-\theta)}}{\mathcal{S}_{2(\phi_1-\theta)}} \\
&= \dot{\sigma}_\theta(x,y,0,t)\frac{-\mathcal{S}_{2(\phi_1-\theta)}}{\mathcal{S}_{2(\phi_1-\theta)}} \\
&= -\dot{\sigma}_\theta(x,y,0,t)
\end{aligned}$$

The analysis works out to be the same if I were to rotate the fiber clockwise. These steps fall apart when $\phi_1 = \theta$ but that is when both $\dot{\sigma}_\theta(x, y, 0, t) = 0$ and $(\sigma + \dot{\pi}/2)_\theta(x, y, 0, t) = 0$. The relationship from the 2D analysis of wave motion orthogonal to propagation direction holds true in 3D for SH-waves.

Bibliography

[1] Emergence of broadband Rayleigh waves from correlations of the ambient seismic noise. *Geophys. Res. Lett.*, 31(7):L07614, 2004.

[2] J. Ajo-Franklin, S. Dou, N. Lindsey, T.M. Daley, B. Freifeld, E.R. Martin, M. Robertson, C. Ulrich, T. Wood, I. Eckblaw, and A. Wagner. Timelapse surface wave monitoring of permafrost thaw using distributed acoustic sensing and a permanent automated seismic source. In *Expanded Abstracts of the 87th SEG Ann. Internat. Mtg.*, pages 5223–5227, 2017.

[3] J. Ajo-Franklin, N. Lindsey, S. Dou, T.M. Daley, B. Freifeld, E.R. Martin, M. Robertson, C. Ulrich, and A. Wagner. A field test of distributed acoustic sensing for ambient noise recording. In *Expanded Abstracts of the 85th SEG Ann. Internat. Mtg.*, pages 2620–2624, 2015.

[4] J.B. Ajo-Franklin, N. Lindsey, S. Dou, B.M. Freifeld, T.M. Daley, C. Tracy, and I. Monga. Dark fiber and distributed acoustic sensing: Applications to monitoring seismicity and near-surface properties. In *AGU Fall Meeting Abstracts*, pages S33B–0870, 2017.

[5] S.K. Bakku. *Fracture Characterization from Seismic Measurements in a Borehole*. PhD thesis, Massachusetts Institute of Technology, Cambridge, MA, 2015.

[6] H. Benioff. A linear strain seismograph. *Bulletin of the Seismological Society of America*, 25(4):283–209, 1935.

[7] G.D. Bensen, M.H. Ritzwoller, M.P. Barmin, A.L. Levshin, F. Lin, M.P. Moschetti, N.M. Shapiro, and Y. Yang. Processing seismic ambient noise data to obtain reliable

broad-band surface wave dispersion measurements. *Geophys. J. Int.*, 169:1239–1269, 2007.

[8] A. Bona, T. Dean, J. Correa, R. Pevzner, K.V. Tertyshnikov, and L. Van Zaanen. Amplitude and phase response of DAS receivers. In *79th EAGE Conference and Exhibition in Paris, France*, page We A5 13, 2017.

[9] E. Castongia, H.F. Wang, N. Lord, D. Fratta, M. Mondanos, and A. Chalari. An experimental investigation of distributed acoustic sensing (das) on lake ice. *Journal of Environmental and Engineering Geophysics*, 22(2):167–176, 2017.

[10] J.P. Chang. Velocity dispersion at Long Beach. In *SEP 150*, pages 101–108, 2013.

[11] J.P. Chang, S.A.L. de Ridder, and B.L. Biondi. High-frequency Rayleigh-wave tomography using traffic noise from Long Beach, California. *Geophysics*, 81(2):B43–B53, 2016.

[12] T. Clements and M. Denolle. Observing drought-induced groundwater depletion in California with seismic noise. In *AGU Fall Meeting Abstract*, pages S31A–0802, 2017.

[13] A. Constantinou, A. Farahani, T. Cuny, and A. Hartog. Improving DAS acquisition by real-time monitoring of wireline cable coupling. In *Expanded Abstracts of the 86th SEG Ann. Internat. Mtg.*, pages 5603–5607, 2016.

[14] T.M. Daley, B.M. Freifeld, J. Ajo-Franklin, S. Dou, R. Pevzner, V. Shulakova, S. Kashikar, D.E. Miller, J. Goetz, J. Henninges, and S. Lueth. Field testing of fiber-optic distributed acoustic sensing (DAS) for subsurface seismic monitoring. *The Leading Edge*, 32:936–942, 2013.

[15] E. Daskalakis, C. Evangelidis, J. Garnier, N. Melis, G. Papanicolaou, and C. Tsoga. Robust seismic velocity change estimation using ambient noise recordings. *Geophys. J. Int.*, 205:1926–1936, 2016.

[16] S. de Ridder. *Passive seismic surface-wave interferometry for reservoir-scale imaging*. PhD thesis, Stanford University, Mar. 2014.

[17] S.A.L. de Ridder and B.L. Biondi. Daily reservoir-scale subsurface monitoring using ambient seismic noise. *Geophys. Res. Lett.*, 40:1–6, 2013.

[18] S.A.L. de Ridder, B.L. Biondi, and R.G. Clapp. Time-lapse seismic noise correlation tomography at Valhall. *Geophys. Res. Lett.*, 41:6116–6122.

[19] T. Dean, T. Cuny T., and A.H. Hartog. The effect of gauge length on axially incident p-waves measured using fibre optic distributed vibration sensing. *Geophysical Prospecting*, 65(1):184–193, 2017.

[20] S. Dou and J.B. Ajo-Franklin. Full-wavefield inversion of surface waves for mapping embedded low-velocity zones in permafrost. *Geophysics*, 79(6):EN107–EN124, 2014.

[21] S. Dou, N. Lindsey, A. Wagner, T. Daley, B. Freifeld, M. Robertson, J. Peterson, C. Ulrich, E. Martin, and J. Ajo-Franklin. Distributed acoustic sensing for seismic monitoring of the near surface: A traffic-noise interferometry example. *Scientific Reports*, 7:article 11620, 2017.

[22] L. Ermert, K. Sager, M. Afanasiev, C. Boehm, and A. Fichtner. Ambient seismic source inversion in a heterogeneous Earth: Theory and application to the Earth's hum. *J. Geophys. Res.: Solid Earth*, 122(11):9184–9207, 2017.

[23] J.R. Evans, R.M. Allen, A.I. Chung, E.S. Cochran, R. Guy, M. Hellweg, and J.F. Lawrence. Performance of several low-cost accelerometers. *Seismol. Res. Lett.*, 85(1):148–158, 2014.

[24] A. Fichtner, L. Stehly, L. Ermert, and C. Boehm. Generalized interferometry - i: theory for interstation correlations. *Geophys. J. Int.*, 208:603–638, 2017.

[25] Incorporated Research Institutions for Seismology. Wilber3. https://ds.iris.edu/wilber3/find_event.

[26] S.M. Hanasoge and M. Branicki. Interpreting cross-correlations of one-bit filtered seismic noise. *Geophys. J. Int.*, 195(3):1811–1830, 2013.

[27] M. Iten. *Novel Applications of Distributed Fiber-optic Sensing in Geotechnical Engineering*. PhD thesis, ETH Zürich, Zürich, Switzerland, 2011.

[28] P. Jousset, T. Reinsch, J. Henninges, H. Blanck, and T. Ryberg. Crustal exploration and monitoring seismic events with a fibre-optic cable deployed at the ground surface in Iceland. In *Abstracts of the EAGE/DGG Workshop on Fibre Optic Technology in Geophysics*, 2017.

[29] M. Karrenbach, D. Kahn, S. Cole, A. Ridge, K. Boone, J. Rich, K. Silver, and D. Langton. Hydraulic-fracturing-induced strain and microseismic using in situ distributed fiber-optic sensing. *The Leading Edge*, Oct.:837–844, 2017.

[30] B.N. Kuvshinov. Interaction of helically wound fibre-optic cables with plane seismic waves. *Geophysical Prospecting*, 64(3):671–688, 2016.

[31] C. Lancelle. *Distributed Acoustic Sensing for Imaging Near-Surface Geology and Monitoring Traffic at Garner Valley, California*. PhD thesis, University of Wisconsin - Madison, Madison, WI, 2016.

[32] T. Lecocq, L. Longuevergne, H.A. Pedersen, F. Brenguier, and K. Stammler. Monitoring ground water storage at mesoscale using seismic noise: 30 years of continuous observation and thermo-elastic and hydrological modeling. *Scientific Rep.*, 7:14241, 2017.

[33] F.C. Lin, M.P. Moschetti, and M.H. Ritzwoller. Surface wave tomography of the western United States from ambient seismic noise: Rayleigh and Love wave phase velocity maps. *Geophys. J. Internat.*, 173:281–298, 2008.

[34] N.J. Lindsey, S. Dou, E.R. Martin, A.M. Wagner, and J.B. Ajo-Franklin. 4D permafrost thaw observations from ambient road traffic noise and a very dense distributed fiber optic sensing array. In *AGU Fall Meeting Abstract*, pages S31A–0804, 2017.

[35] N.J. Lindsey, E.R. Martin, D.S. Dreger, B. Freifeld, S. Cole, S.R. James, B.L. Biondi, and J.B. Ajo-Franklin. Fiber-optic network observations of earthquake wavefields. *Geophys. Res. Lett.*, 44(23):11,792–11,799, 2017.

[36] J.N. Louie. Faster, better: Shear-wave velocity to 100 meters depth from refraction microtremor arrays. *Bulletin of the Seismological Society of America*, 91(2):347–364, 2001.

[37] E.R. Martin, J.B. Ajo-Franklin, N.J. Lindsey, T. Daley, B. Freifeld, M. Robertson, C. Ulrich, S. Dou, and A. Wagner. Applying interferometry to ambient seismic noise recorded by a trenched distributed acoustic sensing array. In *SEP 158*, pages 247–254, 2015.

[38] E.R. Martin, B. Biondi, M. Karrenbach, and S. Cole. Ambient noise interferometry from DAS array in underground telecommunications conduits. In *Technical Programme of the 79th EAGE Conference & Exhibition*, 2017b.

[39] E.R. Martin and B.L. Biondi. Time-lapse changes in ambient noise interferometry and dispersion analysis at the Stanford DAS array. In *SEP Report 170*, pages 45–56, 2017.

[40] E.R. Martin, C.M. Castillo, S. Cole, P.S. Sawasdee, S. Yuan, R. Clapp, M. Karrenbach, and B.L. Biondi. Seismic monitoring leveraging existing telecom infrastructure at the Stanford distributed acoustic sensing array: Active, passive and ambient noise analysis. *The Leading Edge*, 36(12):1025–1031, 2017.

[41] E.R. Martin, F. Huot, Y. Ma, R. Cieplicki, S. Cole, M. Karrenbach, and B.L. Biondi. A seismic shift in scalable acquisition demands new processing: Fiber-optic seismic signal retrieval in urban areas with unsupervised learning for coherent noise removal. *IEEE Signal Processing Magazine*, 35(2):31–40, 2018.

[42] E.R. Martin, N.J. Lindsey, S. Dou, J.B. Ajo-Franklin, A. Wagner, K. Bjella, T.M. Daley, B. Freifeld, M. Robertson, and C. Ulrich. Interferometry of a roadside DAS array in Fairbanks, AK. In *Expanded Abstracts of the 86th SEG Ann. Internat. Mtg.*, pages 2725–2729, 2016.

[43] A. Mateeva, J. Lopez, J. Mestayer, P. Wills, B. Cox, D. Kiyashchenko, Z. Yang, W. Berlang, R. Detomo, and S. Grandi. Distributed acoustic sensing for reservoir monitoring with VSP. *The Leading Edge*, 32:1278–1283, 2013A.

[44] A. Mateeva, J. Lopez, H. Potters, J. Mestayer, B. Cox, D. Kiyashchenko, P. Wills, S. Grandi, K. Hornman, B. Kuvshinov, W. Berlang, Z. Yang, and R. Detomo. Distributed acoustic sensing for reservoir monitoring with vertical seismic profiling. *Geophysical Prospecting*, 62(4):679–692, 2014.

[45] A. Mateeva, J. Mestayer, B. Cox, D. Kiyashchenko, P. Wills, J. Lopez, S. Grandi, K. Hornman, P. Luments, A. Franzen, D. Hill, and J. Roy. Advances in distributed acoustic sensing (DAS) for VSP. In *Expanded Abstracts of the 82nd SEG Ann. Internat. Mtg.*, pages 1–5, 2012.

[46] A. Mateeva, J. Mestayer, Z. Yang, J. Lopez, P. Wills, J. Roy, and T. Bown. Dual-well 3D VSP in deepwater made possible by DAS. In *Expanded Abstracts of the 83rd SEG Ann. Internat. Mtg.*, pages 5062–5066, 2013.

[47] J. Mestayer, B. Cox, P. Wills, D. Kiyashchenko, J. Lopez, M. Costello, S. Bourne, G. Ugueto, R. Lupton, G. Solano, D. Hill, A. Lewis, and Q. Qineti. Field trials of distributed acoustic sensing for geophysical monitoring. In *Expanded Abstracts of the 81st SEG Ann. Internat. Mtg.*, pages 4253–4257, 2011.

[48] D.E. Miller, T.M. Daley, B.M. Freifeld, M. Robertson, J. Cocker, and M. Craven. Simultaneous acquisition of distributed acoustic sensing VSP with multi-mode and single-mode fiber-optic cables and 3C-geophones at the Aquistore CO_2 storage site. *CSEG Recorder*, 41(6):28–33, 2016.

[49] N. Nakata, J.P. Chang, J.F. Lawrence, and P. Boué. Body wave extraction and tomography at Long Beach, California, with ambient noise interferometry. *J. Geophys. Res.: Solid Earth*, 120(2):1159–1173, 2015.

[50] N. Nakata, R. Snieder, T. Tsuji, K. Larner, and T. Matsuoka. Shear wave imaging from traffic noise using seismic interferometry by cross-coherence. *Geophysics*, 76(6):SA97–SA106, 2011.

[51] N. Nakata, R. Snieder, T. Tsuji, K. Larner, and T. Matsuoka. Shear wave imaging from traffic noise using seismic interferometry by cross-coherence. *Geophysics*, 76(6):SA97–SA106, 2012.

[52] E.A. Olafsdottir, S. Erlingsson, and B. Bessason. Tool for analysis of multichannel analysis of surface waves (MASW) field data and evaluation of shear wave velocity profiles of soils. *Canadian Geotechnical Journal*, 55(2):217–233, 2018.

[53] C.B. Park, R.D. Miller, and J. Xia. Multichannel analysis of surface waves. *Geophysics*, 64(3):800–808, 1999.

[54] R. Posey, G.A. Johnson, and S.T. Vohra. Strain sensing based on coherent Rayleigh scattering in an optical fibre. *Electronics Letters*, 36(20):1688–1689, 2000.

[55] J. Pujol. *Elastic Wave Propagation and Generation in Seismology*. Cambridge Univ. Press, Cambridge, UK, 2003.

[56] S. Rost and C. Thomas. Array seismology: methods and applications. *Reviews of Geophysics*, 40:2–1–2–27, 2002.

[57] K.G. Sabra, P. Gerstoft, P. Roux, W.A. Kuperman, and M.C. Fehler. Extracting time-domain Green's function estimates from ambient seismic noise. *Geophys. Res. Lett.*, 32:L03310, 2005.

[58] K.J. Seats, J.F. Lawrence, and G.A. Prieto. Improved ambient noise correlation functions using Welch's method. *Geophys. J. Int.*, 188(2):513–523, 2012.

[59] S.V. Shatalin, V.N. Treschikov, and A.J. Rogers. Interferometric optical time-domain reflectometry for distributed optical-fibre sensing. In *SPIE Conference on Laser Interferometry IX: Applications*, pages 181–191, 1998.

[60] T. Taira, F. Brenguier, and Q. Kong. Ambient noise-based monitoring of seismic velocity changes associated with the 2014 M_w 6.0 South Napa earthquake. *Geophys. Res. Lett.*, 42(17):6997–7004, 2015.

[61] P. Thomas, I. Wong, J. Zachariasen, R. Darragh, and W. Silva. 2013 update to the site-specific seismic hazard analyses and development of seismic design ground motions: Stanford University, California. Technical report, URS Corporation and Pacific Engineering & Analysis, 2013.

[62] I. Vansconcelos and R. Snieder. Interferometry by deconvolution, part 1- theory for acoustic waves and numerical examples. *Geophysics*, 73(3):S115–S128, 2008.

[63] A. Wagner, N.J. Lindsey, S. Dou, A. Gelvin, S. Saari, C. Williams, I. Ekblaw, C. Ulrich, S. Borglin, A. Morales, and J. Ajo-Franklin. Thermokarst-on-demand: Observations from a deep permafrost warming experiment. *preprint*, 2018.

[64] H.F. Wang, X. Zeng, D.E. Miller, D. Fratta, K.L. Feigle, C.H. Thurber, and R.J. Mellors. Ground motion response to a ML 4.3 earthquake using co-located distributed acoustic sensing and seismometer arrays. *Geophys. J. Int.*, 312(3):2020–2036, 2018.

[65] K. Wapenaar, D. Draganov, R. Snieder, X. Campman, and A. Verdel. Tutorial on seismic interferometry: Part 1- basic principles and applications. *Geophysics*, 75(5):75A195–75A209, 2010.

[66] K. Wapenaar, E. Slob, R. Snieder, and A. Curtis. Tutorial on seismic interferometry: Part 2 - underlying theory and new advances. *Geophysics*, 75(5):75A211–75A227, 2010.

[67] R.L. Weaver and O.I. Lobkis. Diffuse fields in open systems and the emergence of the Green's function. *J. Acoust. Soc. Am.*, 116:2731–2734, 2004.

[68] P. Webster, J. Wall, C. Perkins, and M. Molenaar. Micro-seismic detection using distributed acoustic sensing. In *Expanded Abstracts of the 83rd SEG Ann. Internat. Mtg.*, pages 2459–2463, 2013.

[69] W.L. Yeck, G.P. Hayes, D.E. McNamera, J.L. Rubinstein, W.D. Barnhart, P.S. Earle, and H.M. Benz. Oklahoma experiences largest earthquake during ongoing regional wastewater injection hazard mitigation efforts. *Geophys. Res. Lett.*, 44(2):711–717, 2017.

[70] X. Zeng, C. Lancelle, C. Thurber, D. Fratta, H. Wang, N. Lord, A. Chalari, and A. Clarke. Properties of noise cross-correlation functions obtained from a distributed acoustic sensing array at Garner Valley, California. *Bulletin of the Seismological Society of America*, 107(2):603–610, 2017.

[71] X. Zeng, C. Thurber, H. Wang, D. Fratta, E. Matzel, and PoroTomo Team. High-resolution shallow structure revealed with ambient noise tomography on a dense array. *Proceedings, 42nd Workshop on Geothermal Reservoir Engineering*, 2017.

[72] Z. Zhan, V.C. Tsai, and R.W. Clayton. Spurious velocity changes caused by temporal variations in ambient noise frequency content. *Geophys. J. Int.*, 194(3):1574–1581, 2013.

[73] R.W. Zimmerman and M.S. King. The effect of the extent of freezing on seismic velocities in unconsolidated permafrost. *Geophysics*, 51(6):1285–1290.